THE SECRET LIVES OF BATTERY MATERIALS: CORE-LEVEL SPECTROSCOPY AS A PROBE OF COMPOSITIONAL AND ELECTRONIC STRUCTURE INHOMOGENEITIES

A Dissertation

by

LUIS RAFAEL DE JESUS BAEZ

Submitted to the Office of Graduate and Professional Studies of
Texas A&M University
in partial fulfillment of the requirements for the degree of

DOCTOR OF PHILOSOPHY

Chair of Committee,	Sarbajit Banerjee
Committee Members,	James Batteas
	Michael B. Hall
	Raymundo Arroyave
Head of Department,	Simon North

August 2018

Major Subject: Chemistry

ABSTRACT

The invention of rechargeable batteries has dramatically changed our landscapes and lives, underpinning the explosive worldwide growth of consumer electronics, ushering in an unprecedented era of electric vehicles, and potentially paving the way for a much greener energy future. Unfortunately, current battery technologies suffer from a number of challenges, e.g., capacity loss and failure upon prolonged cycling, limited ion diffusion kinetics, and a rather sparse palette of high-performing electrode materials. This dissertation will focus on elucidation of the influence of electronic structure on intercalation phenomena. Mechanistic understanding of compositional and electronic structure heterogeneities spanning from atomistic to mesoscale dimensions is imperative to facilitate the rational design of novel electrode chemistries and architectures. First, this dissertation provides an introduction to the fundamental science challenges involved in electrode design utilizing V_2O_5 as a model system to review means of defining ionic and electronic conduction pathways. Subsequently, the oxidative chemistry of graphite, a canonical anode material, is evaluated with the purpose of understanding the spatial localization and connectivity of functional groups in graphene oxide, which is of utmost relevance to the design of high-performing electrode composites. Furthermore, scanning transmission X-ray microscopy (STXM) observations indicate the formation of lithiation gradients in individual nanowires of layered orthorhombic V_2O_5 that arise from electron localization and local structural distortions. Electrons localized in the V_2O_5 framework couple to a local structural distortion, giving rise to small polarons, which are observed to be trap Li-ions and are found to represent a major impediment to Li-ion diffusion. In

addition, this dissertation presents the first direct visualization of patterns of compositional inhomogeneities within cathode materials during electrochemical discharge. Two distinct patterns are evidenced: core—shell separation and striping modulations of Li-rich and Li-poor domains within individual particles. 3D compositional maps have been developed and translated to stress and strain maps, providing a hitherto unprecedented direct visualization of stress and strain inhomogeneities. Finally, a cluster of interlaced $Li_xV_2O_5$ nanoparticles is evaluated by scanning transmission X-ray microscopy. Increased heterogeneity at the interface between particles suggests the exchange of Li-ions, implying a "winner-takes-all" behavior (corresponding to particle-by-particle lithiation of an ensemble of particles). Such behavior portends the creation of localized hot-spots and provides insight into a possible origin of failure of Li-ion batteries.

DEDICATION

This crazy ride that is graduate school has had many individuals that have served as contributors and support, and everyone deserves a huge appreciation for helping in the process. With that being said, I would like to dedicate this dissertation to three special people in my life: my mother, my father, and my brother. Janice Báez Sánchez, “ma”, even after passing away, all the sacrifices and your instructions paved the way and helped me develop as the professional that I am today. Samuel De Jesús Trujillo, “pa”, thank you for becoming a mental and emotional support during my years as a graduate student. My strength and my will to go through wouldn’t have been the same without you or without your advices. To my brother, Daniel J. De Jesús Báez, it has been a pleasure to enjoy the growth we’ve had together during the last five years. In addition, the support of my family, Abuelo Luis, Abuela Gladys, Abuela Raquel, Abuelo Rafael, Titi Magaly, Titi Tita, Tio Alfredo, Tio Noel, and my closest friends, Hector, Humberto, and Melissa has also been of utmost importance for the formation of the person I am today.

ACKNOWLEDGEMENTS

First and foremost, I cannot express in written words the gratitude and respect that I have of my supervisor, Prof. Sarbajit Banerjee. My tenure as a graduate student has been a complex one and Prof. Banerjee has been able to use every moment to instruct and mentor me to become a better chemist and scientist. It has been my greatest honor to work under the tutelage of an instructor of his caliber.

I would also want to acknowledge my committee members, Prof. James Batteas, Prof. Michael Hall, and Prof. Raymundo Arroyave for their help during my time as a graduate student in Texas A&M University.

Since the start of graduate school, I have been fortunate to collaborate with exceptional research groups and people that have provided paramount help in the process. To this end, I would be remiss if I don't appreciate the help from Dr. Jian Wang at the Canadian Light Source for all the help and guidance whilst using the X-ray microscopy instrument and in every post-processing situation. The instruction from Dr. Jian Wang is what made all of this work possible. Every author that contributed to some extent to the chapters in this dissertation deserves to be appreciated. This dissertation is definitely the epitome of what collaboration can accomplish and, without your help, none of it would have been possible.

Finally, gratitude to friends, family, staff members from the department, faculty, colleagues, and present and past members of the Banerjee lab is necessary; you have definitely been indispensable during the process.

CONTRIBUTORS AND FUNDING SOURCES

Contributors

Contributions in Chapter II came from Dr. Robert Dennis and Dr. Sean Depner at the University of Buffalo – SUNY for their help with the sample preparation and TEM image of mapped sample, respectively. In addition, contributions in Chapter III came from Dr. Gregory Horrocks, Dr. Yufeng Liang, Abhishek Parija, Dr. David Prendergast, Dr. Linda Wangoh, and Prof. Louis Piper for the paramount help in the sample preparation, first-principles calculations, and XPS measurements. Also, contributions from Dr. Peter Stein, Dr. Ying Zhao, and Prof. Bai-Xiang Xu for the phase-field modeling in Chapter IV and Chapter V in this dissertation are recognized.

All of the electronic structure mapping in this dissertation would also not be possible if it were not for the magnificent facilities at the Canadian Light Source in Saskatoon, Saskatchewan, Canada. Specifically, the Spectro-Microscopy beamline is acknowledged for providing the instrument needed to perform all the measurements to acquire the maps.

Funding Sources

The work in this dissertation was supported by the National Science Foundation under the Graduate Research Fellowship under Grant No. 1252521 and also through the National Science Foundation DMR 1504702. In addition, the Natural Sciences and Engineering Research Council of Canada, the National Research Council Canada, the Canadian Institutes of Health Research, the Province of Saskatchewan, Western Economic Diversification Canada, and the University of Saskatchewan support the

Canadian Light Source. Density functional theory simulations were performed as part of a User Project The Molecular Foundry (TMF), Lawrence Berkeley National Laboratory and calculations were executed on their Vulcan and Nano compute clusters, administered by the High-Performance Computing Services Group at LBNL. TMF is supported by the Office of Science, Office of Basic Energy Sciences, of the U.S. Department of Energy, under Contract No. DE-AC02-05CH11231.

TABLE OF CONTENTS

Page

Page

Page

LIST OF FIGURES

Page

Page

Page

LIST OF TABLES

Page

CHAPTER I

INTRODUCTION AND MOTIVATION*

I.1 Introduction

As a result of the sharp fall in the levelized costs of electricity generation from renewable energy sources such as wind and solar and the increasing proportion of electricity generated from such intermittent sources,[1] the development of large-area energy storage formats has emerged as a critical imperative. The last decade has seen the emergence of a thriving landscape of energy storage options spanning the range from flywheels and pumped hydroelectric storage to intercalation, conversion, and flow batteries that each have distinctive advantages and are individually well suited to specific energy conversion scenarios.[2] Rechargeable intercalation batteries have rapidly gained prominence as scalable energy storage vectors that can provide high volumetric and gravimetric energy densities across hundreds of cycles.[3–5] The operation of an intercalation battery is predicated on the reversible insertion/extraction of a charged species (almost always Li-ions in current technologies) between a coupled pair of electrodes separated by an ionically conductive and electrically insulating electrolyte, accompanied by redox processes within the host matrix; the cations diffuse along chemical potential gradients during discharging of the battery and uphill against chemical potential gradients during charging, accompanied by current flow in an external circuit to maintain charge balance.[3–8] Whilst apparently straightforward in

---

conception, the operation of intercalation batteries requires multiscale charge and mass transfer processes across several interfaces. The reversible operation of batteries requires the unimpeded progression of a sequence of chemical reactions and charge transfer processes ranging from solvation/desolvation of cations at electrolyte/electrode interfaces to formation of an ion-permeable surface passivating layer at electrode surfaces, redox reactions at metal sites, and intercalation-induced solid—state transformations. These processes are inevitably also accompanied by less desirable pathways such as defect formation and diffusion, metal plating, and electrolyte decomposition. Mechanistic elucidation and predictive design of battery chemistries and architectures thus necessitate a precise understanding of ion and electron conduction pathways and the dynamical evolution of structure under applied potential, mechanical strain, and large compositional fluctuations.[9–11] Bottlenecks in the diffusion of ions and electrons give rise to pronounced inhomogeneities across porous electrode structures that profoundly impact energy dissipation, cyclability, and the proportion of actively intercalating materials. In this chapter, we review mechanistic ideas for directing cation diffusion across multiscale electrode architectures based on mapping of lithiation gradients, modeling of diffusion pathways, and topochemical stabilization of metastable polymorphs providing a variety of different conduction paths. Diffusion limitations are considered with respect to electron transport, ion diffusion, and coupled phenomena. A classical intercalation host, vanadium pentoxide (V_2O_5), having numerous accessible polymorphs in addition to the thermodynamically stable phase, is used as a model system to develop mechanistic ideas.[12,13]

Electrode materials for intercalation batteries must be designed keeping in mind a number of constraints related to the thermodynamics and kinetics of cation diffusion.[14–17] In order to obtain a large voltage, the differential in free energies of Li-ions across the pair of electrodes must be high; however, even the thermodynamically uphill process needs to be accessible under a potential bias (and must not be kinetically blocked). The insertion of Li-ions requires that the intercalation host have available a high density of available redox-active centers and insertion sites) and that intercalation sites are interconnected by low-energy diffusion pathways.[18]

Two broad classes of crystalline intercalation hosts can be distinguished based on the nature of their phase diagrams and intercalation mechanisms; materials wherein Li-ions are incorporated through formation of a continuous solid solution[19–21] and materials wherein Li-ion intercalation brings about a pronounced structural phase transformation. As arguably a case in point of the former, the layered structure of Li_xCoO_2 (and related solid solutions with substitutional incorporation of other elements on the Co site) is preserved over a broad range of Li-ion concentrations, yielding a structure that comports as a solid-solution across a considerable range of electrochemical conditions.[19,22] In the case of Li_xFePO_4, a classical nucleation and growth mechanism involving the initial nucleation of a Li-rich Li_xFePO_4 upon supersaturation of a Li-poor matrix and its subsequent propagation (with a considerable miscibility gap between the two phases) is supplanted by a much more rapid solid-solution formation pathway for nanometer-sized particles at high current rates and temperatures.[9,23–28] Both classes of structural transformations can give rise to multiscale inhomogeneous lithiation gradients as a result

of diffusion limitations. The consequences of such largescale inhomogeneities are profound, spanning the range from non-uniform energy dissipation and the creation of localized "hot spots" to large anisotropic stress that brings about electrode pulverization.

A critical imperative that has emerged is the identification of electrode chemistries and the design of precisely structured architectures that allow for diffusion of cations along programmable pathways. Such electrode design requires consideration of phenomena spanning the range from atomistic to mesoscale dimensions and events spanning the range from individual hopping of cations between adjacent sites to shearing of lattices to accommodate phase transformations and the entire deformation of particles and porous particulate networks. In order to facilitate electrode design, detailed multiscale understanding of diffusion phenomena must be coupled with predictive modeling and synthetic schemes. The subsequent sections review recent results related to deciphering multiscale diffusion phenomena using a layered classical intercalation host V_2O_5 as a model system along with advances related to atomistic and mesoscale design implemented as a means of circumventing the diffusion bottlenecks identified in mechanistic studies.

α-V_2O_5 is an orthorhombic, layered compound that crystallizes with a space group symmetry of *Pmmn*.[29] In this structure, [VO_5] pyramids, the fundamental building block of α-V_2O_5, are connected by shared edges and corners to form zigzag lamellar sheets along the crystallographic *a*-direction (Fig. I.1a). These lamellar sheets, with separation of 4.368 Å, are held together by van der Waals' forces to form a layered compound as shown in Figure I.1a.[29] α-V_2O_5 has a high theoretical capacity (450 $mAhg^{-}$

[1]) and a large open circuit voltage[30]; however, despite the excellent theoretical metrics, α-V_2O_5 continues to be plagued by myriad issues including low conductivity, phase inhomogenity[31–33], and irreversibility after lithiation beyond x=1.0.[34] Several of these observed problems are a result of diffusion limitations that are ionic, electronic, or coupled ionic—electronic in origin.[35] In the following three sections, we discuss fundamental impediments to cation diffusion within α-V_2O_5 as unraveled using scanning transmission X-ray microscopy, X-ray spectroscopy, and density functional theory calculations which relate to Chapter III, IV, and V of this dissertation; the subsequent two sections discuss potential approaches to mitigate these shortcomings utilizing nanostructuring and stabilization of metastable structures. We conclude this chapter with a discussion of cathode materials for 'beyond-Li' batteries and opportuities for mining novel compositional phase space to design potential intercalation hosts as well as outlining prospects for bridging critical knowledge gaps regarding intercalation mechanisms

I.1.1 Atomistic Diffusion Pathways, Electronic Conduits, & Polaron Bottlenecks

The availability of nudged elastic band (NEB) and associated methods for mapping of energy landscapes have allowed for density functional theory (DFT) modeling of likely diffusion pathways in crystalline materials, providing an atomistic view of ion diffusion pathways and allowing for a comparative evaluation of the energetics of diffusion barriers.[36–38] Figures I.1a–b depict the diffusion pathway of Li-ions in α-V_2O_5. Diffusion is observed to be strongly favored along the crystallographic *b* axis and involves substantial changes in local coordination. The inserted Li-ion is

ensconced within an approximately octahedral coordination environment but needs to transit through a relatively tightly spaced trigonal planar coordination environment defined by three oxide ions to get to an adjacent symmetry-equivalent empty octahedral coordination site (Fig. I.1c). The barrier for hopping of Li-ions from one site to another is estimated to be *ca.* 0.22 eV (Fig. I.1d). Such a barrier can be correlated to the diffusion coefficient (with knowledge of the attempt frequency) and is modified by increasing Li-ion occupancy. As a result of the relatively large change of local coordination environment and the narrow transition state, the migration barrier is relatively high for α-

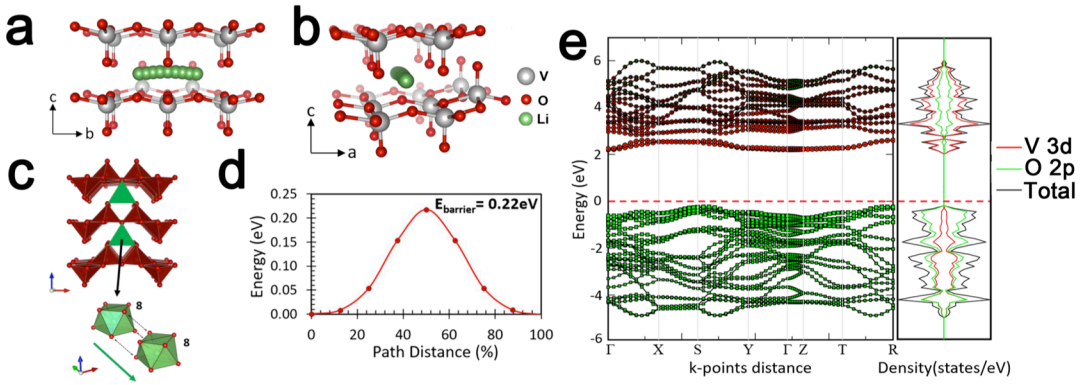

Figure I.1. Charge transport in α-V_2O_5. (a,b) Calculated diffusion pathway followed by Li-ions along the b-axis of α-V_2O_5, as determined from nudged elastic band calculations; the panels depict the pathway viewed along the a- and b-axes, respectively (adapted from Ref. 31 from Chapter I with permission under the terms of the Creative Commons CC BY). Vanadium atoms are depicted as grey spheres, oxygen atoms are depicted as red spheres, and Li atoms are depicted as green spheres. (c) As Li-ions diffuse between the layers of V_2O_5, they hop between quasi-octahedral coordination environments transiting across a spatially constrained trigonal planar coordination environment. (reprinted from Ref. 54 from Chapter I with permission from Elsevier) (d) The diffusion barrier for migration of Li-ions is calculated to be 0.22 eV (adapted from Ref. 31 with permission under the terms of the Creative Commons CC BY) (e) Calculated band structure and orbital-projected density of states for bulk V_2O_5, depicting the mostly O 2p character of the valence band (green lines), and the primarily V 3d character of the conduction band (red lines).

V_2O_5 and indeed this limitation is considerably amplified for larger and/or more polarizing cations such as Na^+, Mg^{2+}, Ca^{2+}, and Al^{3+}.[39–42]

Diffusion pathways represent an intrinsic property of a crystal structure but can be potentially modulated through either (a) atomistic design to identify and stabilize alternative polymorphs or (b) dimensional reduction, which is especially opportune for 2D van der Waals's solids, wherein bulk diffusion is supplanted by surface diffusion. Based on extensive computational analyses of diffusion pathways, the idea of "frustrated coordination" has been put forth wherein sub-optimal coordination environments are thought to particularly facilitate cation diffusion since cations within such environments do not represent deep wells in the free energy landscape[43] and can readily hop across local minima. Furthermore, relatively small changes in coordination environments are thought to be conducive to lower migration barriers as a result of a decreased amount of bond-breaking and bond formation needed to access the transition state. Advances in atomistic design to mitigate diffusion logjams both for Li- and multivalent ions are discussed in subsequent sections.

During discharge of the battery, insertion of Li-ions within the cathode at the electrolyte interface is balanced by electron flow from the current collector to the cathode material to maintain charge balance. Conversely, during charging of the battery, the transition metal sites are oxidized as cations are extracted at the electrolyte interface and the electron density is extracted at the current collector. Consequently, electron transport and not just ion diffusion is necessary within the electrode architecture to facilitate redox processes at transition metal sites. Transition metal oxides used as

cathodes typically have valence bands that are predominantly O 2p in origin and conduction bands that are derived from metal d states. Figure I.1e plots the calculated band structure of α-V_2O_5 depicting the V 3d nature of the conduction band states. The narrow energy dispersion of the conduction band states and the appearance of a split-off conduction band derived from V $3d_{xy}$ states results in a high effective mass and low mobility of electrons, thereby resulting in a relatively poor electrical conductivity for this material.[44–47] Indeed, the primary mode of charge transport in this material is believed to be the diffusion of small polarons.[48] The electrical conductivity of such oxides can be modulated to some extent through extrinsic aliovalent doping or the inclusion of conductive additives. In the latter case, the conductive additives necessarily must be closely interfaced with the active electrode materials such as in the form of 2D stacked heterostructures proposed by Pomerantsova and Gogotsi to enable coupling of ionic and electronic diffusion.[49] Smaller bandgap polymorphs or materials with more extensive energy dispersion of conduction band states (and thus a lower effective mass of electrons) are furthermore attractive alternatives from an atomistic design perspective (but this often carries a voltage penalty).

The coupling of cation diffusion with electron density, as inevitably occurs within a cathode material during redox processes, is effectively probed using X-ray absorption spectroscopy (XAS) and imaging methods such as scanning transmission X-ray microscopy (STXM) that capture inhomogeneities in the electronic structure of the cathode material and provide a chemically specific compositional map.[50] Examining the spatiotemporal evolution of spectroscopic signatures provides a detailed perspective of

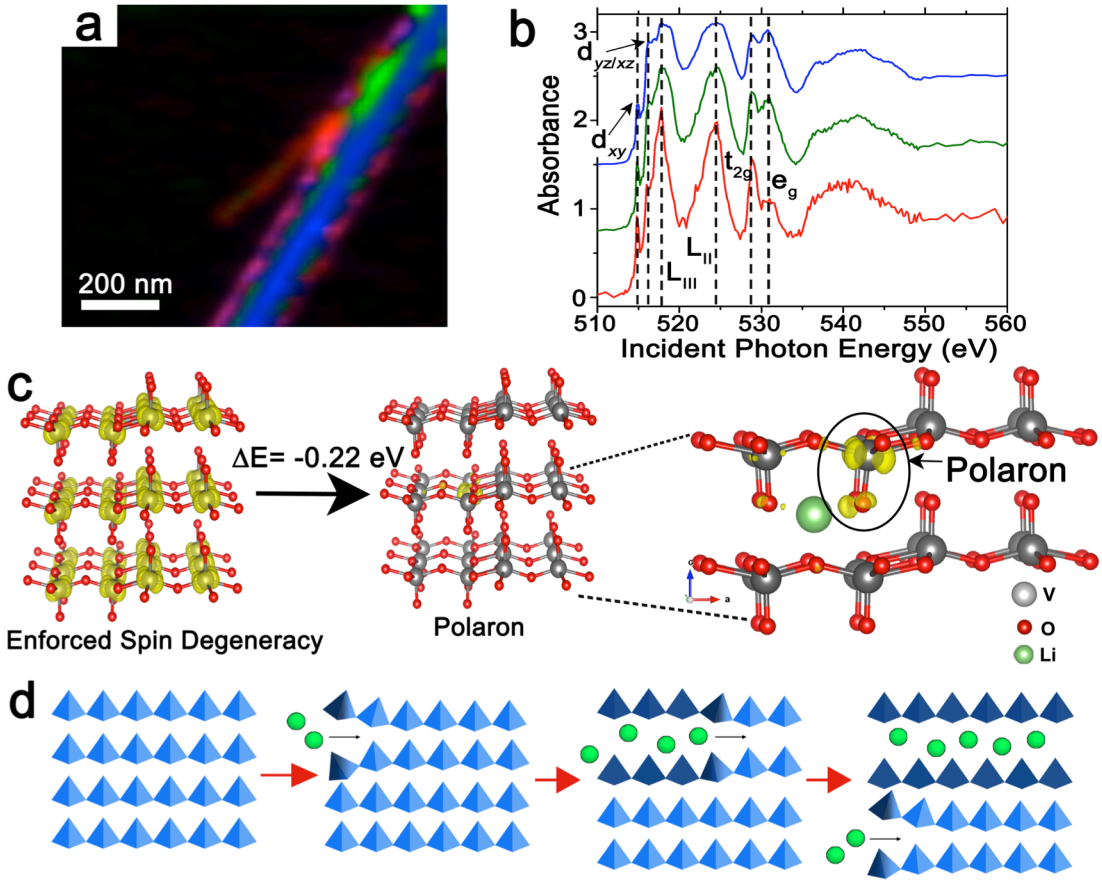

Figure I.2. Polaronic and staging origins of inhomogeneous lithiation. (a) Scanning transmission X-ray microscopy image showing the inhomogeneous spatial distribution of Li-ions across a V_2O_5 nanowire as indicated by the spatially localized contributions of spectra plotted in (b); the red, green, and blue components correspond to low, intermediate, and high concentrations of Li-ions, respectively. (c) Scheme depicting the energetic benefits of charge localization and lifting of spin degeneracy upon addition of a single electron to V_2O_5. The right panel depicts the stabilization of a small polaron (adapted from Ref. 31 from Chapter I with permission under the terms of the Creative Commons CC BY). (d) Illustration of stage-ordering phenomena. The initial stochastic intercalation of ions between two specific layers results in a local expansion of the interlayer spacing and facilitates insertion of a second ion within the same layer, contributing to lithiation gradients along the nanowire seen in (a).

the coupled electronic—ionic origins of diffusion limitations.[30–32,44] Whilst to a first approximation, the XAS methods probe the unoccupied density of states and thus the

formal valence and electron localization in vanadium atoms, the inhomogeneities observed are reflective of lithiation gradients given the redox processes accompanying Li-ion insertion/extraction.[30,31] Figure I.2 depicts a STXM image indicating the heterogeneous distribution of different lithiated phases in chemically lithiated V_2O_5 measured with single-particle resolution.[31,32] Figure I.2a maps the spatial distribution of three spectral components identified within the sample (and plotted in Fig. I.2b); each of the components correspond to X-ray absorption near-edge structure (XANES) spectra acquired at V L- and O K-edges of the imaged region. The V L-edge XANES spectra comprise two sets of spectral features split as a result of spin–orbit coupling by *ca*. 7 eV. The first spectral feature centered at *ca.* 518 eV (V L_{III}) corresponds to transitions from the V $2p_{3/2} \rightarrow$ V 3d states, whereas the second set of spectral features centered at *ca.* 525 eV, (V L_{II}), correspond to transitions from V $2p_{1/2} \rightarrow$ V 3d states.[44,45,51,52] The V L_{III}-edge spectral feature is characterized by fine spectral structure and provides a glimpse of the start of the conduction band in V_2O_5. The two spectral features at *ca.* 515.6 and 516.8 eV can be attributed to transitions of V 2p→V $3d_{xy}$ and V 2p → V $3d_{xz/yz}$ character at the bottom of the V_2O_5 conduction band, respectively, as elucidated by DFT calculations performed by Neese and co-workers.[45] In contrast, the O K-edge XANES spectra comprise features corresponding to transitions from O 1s core states to O 2p states hybridized with V 3d states, which are split into t_{2g} and e_g* states as result of the approximately octahedral crystal field of the oxide ligands.[44] The absorption feature at *ca.* 529 eV (t_{2g}) arises primarily from a transition to a final state derived from the hybridization of $2p_{x/y}$ states of vanadyl oxygen atoms with V $3d_{xz/yz}$ orbitals and from the

hybridization of oxygen $2p_x$ orbitals of bridging oxygen atoms with V $3d_{xy}$ states. In contrast, the spectral feature at *ca.* 531 eV (denoted as e_g in Fig. I.2b) results from a final state that has contributions from O 2p states hybridized with V $3d_{z^2}$ and V $3d_{x^2-y^2}$ states.[51,52]

The relative intensities of the spectral features are found to be strongly dependent on the filling of the conduction band resulting from reduction of V_2O_5 upon chemical lithiation. Specifically, the intensities of the V $3d_{xy}$ absorption at the V L_{III}-edge and the ratio between t_{2g} and e_g features at the O K-edge are greatly modified with increasing levels of lithiation.[31,53] For the former, the filling of the lowest-lying "split-off" V $3d_{xy}$ states results in suppression of the lowest-energy absorption feature at the V L_{III}-edge as a result of Pauli blocking. At the O K-edge, the diminished intensity of the t_{2g} absorption with respect to the e_g absorption arises from the lifting of the electron spin degeneracy, caused by the emergence of electron correlation effects as well as the structural distortion of the lattice arising from Li-ion intercalation.[31]

Figure I.2a depicts heterogeneous domains of a pair of $Li_xV_2O_5$ nanowires; the red, green, and blue regions correspond to successively increasing extents of lithiation. The larger nanowire is ca. 250 nm in thickness and *ca.* 400 nm in diameter, whereas the smaller nanowire is *ca.* 50 nm thick and *ca.* 100 nm in diameter.[31] The heterogeneity of lithiation attributed to two distinct origins: i) diffusion limitations resulting from stabilization of small polarons, specifically, the stabilization of quasi-particles wherein localized electron density on a vanadium atom is coupled to the structural distortion of the lattice induced as a result of Li-ion intercalation (Fig. I.2c); ii) the manifestation of

stage ordering phenomena wherein the insertion of an initial Li-ion within a particular layer is followed by a successive insertion of Li-ions within the same layer (which has already been expanded) instead of adjacent layers (Fig. I.2d).[31] The first-mentioned polaronic bottleneck is especially pronounced as a result of the narrow split-off conduction band derived from V $3d_{xy}$ states in α-V_2O_5 and underlines the pronounced role of electronic structure in mediating Li-ion diffusion[31,42] (*vide infra*); upon initial reduction, the electron density is localized within these states and can serve to self-trap adjacent Li-ions. Indeed, spectral features corresponding to such localized "mid-gap" polaronic states are observed just above the valence band edge in high-energy X-ray photoemission spectra of these systems.[31] While atomistic in origin, the polaronic bottleneck brings about pronounced lithiation gradients even within individual particles (Fig. I.2a). As will be discussed below, increasing lithiation brings about a sequence of intercalation-induced phase transformations in V_2O_5 and thus the spatiodynamic propagation of such phase transformations is greatly influenced by such polaronic barriers. Given the highly coupled nature of electronic and ionic diffusion processes, a realistic deconvolution is difficult but polaron diffusion phenomena have been estimated to account for a substantial portion of the migration barrier in several oxide materials.[54]

Understanding diffusion limitations thereby necessitates an accurate description of atomistic diffusion pathways, electron transport, and coupled polaron diffusion phenomena. While a plethora of articles examining diffusion pathways using density functional theory calculations have become available in recent years, the latter two considerations are often neglected and this is arguably a major origin of the current

inadequate predictive power of first-principles calculations. A precise understanding of the evolution of electronic structure as a function of lithiation is necessary as is a more exact treatment of electron correlation. Experimental probes of electronic structure such as resonant inelastic X-ray scattering and X-ray absorption spectroscopy hold promise for enabling the benchmarking of first-principles calculations. Increasing the accuracy of calculations will allow for the development of improved design principles that take into account the full complexity of coupled ionic and electronic diffusion.

I.1.2 Stabilization and Diffusion of Polarons in Cathode Materials

From an electronic structure perspective, during reduction and concomitant intercalation of the cathode material, the added electrons begin to fill unoccupied states starting from the bottom of the conduction band. As illustrated by the two competing states in Figure I.2c, the extent to which electron density will be delocalized across different metal centers (or localized on a transition metal center) depends on the balance between the kinetic energy gained by delocalizing the electron density across a band, the penalty incurred as a result of Coulombic repulsions between delocalized electrons (electron correlation), and the energetic stabilization gained by inducing a local lattice distortion (an electron—phonon coupling interaction).[12] Given the narrow 3d bands of vanadium and the manifestation of strong electron correlation in most transition metal oxides, electron localization is energetically strongly preferred over delocalization of electron density across the unit cell. The combination of localized electron density and lattice distortion constitutes a polaron. The localized polaron is further stabilized by interactions with Li-ions. As shown in Figure I.3a, depending on the electronic structure

of the material and the specific states available, reduction of the metal oxide yields new occupied bands below the Fermi level (as observed using hard X-ray photoemission spectroscopy in the case of $Li_xV_2O_5$)[31,42] and such a polaronic feature essentially splits off from the rest of the conduction band instead of forming a half-filled band. From a structural perspective, the inserted Li-ions also polarize the framework as represented schematically in Figure I.3b and thereby displace atoms in their immediate vicinity from their equilibrium positions in the pristine unintercalated phase. The coupling of the localized electron density with its lattice distortion and adjacent Li-ions yields a self-trapped polaron that then diffuses through the lattice in a conjoined manner. The hopping from one localized well to another is intrinsically coupled to diffusion of the intercalating species and manifests practically in a greater local diffusion barrier of the intercalating species, leading to atomic-scale 'traffic-jams'.[31,32,53,55–57] The effective mass of the polaron and its barrier to diffusion depends on the strength of the electron—phonon coupling and the strength of the self-trapping interaction with the Li-ions. When polarons with deep wells occur in cathode materials, the observed diffusivity of the materials is dramatically dampened. With increasing lithiation and an increased density of polarons, Figures I.3a and b illustrate the closer proximity of such distortions resulting in easier diffusion through stabilization of a percolative network or eventually phase transformation to a structure that can better accommodate a periodic array of structural distortions.

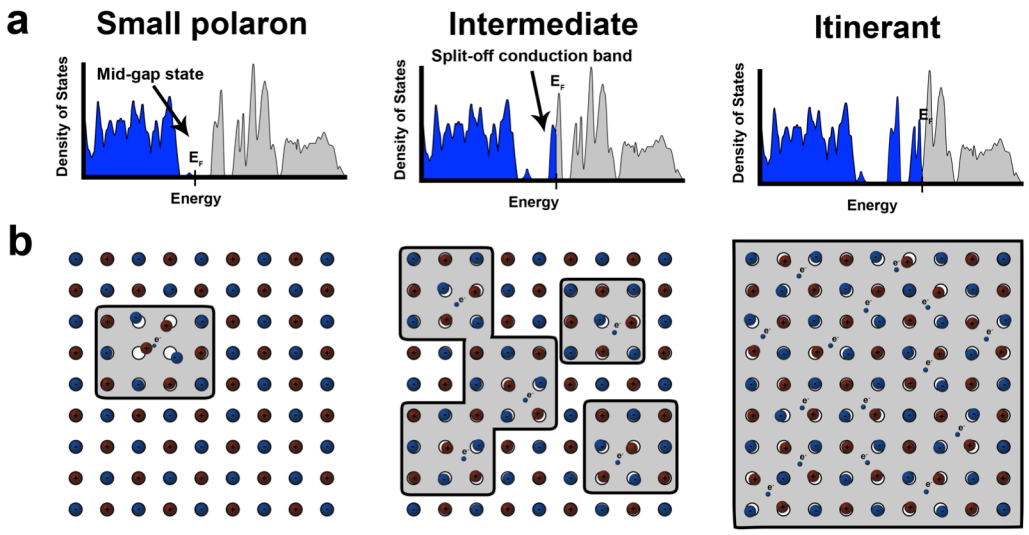

Figure I.3. Electronic and atomistic structure implications of polaron formation. (a) Evolution of the density of states of a representative cathode material and (b) a schematic depiction of the corresponding structural perturbation induced as a result of polaron formation at varying degrees of lithiation. The blue and red spheres represent the anionic and cationic sublattices upon lithiation and the grey shaded regions denote the spatial extent of the lattice that is distorted the structure.

The split-off V $3d_{xy}$-derived band of α-V_2O_5 provides a facile set of states for localization of electrons.[30,31,46] The formation of the polaron in α-V_2O_5 is depicted in Fig. I.2c. Upon lithiation, the electron localizes on the $3d_{xy}$ orbital of a nearby vanadium site (Fig. I.2c), inducing a subtle perturbation of the surrounding framework. Similarly, the presence of a charged cation within an interstitial site between layers of α-V_2O_5 induces a substantial polarization of the framework where the oxygen atoms pucker towards the lithium and the vanadium atoms are slightly repelled.[31,40] The formation energy of the polaron in α-V_2O_5 is a thermodynamically favorable value of -0.41 eV. This results in higher energy barriers values for hoping mechanisms, thus sluggish diffusion, of Li ions and the polaron of 0.22 eV and 0.34 eV, respectively.[31,40]

It is important to note that even while the localization of electron density at vanadium centers is particularly prominent in this example, these considerations are broadly generalizable to early first-row transition metal oxides given their constricted 3d-derived states and the manifestation of electron correlation effects.[55,56,58,59] Sluggish diffusion kinetics resulting from polaronic confinement of intercalating species are thus likely quite pervasive in oxide cathode materials.[31,56,60–62] While first row transition metals are particularly attractive from an earth abundance perspective, and given their low atomic masses, allow for high energy densities, the aforementioned localization and trapping phenomena need to be mitigated to facilitate cation diffusion. In other words, defining cation diffusion pathways necessitates not just consideration of the local coordination environments for hopping of cations as defined by a crystal structure but also electron—phonon coupling and electron correlation as it pertains to polaron stabilization and diffusion. It is worth noting that depending on the specific transition metal and intercalating species, the diffusion of electron as well as hole polarons associated with transition metal centers require mitigation.[58,63] Subsequent sections will address mitigation of these diffusion gridlocks both in terms of atomistic design of novel materials as well as nano-[31,33,44] and meso-structuring[64] of existing cathode materials to offset the impact of diffusion impediments by truncating solid-state diffusion path lengths.

I.1.3 Intercalation-Induced Phase Transformations and Phase Boundaries

Structural distortions induced upon cation intercalation (or for that matter in response to external stimuli such as temperature, strain, or pressure) are initially

accommodated through local distortions; however, depending on the nature of the free energy landscape, given the availability of a sufficient amount of energy, a structure will relax towards a more energetically favorable arrangement of atoms. Phase-transformation phenomena thus arise from the *sine qua non* of solids to re-accommodate their atoms to better reach a stable conformer in response to external forces (*e.g.*, pressure and temperature)[12,65] or compositional modulation achieved through intercalative or doping reactions.[66] The transformations can be considered to be either displacive or reconstructive with the specific designation depending on the magnitude and nature of atomic displacements required to stabilize a new phase.[67–70] In the former, the concerted motion of atoms brings about a rearrangement of the unit cell, thereby stabilizing a new phase that bears a direct symmetry relationship to the parent structure as observed with Martensitic transitions in VO_2 and HfO_2. The latter type of transformation necessitates a complete restructuring of the material with the cleavage of existing bonds and formation of new bonds to stabilize a new phase that is entirely transformed from the parent structure as evidenced in the transformation between the anatase and rutile phases of TiO_2.[71]

α-V_2O_5 serves as an excellent example of a material that initially undergoes a series of displacive transformations with increasing intercalation of Li-ions.[33] Upon initial lithiation up to a low lithium content ($x \leq 0.1$), the α-V_2O_5 phase retains its structure, albeit with puckering of the layers and a slight expansion of the interlayer spacing.[69,72] However, further Li-ion intercalation stablizes the ε-$Li_xV_2O_5$ phase ($0.33 \leq x \leq 0.80$) with a space group of *Pmmn*.[68,73] This structure defines eight-coordinated

distorted bicapped triangular prismatic coordination environments for Li-ions between the layers of V_2O_5. As denoted by the arrows in Figure I.4b, the apical V=O bonds of the [VO_5] units are puckered towards the lithium atoms intercalated within the prismatic environment as a result of electrostatic interactions between the oxygen lone pairs and the Li-ions. With still further insertion of Li-ions ($0.88 \leq x \leq 1.0$), the δ-$Li_xV_2O_5$ phase is stabilized in the orthorhombic system.[68,73,74] The lamellar sheets of α-, ε- and the δ-phase are similar in terms of local vanadium geometry; however, in order to accommodate a higher lithium content, the stacking sequence is shifted along the *b*-axis by half a unit

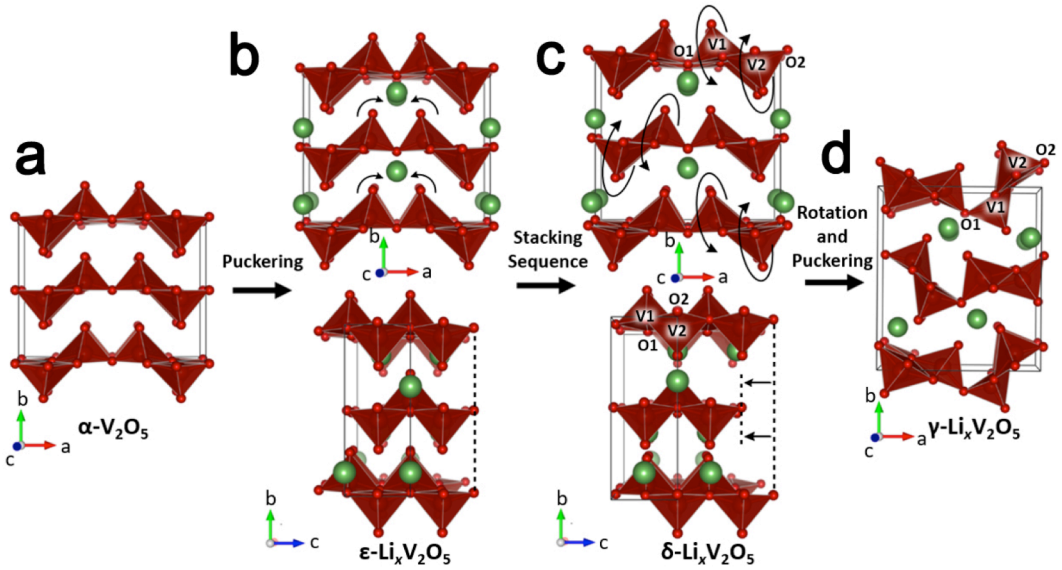

Figure I.4. Sequence of intercalation-induced structural phase transformations in V_2O_5**.** Supercell structures of (a) α-V_2O_5, (b) ε-$Li_xV_2O_5$, (c) δ-$Li_xV_2O_5$, and (d) γ-$Li_xV_2O_5$. Green and red spheres represent lithium and oxygen atoms, respectively; the solid red pyramids represent [VO_5] units. The structural distortions induced as a result of Li-ion intercalation are delineated in the figure.

cell length in the δ-phase polymorph (Fig. I.4c); the space group symmetry is thus changed to *Amma*.[33] The local coordination environment of the Li-ions changes from the

eight-coordinated bicapped trigonal prismatic environment in ε-$Li_xV_2O_5$ to an approximately tetrahedral coordination in δ-$Li_xV_2O_5$.[75] Finally, with even further lithiation, in the Li-range $1.0 < x < 2.0$ of $Li_xV_2O_5$, the γ-phase is stabilized with a space group symmetry of *Pnma*.[76] The formation of the γ-$Li_xV_2O_5$ phase from δ-$Li_xV_2O_5$ can be conceptualized by rotation of the two edge-shared [VO_5] square pyramidal units by 90°, in opposite directions, along the V1—O1, and V2—O2 bonds, respectively, as delineated by a pair of curved arrows in Figure I.4c. Notably, only alternate pairs of edge-shared [VO_5] pairs are puckered in a lamellar sheet of V_2O_5. This results in the apical V=O bonds being slightly skewed from the crystallographic *b*-axis. In comparison, the apical V=O bonds in α-, ε-, and δ-V_2O_5 are oriented directly along the *b* axis. This distortion of the vanadyl directionality drastically changes the coordination environment of the intercalated lithium from six-coordinated to define approximately tetrahedral coordination environments, which furthermore allow for accommodation of higher lithium concentrations. Still further lithiation appears to induce an irreversible reconstructive phase transformation to a cubic ω-$Li_3V_2O_5$ phase; a detailed structure elucidation for this phase remains elusive and some authors have suggested that the structure might indeed be a mixture of lithium vanadates and oxides.[77]

The multiphasic domains stabilized when the composition approaches phase limits in the phase diagram and the experimentally observed manifestation of extended phase coexistence regimes furthermore necessitate the diffusion of Li-ions across multiple phase boundaries within particles and across the interconnected network of particles that constitute the active electrode. Such phase boundaries thus further limit Li-

ion diffusion and phase propagation across multiple Li-ion concentration windows in $Li_xV_2O_5$. A clear delineation of the effects of phase segregation on the thermodynamics and kinetics of intercalation phenomena remains to be established and neccessitates coupling electrochemical measurements to probes of atomistic and electronic structure.

I.1.4 Inhomogeneous Lithiation and Phase Inhomogeneities Across Ensembles of Particles

Figures I.1 and I.2 illustrate the idea of ionic and coupled ionic—electronic polaronic diffusion barriers that give rise to bottlenecks for Li-ion diffusion. Figure I.4 illustrates the intercalation-induced phase transformations induced within this system. Limitations in the uptake of Li-ions thus result in lithiation gradients that are further translated to phase inhomogeneities across individual particles and across ensembles of particles. The progression of nucleation and growth of lithiated phases are dictated by local concentration gradients and intercalation phenomena rather than by the global voltage across the cell.[9,53,78–80] As such, the dimensions of particles, specific morphological features, inter-particle connectivity, the presence of extended defects, and the exposed crystallographic facets determine in large measure the sequence of phase propagation events.[53,78]

Figure I.5 depicts STXM maps acquired across ensembles of interlaced particles clearly illustrating the broad variation of Li-content (correlated also to phase inhomogeneities) across the ensembles at different length scales. The color scheme again corresponds to increasing lithiation in going from red to green to blue domains in the images. The corresponding XAS spectra are shown alongside for Figures I.5c and e.

Figure I.5a provides an example of multimodal electron microscopy and STXM imaging of the same small ensemble of particles.[53] Based on STXM imaging of lithiation concentrations in these (and other) small interconnected networks of particles, intercalation-induced phase transformations appear to have a strong preference for propagation in a sequential manner along individual particles (even at the cost of

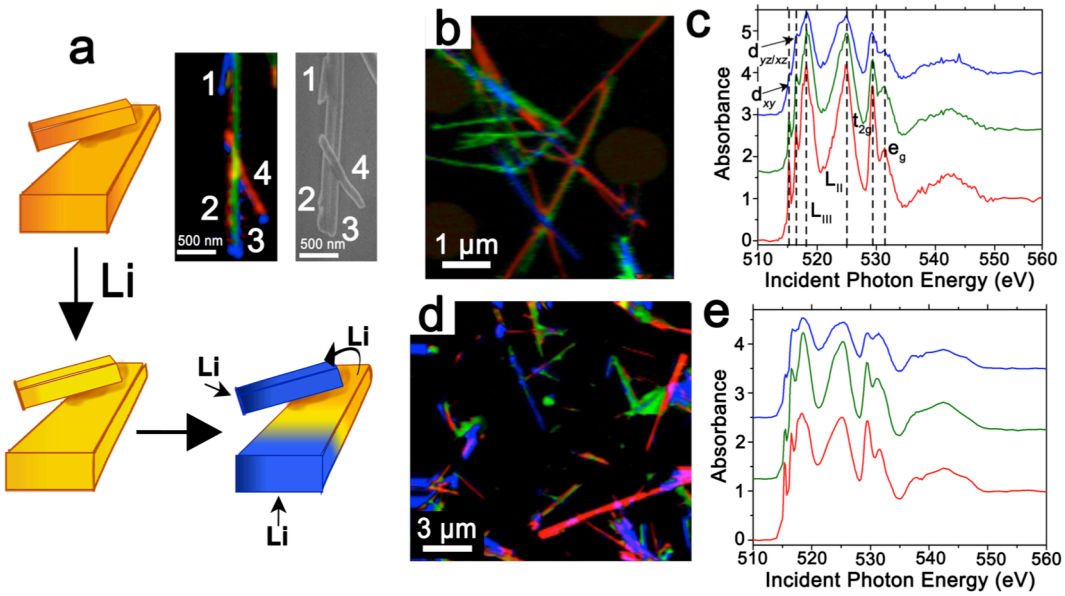

Figure I.5. Inhomogeneous lithiation across ensembles of particles. (a) Schematic depiction of inhomogeneous lithiation of two interconnected particles—both particles are initially homogeneously lithiated to a low-Li-content phase. However, one of the particle gains an advantage and lithiates preferentially with respect to its underlying counterpart depleting the particle below of its Li-content to facilitate rapid phase propagation of a Li-rich phase as per a "winner takes all" mode. The insets depict STXM and scanning electron microscopy images of the model system (adapted from Ref. 53 from Chapter I with permission from The Royal Society of Chemistry). (b) A larger area STXM image of a cluster of several interconnected particles; the corresponding spectra are plotted in (c); the regions demarcated in red, green, and blue correspond to low, intermediate, and high Li-ion concentrations. (d) Large-area STXM image depicting considerable inhomogeneity of lithiation; the corresponding spectra are plotted in (e)

depleting adjacent particles of Li-ions) instead of concurrently across the entire network (as schematically illustrated in Fig. I.5a).[53,78] These differences indicate the role of inter-particle connectivity within a group of particles. Indeed, it appears that in such phase-separating materials, any particle that has a slight advantage over another in initially inserting Li-ions (owing to a locally high concentration gradient, a surface that is favorably disposed to intercalate Li-ions, or as a result of sheer stochastics) will rapidly continue to lithiate at the expense of adjacent particles (as schematically illustrated in Fig. I.5a), following a sequential particle-by-particle process;[79] Zhao and colleagues have demonstrated using phase-field modeling that indeed an actively lithiating (and phase-transforming particle) depletes an adjacent interconnected particle via an interface.[78] Such a sequential mode of lithiation gives rise to large concentration gradients that inevitably then bring about phase inhomogeneities and coherent strain as well as diffusion limitations at phase boundaries.

Figures I.5b and d show larger-area views of phase and concentration inhomogeneities in ensembles of particles. Intriguingly, a low level of lithiation to the ($x \sim 0.1$) α-$Li_xV_2O_5$ phase is observed to occur fairly homogeneously across the entire network. However, subsequent nucleation and growth of lithiated domains occurs seemingly stochastically driven by local intercalation phenomena. Across ensembles of particles, considerable heterogeneity is observed between particles exhibiting deep lithiation and sparsely lithiated particles. Within individual nanowires, both lateral and length-wise domains are stabilized. Some nanowires show approximately core—shell behavior with more highly lithiated shells and Li-poor cores; the shells are observed in

ex situ measurements to form compositional stripes of Li-rich and Li-poor domains as a result of differential rates of Li-ion intercalation and diffusion.[81] A similar result of initially homogeneous lithiation followed by phase segregation has also been deduced from principal component analysis of V K-edge XANES spectra.[32]

The creation of "hot spots" results in strongly amplified current density within specific electrode regions during charge/discharge processes, which thereby controls the localized energy dissipation profile and increases the probability of parasitic reactions that eventually result in loss of capacity and degradation. The complexity of phase evolution and the stabilization of distinctive lateral and longitudinal domains within individual particles as well as across networks is best captured by methods such as phase field modeling. For example, utilization of phase field modeling in conjunction with STXM has enabled mapping of tensile and compressive stress within individual nanowires of $Li_xV_2O_5$ resulting from compositional modulations.[81] Core—shell separation and striations along the shell give rise to a considerably inhomogeneous stress profile that can bring about the fracture of typically brittle oxide cathodes upon prolonged cycling. Further phase heterogeneity (discernible in the inset to Fig. I.5a) stems from the presence of screw dislocations and the secondary growth of Li-rich phases at nanowire tips. Indeed, the role of extended defects such as dislocations in enabling or impeding Li-ion diffusion represents a tantalizing subject that is yet to be explored in detail.

While homogeneous intercalation across an entire porous electrode may be very difficult to accomplish in practice, the design of mesoscale architectures wherein

intercalation and phase propagation proceeds via a deterministic instead of probabilistic or stochastic manner would represent a major advance. In order to achieve the deterministic diffusion of Li-ions and propagation of phase transformations, a deeper understanding of fundamental mechanisms is imperative. While individual analytical methods provide valuable clues to underlying mechanisms of charge and mass transport, there exists a considerable knowledge gap between the high spatial resolution that can be accessed through advanced electron microscopy techniques, the energy resolution accessible using synchrotron-based X-ray absorption/emission spectroscopies, and the larger (perhaps more representative) volumes sampled using micro-X-ray diffraction methods. Multimodal characterization is thus imperative to develop a precise understanding of mechanism and to rationally guide the design of electrode architectures. Being able to accurately translate atomistic phenomena to continuum scales taking into account the coupling of chemistry, mechanics, and electric fields through scale bridging models will be essential to inform the design of patterned electrodes.[82] Multiple approaches exist for precisely structuring matter but a clear description of optimal mesoscale architectures has hitherto not been developed with a few exceptions. In a similar vein, while the programmable placement of defects represents a difficult task, their patterned incorporation through surface functionalization, templating, differential strain,[81,83,84] or specific growth conditions that promote microtwinning would provide access to well-defined ion diffusion pathways and provide a means to direct cation diffusion.

In the next two sections, we address two distinct approaches to overcome the multiscale diffusion limitations derived from polarons and phase boundaries. The first approach seeks to mitigate the influence of polarons and phase inhomogeneities by control over dimensionality, essentially by limiting the diffusion path lengths and by defining particle sizes below the critical dimensions wherein phase boundaries can be stabilized. The second approach focuses on the bottom-up design of materials that allow for more facile diffusion of ions and polarons. It is important to note that these two approaches are not mutually exclusive, but can be combined synergistically to harness additive benefits.

I.1.5 Mitigating Gridlock by Truncating Diffusion Pathlengths

Methods for nanostructuring of cathode materials have proven to be successful in enhancing cycling stabilities, specific charge capacities, and power densities.[33,64] Some of the advantages of nanostructured materials include: increased ability to accommodate strain gradients introduced upon inhomogeneous-lithiation-induced phase transformations; increased electrolyte-electrode-surface interface derived from high surface areas; additional capacitative and pseudo-capacitative charge storage as a result of increased surface areas; and shorter diffusion path lengths within nanoparticles for Li-ion intercalation.[8,33,85]

Remarkably, the sequence of lithiation and the associated phase transformations in V_2O_5 are found to strongly depend on particle size.[33] The lithiation process is homogeneous and phase separation in greatly reduced for nanoplatelets with thickness in the order of 20–50 nm; in contrast, multi-phase domains are stabilized for nanowires

with thicknesses on the order of 150–250 nm, suggestive of a two-phase nucleation and growth scenario. These findings have been rationalized based on phase-field modeling studies of intra-particle phase separation.[78] Larger particles are predicted to exhibit compositional modulation of periodic Li-rich and Li-poor domains, whereas in smaller particles the phase separation is suppressed as a result of the faster ratio of reaction to diffusion rate and the inability to stabilize an interfacial boundary (alternatively, the interface can be considered to grow on the free surface). The critical size wherein phase segregation is suppressed will depend on the temperature and charge/discharge rate but appears to be in the range of 20—50 nm for V_2O_5 when α-V_2O_5 is intercalated by Li-ions. The critical size representing a cross-over between phase separating and single-phase behavior will furthermore depend on the morphology given the potentially counteracting effects of surface and bulk free energies. For multivalent cations, this critical size appears to be much smaller (on the order of 10 nm) given the higher diffusion barriers encountered in intercalation hosts thus far.[86]

Figure I.6 depicts the use of STXM as a local structure probe to correlate the extent of lithiation (depth of discharge) and phase separation with particle size of V_2O_5 upon chemical lithiation. Figure I.6a shows a high-resolution scanning electron microscope (HR-SEM) image of the same region imaged by STXM, indicating a broad range of particle sizes. The long axis of the particles vary from 0.1 to 5 μm. Figures I.6b—d shows the spectral intensity maps of three components corresponding to increasing extents of lithiation. The intensity maps have been derived based on a singular value decomposition (SVD) analysis of the STXM image stack using the component

spectra (plotted in Fig. I.6f) as reference spectra (labeled as i, ii, and iii). The heat maps in Figures I.6b—d indicate the relative abundance of the component at a specific pixel on a scale that increases from deep blue to red. The graded contributions of each of the components at each pixel has been determined, allowing for the construction of maps delineating the relative abundance of each of the spectral components at each pixel within the imaged region (Fig. I.6e). Indeed, spatial mapping of the three spectral components clearly indicates that the red component (Fig. I.6b), which has the highest t_{2g}/e_g intensity ratio (corresponding to the lowest extent of lithiation), is more localized

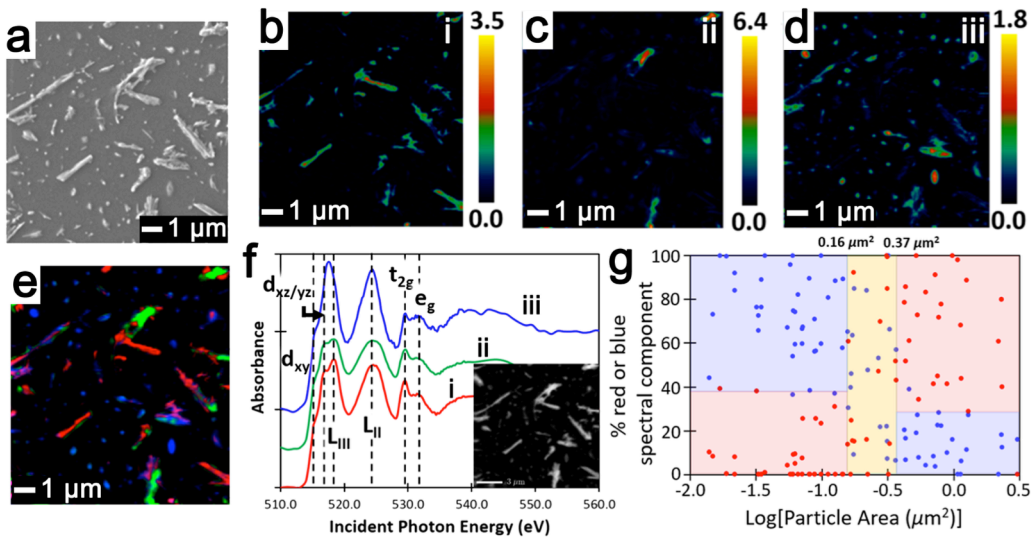

Figure I.6. Size dependence of diffusion limitations. (a) SEM image of an ensemble of $Li_xV_2O_5$ nanoparticles (lithated for 1 h) with a substantially polydisperse size distribution. (b—d) Intensity maps of the three spectral components (the intensity of the spectrum at each pixel is denoted by the color bar) as identified by SVD analysis of hyperspectral STXM data. (e) A false color map showing the relative localization of the three components, the color at each pixel represents the major spectral contribution (blue –most lithiated– or green –mildly lithiated– or red –least lithiated– consistent with the color of the spectra in (f)). (g) Percentage contribution of the high-Li-content (blue) and low-Li-content (red) spectral components in each particle plotted as a function of the area of the nanoparticles.

on relatively larger particles, whereas the component resulting from the blue spectrum (Fig. I.6d), with the least t_{2g}/e_g intensity ratio (highest lithiation), is predominant on the relatively smaller particles. The component plotted as the green spectrum presenting an intermediate t_{2g}/e_g intensity ratio (intermediate lithiation), is localized on relatively few (larger) particles. Figure I.6e depicts the clear size-dependent segregation of the spectral signatures. After 1 h of chemical lithiation, the smaller particles are clearly more extensively lithiated; furthermore, the particles do not show any evidence for phase segregation, whereas multiphasic domains can be distinguished for several of the larger particles.

A more quantitative analysis has been performed by plotting the percentage contribution of the blue (most lithiated) and red (least lithiated) spectral components to each particle as a function of the logarithmic cross-sectional area (Fig. I.6g). Since, there are only a few particles with intermediate lithiation (suggesting a primarily two-phase process) these are not included in the analysis. Indeed, the percent contribution of the blue component is above ca. 39% (region outlined as blue rectangle) and the red component below 39% (region outlined as red rectangle), respectively, in all the particles with cross-sectional area bigger than 0.16 μm^2, whereas the red component contributes below 29% and red component above 29%, respectively, to all the particles with cross-sectional area greater than 0.37 μm^2. When the cross-sectional area of the particles is between 0.16 μm^2 and 0.37 μm^2, there is no clear selectivity between blue or red components (region outlined as yellow rectangle). The observed correlation of particle area with increasing lithiation as well as the observed single-phase lithiation of smaller

particles suggests that the particle dimensions play a critical role in determining the nucleation and propagation of intercalation-induced transformations. Indeed, these results suggests that decreasing the particle size of actively intercalating domains below a critical dimension (below a critical nucleation volume) can enable more homogeneous single-phase lithiation, thereby suppressing diffusion limitations at phase boundaries and also mitigating the coherent strain at such boundaries.[78,87] Single-phase lithiation along with shorter pathlengths for coupled ionic-electronic diffusion represent a major advantage of nanostructuring. Unfortunately, decreasing the size of the nanoparticle comes with a caveat: the capacity of the single particle is reduced as a result of surface tension effects[88] with added deleterious effects of increased surface reactions[89] and potential agglomeration, which can render primary particles within the agglomerate inaccessible to intercalation.

An interconnected network of particles with well-defined dimensions of diffusion pathways is thus desirable—the precise structuring required to mitigate phase transformations and promote homogeneous lithiation represents an inverse design problem that requires coupling of experimental observables with atomistic as well as continuum scale modeling. Developing viable synthetic approaches that yield mesostructured networks with desired crystallite size and interconnectivity remains a formidable challenge. Once templates have been identified through multiscale inverse design approaches, they will need to be elaborated and replicated within large area formats. It is worth noting that in addition to particle size, the exposed crystallographic facets and orientation of the channels within the particles is furthermore of utmost

importance as illustrated by Kohyama *et al*.[90] As an illustrative example of the design of patterned substrates, colloidal crystal templating, with the use of polystyrene microspheres as removable templates, has been used to create a porous mesostructured α-V_2O_5 architecture, which provides both a higher capacity as well as improved cyclability and a sharper phase transition (with a decreased phase coexistence regime) as compared to an unpatterned thin film.[64] However, an inevitable limitation of such approaches is that smaller domain sizes oftentimes result in lower volumetric capacities, which is especially a challenge for mobility applications wherein volumetric capacity represents a paramount consideration. Templating is just one example of a method to develop mesostructured intercalation electrode architectures; directed assembly mediated by electric or magnetic fields or specific drying patterns can furthermore aid the preparation of textured substrates; the viable large-area manufacturing of cathode materials will need to be developed to take advantage of opportunities made available by truncating diffusion path lengths.

I.1.6 Mitigating Polaronic Confinement and Facilitating Cation Diffusion using Atomistic Materials Design

A second approach for facilitating cation diffusion and mitigating coupled polaronic barriers involves the tailored design of entirely new crystal structures as summarized in Figure I.7. In this section, we turn our attention to alternative metastable polymorphs of V_2O_5 that show distinctive structural motifs in comparison to α-V_2O_5, the thermodynamically stable polymorph discussed above. As illustrated by Figure I.4, different polymorphs of V_2O_5 define distinctively different local coordination geometries

for intercalated Li-ions. The accessible diffusion pathways are considerably modified in each case as a result of changes in V—O connectivity. A much richer palette of V_2O_5 polymorphs is accessible based on topochemical extraction of M-cations from a versatile family of crystalline ternary vanadium oxide bronzes with the composition $M_xV_2O_5$[91] where the cation M can be varied across a broad compositional and stoichiometric range (x) within a diverse range of V_2O_5 structural frameworks with varying V—O connectivity.[12] Another class of related compounds have intercalated cations or trapped solvent molecules; the pillaring cations serve to separate V_2O_5 single or double layers.[92,93] Expanded structures with short-range order are furthermore accessible for V_2O_5 such as aerogels[94–96] and xerogels.[97,98] Such a rich structural palette provides access to a myriad range of diffusion pathways showing extensive variability of cation coordination environments as a function of the V—O connectivity, the linkages of vanadium-centered polyhedra, and the stacking of single- or double-layered [V_2O_5] sheets whilst still retaining multi-electron redox vanadium centers.[39,40,46,99] Pillaring cations and intercalated solvent molecules provide further opportunities for screening of polarization induced by cations. As such, the ability to stabilize metastable polymorphs opens up a versatile design space where design elements theorized to facilitate cation diffusion such as frustrated coordination and spacious transition states can be sought. Furthermore, as a result of the varying V—O connectivity, considerable modulation of the extent of ionicity/covalency is possible across these polymorphs, which has tremendous implications for the width of the 3d-derived conduction band (which determines the electron mobility and thus electronic conductivity), the extent to which

the diffusing cation is able to polarize the anion lattice, as well as the extent to which the cation can be trapped by an adjacent electron to form a polaron. In order words, the changes in connectivity between the atoms in metastable V_2O_5 polymorphs allow for considerable flexibility in the design of conduction pathways for both ions and electrons, allowing for a means to alleviate the shortcomings of the thermodynamically stable α-V_2O_5 phase described in the previous sections.

A metastable polymorph that has proven to be an excellent intercalation host is the quasi-1D tunnel-structured ζ-V_2O_5 phase, which retains the primary structural motif of the parent ternary β-$Ag_xV_2O_5$ Wadsley bronze, from which it is derived (Fig. I.7).[40,42,46,54,100] The lower Li-ion and polaron diffusion barriers (0.13 and 0.24 eV, respectively) as compared to α-V_2O_5 (0.22 and 0.34 eV, respectively) within this structure stems from several aspects of its atomistic and electronic structure. Figure I.7a contrasts the total (grey shaded region) and vanadium-projected density of states (DOS) calculated for the two polymorphs.[46] As noted above, because α-V_2O_5 has only a single distinct vanadium site, the crystal field splitting in an approximately square pyramidal geometry results in a distinct "split-off" conduction band with d_{xy} character lower in energy than the $d_{xz/yz}$ states (highlighted by the transparent grey box). DFT calculations show that in α-V_2O_5, a single electron donated by the intercalating species localizes in the V d_{xy} orbital of the nearest vanadium site, giving rise to a polaron.[31] In contrast, ζ-V_2O_5 has three distinct vanadium sites with different ligand field splitting than observed for the lone vanadium site in α-V_2O_5, resulting in a broader more energy degenerate d-band and a smaller bandgap (1.50±0.20 eV as compared to 1.90±0.20 eV for α-V_2O_5).[46]

The lower effective mass and resulting increased mobility of electrons in this structure effectively diminishes the strength of the polaron and allows for easier polaron diffusion. Furthermore, the vanadium—oxygen bonds within the material are much more covalent (owing to greater overlap of d-bands), which reduces the polarization of the framework induced by the diffusing electropositive Li-ions (due to reduced effective partial charge on the coordinating oxygen ligands).[46]

The diffusion pathway of Li- and Mg-ions in ζ-V_2O_5, as calculated from NEB calculations, is depicted in Figure I.7b and represents a considerable departure from the diffusion pathway traced by Li-ions in α-V_2O_5. In the case of α-V_2O_5, the change in coordination number across the diffusion pathway linking two symmetry-equivalent sites is 8 → 3 (transition state) → 8 with a trigonal planar transition state as shown in Fig. I.1c. However, in ζ-V_2O_5 the change in coordination number across the diffusion pathway is considerably less pronounced changing from 4 → 3 (transition state) → 5 → 3 (transition state) → 4. The smaller changes in coordination number equate to a relatively lesser extent of bond-breaking and bond formation required to diffuse the cation and translates to a *ca.* 0.09 eV reduction of the Li-ion diffusion barrier. This polymorph thus serves as an excellent validation of the concept of frustrated coordination. The significant improvement in diffusion kinetics for ζ-V_2O_5 derives not only from the wider d-bands and lower energy cation diffusion pathways discussed above but also reflect the relative stability of the rigid tunnel framework, which can accommodate Li ions through solid-solution formation over a broad range ($0 < x < 0.66$) without substantial structural distortions, thereby substantially mitigating the creation of

phase boundaries and diminishing the energy dissipation that inevitably accompanies phase transitions.[25,33,53,101] In recent work, we have used Bayesian principal component analysis (PCA) analysis of STXM data to demonstrate that ζ-V_2O_5 undergoes single-phase lithiation with only a single spectral component discernible across multiple nanowires, whereas pronounced inter-and intra-particle inhomogeneities and distinctive spectroscopic signatures of Li-rich and Li-poor domains are identified for α-V_2O_5 upon lithiation (as also readily apparent in Figs. I.2 and I.5).[42] The 1D ζ-phase thus intercalates Li-ions through a continuous lithiation pathway that is starkly different from the sequential intercalation-induced structural transformations observed in α-V_2O_5.

The diffusion pathways of Li- and Mg-ions in two other metastable compounds, γ′-V_2O_5 and ε′-V_2O_5 are also depicted in Figure I.7b. The puckered single-layered γ'-phase exhibits a 4 → 3 (transition state) → 5 → 3 (transition state) → 4 diffusion pathway with a cation diffusion barrier in the range of 0.15—0.18 eV depending on the Li-ion concentration. In contrast, in the double-layered ε-phase, a 4 → 4 (transition state) → 4 pathway is traced by the cations yielding an exceedingly low diffusion barrier of 0.10 eV. The greater rigidity of the double-layered ε'-phase phase renders it less amenable to polarization by intercalated cations as compared to the single-layered γ' and α-polymorphs. Intriguingly, the stacking sequence of [V_2O_5] sheets have been found to strongly influence the nature of the diffusion pathways, the size of the transition state, and thus the migration barriers. δ' and ρ'-phases can be conceptualized to result from the ε'-phase based on a sliding of the [V_4O_{10}] layers with respect to one another. Alteration of the stacking sequence yields very different conduction pathways. Li-ions in the δ'-

phase undergo migration through 5 → 3 (transition state) → 4 → 3 (transition state) → 5 with a diffusion barrier in the range of 0.07−0.19 eV. In the case of the ρ'-phase, migration of ions occur through a change in coordination environment from 6 → 4 (transition state) → 6 → 4 (transition state) → 6. The predicted migration barrier is 0.07 eV, which is greatly reduced as compared to the other polymorphs as a result of the specific diffusion pathway and relatively spacious transition states.[39] The layered metastable polymorphs furthermore hold potential for exfoliation down to single sheets wherein surface diffusion phenomena can potentially be facilitated.[102] Figure I.7c shows the structure of several target metastable frameworks potentially accessible from topochemical extraction of native cations from $M_xV_2O_5$ ternary vanadium oxide bronzes. The parent phases are delineated in the next section.

Indeed, one can extrapolate that thermodynamically stable phases are inimical to cation mobility since they most often bind the cation that is sought to be diffused within tightly defined and favorable coordination environments where their mobility is severely restricted; metastable structures that do not represent the absolute thermodynamic minima for a specific composition (and thus oftentimes are inaccessible from direct synthesis) can oftentimes accommodate cations with some degree of frustration. Cations inserted within these structures encounter sub-optimal coordination environments, which facilitate easier ion diffusion.[42,54]

The rugged energy landscape of the binary vanadium oxide VO_2 holds further lessons for the design of an even more expanded palette of V_2O_5 polymorphs. For instance, substitutional doping of VO_2 with Al or Cr allows for the stabilization of an

insulating monoclinic M_2 polymorph, which is distinct from the thermodynamically stable M_1 phase.[103,104] In contrast, substitutional incorporation of W and Mo on the vanadium sublattice as well as interstitial incorporation of B atoms stabilizes the metallic rutile phase, thereby shifting the canonical metal—insulator transition of VO_2 down below room temperature. The interstitial doping of atomic hydrogen stabilizes distinctive orthorhombic O_1 and O_2 metallic phases.[66,105–107] The use of substitutional doping to stabilize metastable polymorphs of V_2O_5 is less explored and represents a potentially rich area of discovery.

Metastable structures in tandem with pre- or co-intercalation of ions could further facilitate the intercalation of monovalent and multivalent ions.[98,108–110] For example, hydrated versions of double-layered V_2O_5 (similar in structure to the ε-phase) have been shown to exhibit excellent performance as Na- and K-ion intercalation hosts.[98,111] Pre-intercalated structures wherein V_2O_5 layers are separated by pillaring cations show proportionately improved performance with increasing interlayer separation.[93] An important caveat must be noted for metastable intercalation hosts. Stabilization of such polymorphs represents a considerable synthetic challenge. The most common strategy to stabilize such polymorphs is to synthetically access a region of a multidimensional phase diagram (spanning composition, temperature, pressure, and related variables) wherein such structures are in fact the lowest energy polymorph, followed by quenching to ambient conditions;[112] however, in the absence of a detailed understanding of energy landscapes, predictive design of synthetic approaches represents a considerable challenge. The barrier to reversion to the thermodynamically stable polymorph further

represents an important consideration. A detailed understanding of energy landscapes of intercalation hosts is imperative to understand transformation pathways and energy differentials. Such understanding will further provide critical guidance for the design of synthetic approaches.

I.1.7 Double Trouble: Diffusing Multivalent Cations

The ionic and coupled ionic—electronic roadblocks discussed above for α-V_2O_5 are further exacerbated for multivalent cations[31,60–62] as a result of their stronger polarizing nature, which contributes to a severe paucity of viable cathode materials capable of reversibly intercalating multivalent ions such as Mg^{2+}, Ca^{2+}, and Al^{3+}.[113] Current strategies to design diffusion pathways involve screening charge through the use of covalent Mo_6S_8 Chevrel phases (which, however, comes at the cost of a low operating voltage)[114,115] or screening charge through solvation of Mg-ions.[110,116] Based on DFT calculations, we have predicted a much smaller diffusion barrier for Mg^{2+} diffusion in metastable ζ-V_2O_5 derived from the smaller changes in the coordination environment along the diffusion pathway (accounting for a suppression of the diffusion barrier from 1.2 eV predicted for α-V_2O_5 to 600—900 meV in ζ-V_2O_5) and a reduced polaron diffusion barrier (reduced from 340 meV to 240 meV for a single polaron).[40,46] Indeed, in recent work, we have demonstrated that nanowires of this phase can reversibly intercalate 90 mAh/g of Mg-ions with excellent cyclability up to 100 cycles and an average operating potential of 1.65 V versus Mg^{2+}/Mg^0.[54] The observed capacity has been observed to arise from Mg-ion intercalation within 1D tunnels up to a stoichiometry of $Mg_{0.33}V_2O_5$ as unequivocally established using high-angle annular dark

field scanning transmission electron microscopy (STEM) imaging and XAS. These parameters immediately render this material one of the most promising Mg-ion cathode materials thus far discovered and provides strong validation of the idea of metastable phases as cathode materials to define desired diffusion pathways. Further elaboration of the material through aliovalent doping, control of particle size, and structured enmeshment with conductive additives will likely yield further enhancements of

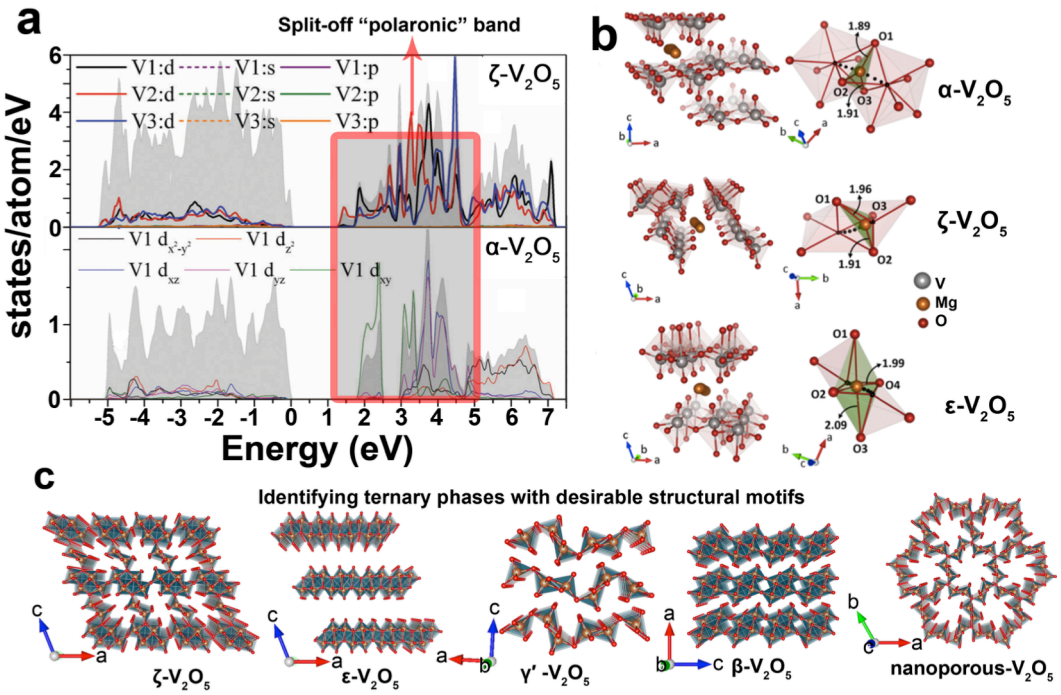

Figure I.7. Metastable frameworks as a means of mitigating diffusion limitations. (a) Calculated projected (colored traces) and total (grey) density of states for ζ-V_2O_5 and α-V_2O_5 (adapted from Ref. 46 from Chapter I with permission from the PCCP Owner Societies). The characteristic split-off conduction band of α-V_2O_5 is not observed for ζ-V_2O_5 owing to increased energetic overlap of V 3d orbitals. (b) The calculated diffusion pathway for Li-ions in three metastable polymorphs of V_2O_5 depicting frustrated coordination environments, as well as the geometry of the resulting transition state (reprinted with permission from citation 40. Copyright 2016 American Chemical Society) (c) Several metastable frameworks potentially accessible from topochemical extraction of native cations from $M_xV_2O_5$ ternary vanadium oxide bronze phases.

diffusion rates. Still lower barriers, ca. 0.21−0.24 eV and 0.28−0.46 eV, respectively, have been predicted for Mg-ion diffusion in double-layered ε'- and ρ′-V_2O_5 polymorphs that differ only in the stacking of [V_4O_{10}] layers.[39,40] Indeed, restacking of 2D layers can serve as a further design tool to define specific conduction pathways for multivalent cations. The diffusion of Ca-ions necessitates somewhat large transition states; For Ca-ion diffusion, the barriers deduced from NEB calculations are ca. 0.37−0.55 eV in ρ′-V_2O_5, ca. 0.56−0.65 eV in δ′-V_2O_5, and ca. 0.59−0.68 eV in γ′−V_2O_5. These values are within the range wherein viable Ca-ion mobility can be expected especially upon reducing particle size.[39]

In addition to the ζ-phase, the metastable γ′-V_2O_5[34,117] polymorph has been stabilized based on delithiation of the γ-$Li_xV_2O_5$ ternary phase. However, it remains to be evaluated for multivalent intercalation. Based on extensive DFT calculations and experimental realization of ζ-V_2O_5 as a viable high-voltage, high cyclability, and high-capacity material, a blueprint for defining conduction pathways for multivalent ions can be broadly put forth. In this approach, ternary vanadium oxides of the form $M_xV_2O_5$ with desirable structural motifs are identified from the crystallographic and mineralogical literature and the corresponding empty polymorphs are evaluated using DFT in terms of their stability and diffusion barriers. For structures determined to be intriguing, the intercalated cation is leached topochemically *via* topotactic *chimie douce* methods that allow for retention of the structural framework while extracting the "native" cations. The stabilized structure can then be chemically or electrochemically intercalated with Li- or multivalent cations to prepare a cathode material with well-defined conduction pathways

that are distinctly different from that of α-V_2O_5. Such an approach thus greatly expands the available palette of binary polymorphs of V_2O_5. Figure I.7c depicts the structures of different metastable V_2O_5 frameworks conceptually derived from topochemical extraction of the native cations of[39,40] ε/δ/ρ-$M_xV_2O_5$ (where M= ε-$Cu_xV_2O_5$, δ-$Ag_xV_2O_5$ or δ-$Ca_xV_2O_5$, and ρ-$K_xV_2O_5$ yield ε'/δ'/ρ'-V_2O_5)[39], $[(Me)_4N]_{0.25}V_2O_5$ (yielding β-V_2O_5)[118,119], and $Cs_{0.35}V_3O_7$ (yielding microporous V_2O_5)[120]. Topochemical leaching can be achieved using Br_2 or I_2 solution or by reaction with $NOBF_4$ or NO_2BF_4.[54,121] It is worth noting that such a topochemical mapping of metastable phase space will furthermore be applicable to other oxide or sulfide frameworks, and suggests a versatile means of defining conduction pathways to enforce design elements such as frustrated coordination and mitigation of large structural transformations.[122,123] Experimental studies of cation intercalation in broader palettes of structures characterized by distinctive structural motifs, variations of polyhedral connectivity, and electronic structure is anticipated to yield richer descriptors of specific atomistic elements that can facilitate multivalent diffusion while meeting the other constraints required for use as a viable intercalation host (e.g., chemical and mechanical stability, criticality).

I.2 Conclusion and Dissertation Outlook

In this dissertation, we provide a summary of work performed to evaluate the mechanism of insertion of Li-ion within a cathode material. We also use scanning transmission X-ray microscopy to evaluate changes in electronic structure and intercalation-induced phase transformations resulting from insertion processes. We start in Chapter II, where we discuss the oxidative chemistry of graphite, which has attracted

renewed interest, given the importance of exfoliated graphene oxide (GO) as a precursor to chemically derived reduced graphene oxide (r-GO), which is finding increasing use as the active element of anode architectures. The development of structured carbon composites provides a means to improve the number of cycles, capacity, and rate performance of anode materials. Functionalization of nanostructured carbons is imperative to facilitate the formation of structured anode composites. In Chapter II, we demonstrate the application of principal component analysis to scanning transmission X-ray microscopy data for the construction of detailed real-space chemical maps of graphene oxide. These chemical maps indicate very distinct functionalization motifs at the edges and interiors, and in conjunction with angle-resolved near-edge X-ray absorption fine structure spectroscopy enable determination of the spatial location and steric orientations of functional groups. In Chapter III, we turn our focus to the origin of intercalation-induced transformations and phase heterogeneities within individual V_2O_5 nanowires upon chemical lithiation, which are seen to strongly depend on the formation of polarons coupling electron diffusion barriers with structural distortions. We demonstrate using scanning transmission X-ray microscopy (STXM) that in individual nanowires of layered V_2O_5, lithiation gradients observed upon Li-ion intercalation arise from electron localization and local structural distortions. The electron localized on the V_2O_5 framework couples to a local structural distortion, giving rise to a small polaron that serves as a bottleneck for further Li-ion insertion. The stabilization of this polaron traps Li-ions giving and impedes equilibration of charge density across the nanowire, which in turn gives rise to distinctive domains. The enhancement in high rate

charge/discharge for this material upon nanostructuring can be attributed to circumventing challenges with charge transport from polaron formation. In Chapter IV we demonstrate compositional striping modulations between Li-rich and Li-poor domains along the edges of individual nanowires of Li-ion-intercalated V_2O_5 based on analysis of hyperspectral X-ray microscopy data. Analysis of scanning transmission X-ray microscopy data using singular value decomposition and principal component analysis provides a means to map compositional inhomogenieties across individual nanowires and ensembles of nanowires alike. The compositional maps are further transformed to stress and strain maps, which depict the localization of tensile stress and strain within individual nanowires of $Li_xV_2O_5$. The core/shell and compositional striping modulations manifested here and the resulting strain gradients point to the need to design cathode materials and electrode architectures to mitigate such pronounced local inhomoegeneities in Li-ion intercalation and diffusion. Finally, in Chapter V, we show based on scanning transmission X-ray microscopy studies of Li-ion intercalation within interconnected V_2O_5 particle networks that interconnects between cathode particles strongly influence the transport of Li-ions and the resulting spatial propagation of phase transformations across the network. Considerable phase heterogeneity is observed across interfaces that are rationalized based on phase field models that suggest that the propagation of Li-rich domains occurs preferentially across a single particle instead of concurrent lithiation and nucleation of Li-rich domains across the entire network. Further phase heterogeneity arises from defects and secondary growth of Li-rich phases at nanowire tips. These findings suggest that mesoscale architectures can potentially be

designed with appropriately positioned interconnects to maximize the proportion of actively intercalating regions and to ensure equilibration of local current densities.

I.3 References

(1) Creutzig, F.; Agoston, P.; Goldschmidt, J. C.; Luderer, G.; Nemet, G.; and Pietzcker, R. C. The underestimated potential of solar energy to mitigate climate change. *Nature Energy*. **2017**, *2*, 1-9.

(2) Dunn, B.; Kamath, H.; and Tarascon, J. M. Electrical energy storage for the grid: a battery of choices. *Science*. **2011**, *334*, 928–935.

(3) Tarascon, J.-M. and Armand, M. Issues and challenges facing rechargeable lithium batteries. *Nature.* **2001**, *414*, 359–367.

(4) Goodenough, J. B. Rechargeable batteries: challenges old and new. *J. Solid State Electrochem.* **2012**, *16*, 2019–2029.

(5) Goodenough, J. B. and Park, K.-S. The Li-ion rechargeable battery: a perspective. *J. Am. Chem. Soc.* **2013**, *135*, 1167–1176.

(6) Kang, B. and Ceder, G. Battery materials for ultrafast charging and discharging. *Nature.* **2009**, *458*, 190–193.

(7) Nitta, N.; Wu, F.; Lee, J. T.; and Yushin, G. Li-ion battery materials: present and future. *Mater. Today* **2015**, *18*, 252–264.

(8) Whittingham, M. S. Lithium batteries and cathode materials. *Chem. Rev.* **2004**, *104*, 4271–4301.

(9) Lim, J.; Li, Y.; Alsem, D. H.; So, H.; Lee, S. C.; Bai, P.; Cogswell, D. A.; Liu, X.; Jin, N.; Yu, Y.; et al. Origin and hysteresis of lithium compositional

spatiodynamics within battery primary particles. *Science.* **2016**, *353*, 566–571.

(10) Hernández-Burgos, K.; Barton, Z. J.; and Rodríguez-López, J. Finding harmony between ions and electrons: new tools and concepts for emerging energy storage materials. *Chem. Mater.* **2017**, *29*, 8918–8931.

(11) Barai, P. and Mukherjee, P. P. Mechano-electrochemical stochastics in high-capacity electrodes for energy storage. *J. Electrochem. Soc.* **2016**, *163*, A1120–A1137.

(12) Marley, P. M.; Horrocks, G. A.; Pelcher, K. E.; and Banerjee, S. Transformers: the changing phases of low-dimensional vanadium oxide bronzes. *Chem. Commun.* **2015**, *51*, 5181–5198.

(13) Chernova, N. A.; Roppolo, M.; Dillon, A. C.; and Whittingham, M. S. Layered vanadium and molybdenum oxides: batteries and electrochromics. *J. Mater. Chem.* **2009**, *19*, 2526–2552.

(14) Meng, Y. S.; and Arroyo-De Dompablo, M. E. Recent advances in first principles computational research of cathode materials for lithium-ion batteries. *Acc. Chem. Res.* **2013**, *46*, 1171–1180.

(15) Van Der Ven, A.; Bhattacharya, J.; and Belak, A. A. Understanding Li diffusion in Li-intercalation compounds. *Acc. Chem. Res.* **2013**, *46*, 1216–1225.

(16) Lozano, A.; Escribano, B.; Akhmatskaya, E.; and Carrasco, J. Assessment of van der Waals inclusive density functional theory methods for layered electroactive materials. *Phys. Chem. Chem. Phys.* **2017**, *19*, 10133–10139.

(17) Carrasco, J. Role of van der Waals forces in thermodynamics and kinetics of

layered transition metal oxide electrodes: alkali and alkaline-earth ion insertion into V_2O_5. *J. Phys. Chem. C* **2014**, *118*, 19599–19607.

(18) Whittingham, M. S. The role of ternary phases in cathode reactions. *J. Electrochem. Soc.* **1976**, *123*, 315–320.

(19) Mizyshima, K.; Jones, P. C.; Wiseman, P. J.; and Goodenough, J. B. Li_xCoO_2 ($0 < x \leq 1$): a new cathode material for batteries of high energy density. *Mat. Res. Bull.* **1980**, *15*, 783–789.

(20) Kan, W. H.; Kuppan, S.; Cheng, L.; Doe, M.; Nanda, J.; and Chen, G. Crystal chemistry and electrochemistry of $Li_xMn_{1.5}Ni_{0.5}O_4$ solid solution cathode materials. *Chem Mater* **2017**, *29*, 6818–6828.

(21) Jarvis, K. A.; Deng, Z.; Allard, L. F.; Manthiram, A.; and Ferreira, P. J. Atomic structure of a lithium-rich layered oxide material for lithium-ion batteries: evidence of a solid solution. *Chem. Mater.* **2011**, *23*, 3614–3621.

(22) Reimers, J. N. and Dahn, J. R. Electrochemical and in situ X-ray diffraction studies of lithium intercalation in Li_xCoO_2. *J. Electrochem. Soc.* **1992**, *139*, 2091–2097.

(23) Yu, Y. S.; Kim, C.; Shapiro, D. A.; Farmand, M.; Qian, D.; Tyliszczak, T.; Kilcoyne, A. L. D.; Celestre, R.; Marchesini, S.; Joseph, J.; et al. Dependence on crystal size of the nanoscale chemical phase distribution and fracture in Li_xFePO_4. *Nano Lett.* **2015**, *15*, 4282–4288.

(24) Abdellahi, A.; Akyildiz, O.; Malik, R.; Thornton, K.; and Ceder, G. Particle-size and morphology dependence of the preferred interface orientation in $LiFePO_4$

nano-particles. *J. Mater. Chem. A* **2014**, *2*, 15437-15447.

(25) Li, Y.; El Gabaly, F.; Ferguson, T. R.; Smith, R. B.; Bartelt, N. C.; Sugar, J. D.; Fenton, K. R.; Cogswell, D. A.; Kilcoyne, A. L. D.; Tyliszczak, T.; et al. Current-induced transition from particle-by-particle to concurrent intercalation in phase-separating battery electrodes. *Nat. Mater.* **2014**, *13*, 1149–1156.

(26) Bai, P.; Cogswell, D. A.; and Bazant, M. Z. Suppression of phase separation in $LiFePO_4$ nanoparticles during battery discharge. *Nano Lett.* **2011**, *11*, 4890–4896.

(27) Delacourt, C.; Poizot, P.; Tarascon, J.-M.; and Masquelier, C. The existence of a temperature-driven solid solution in Li_xFePO_4 for $0 \leq x \leq 1$. *Nat. Mater.* **2005**, *4*, 254–260.

(28) Nishimura, S.; Kobayashi, G.; Ohoyama, K.; Kanno, R.; Yashima, M.; and Yamada, A. Experimental visualization of lithium diffusion in Li_xFePO_4. *Nat. Mater.* **2008**, *7*, 707–711.

(29) Byström, A.; Wilhelmi, K.-A.; and Brotzen, O. Vanadium pentoxide: a compound with five-coordinated vanadium atoms. *Acta Chemica Scandinavica*. **1950**, 1119–1130.

(30) Horrocks, G. A.; De Jesus, L. R.; Andrews, J. L.; and Banerjee, S. X-ray spectroscopy and imaging as multiscale probes of intercalation phenomena in cathode materials. *JOM* **2017**, *69*, 1469–1477.

(31) De Jesus, L. R.; Horrocks, G. A.; Liang, Y.; Parija, A.; Jaye, C.; Wangoh, L.; Wang, J.; Fischer, D. A.; Piper, L. F. J.; Prendergast, D.; and Banerjee, S.

Mapping polaronic states and lithiation gradients in individual V_2O_5 nanowires. *Nat. Commun.* **2016**, *7*, 12022:1–9.

(32) Horrocks, G. A.; Braham, E. J.; Liang, Y.; De Jesus, L. R.; Jude, J.; Velázquez, J. M.; Prendergast, D.; and Banerjee, S. Vanadium K-edge X-ray absorption spectroscopy as a probe of the heterogeneous lithiation of V_2O_5: first-principles modeling and principal component analysis. *J. Phys. Chem. C* **2016**, *120*, 23922–23932.

(33) Horrocks, G. A.; Likely, M. F.; Velazquez, J. M.; and Banerjee, S. Finite size effects on the structural progression induced by lithiation of V_2O_5: a combined diffraction and Raman spectroscopy study. *J. Mater. Chem. A* **2013**, *1*, 15265–15277.

(34) Galy, J.; Darriet, J.; and Hagenmuller, P. Les bronzes $Li_xV_2O_5$: structure de la phase β' et affinement de la structure de la phase γ. *Rev. Chim. Miner.* **1971**, *8*, 509–522.

(35) Suthirakun, S.; Genest, A.; and Rösch, N. Modeling polaron-coupled Li cation diffusion in V_2O_5 cathode material. *J. Phys. Chem. C* **2018**, 122, 150–157.

(36) Kulish, V. V. and Manzhos, S. Comparison of Li, Na, Mg and Al-ion insertion in vanadium pentoxides and vanadium dioxides. *RSC Adv.* **2017**, *7*, 18643–18649.

(37) Kang, K.; Morgan, D.; and Ceder, G. First principles study of Li diffusion in I-Li_2NiO_2 structure. *Phys. Rev. B - Condens. Matter Mater. Phys.* **2009**, *79*, 1–4.

(38) Ong, S. P.; Chevrier, V. L.; Hautier, G.; Jain, A.; Moore, C.; Kim, S.; Ma, X.; and Ceder, G. Voltage, stability, and diffusion barrier differences between

sodium-ion and lithium-ion intercalation materials. *Energy Environ. Sci.* **2011**, *4*, 3680–3688.

(39) Parija, A.; Prendergast, D.; and Banerjee, S. Evaluation of multivalent cation insertion in single- and double-layered polymorphs of V_2O_5. *ACS Appl. Mater. Interfaces* **2017**, *9*, 23756–23765.

(40) Parija, A.; Liang, Y.; Andrews, J.; De Jesus, L. R.; Prendergast, D.; and Banerjee, S. Topochemically de-intercalated phases of V_2O_5 as cathode materials for multivalent intercalation batteries: a first-principles evaluation. *Chem. Mater.* **2016**, *28*, 5611–5620.

(41) Sai Gautam, G.; Canepa, P.; Abdellahi, A.; Urban, A.; Malik, R.; and Ceder, G. The intercalation phase diagram of Mg in V_2O_5 from first-principles. *Chem. Mater.* **2015**, *27*, 3733–3742.

(42) Horrocks, G. A.; Parija, A.; De Jesus, L. R.; Wangoh, L.; Sallis, S.; Luo, Y.; Andrews, J. L.; Jude, J.; Jaye, C.; Fischer, D. A.; et al. Mitigating cation diffusion limitations and intercalation-induced framework transitions in a 1D tunnel-structured polymorph of V_2O_5. *Chem. Mater.* **2017**, *29*, 10386–10397.

(43) Rong, Z.; Malik, R.; Canepa, P.; Sai Gautam, G.; Liu, M.; Jain, A.; Persson, K.; and Ceder, G. Materials design rules for multivalent ion mobility in intercalation structures. *Chem. Mater.* **2015**, *27*, 6016–6021.

(44) Velazquez, J. M.; Jaye, C.; Fischer, D. A.; and Banerjee, S. Near edge X-ray absorption fine structure spectroscopy studies of single-crystalline V_2O_5 nanowire arrays. *J. Phys. Chem. C* **2009**, *113*, 7639–7645.

(45) Maganas, D.; Roemelt, M.; Hävecker, M.; Trunschke, A.; Knop-Gericke, A.; Schlögl, R.; and Neese, F. First principles calculations of the structure and V L-edge X-ray absorption spectra of V_2O_5 using local pair natural orbital coupled cluster theory and spin-orbit coupled configuration interaction approaches. *Phys. Chem. Chem. Phys.* **2013**, *15*, 7260–7276.

(46) Tolhurst, T. M.; Leedahl, B.; Andrews, J. L.; Marley, P. M.; Banerjee, S.; and Moewes, A. Contrasting 1D tunnel-structured and 2D layered polymorphs of V_2O_5: relating crystal structure and bonding to band gaps and electronic structure. *Phys. Chem. Chem. Phys.* **2016**, *18*, 15798–15806.

(47) Bhandari, C.; Lambrecht, W. R. L.; and Van Schilfgaarde, M. Quasiparticle self-consistent GW calculations of the electronic band structure of bulk and monolayer V_2O_5. *Phys. Rev. B -Condens. Matter Mater. Phys.* **2015**, *91*, 1-12.

(48) Ioffe, V.A. and Patrina, I. B. Comparison of the small-polaron theory with the experimental data of current transport in V_2O_5. *Phys. Status Solidi* **1970**, *389*, 389–395.

(49) Pomerantseva, E. and Gogotsi, Y. Two-dimensional heterostructures for energy storage. *Nat. Energy* **2017**, *2*, 1-6.

(50) Wolf, M.; May, B. M.; and Cabana, J. Visualization of electrochemical reactions in battery materials with X-ray microscopy and mapping. *Chem. Mater.* **2017**, *29*, 3347–3362.

(51) Eyert, V. and Höck, K.-H. Electronic structure of V_2O_5: role of octahedral deformations. *Phys. Rev. B* **1998**, *57*, 12727–12737.

(52) Goering, E., Müller, O., Klemm, M., denBoer, M. L., and Horn, S. Angle dependent soft-X-ray absorption spectroscopy of V_2O_5. *Philos. Mag. B* **1997**, *75*, 229–236.

(53) De Jesus, L. R.; Zhao, Y.; Horrocks, G. A.; Andrews, J.; Stein, P.; Xu, B.-X.; and Banerjee, S. Lithiation across interconnected V_2O_5 nanoparticle networks. *J. Mater. Chem. A* **2017**, *5*, 20141–20152.

(54) Andrews, J. L.; Mukherjee, A.; Yoo, H. D.; Parija, A.; Marley, P. M.; Prendergast, D.; Cabana, J.; Klie, R. F.; and Banerjee, S. Reversible Mg-ion insertion in a metastable one-dimensional polymorph of V_2O_5. *Chem* **2018**, *4*, 564–585.

(55) Maxisch, T.; Zhou, F.; and Ceder, G. Ab initio study of the migration of small polarons in olivine Li_xFePO_4 and their association with lithium ions and vacancies. *Phys. Rev. B* **2006**, *73*, 1-6.

(56) Tahini, H. A.; Tan, X.; Lou, S. N.; Scott, J.; Amal, R.; Ng, Y. H.; and Smith, S. C. Mobile polaronic states in α-MoO_3: an ab initio investigation of the role of oxygen vacancies and alkali ions. *ACS Appl. Mater. Interfaces* **2016**, *8*, 10911–10917.

(57) Ding, H.; Lin, H.; Sadigh, B.; Zhou, F.; Ozoliņš, V.; and Asta, M. Computational investigation of electron small polarons in α-MoO_3. *J. Phys. Chem. C* **2014**, *118*, 15565–15572.

(58) Liu, Z.; Balbuena, P. B.; and Mukherjee, P. P. Revealing charge transport mechanisms in Li_2S_2 for Li-sulfur batteries. *J. Phys. Chem. Lett.* **2017**, *8*, 1324–

1330.

(59) Ping Ong, S.; Chevrier, V. L.; and Ceder, G. Comparison of small polaron migration and phase separation in olivine $LiMnPO_4$ and $LiFePO_4$ using hybrid density functional theory. *Phys. Rev. B* **2011**, *83*, 75112.

(60) Yu, J.; Sushko, M. L.; Kerisit, S.; Rosso, K. M.; and Liu, J. Kinetic Monte Carlo study of ambipolar lithium ion and electron − polaron diffusion into nanostructured TiO_2. *J. Phys. Chem. Lett.* **2012**, *3*, 2076–2081.

(61) Luntz, A. C.; Viswanathan, V.; Voss, J.; Varley, J. B.; Nørskov, J. K.; Scheffler, R.; and Speidel, A. Tunneling and polaron charge transport through Li_2O_2 in Li–O_2 Batteries. *J. Phys. Chem. Lett.* **2013**, *4*, 3494–3499.

(62) Ellis, B.; Perry, L. K.; Ryan, D. H.; and Nazar, L. F. Small polaron hopping in Li_xFePO_4 solid solutions: coupled lithium-ion and electron mobility. *J. Am. Chem. Soc.* **2006**, *128*, 11416–11422.

(63) Carneiro, L. M.; Cushing, S. K.; Liu, C.; Su, Y.; Yang, P.; Alivisatos, A. P.; and Leone, S. R. Excitation-wavelength-dependent small polaron trapping of photoexcited carriers in α-Fe_2O_3. *Nat. Mater.* **2017**, *16*, 819–825.

(64) Chalker, C. J.; An, H.; Zavala, J.; Parija, A.; Banerjee, S.; Lutkenhaus, J. L.; and Batteas, J. D. Fabrication and electrochemical performance of structured mesoscale open shell V_2O_5 networks. *Langmuir* **2017**, *33*, 5975–5981.

(65) Hudak, B. M.; Depner, S. W.; Waetzig, G. R.; Talapatra, A.; Arroyave, R.; Banerjee, S.; and Guiton, B. S. Real-time atomistic observation of structural phase transformations in individual hafnia nanorods. *Nat. Commun.* **2017**, *8*, 1-9.

(66) Alivio, T. E. G.; Sellers, D. G.; Asayesh-Ardakani, H.; Braham, E. J.; Horrocks, G. A.; Pelcher, K. E.; Villareal, R.; Zuin, L.; Shamberger, P. J.; Arróyave, R.; et al. Postsynthetic route for modifying the metal-insulator transition of VO_2 by interstitial dopant incorporation. *Chem. Mater.* **2017**, *29*, 5401–5412.

(67) Buerger, M. J. Polymorphism and phase transformations. *Fortschr. Miner.* **1961**, *39,* 9-24.

(68) Galy, J.; Satto, C.; Sciau, P.; and Millet, P. Atomic modeling of the δ⇔ε LiV_2O_5 phase transition and simulation of the XRD powder pattern evolution. *J. Solid State Chem.* **1999**, *146*, 129–136.

(69) Galy, J. Vanadium pentoxide and vanadium oxide bronzes—structural chemistry of single (S) and double (D) layer $M_xV_2O_5$ phases. *J. Solid State Chem.* **1992**, *100*, 229–245.

(70) Zahn, D. and Leoni, S. Nucleation and growth in pressure-induced phase transitions from molecular dynamics simulations: mechanism of the reconstructive transformation of NaCl to the CsCl-type structure. *Phys. Rev. Lett.* **2004**, *92*, 1-4.

(71) Hanaor, D. A. H. and Sorrell, C. C. Review of the anatase to rutile phase transformation. *Journal of Materials Science*. **2011**, *46*, 855–874.

(72) Whittingham, M. S. and Dines, M. B. n-butyllithium—An effective, general cathode screening agent. *J. Electrochem. Soc.* **1977**, *124*, 1387–1388.

(73) Satto, C.; Sciau, P.; Dooryhee, E.; Galy, J.; and Millet, P. The δ→ε→γ LiV_2O_5 "high temperature" phase transitions evidenced by synchrotron X-ray powder

diffraction analysis. *J. Solid State Chem.* **1999**, *109*, 103–109.

(74) Murphy, D. W.; Christian, P. A.; DiSalvo, F. J.; and Waszczak, J. V. Lithium incorporation by vanadium pentoxide. *Inorg. Chem.* **1979**, *18*, 2800–2803.

(75) Millet, P.; Satto, C.; Sciau, P.; and Galy, J. MgV_2O_5 and $Li_xV_2O_5$: a comparative structural investigation. *J. Solid State Chem.* **1998**, *62*, 56–62.

(76) Wang, W.; Wang, H.; Liu, S.; and Huang, J. Synthesis of γ-LiV2O5 nanorods as a high-performance cathode for Li ion battery. *J. Solid State Electrochem.* **2012**, *16*, 2555–2561.

(77) Rozier, P.; Savariault, J. M.; and Galy, J. A new interpretation of the $Li_xV_2O_5$ electrochemical behaviour for $1<x<3$. *Solid State Ionics* **1997**, *98*, 133–144.

(78) Zhao, Y.; De Jesus, L. R.; Stein, P.; Horrocks, G. A.; Banerjee, S.; and Xu, B.-X. Modeling of phase separation across interconnected electrode particles in lithium-ion batteries. *RSC Adv.* **2017**, *7*, 41254–41264.

(79) Orvananos, B.; Ferguson, T. R.; Yu, H.-C.; Bazant, M. Z.; and Thornton, K. Particle-level modeling of the charge-discharge behavior of nanoparticulate phase-separating Li-ion battery electrodes. *J. Electrochem. Soc.* **2014**, *161*, A535–A546.

(80) Yu, Y.; Farmand, M.; Kim, C.; Liu, Y.; Grey, C. P.; Strobridge, F. C.; Tyliszczak, T.; Celestre, R.; Denes, P.; Joseph, J.; et al. Three dimensional localization of nanoscale battery reactions using soft X-ray tomography. *arxiv.org/abs/1711.01525v1,* **2017**, 1–36.

(81) De Jesus, L. R.; Stein, P.; Andrews, J. L.; Luo, Y.; Xu, B.-X.; and Banerjee, S.

Striping modulations and strain gradients within individual particles of a cathode material upon lithiation. *Mater. Horizons* **2018**, *5,* 486-498.

(82) Zhao, Y.; Schillinger, D.; and Xu, B. X. Variational boundary conditions based on the Nitsche method for fitted and unfitted isogeometric discretizations of the mechanically coupled Cahn–Hilliard equation. *J. Comput. Phys.* **2017**, *340*, 177–199.

(83) Muralidharan, N.; Brock, C. N.; Cohn, A. P.; Schauben, D.; Carter, R. E.; Oakes, L.; Walker, D. G.; and Pint, C. L. Tunable mechanochemistry of lithium battery electrodes. *ACS Nano* **2017**, *11*, 6243–6251.

(84) Chen, C.; Boota, M.; Urbankowski, P.; Anasori, B.; Miao, L.; Jiang, J.; and Gogotsi, Y. Effect of glycine functionalization of 2D titanium carbide (MXene) on charge storage. *J. Mater. Chem. A* **2018**, *6,* 4617-4622.

(85) Kohandehghan, A.; Cui, K.; Kupsta, M.; Memarzadeh, E.; Kalisvaart, P.; and Mitlin, D. Nanometer-scale Sn coatings improve the performance of silicon nanowire LIB anodes. *J. Mater. Chem. A* **2014**, *2*, 11261–11279.

(86) Wu, N.; Lyu, Y.-C.; Xiao, R.-J.; Yu, X.; Yin, Y.-X.; Yang, X.-Q.; Li, H.; Gu, L.; and Guo, Y.-G. A highly reversible, low-strain Mg-ion insertion anode material for rechargeable Mg-ion batteries. *Npg Asia Mater.* **2014**, *6*, e120:1-7.

(87) Bazito, F. F. C. and Torresi, R. M. Cathodes for lithium ion batteries: the benefits of using nanostructured materials. *J. Braz. Chem. Soc.* **2006**, *17*, 627–642.

(88) Stein, P.; Zhao, Y.; and Xu, B.-X. Effects of surface tension and electrochemical reactions in Li-ion battery electrode nanoparticles. *J. Power Sources* **2016**, *332*,

154–169.

(89) Whittingham, M. S. Inorganic nanomaterials for batteries. *Dalt. Trans.* **2008**, 40, 5424–5431.

(90) Kikkawa, J.; Kitta, M.; and Kohyama, M. Nanometer-thick V_2O_5 sheets on aluminum foil for an additive-free positive electrode of lithium-ion batteries. *Chem. Phys. Lett.* **2014**, *592*, 56–58.

(91) Zavalij, P. Y. and Whittingham, M. S. Structural chemistry of vanadium oxides with open frameworks. *Acta Crystallogr.* **1999**, *B55*, 627–663.

(92) Tepavcevic, S.; Xiong, H.; Stamenkovic, V. R.; Zuo, X.; Balasubramanian, M.; Prakapenka, V. B.; Johnson, C. S.; and Rajh, T. Nanostructured bilayered vanadium oxide electrodes for rechargeable sodium-ion batteries. *ACS Nano* **2012**, *6*, 530–538.

(93) Clites, M. and Pomerantseva, E. Bilayered vanadium oxides by chemical pre-intercalation of alkali and alkali-earth ions as battery electrodes. *Energy Storage Mater.* **2018**, *11*, 30–37.

(94) Moretti, A.; Maroni, F.; Osada, I.; Nobili, F.; and Passerini, S. V_2O_5 aerogel as a versatile cathode material for lithium and sodium batteries. *ChemElectroChem* **2015**, *2*, 529–537.

(95) Moretti, A.; Secchiaroli, M.; Buchholz, D.; Giuli, G.; Marassi, R.; and Passerini, S. Exploring the low voltage behavior of V_2O_5 aerogel as intercalation host for sodium ion battery. *J. Electrochem. Soc.* **2015**, *162*, A2723–A2728.

(96) Moretti, A.; Giuli, G.; Trapananti, A.; and Passerini, S. Electrochemical and

structural investigation of transition metal doped V_2O_5 sono-aerogel cathodes for lithium metal batteries. *Solid State Ionics* **2018**, *319*, 46–52.

(97) Tian, B.; Tang, W.; Su, C.; and Li, Y. Reticular $V_2O_5 \cdot 0.6H_2O$ xerogel as cathode for rechargeable potassium ion batteries. *ACS Appl. Mater. Interfaces* **2018**, *10*, 642-650.

(98) Wei, Q.; Liu, J.; Feng, W.; Sheng, J.; Tian, X.; He, L.; An, Q.; and Mai, L. Hydrated vanadium pentoxide with superior sodium storage capacity. *J. Mater. Chem. A* **2015**, *3*, 8070–8075.

(99) Tolhurst, T. M.; Leedahl, B.; Andrews, J. L.; Banerjee, S.; and Moewes, A. The electronic structure of ε′-V_2O_5: an expanded band gap in a double-layered polymorph with increased interlayer separation. *J. Mater. Chem. A* **2017**, *5*, 23694–23703.

(100) Marley, P. M.; Abtew, T. A.; Farley, K. E.; Horrocks, G. A.; Dennis, R. V; Zhang, P.; and Banerjee, S. Emptying and filling a tunnel bronze. *Chem. Sci.* **2015**, *6*, 1712–1718.

(101) Dreyer, W.; Guhlke, C.; and Huth, R. The behavior of a many-particle electrode in a lithium-ion battery. *Phys. D Nonlinear Phenom.* **2011**, *240*, 1008–1019.

(102) Andrews, J. L.; De Jesus, L. R.; Tolhurst, T. M.; Marley, P. M.; Moewes, A.; and Banerjee, S. Intercalation-induced exfoliation and thickness-modulated electronic structure of a layered ternary vanadium oxide. *Chem. Mater.* **2017**, *29*, 3285–3294.

(103) Pouget, J. P.; Launois, H.; Rice, T. M.; Dernier, P.; and Gossard, A. Dimerization

of a linear Heisenberg chain in the insulating phases of $V_{1-x}Cr_xO_2$. *Phys. Rev. B* **1974**, *10*, 1801–1815.

(104) Ghedira, M.; Vincent, H.; Marezio, M.; and Launay, J. C. Structural aspects of the metal-insulator transitions in $V_{0.985}Al_{0.015}O_2$. *J. Solid State Chem.* **1977**, *22*, 423–438.

(105) Whittaker, L.; Wu, T.-L.; Patridge, C. J.; Sambandamurthy, G.; and Banerjee, S. Distinctive finite size effects on the phase diagram and metal–insulator transitions of tungsten-doped vanadium(IV) oxide. *J. Mater. Chem.* **2011**, *21*, 5521–5828.

(106) Patridge, C. J.; Whittaker, L.; Ravel, B.; and Banerjee, S. Elucidating the influence of local structure perturbations on the metal-insulator transitions of $V_{1-x}Mo_xO_2$ nanowires: mechanistic insights from an X-ray absorption spectroscopy study. *J. Phys. Chem. C* **2012**, *116*, 3728–3736.

(107) Filinchuk, Y.; Tumanov, N. A.; Ban, V.; Ji, H.; Wei, J.; Swift, M. W.; Nevidomskyy, A. H.; and Natelson, D. In situ diffraction study of catalytic hydrogenation of VO_2: stable phases and origins of metallicity. *J. Am. Chem. Soc.* **2014**, *136*, 8100–8109.

(108) Charles, D. S.; Feygenson, M.; Page, K.; Neuefeind, J.; Xu, W.; and Teng, X. Structural water engaged disordered vanadium oxide nanosheets for high capacity aqueous potassium-ion storage. *Nat. Commun.* **2017**, *8*, 1–8.

(109) Tepavcevic, S.; Liu, Y.; Zhou, D.; Lai, B.; Maser, J.; Zuo, X.; Chan, H.; Král, P.; Johnson, C. S.; Stamenkovic, V.; et al. Nanostructured layered cathode for

rechargeable Mg-ion batteries. *ACS Nano* **2015**, *9*, 8194–8205.

(110) Yoo, H. D.; Liang, Y.; Dong, H.; Lin, J.; Wang, H.; Liu, Y.; Ma, L.; Wu, T.; Li, Y.; Ru, Q.; et al. Fast kinetics of magnesium monochloride cations in interlayer-expanded titanium disulfide for magnesium rechargeable batteries. *Nat. Commun.* **2017**, *8*, 339:1–10.

(111) Clites, M.; Hart, J. L.; Taheri, M. L.; and Pomerantseva, E. Chemically preintercalated bilayered $K_xV_2O_5 \cdot nH_2O$ nanobelts as a high-performing cathode material for K-ion batteries. *ACS Energy Lett.* **2018**, *3*, 562–567.

(112) Sun, W.; Dacek, S. T.; Ong, S. P.; Hautier, G.; Jain, A.; Richards, W. D.; Gamst, A. C.; Persson, K. A.; and Ceder, G. The thermodynamic scale of inorganic crystalline metastability. *Sci. Adv.* **2016**, *2*, 1–8.

(113) Levi, E.; Gofer, Y.; and Aurbach, D. On the way to rechargeable Mg batteries: the challenge of new cathode materials. *Chem. Mater.* **2010**, *22*, 860–868.

(114) Wan, L. F.; Perdue, B. R.; Apblett, C. A.; and Prendergast, D. Mg desolvation and intercalation mechanism at the Mo_6S_8 Chevrel phase surface. *Chem. Mater.* **2015**, *27*, 5932–5940.

(115) Thole, F.; Wan, L. F.; and Prendergast, D. Re-examining the Chevrel phase Mo_6S_8 cathode for Mg intercalation from an electronic structure perspective. *Phys. Chem. Chem. Phys.* **2015**, *17*, 22548–22551.

(116) Liang, Y.; Yoo, H. D.; Li, Y.; Shuai, J.; Calderon, H. A.; Robles Hernandez, F. C.; Grabow, L. C.; and Yao, Y. Interlayer-expanded molybdenum disulfide nanocomposites for electrochemical magnesium storage. *Nano Lett.* **2015**, *15*,

2194–2202.

(117) Cocciantelli, J. M.; Gravereau, P.; Doumerc, J. P.; Pouchard, M.; and Hagenmuller, P. On the preparation and characterization of a new polymorph of V_2O_5. *J. Solid State Chem.* **1991**, *93*, 497–502.

(118) Chirayil, T.; Zavalij, P. Y.; and Whittingham, M. S. Synthesis and characterization of a new vanadium oxide, $TMAV_8O_{20}$. *J. Mater. Chem.* **1997**, *7*, 2193–2195.

(119) Zibrov, I. P.; Filomenko, V. P.; Lyapin, S. G.; and Sidorov, V. A. The high pressure phases β- and δ-V_2O_5: structure refinement, electrical and optical properties, thermal stability. *High Press. Res.* **2013**, *33*, 399–408.

(120) Waltersson, K. and Forslund, B. On the crystal structure of $Cs_xV_3O_7$ (x~0.35), a new hexagonal vanadium bronze structure type. *Acta Crystallogr.* **1977**, *307*, 775–779.

(121) Lee, K. T.; Ramesh, T. N.; Nan, F.; Botton, G.; and Nazar, L. F. Topochemical synthesis of sodium metal phosphate olivines for sodium-ion batteries. *Chem. Mater.* **2011**, *23*, 3593–3600.

(122) Whittingham, M. S.; Guo, J.-D.; Chen, R.; Chirayil, T.; Janauer, G.; and Zavalij, P. The hydrothermal synthesis of new oxide materials. *Solid State Ionics* **1995**, *75*, 257–268.

(123) Mazur, M.; Wheatley, P. S.; Navarro, M.; Roth, W. J.; Položij, M.; Mayoral, A.; Eliášová, P.; Nachtigall, P.; Čejka, J.; and Morris, R. E. Synthesis of "unfeasible" zeolites. *Nat. Chem.* **2015**, *8*, 58–62.

CHAPTER II

INSIDE AND OUTSIDE: X-RAY ABSORPTION SPECTROSCOPY MAPPING OF CHEMICAL DOMAINS IN GRAPHENE OXIDE*

II.1 Introduction

The oxidative chemistry of graphite was first investigated over 150 years ago but has enjoyed a renaissance of sorts in recent years as researchers have sought to develop exfoliation and defunctionalization pathways to transform this material into a form more analogous to its celebrated cousin, single-layered graphene.[1–5] Similar to the extraction of graphene from graphite, the layered compound graphite oxide can be readily cleaved and exfoliated to yield single- and few-layered graphene oxide.[2–4] The intense interest in the chemical reactivity of graphene oxide originates primarily from the notion that elimination of its pendant functional groups and restoration of conjugated domains will allow for reconstitution of the sp^2-hybridized framework of single-layered graphene, thereby yielding a scalable wet-chemical route for transformation of graphite to graphene without necessitating high-temperature processing.[2,3,6] However, some fairly detailed structural studies that have emerged indicate some key differences in the geometric and electronic structure of reduced graphene oxide (often denoted as chemically derived graphene) as compared to single-layered graphene obtained through mechanical exfoliation, chemical vapor deposition, or recrystallization of SiC surfaces.[7–10] In particular, chemically derived graphene is characterized by remnant functional

---

* Reproduced with permission from De Jesus, L. R.; Dennis, R. V.; Depner, S. W.; Jaye, C.; Fischer, D. A.; Banerjee, S. Inside and Outside: X-Ray Absorption Spectroscopy Mapping of Chemical Domains in Graphene Oxide. *J. Phys. Chem. Lett.* **2013**, *4*, 3144–3151.

groups, nanoscopic holes, misaligned sp^2-hybridized domains, and topological defects such as single-bond rotations and dislocation cores; taken together, these imperfections obscure manifestation of the full range of Dirac physics expected for single-layered graphene although the conductivity of graphene oxide is enhanced by several orders of magnitude upon chemical or thermal reduction.[7,8] Understanding the bond connectivities, steric orientations, and spatial distribution of functional groups in graphene oxide along with their influence on local electronic structure is imperative to the manipulation, derivatization, and defunctionalization of this material, especially as graphene oxide emerges as an interesting material in its own right with applications in chemical and biological labeling, supported catalysis, polymer fillers, and capacitative energy storage.[2,3,11–13] While numerous high-resolution transmission electron microscopy (HRTEM), scanning tunneling microscopy, and solid-state nuclear magnetic resonance (NMR) studies have provided important insights into the structure of graphene oxide, chemical mapping of this highly inhomogeneous material remains much less explored.[7–10,14–18] Here, we use principal component analysis in tandem with scanning transmission X-ray microscopy (STXM) and high-resolution near-edge X-ray absorption fine structure (NEXAFS) spectroscopy at C and O K-edges to delineate distinct differences in the functionalization motifs at the edges and interior basal planes of graphene oxide.

Theories regarding the structure of graphite oxide and its constituent layers date as far back as the original synthesis. Several models that have been advanced over the years can be roughly categorized based on the periodic and non-periodic organization of functional groups with specific models invoking the increased abundance of a specific

type of functionality.[2,10,19,20] An additional important distinction pertains to retaining planarity or requiring puckering of the framework of hexagonally arrayed carbon atoms to accommodate the presence of functional groups. Without attempting to be comprehensive, different models of the structure of graphene oxide can be summarized as follows: Hofmann proposed a model wherein 1,2-epoxy functionalities are dispersed on either face of planar graphene sheets with extensive loss of aromaticity; Ruess suggested an alternative puckered framework linking together periodically aligned cyclohexane units in chair configurations functionalized with hydroxyl and 1,3-epoxide moieties; Scholz-Boehm proposed a different repeating unit with 1D aromatic chains separated by corrugated backbone features comprising hydroxyl and quinoidal species; Nakajima-Matsuo proposed a completely puckered periodic lattice framework distorted from planarity with electron delocalization at the C=O groups; and Dekany proposed a modification of the Ruess and Scholz-Boehm models wherein alternating chains of aromatic domains are held together by periodic *trans*-linked cyclohexyl regions bearing quinoidal, 1,3-ether, and tertiary alcohol species.[2,14,20] While Pacile et al. have posited the alignment of functional groups in a periodic array (as would be expected from the Dekany model) based on polarization dependence of O K-edge absorption features in a NEXAFS spectroscopy experiment, the vast majority of experimental evidence thus far provides support for yet another model, proposed by Lerf and Klinowski, wherein the planarity and long-range orientational order of sp^2-hybridized graphene is preserved.[7,10,14,18–20] According to this model, extended nanometer-sized regions of unperturbed graphene with a high degree of crystalline order are interspersed with

heavily functionalized domains wherein the basal planes bear randomly oriented 1,2 epoxide and tertiary alcohol species.[19,21] In addition, carboxylic acid groups and quinoidal species are located at edges and at the reconstructed corners of nanoscopic holes. This model has been further refined based on solid-state NMR studies by Ajayan and co-workers to incorporate five- and six-membered lactol rings at the edges along with esters of tertiary alcohols (likely formed by condensation of proximal tertiary alcohol and carboxylic acid groups located within the same sheet or on adjacent sheets).[10]

An extensive suite of experimental tools has been brought to bear on the task of deducing the structure of non-stoichiometric, apparently non-periodic graphene oxide. Cross-polarized 2D NMR experiments have confirmed the presence of the functional groups cited above for the Lerf-Klinowski model and have suggested that the sp^2-hybridized carbon atoms are bound to 1,2-epoxide and tertiary alcohol functionalities while indicating that the carboxylic acid and ketone moieties are spatially segregated from the extended conjugated domains.[10,17] The identification of these functional groups and their mobilization and temperature evolution has further been extensively investigated by Fourier transform infrared (FTIR) spectroscopy.[22] High-resolution transmission electron microscopy and electron diffraction experiments have evinced the non-periodic nature of the distribution of functional groups and the remnance of largely unperturbed and unstrained sp^2-hybridized domains while further suggesting the introduction of topological defects.[7,8,14,15] However, scarce little is known about the spatial correlation of the functional group distribution and the validity therein of the

Lerf-Klinowski model. As ensemble analytical techniques, FTIR, solid-state NMR, and photoemission spectroscopies do not allow for investigation of the spatial localization of different functional groups. In contrast, while HRTEM enables precise identification of crystalline order and real space atomic positions, it does not allow clear mapping of chemical domains, particularly in heavily functionalized seemingly amorphous regions. Here, we turn to STXM to probe the pattern of functionalization in graphene oxide with a high degree of chemical sensitivity. The lower radiation damage induced in the samples as compared to electron microscopy and the use of incident soft X-rays with a high degree of polarization enables clear visualization of spatial inhomogeneities in the functionalization of graphene.

II.2 Methodology

II.2.1 Preparation of Graphene Oxide

Graphene oxide was synthesized using the modified Hummers method[1] utilizing natural flake graphite from Bay Carbon Inc. (Michigan, USA). Briefly, graphite was oxidized using $KMnO_4$ and H_2O_2 and the expanded graphite oxide was exfoliated to yield graphene oxide. A graphene oxide solution in deionized water was vacuum filtered through a silicon nitride TEM window with ca. 2 μm holes and 3 μm spacing between holes. The silicon nitride membrane has a thickness of 50 nm and a window size of 0.5 mm × 0.5 mm. A single flake of few-layered graphene oxide was identified using transmission electron microscopy and further characterized by STXM and Raman spectroscopy. Ensemble NEXAFS measurements were performed on graphene oxide from the same batch as was vacuum filtered through the silicon nitride membrane by

preparing a free-standing GO paper by vacuum filtration through a nitrocellulose membrane.

II.2.2 Scanning Transmission X-ray Microscopy

STXM data was collected at spectromicroscopy beamline 10ID-1 of the Canadian Light Source, Saskatoon, SK, a 2.9 GeV third-generation synchrotron light source. The STXM end-station is equipped with an elliptically polarized undulator source (APPLE II) and a slitless entrance-plane grating monochromator. Incoming X-rays were focused using a Fresnel lens zone plate including an order-sorting aperture to eliminate unwanted diffraction orders. The optical design allows for high flux in transmission geometry and yields a spatial resolution of ~30 nm. Plane grating monochromators with 250-line mm^{-1} and a 500-line mm^{-1} were used for the C and O K-edge measurements, respectively. A pixel size of 30 nm was used with a 1 ms dwell time at each pixel location. The areas of interest were raster scanned through the focal point of the X-ray beam, and transmitted beam intensities were measured at the detector. Energy scans were performed stepwise through regions of interest with typical resolving power ($\Delta E/E$) of 2×10^{-4} to acquire sequences of images denoted as image stacks. The image stacks were analyzed using Jacobsen's Principal Components Analysis (PCA) suite and aXis2000 (available free for non-commercial applications at http://unicorn.mcmaster.ca/aXis2000.html). Principal component analysis was used to orthogonalize and noise-filter the spectral features of the STXM image stacks. This involves deconvoluting the spectra into discrete abstract orthogonalized components that each represent a linear combination of spectral signatures from multiple chemical

species. Subsequently, cluster analysis (as a pattern matching mode) was used to classify pixels by spectral similarity to extract average spectra with improved signal-to-noise characteristics across the given cluster. The graded contributions of the orthogonalized spectral components at each pixel were also determined, allowing for construction of maps indicating their relative abundance at each pixel within the area of interest. Application of this multivariate analysis method allows for nanoscale visualization of chemical speciation (such as in Fig. II.3B) by reconstructing images from eigenspectra in complex samples without requiring *a priori* knowledge of reference spectra of the different chemical species. The angle dependence cutoff was set to the point just before the highest pixel contribution. This approach eliminates thickness variations and allows for mapping of variations in chemical signatures.

II.2.3 Transmission Electron Microscopy

TEM images were acquired using a JEOL 2010 instrument operating at 200kV using the same Norcada grids as noted above.

II.2.4 Raman Spectroscopy

The Raman spectrum of the graphene oxide flake was acquired in back-scattered mode using a Horiba Jobin-Yvon Labram HR system with 514.5 nm laser excitation using an edge filter for Rayleigh line rejection and an Andor Peltier-cooled CCD camera. The spectrum was acquired using a 600 lines mm^{-1} grating yielding a resolution of 1.5 cm^{-1}.

II.2.5 Near-Edge X-ray Absorption Spectroscopy

Carbon K-edge NEXAFS experiments were performed at National Institute of Standards and Technology (NIST) beamline U7A of the National Synchrotron Light Source at Brookhaven National Laboratory. A 600 lines/mm toroidal spherical grating monochromator was used yielding an energy resolution of approximately 0.08 eV. The entrance slits were set to 30 μm × 30 μm. The spectra were acquired in partial electron yield (PEY) mode using a channeltron electron multiplier detector with an entrance grid bias set to -150 V to enhance surface sensitivity and limit noise. A charge compensating electron gun was used to neutralize the effects of sample charging. The PEY signals were normalized using the incident beam intensity obtained from the photoemission yield of a freshly evaporated Au grid with 90% transmittance placed along the path of the incident X-ray beam to eliminate the effects of beam fluctuations and

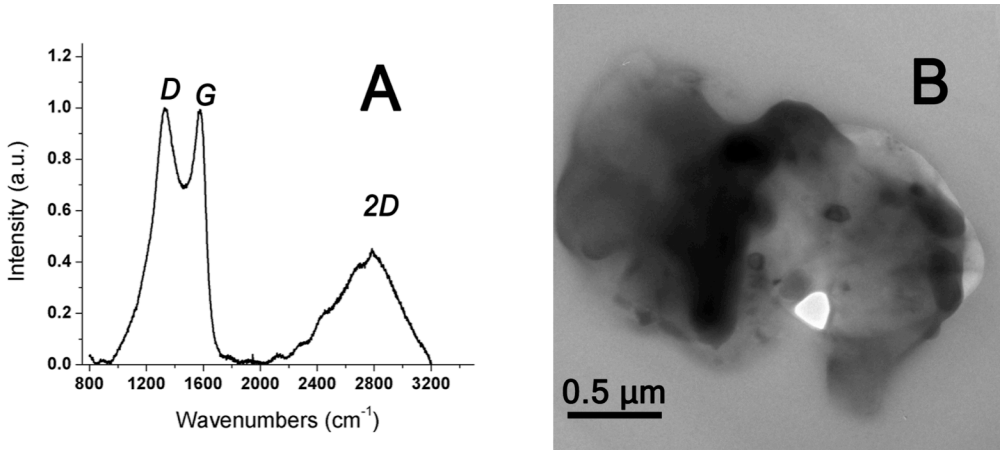

Figure II.1. Raman spectrum and TEM image of a graphene oxide flake located within an amorphous silicon nitride window. (A) The *D*, *G*, and *2D* bands of graphene oxide are apparent in the spectrum. (B) TEM image indicating regions with varying electron contrast.

monochromator absorption features. The C K-edge spectra were calibrated to an amorphous carbon mesh with a π* transition at 285.1 eV. Pre- and post-edge normalization of the data was performed using the Athena suite of programs.

II.3 Results and Discussion

STXM yields a stack of element-specific X-ray absorption spectra with *ca.* 30 nm spatial resolution.[18,23,24] As a first approximation, features in X-ray absorption spectra represent a replica of the atom-projected unoccupied density of states weighted by the absorption cross-section as modified by dipolar selection rules and perturbed by core—hole interactions. More specifically, for graphene oxide considered here, the observed spectral features represent the superposition of dipole-allowed transitions from locally modified C—C and C—O core levels to unoccupied and partially occupied states above the Fermi level.[25–30] By raster scanning a finely focused soft X-ray beam over the

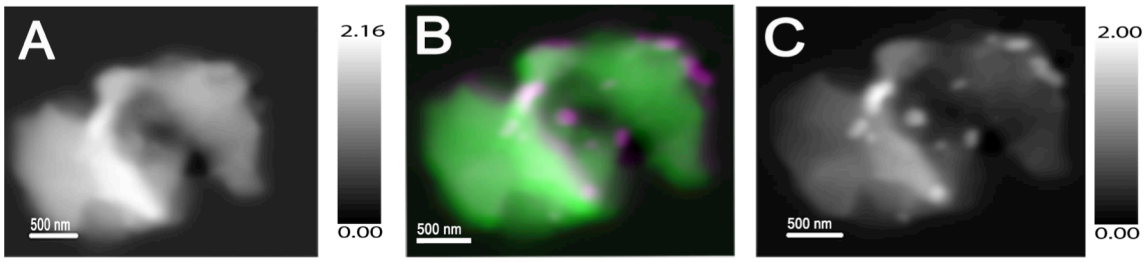

Figure II.2. Integrated STXM image stacks acquired at the C and O K-edges for a graphene oxide flake. The transmission data is changed into optical density (OD) by calculating I/I_0, where I, the intensity transmitted through the sample is divided by I_0, the background signal measured within a hole. A) C K-edge STXM image integrating the spectral features in the range between 280-320 eV; the vertical grey scale represents the optical density (B) Overlay of the C K-edge image (green) and the O K-edge image (purple) optical density maps indicating the spatial inhomogeneities in the extent of functionalization across the flake. (C) O K-edge STXM image integrating the absorbance in the range between 280-320 eV; the vertical grey scale represents the optical density.

area of interest, it is thus possible to construct a spatially resolved map of the local perturbations to the electronic structure induced as a result of chemical functionalization, thereby providing a means to explore inhomogeneities in the functionalization pattern. In past work, we have used STXM to map electronic asperities and locally doped domains in CVD-grown graphene based on the polarization dependence of the π^* resonance and the intensity of a pre-edge absorption feature.[24] STXM mapping of reduced graphene oxide has allowed for quantitative evaluation of the number of layers at the edges and interiors based on the normalized optical density, and have further shown intriguing azimuthal angle dependences at the edges of the reduced graphene oxide sheets suggesting the stabilization of electronic states associated with a specific edge termination motif (zigzag versus armchair).[9,24] Another remarkable study has indicated charge redistribution at Co_3O_4/N-doped graphene interfaces with the reduction of Co apparently spatially correlated with nitrogen incorporation.[23] However, to the best of our knowledge, detailed STXM chemical mapping of graphene oxide has not been reported thus far. In this study, we correlate spatially resolved STXM data to transmission electron microscopy and Raman spectroscopy data acquired for the same graphene oxide flake and further examine high-resolution NEXAFS spectra to probe the functional group distribution and orientation.

Graphene oxide has been prepared by using a modified Hummer's approach (see detailed description in Experimental section) and is deposited onto an amorphous silicon nitride window through vacuum filtration. X-ray photoelectron spectroscopy analysis suggests extensive oxidation with the incorporation of 31.4% oxygen.[30] A large few-

layered graphene oxide flake that has lateral dimensions of *ca.* 4 μm has been identified by optical microscopy and is further characterized by TEM, STXM, and Raman spectroscopy. Figure II.1A shows the Raman spectrum of the graphene oxide flake with Figure II.1B depicting the corresponding electron microscopy image.

The Raman spectrum of graphene oxide is characterized by a *G* band derived from doubly degenerate (comprising both longitudinal and transverse optic contributions) phonon modes of E_{2g} symmetry at Brillouin zone center of graphene, an energy dispersive *2D* band arising from a double resonance process required to maintain momentum conservation, and a disorder-activated *D* band, which becomes Raman active due to phonon divergence processes within the interior of the graphene Brillouin zone, and is activated by defect sites and edges.[31–33] The *G*, *2D*, and *D* modes appear at 1576, 2785, and 1330 cm^{-1}, respectively. The inevitable breaking of the periodic symmetry of sp^2-hybridized graphene, sp^3-rehybridization of a significant fraction of sites, and the introduction of defects leads to a pronounced increase of the *D* band intensity of graphene oxide (up to a I_D/I_G value ~ 1) as compared to single-layered graphene.[25,34] Figure II.1B shows a low-magnification TEM image of the same graphene oxide flake studied by Raman spectroscopy. The TEM image indicates that the graphene oxide flake is ~4 μm in size and has varying areas of electron contrast due to increased flake thickness, presence of folds, and varying extents of functionalization, as further corroborated by STXM elemental maps.

Figures II.2A and II.2C show integrated STXM image stacks acquired for the graphene oxide flake (the same flake as indicated in Figure 1) at the C K-edge (in the

range between 280—320 eV) and the O K-edge (in the range between 525—560 eV), respectively. The transmission data have been mapped in terms of integrated optical density (OD) across the energy windows of interest. Both the sample (I) and an empty space or hole within the area of interest (I_o) is simultaneously imaged during acquisition of the image stacks. Higher optical density regions in the images correlate directly to greater elemental concentrations of carbon and oxygen within these areas. Figure II.2B depicts a composite map blending the optical density plots from Figures II.2A and II.2C, wherein carbon is represented in green and oxygen is represented in purple. This image clearly suggests an increased concentration of oxygen within specific domains of the graphene oxide flake, providing evidence for inhomogeneities in the extent of functionalization. Notably, the C K-edge map in Figure II.2A does not indicate discernible particle-like contrast in regions that appear purple in the composite map of Figure II.2B, suggesting that the additional contrast seen in TEM and the distinctive features in the composite map arise from heavily functionalized domains rather than thickness variations. Corrugations are also visible in Figure II.1A and in previous work we have indicated the ability of STXM to map electronic corrugations in graphene.[24] Figure II.3 shows C K-edge NEXAFS data acquired for a free-standing graphene oxide paper from the same batch as deposited onto the TEM grid for STXM analysis. NEXAFS data has been acquired at 25˚, 54.7˚ (magic angle), and 85˚ incidence of the soft-X-ray beam to probe the steric orientations of the functional groups on graphene oxide. As noted above, element-specific C K-edge NEXAFS spectra correspond to dipolar transitions from carbon 1*s* core levels (as modified by chemical

functionalization) to unoccupied states possessing carbon 2*p* character. The transition matrix element is subject to the angular overlap of the polarization vector of the incident electromagnetic radiation and linear momentum operator of electrons, thereby enabling NEXAFS spectroscopy to serve as a sensitive orbital-specific probe for examining the orientation of molecular frameworks and periodic solids.[9,24–27,30,35]

At near-normal incidence of the incident X-rays, the electric-field vector is aligned along the plane of a hypothetically flat graphene sample, and thus predominantly

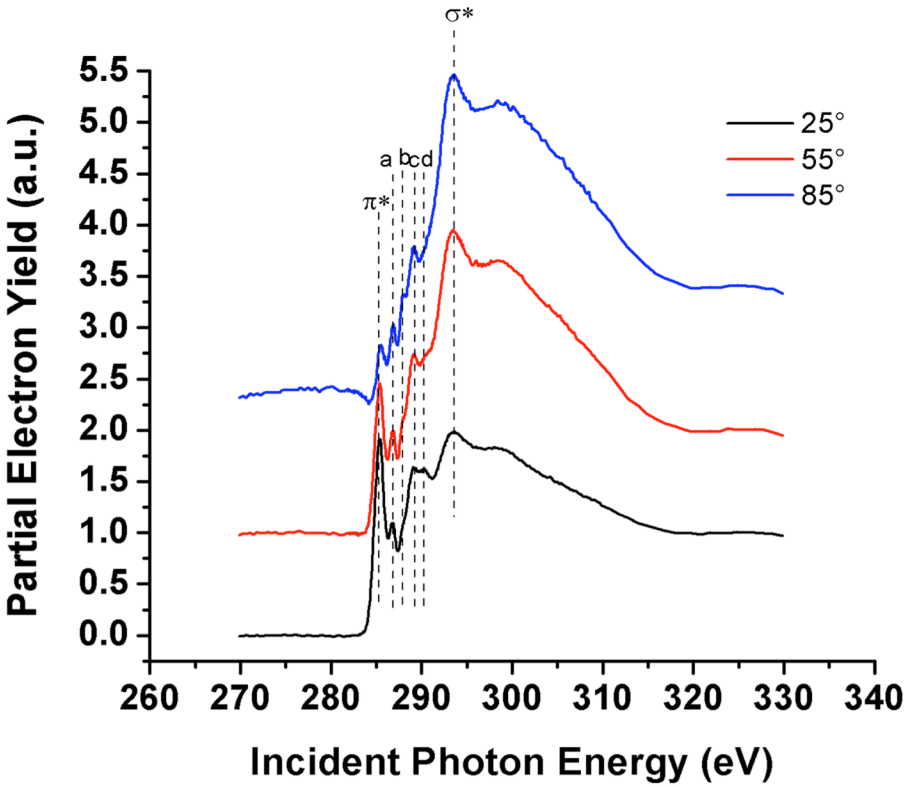

Figure II.3. C K-edge NEXAFS spectra of graphene oxide acquired at three different angles (25˚, 54.7˚ and 85˚) of incidence of the X-ray beam. The peak assignments are noted in Table 1 and further elaborated in the text. The spectra have been offset for clarity.

probes states of σ* symmetry. However, at glancing incidence, the electric-field vector is essentially perpendicular to the plane of graphene, thus primarily probing states of π*

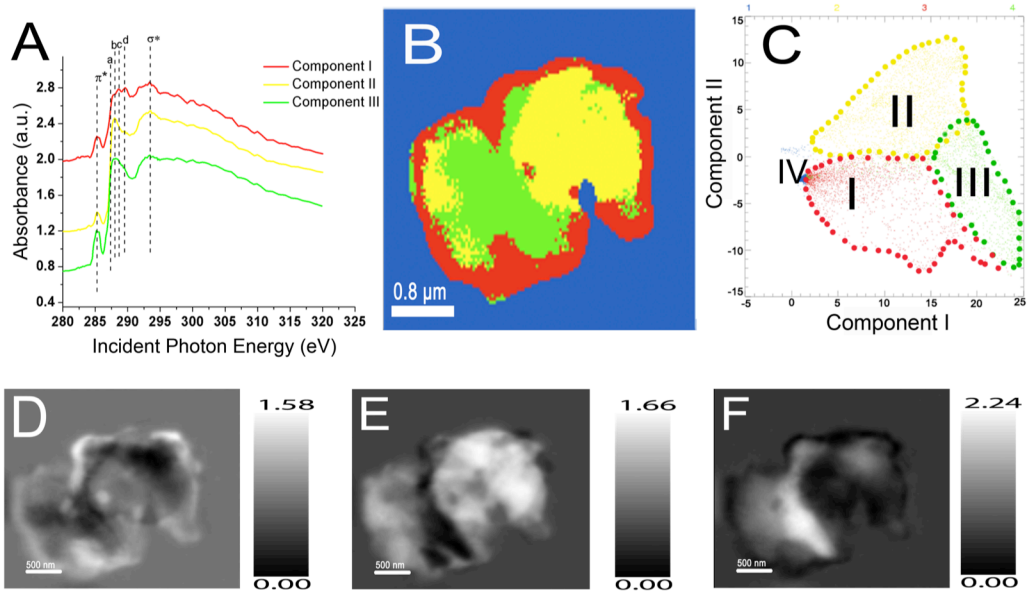

Figure II.4 Chemical domain mapping of graphene oxide. (A) Orthogonalized eigenspectra derived from STXM spectral stacks by principal component analysis. (B) Real space cluster map representing the relative contributions of the different orthogonalized components in different regions of the sample. Red represents Component I, Yellow represents Component II, Green represents Component III, and Blue represents the background (Component IV). (C) 2D scatter plot with pixels plotted according to their weights along Component II and I, dotted lines segregating the components are intended to be guides to the eye. (D—F) Graded STXM maps depicting the contributions of each component across the graphene oxide flake: (D) Component I; (E) Component II; and (F) Component III are STXM images of the regions assigned by PCA.

symmetry. NEXAFS data collected at 54.7˚ (magic angle) allow for the elimination of effects from preferential orientation.

The lowest energy peak in Figure II.3 at ~285.39 eV (labeled π*) can be assigned to the transition of C 1*s* core level electrons into states of π* symmetry around the M and

L points of the graphene Brillouin zone above the Fermi level, whereas the highest energy peak positioned at ~293.49 eV (labeled σ*) corresponds to the excitation of C 1*s* core level electrons to dispersionless states of σ* symmetry.[25,31,36,37] Both the π* and σ* features are thought to be excitonic in sp^2-hybridized single-layered graphene but have diminished lifetimes in graphene oxide.[26] Significant diminution in the intensity of the π* feature is noted when going from near-glancing (25°) to near normal (85°) incidence, suggestive of substantial anisotropy (alignment of graphene oxide flakes parallel to the substrate) within the graphene oxide paper and indicating that graphene oxide substantially retains the planar framework of sp^2-hybridized graphene. Intermediate to the π* and σ* resonances are four features labeled *a* (~286.89 eV), *b* (~287.99 eV), *c* (~289.19 eV), and *d* (~290.45 eV), which can be assigned to functional groups that decorate the basal plane and edges of the graphene oxide sheets (Table II.1). These assignments are consistent with previous experimental spectra of the graphene oxide, functionalized carbon nanotubes, and are further validated by spectra acquired for molecular building blocks containing these functional groups.[26,27,38] The assignments are further supported by NEXAFS spectra of molecular standards collected within the McMaster University database.[38] The relatively higher electronegativity of oxygen with respect to carbon leads to increased stabilization of C-O core levels (as compared to C-C states). Furthermore, bonding C-O states are stabilized and their replica antibonding states are destabilized with respect to the Fermi level as compared to homopolar C-C bonds. Consequently, the increased energy separation between modified C-O core levels and the corresponding anti-bonding states is reflected in the absorption features ascribed

Energy (eV)	Chemical Identity
285.39_{π^*}	π* C=C
286.89_a	π* C-OH
287.99_b	σ* C-O (epoxide)
289.19_c	π* C=O
290.45_d	π* O=C-O
293.49_{σ^*}	σ* C-C

Table II.1. Functional Group Assignments of Spectral Features Observed in C K-edge Spectra for STXM and NEXAFS.

to the functional groups appearing at relatively higher energies as compared to the π* resonances. All four intermediate resonances are observed at magic angle incidence as shoulders or distinct peaks due to elimination of angular dependence of intensity induced by the steric orientations of the different functional groups.

The feature labeled *a* can be assigned to transitions from C 1*s* core levels to π* states of C-O bonds derived from hydroxyl groups, whereas the resonance labeled *b* can be ascribed to the transition of C 1*s* core level electrons to antibonding C-O states that are derived from epoxides, both these moieties have been postulated to be decorating the basal plane of graphene oxide as per the Lerf-Klinowski model.[25,28,39] The pronounced feature evident at ~289.19 eV (labeled *c*) can be attributed the excitation of C 1*s* core level electrons to states of π* symmetry primarily localized at C=O bonds from carbonyl groups.[29,39] The resonance labeled *d* is visible as a distinct resonance at 25° and as a shoulder at 54.7° and 85° incidence of the X-ray beam. This feature can be ascribed to

transitions to antibonding states of C=O bonds from carboxylic acid (-COOH) functionalities.[29,39] The emergence of this feature at glancing incidence is particularly telling regarding the orientation of the carboxylic acid moieties and suggest that localized π* orbitals are parallel to the π* cloud of graphene, which can only be possible if the carboxylic acids are splayed parallel to the plane of the flake. Such a steric orientation is consistent with the modified Lerf-Klinowski model, which places carboxylic acid groups (and lactols) at edge sites.[19] Such an angular dependence of the carboxylic acid resonances has heretofore not been observed in NEXAFS studies of graphene oxide and are further corroborated by STXM data (*vide infra*). Another notable feature in Figure II.3 is the emergence of σ* C-O feature ascribed to epoxides at near normal incidence (85°). The pronounced polarization dependence of this feature suggests a significant fraction of 1,2-epoxides that lie in-plane as well as indicate some distortion from planarity for epoxide-functionalized carbon atoms.

Figure II.4A shows the eigenspectra for the different orthogonalized components at the C K-edge derived from PCA treatment of the STXM data.[40,41] It should be noted that the eigenvalues extracted from the deconvolution of the data do not specifically represent a specific functional group. Through the use of mathematical operators, orthogonalized eigenspectra can be extracted from the data and encompass linear combinations of spectral features from specific functional groups; which upon evaluation (as shown in Fig. II.4A) can have greater spectral weight from an individual functional group. The PCA analysis method has been more extensively discussed in the Supporting Information. These spectra are calibrated to the π* feature at 285.3 eV. The

π* peak is of relatively lower intensity since the electric-field vector of the incident X-rays interacts overlaps predominantly with σ* final states in the basal plane of GO at normal incidence. The functional group absorptions are labeled a—d as noted in Table II.1 with the same assignments as discussed above for the NEXAFS spectra. The component spectra plotted in Figure II.4A represent linear combinations of spectral signatures of different functional groups and exhibit some notable differences. All four functional groups are represented in Component III. In contrast, the ketone (feature C) and carboxylate (feature D) functionalities are especially pronounced and the epoxide contribution (feature B) is relatively diminished in Component I. Component II has a high epoxide concentration analogous to Component III but has lower hydroxyl (feature A) and quinoidal (feature C) concentrations. Moreover, Component III is distinct from Component II in having increased π* intensity. Given the linear polarization of the incident X-ray beam this would suggest a greater concentration of wrinkles and folds in this region, which would allow for better coupling of the sp^2-hybridized framework with the electric field vector of the normally incident X-rays.[24]

Figures II.4D-F indicates graded maps depicting the contribution of the individual orthogonalized components at each pixel within the graphene oxide flake. The PCA software affords the ability to use an angle distance measure (between the different components) to specify a radius below which pixels are not included in the determination of cluster centers; thereby substantially mitigating thickness variations in the optical density map and enabling chemically sensitive imaging.[41] The angle dependence cutoff has been set to the point just before the highest pixel contribution. In

other words, such a cutoff enables distinct chemical signatures to be emphasized over intensity variations derived from greater abundance of a specific chemical species within a thicker region.[41] Figure II.4B presents a PCA cluster image with different color representations of the orthogonalized components plotted in Figure II.4A. Consistent with the graded maps of the spectral contributions in Figures II.4D-F, Figure II.4B suggests a greater contribution for Component I at the edges and within a select few interior domains of the graphene oxide flake. In contrast, Components II and III are more heavily weighted within the interior of the graphene oxide flake. Figure II.4C shows a scatter plot with pixels plotted according to their weights in two specific component axes. Similar 2D scatter plots can be constructed for each pair of components identified here.

The "outer ring" feature of Component I is particularly instructive and provides direct evidence that carboxylic acid and ketone groups are situated preponderantly on the edges of graphene oxide (our spatial resolution is *ca.* 30 nm). Note that the increased presence of folds and corrugations near edges could make this region appear to somewhat broader in terms of lateral dimensions. The observed weighting in the PCA cluster map provides the first spatially resolved verification of the modified Lerf-Klinowski model.[10,19] This observation further corroborates the angular dependence of the carboxylic acid resonance observed in ensemble angle-resolved NEXAFS spectra of Figure II.3, which appears to indicate that the carboxylic acid moieties are held parallel to the graphene plane. Such a steric orientation can be accommodated only at edges and in proximity of holes. Components II and III, which have greater contributions from

epoxide moieties are found to be weighted much more heavily within the interiors of the graphene oxide flakes consistent again with the Lerf-Klinowski picture, which suggests that the basal planes are functionalized with hydroxyl and 1,2-epoxide groups. Ajayan and co-workers have observed close correlations between sp^2-hybridized carbon atoms and these two functional groups in cross polarized NMR studies but have found that the carboxylic acid moieties are spatially segregated from the conjugated framework (as is indeed evidenced here from their location at edge sites). As noted above, Component II

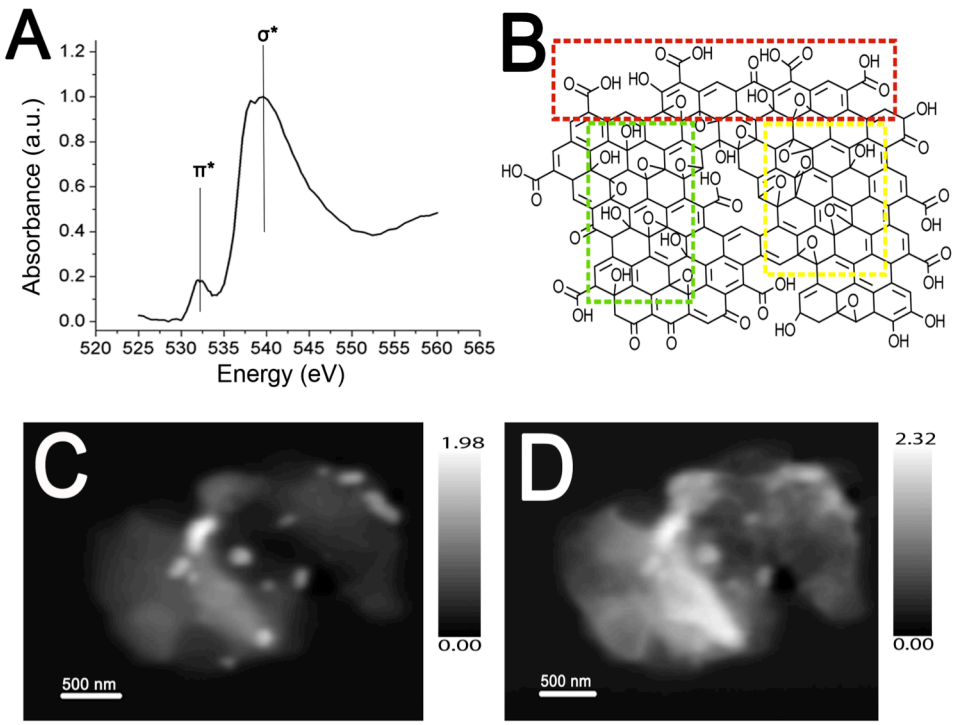

Figure II.5. STXM image and integrated NEXAFS spectrum acquired at the O K-edge. (A) Integrated O K-edge X-ray absorption spectrum measured for the graphene oxide flake; (B) Depiction of the Lerf-Klinowski model describing three components, I (red), II (yellow), III (green) with functional group distributions consistent with the eigenspectra of the same colors shown in Figure II.4; (C) STXM image plotting the intensity of the π* C=O feature across the sample; and (D) STXM image plotting the C-O σ* intensity across the sample.

has a higher π* intensity suggesting a greater density of wrinkles and folds within the green domains of Figure II.4B.

Figure II.5A shows X-ray absorption spectra acquired at the O K-edge integrated across the entire sample. Two well-separated absorption features are observed at 531eV and a broader peak around 539 to 542 eV. The feature at ca. 531 eV can be attributed to transitions from O 1*s* core levels to π* C=O states derived from carboxylic acid and ketone moieties, whereas the broad absorption feature centered around 539—542 eV can be attributed to the superposition of transitions from O 1*s* core levels to finals states of σ* symmetry localized on O-H, C-O and C=O bonds.[18,25,26,39] Shown in Figure II.5B is a depiction of the Lerf-Klinowski model highlighting the functionalization motifs of the three components extracted by PCA in their respective colors (I-red, II-yellow, and III-green, as per Fig. II.4). Figures II.5C and 5D are optical density maps acquired for the graphene oxide flake at 531 and 542 eV, respectively. Figure II.5C maps the concentration of π* C=O species and matches well with the highly oxidized regions seen in the TEM image of Figure II.1B and the composite oxygen maps shown in Figure II.2B and C. Figure II.5D depicts the STXM map for C-O σ* states centered at 542 eV with areas of overall greater oxidation prominently discernible as bright spots.

II.4 Conclusions

In conclusion, we have developed the first experimentally verified spatially resolved description of the functionalization of graphene oxide. Using a combination of PCA analysis of STXM data and angle-resolved high-resolution NEXAFS spectroscopy experiments we have been able to chemically map functionalization patterns and to

determine steric orientations of functional groups in graphene oxide. We note first the inhomogeneous functionalization of graphene oxide with highly functionalized domains interspersed between more planar and crystalline regions. A second major finding pertains to chemically mapping the functional group distribution. The segregation of quinoidal and carboxylate species at the edges of graphene oxide has been a longstanding postulate and constitutes a key component of the Lerf-Klinowski model of graphene oxide. We present here the first experimental validation unequivocally demonstrating that the carboxylate functional groups are located primarily on the outer edges of graphene oxide, with epoxide and hydroxyl groups concentrated within the interior of the graphene oxide flake. Finally, we have been able to deduce the planarity of carboxylic acid groups and the specific orientations adopted by 1,2-epoxides based on angle-resolved NEXAFS measurements of graphene oxide sheets. Careful functionalization protocols targeted to these functional groups may be able to tether specific moieties with control of steric orientation (pendant from edges versus residing atop graphene oxide planes). Analogous functional group distribution is expected for oxidized graphene produced by similar aggressive acid oxidation methods. Understanding the spatial distribution of functional groups and the distinct functionalized domains within graphene oxide paves the way for targeted tethering of other moieties and is critical for incorporation of this material within polymer and metal composites, biomaterial constructs, and nanostructured heterostructures.

II.5 References

(1) Brodie, B. C. On the atomic weight of graphite. *Philos. T. Roy. Soc.* **1859**, *149* , 249–259.

(2) Dreyer, D. R.; Park, S.; Bielawski, C. W.; and Ruoff, R. S. The chemistry of graphene oxide. *Chem. Soc. Rev.* **2010**, *39*, 228–40.

(3) Loh, K. P.; Bao, Q.; Eda, G.; and Chhowalla, M. Graphene oxide as a chemically tunable platform for optical applications. *Nat. Chem.* **2010**, *2*, 1015–24.

(4) Mao, S.; Pu, H.; and Chen, J. Graphene oxide and its reduction: modeling and experimental progress. *RSC Advances* **2012**, *2*, 2643–2662.

(5) Novoselov, K. S.; Geim, A. K.; Morozov, S. V; Jiang, D.; Katsnelson, M. I.; Grigorieva, I. V; Dubonos, S. V; and Firsov, A. A. Two-dimensional gas of massless Dirac fermions in graphene. *Nature* **2005**, *438*, 197–200.

(6) Park, S. and Ruoff, R. S. Chemical methods for the production of graphene. *Nat. Nano* **2009**, *4*, 217–224.

(7) Gómez-Navarro, C.; Meyer, J. C.; Sundaram, R. S.; Chuvilin, A.; Kurasch, S.; Burghard, M.; Kern, K.; and Kaiser, U. Atomic structure of reduced graphene oxide. *Nano Lett.* **2010**, *10*, 1144–1148.

(8) Erickson, K.; Erni, R.; Lee, Z.; Alem, N.; Gannett, W.; and Zettl, A. Determination of the local chemical structure of graphene oxide and reduced graphene oxide *Adv. Mater.* **2010**, *22*, 4467–4472.

(9) Zhou, J. G.; Wang, J.; Sun, C. L.; Maley, J. M.; Sammynaiken, R.; Sham, T. K.; and Pong, W. F. Nano-scale chemical imaging of a single sheet of reduced graphene oxide. *J. Mater. Chem.* **2011**, *21*, 14622–14630.

(10) Gao, W.; Alemany, L. B.; Ci, L.; and Ajayan, P. M. New insights into the structure and reduction of graphite oxide. *Nat. Chem.* **2009**, *1*, 403–408.

(11) Kim, H.; Abdala, A. A.; and Macosko, C. W. Graphene/polymer nanocomposites. *Macromolecules* **2010**, *43*, 6515–6530.

(12) Seger, B. and Kamat, P. V Electrocatalytically Active Graphene-Platinum Nanocomposites. Role of 2-D carbon support in pem fuel cells. *J. Phys. Chem. C* **2009**, *113*, 7990–7995.

(13) Kamat, P. V Graphene-based nanoassemblies for energy conversion. *J. Phys. Chem. Lett.* **2011**, *2*, 242–251.

(14) Wilson, N. R.; Pandey, P. A.; Beanland, R.; Young, R. J.; Kinloch, I. A.; Gong, L.; Liu, Z.; Suenaga, K.; Rourke, J. P.; York, S. J.; *et al.* Graphene oxide: structural analysis and application as a highly transparent support for electron microscopy. *ACS Nano* **2009**, *3*, 2547–2556.

(15) Mkhoyan, K. A.; Contryman, A. W.; Silcox, J.; Stewart, D. A.; Eda, G.; Mattevi, C.; Miller, S.; and Chhowalla, M. Atomic and electronic structure of graphene-oxide. *Nano Lett.* **2009**, *9*, 1058–1063.

(16) Pandey, D.; Reifenberger, R.; and Piner, R. Scanning probe microscopy study of exfoliated oxidized graphene sheets. *Surf. Sci.* **2008**, *602*, 1607–1613.

(17) Cai, W.; Piner, R. D.; Stadermann, F. J.; Park, S.; Shaibat, M. A.; Ishii, Y.; Yang, D.; Velamakanni, A.; An, S. J.; Stoller, M.; *et al.* Synthesis and Solid-state nmr structural characterization of 13C-labeled graphite oxide. *Science* **2008**, *321*, 1815–1817.

(18) Pacilé, D.; Meyer, J. C.; Fraile Rodríguez, A.; Papagno, M.; Gómez-Navarro, C.; Sundaram, R. S.; Burghard, M.; Kern, K.; Carbone, C.; and Kaiser, U. Electronic properties and atomic structure of graphene oxide membranes. *Carbon* **2011**, *49*, 966–972.

(19) Lerf, A.; He, H.; Forster, M.; and Klinowski, J. Structure of graphite oxide revisited. *J. Phys. Chem. B.* **1998**, *102*, 4477–4482.

(20) Szabó, T.; Berkesi, O.; Forgó, P.; Josepovits, K.; Sanakis, Y.; Petridis, D.; and Dékány, I. Evolution of surface functional froups in a series of progressively oxidized graphite oxides. *Chem. Mater.* **2006**, *18*, 2740–2749.

(21) He, H.; Klinowski, J.; Forster, M.; and Lerf, A. A new structural model for graphite oxide. *Chem. Phys. Lett.* **1998**, *287*, 53–56.

(22) Acik, M.; Lee, G.; Mattevi, C.; Pirkle, A.; Wallace, R. M.; Chhowalla, M.; Cho, K.; and Chabal, Y. The role of oxygen during thermal reduction of graphene oxide studied by infrared absorption spectroscopy. *J. Phys. Chem. C.* **2011**, *115*, 19761–19781.

(23) Wang, J.; Zhou, J.; Hu, Y.; and Regier, T. Chemical interaction and imaging of single Co_3O_4/graphene sheets studied by scanning transmission X-ray

microscopy and x-ray absorption spectroscopy. *Energy & Environ. Sci.* **2013**, *6*, 926–934.

(24) Schultz, B. J.; Patridge, C. J.; Lee, V.; Jaye, C.; Lysaght, P. S.; Smith, C.; Barnett, J.; Fischer, D. A; Prendergast, D.; and Banerjee, S. Imaging local electronic corrugations and doped regions in graphene. *Nat. Commun.* **2011**, *2*, 372:1-8.

(25) Lee, V.; Whittaker, L.; Jaye, C.; Baroudi, K. M.; Fischer, D. A.; and Banerjee, S. Large-area chemically modified graphene films: electrophoretic deposition and characterization by soft x-ray absorption spectroscopy, *Chem. Mater.* **2009**, *21*, 3905–3916.

(26) Lee, V.; Dennis, R. V; Schultz, B. J.; Jaye, C.; Fischer, D. A.; and Banerjee, S. Soft X-ray absorption spectroscopy studies of the electronic structure recovery of graphene oxide upon chemical defunctionalization. *J. Phys. Chem. C* **2012**, *116*, 20591–20599.

(27) Lee, V.; Dennis, R. V.; Jaye, C.; Wang, X.; Fischer, D. A.; Cartwright, A. N.; and Banerjee, S. In situ near-edge X-ray absorption fine structure spectroscopy investigation of the thermal defunctionalization of graphene oxide. *J. Vac. Sci. Technol., B* **2012**, *30*, 061206:1-8.

(28) Jeong, H.-K.; Colakerol, L.; Jin, M. H.; Glans, P. A.; Smith, K. E.; and Lee, Y. H. Unoccupied electronic states in graphite oxides. *Chem. Phys. Lett.* **2008**, *460*, 499–502.

(29) Ganguly, A.; Sharma, S.; Papakonstantinou, P.; and Hamilton, J. Probing the thermal deoxygenation of graphene oxide using high-resolution in situ x-ray-based spectroscopies. *J. Phys. Chem. C.* **2011**, *115*, 17009–17019.

(30) Dennis, R. V.; Schultz, B. J.; Jaye, C.; Wang, X.; Fischer, D. A.; Cartwright, A. N.; and Banerjee, S. Near-edge X-ray absorption fine structure spectroscopy study of nitrogen incorporation in chemically reduced graphene oxide. *J. Vac. Sci. & Technol. B* **2013**, *31*, 41204:1-9.

(31) Lee, V.; Park, C.; Jaye, C.; Fischer, D. A.; Yu, Q.; Wu, W.; Liu, Z.; Bao, J.; Pei, S.-S.; Smith, C.; *et al.* Substrate hybridization and rippling of graphene evidenced by near-edge X-ray absorption fine structure spectroscopy. *J. Phys. Chem. Lett.* **2010**, *1*, 1247–1253.

(32) Ferrari, A. C. and Basko, D. M. Raman spectroscopy as a versatile tool for studying the properties of graphene. *Nat. Nanotechnol.* **2013**, *8*, 235–246.

(33) Moon, I. K.; Lee, J.; Ruoff, R. S.; and Lee, H. Reduced graphene oxide by chemical graphitization. *Nat. Commun.* **2010**, *1*, 73:1-6.

(34) Kudin, K. N.; Ozbas, B.; Schniepp, H. C.; Prud'homme, R. K.; Aksay, I. A.; and Car, R. Raman spectra of graphite oxide and functionalized graphene sheets. *Nano Lett.* **2007**, *8*, 36–41.

(35) Schultz, B. J.; Jaye, C.; Lysaght, P. S.; Fischer, D. A.; Prendergast, D.; and Banerjee, S. On chemical bonding and electronic structure of graphene-metal contacts. *Chemical Science* **2013**, *4*, 494–502.

(36) Pacilé, D.; Papagno, M.; Rodríguez, A.; Grioni, M.; Papagno, L.; Girit, Ç.; Meyer, J.; Begtrup, G.; and Zettl, A. Near-Edge x-ray absorption fine-structure investigation of graphene. *Phys. Rev. Lett.* **2008**, *101*, 066806:1-4.

(37) Fischer, D.; Wentzcovitch, R.; Carr, R.; Continenza, A.; and Freeman, A. Graphitic interlayer states: a carbon K near-edge x-ray-absorption fine-structure study. *Phys. Rev. B* **1991**, *44*, 1427–1429.

(38) Gas phase core excitation database. http://unicorn.mcmaster.ca/corex/cedb-itle.html (accessed June 12, 2013)

(39) Jeong, H.-K.; Noh, H.-J.; Kim, J.-Y.; Jin, M. H.; Park, C. Y.; and Lee, Y. H. X-ray Absorption spectroscopy of graphite oxide. *Europhys. Lett.* **2008**, *82*, 67004.

(40) Lerotic, M.; Jacobsen, C.; Schäfer, T.; and Vogt, S. Cluster analysis of soft x-ray spectromicroscopy data. *Ultramicroscopy* **2004**, *100*, 35–57.

(41) Lerotic, M.; Jacobsen, C.; Gillow, J. B.; Francis, A. J.; Wirick, S.; Vogt, S.; and Maser, J. Cluster analysis in soft x-ray spectromicroscopy: finding the patterns in complex specimens. *J. Electron Spectrosc.* **2005**, *144*, 1137–1143.

CHAPTER III

MAPPING POLARONIC STATES, LITHIATION GRADIENTS, AND PHASE NUCLEATION IN INDIVIDUAL V_2O_5 NANOWIRES*

III.1 Introduction

The inadequacies of Li-ion batteries have emerged as a major constraint in many areas of technological design and can be attributed in large measure to challenges with the identification of optimal cathode chemistries and architectures.[1–4] In essence, a cathode material ought to be able to reversibly store a high concentration of inserted ions and furthermore the insertion/extraction and intervening diffusion of ions through the host matrix must occur rapidly to facilitate the efficient discharging/charging of the battery. There are numerous other caveats related to charge transfer at interfaces, earth abundance of the constituent elements, and safety considerations that are vital for cathode design. Even this simplified description illustrates the critical imperative to carefully match thermodynamic driving forces of charge transfer (the free energy of the ion insertion reaction) with the kinetics of ion diffusion. In the most ubiquitous example of a Li-ion battery, correlated motion of both ions and electrons must often be considered. These correlations can be driven by the chemical composition, crystal structure, and/or electrode geometry of the cathode.[1,5,6] Electron microscopy and microanalysis probes along with local-structure characterization methods, such as total scattering, have provided great insight into the transformation of crystal structures upon

---

*Reproduced with permission from De Jesus, L. R.; Horrocks, G. A.; Liang, Y.; Parija, A.; Jaye, C.; Wangoh, L.; Wang, J.; Fischer, D. A.; Piper, L. F. J.; Prendergast, D.; and Banerjee, S. Mapping Polaronic States and Lithiation Gradients in Individual V_2O_5 Nanowires. *Nat. Commun.* **2016**, *7*, 12022:1–9. Reproduced with permission under the terms of the Creative Commons CC BY

ion insertion and have enabled identification of numerous bottle-necks, for instance: fracture dynamics; formation of deleterious side-products;[7–10] stabilization of metastable structures; or loss of structural homogeneity over repeated charge/discharge cycles. However, the role of electronic structure and its contribution to diffusion barriers for ion migration is less appreciated.[5,11] Such diffusion barriers are responsible for the limitations of V_2O_5 as a cathode material at high rates and the remarkable (>100,000-fold) enhancement in the performance of this material upon nanostructuring.[12–14] Understanding the origin of these diffusion barriers is imperative for developing fundamental design rules for cathode materials to alleviate charge localization.

V_2O_5 crystallizes in an orthorhombic layered structure with space group *Pmmn* with a van der Waals' separation of 4.368 Å between the layers (Fig. III.1a).[15,16] Three distinct types of oxygen sites can be identified: vanadyl (V=O) oxygen atoms that point between the layers and bridging and chaining oxygen atoms that connect the polyhedra. V_2O_5 was first proposed as a Li-ion intercalation host by Whittingham in 1976 owing to: the abundance of interlayer sites that can accommodate Li-ions; the readily accessible V^{5+}/V^{4+} and V^{4+}/V^{3+} redox couples; and the strong enthalpic driving forces for Li-ion insertion within this structure.[12,17–19] However, despite these promising attributes the poor high-rate performance of these materials and issues with retention of capacity over prolonged cycling have limited the widespread commercial development of this material. In recent years, this material has enjoyed a resurgence of sorts with the realization that the galleries between V_2O_5 layers can accommodate not just Li-ions but also other main-group and transition metal cations of interest to "beyond-Li" battery chemistries, as well

as the understanding that the sluggish kinetics of Li-ion insertion/extraction can be considerably accelerated by scaling to nanometer-sized dimensions.[19–22]

Electrochemical measurements and spectroscopic probes often reveal the presence of two or more phases when a phase transition accompanies lithiation of a cathode material. In many commercial cathode materials such as $LiCoO_2$ or $LiMn_2O_4$, Li-insertion occurs with only modest first order transitions (driven by Li ordering). However, in $LiFePO_4$ a pronounced structural transformation between Li-rich and Li-poor phases is involved. Similarly, a number of intercalated phases can be distinguished for $Li_xV_2O_5$ with varying values of x depending on the concentration of Li ions inserted within the structure. Figures 1a and b show the structural progression of V_2O_5 with increasing intercalation of Li ions; a slightly distorted α-phase is initially stabilized for $x < 0.1$ and with further lithiation is transformed to the ε-phase (Fig. III.1a), which is stabilized in the range $0.35 < x > 0.8$ with initially cubooctahedral and then tetrahedral coordination of Li ions; with still more lithiation, a puckered δ-phase is stabilized for ca. $0.8 < x > 1.0$ (Fig. III.1b). In this regime, the phase transitions involve increased separation of the V_2O_5 layers and their puckering and gliding motions to accommodate the structural distortions induced by an increasing concentration of Li ions without requiring cleavage of V—O bonds.[1,12,15] Further lithiation ($x > 1.0$) brings about more pronounced structural distortions that involve bond-breaking and inversion of $[VO_5]$ polyhedra that are irreversible in the bulk, although there is evidence for recovery of the orthorhombic structure upon delithiation for nanostructures[21,22] even for x approaching 3 in $Li_xV_2O_5$.[23] In V_2O_5, the phase transitions across the structures depicted in Figures 1a

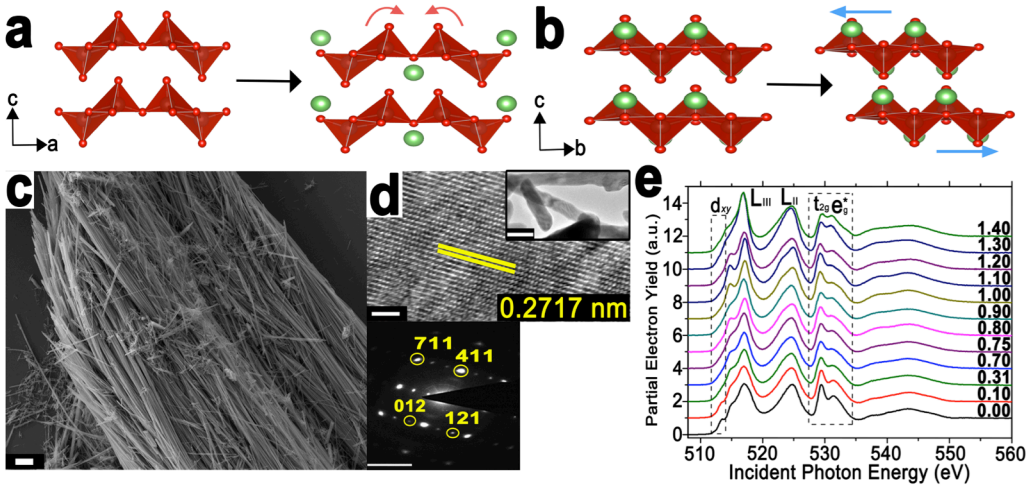

Figure III.1. Structural distortions induced upon insertion of Li-ions and characterization of geometric and electronic structure As the layered structure of V_2O_5 is intercalated with Li-ions, it undergoes a series of phase transformations, to a puckered ε-phase (a); upon further lithiation, the ε-phase transforms with an in-plane shift to a δ-phase (b). (c) Scanning electron microscopy images depict V_2O_5 nanowires with lengths spanning hundreds of microns (scale bar, 3 μm). (d) High-resolution transmission electron microscopy (TEM) image of an individual V_2O_5 wire (scale bar, 5 nm) indicating the separation between the (711) lattice planes of orthorhombic V_2O_5. The top inset shows a low-magnification TEM image of several nanowires (scale bar, 0.2 μm), whereas the bottom inset indicates an indexed selected area-electron diffraction pattern (scale bar, 5 per nm). (e) X-ray absorption near edge structure (XANES) measurements of stoichiometrically lithiated V_2O_5 depicts a reduction of the $3d_{xy}$ resonance at the V L-edge and a diminution of the t_{2g} to e_g* ratio at the O K-edge with increasing lithiation.

and b are rapidly accelerated, by up to 100,000 times, upon scaling to nanometer-sized dimensions yet there is evidence from combined Raman and powder diffraction studies of substantial variations in the extents of surface and bulk lithiation.[15,24] Understanding the origin of such phase segregation is imperative for the design of cathode materials and geometries.

Upon chemical lithiation, the ionized Li-ion as well as the electron must diffuse through the solid matrix with the localization of the latter often bringing about a

pronounced structural distortion; the combination of the electron and its structural distortion is termed a small polaron, provided the distortion has a length scale comparable to the primitive unit cell of the host material. The signatures of polaron formation and polaron hopping energies have been predicted theoretically, but direct experimental evidence of polaron formation and the accompanying geometric distortions have hitherto not been examined.[5,25–28] Here, we present direct evidence of inhomogeneities in charge localization and local structural distortions induced upon lithiation using scanning transmission X-ray microscopy (STXM) and corroborate theoretical predictions of a distinctive polaronic state using X-ray absorption near-edge structure and hard-energy X-ray photoemission spectroscopies. The polaron hopping barrier impedes electron diffusion and gives rise to phase inhomogeneity evident as lithiation gradients across an individual particle.

III.2 Results and Discussion

Chemical lithiation using *n*-butyllithium is used to model Li-ion insertion within a cathode as per the reaction:[29]

$$V_2O_5 + xC_4H_9Li \rightarrow Li_xV_2O_5 + \frac{x}{2}C_8H_{18} \quad \text{(EQUATION III. 1)}$$

Figures III.1c and d indicate scanning electron microscopy (SEM) and transmission electron microscopy (TEM) images of V_2O_5 nanowires grown by a previously reported hydrothermal method; the nanowires range from 150—250 nm in diameter and span several hundred micrometers in length.[15] The lattice-resolved TEM image in Figure 1d shows the separation between (711) planes of orthorhombic V_2O_5 and, along with the accompanying selected area electron diffraction pattern, indicates that the single-

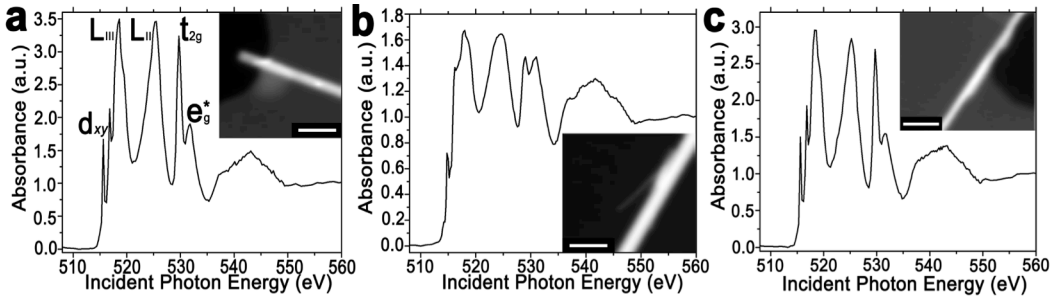

Figure III.2. Evaluating electronic structure changes caused by lithium-ion incorporation Scanning transmission X-ray microscopy (STXM) image and integrated X-ray absorption near edge structure (XANES spectrum acquired for (a) an individual V_2O_5 nanowire (scale bar, 500 nm), (b) an individual nanowire after 1 min of chemical lithiation (scale bar, 200 nm), and (c) a lithiated nanowire subjected to delithiation in Br_2 solution (scale bar, 500 nm). Pronounced differences are discernible after lithiation including diminution of the V L_{III}-edge feature attributed to a V $3d_{xy}$ final state and the reduction of the t_{2g}:e_g* ratio. The complete recovery of the electronic structure upon delithiation suggests that the spectral changes can be directly attributed to Li-ion intercalation. All spectra have been pre- and post-edge normalized to a unitary absorption cross-section to depict the relative spectral intensities.

crystalline nanowire grows along the crystallographic *c* direction without any discernible extended defects.

Fig. A.1 shows an integrated V L- and O K-edge X-ray absorption near edge structure (XANES) spectrum acquired for an individual nanowire of V_2O_5 along with putative assignments derived from restricted open shell configuration interaction with singles (ROCIS) quantum chemistry calculations reported by Neese and co-workers[30] for the V L-edge and a density functional theory calculation for the O K-edge, further elaborated below. As an element- and edge-specific probe of unoccupied states, XANES serves as a valuable tool to probe electronic structure and chemical bonding in extended solids and single molecules alike.[31,32] The V L-edge is characterized by V L_{III} and V L_{II} spectral features corresponding to transitions from V $2p_{3/2}$ → V 3d (ca. 518 eV) and V

$2p_{1/2} \rightarrow$ V 3d (ca. 525 eV) states, respectively,[30,33,34] which are split by the spin-orbit coupling of the V 2p atomic orbitals of *ca.* 7 eV. In turn, the O K-edge corresponds to transitions from O 1s states to states with O 2p character. As a result of substantial V 3d—O 2p orbital hybridization, two distinct sets of resonances are observed, reflecting the crystal field splitting of the V 3d orbitals. Assignments of the spectral features illustrated in Fig. A.1 are derived from density functional theory modeling and are further corroborated by angle-resolved XANES experiments (wherein the modulation in the intensity of resonances as a function of the polarization reflects the orbital symmetry of the final states).[30,33,34]

A Coster—Kronig Auger decay process into a $2p_{3/2}$ hole renders the V L_{II} feature less informative;[34] however, the V L_{III} resonance indicates fine-structure features that strongly depend on the polarization vector; these transitions comprise transitions from the singlet V $2p^6 3d^0$ into V $2p^5 3d^1$ states split by crystal field and multiplet effects.[30] Despite convoluting multiplet effects, ROCIS calculations[30] indicate that the first two sharp resonances at 515.6 and 516.8 eV, respectively, correspond to final states that have relatively "pure" V $3d_{xy}$ and $3d_{xz/yz}$ character and indeed angle-resolved XANES studies bear out these proposed orbital symmetries.[30,33,34] In contrast, the O K-edge is not convoluted by multiplet effects and can be clearly distinguished as three sets of transitions from O 1s core levels to (a) O $2p_x$ and $2p_y$ states that engage in π interactions with the t_{2g} (V $3d_{xz}$, $3d_{xy}$, $3d_{yz}$) states of the metal cations (at 529.7 eV); and overlapping σ states that represent direct end-on hybridization of (b) O $2p_x$ and $2p_y$ with V $3d_{x^2-y^2}$ states at 531.6 eV and (c) O $2p_z$ with V $3d_{z^2}$ states at 533.1 eV. The calculated XCH-

XAS spectrum shown in supplementary Fig. 1b suggests that the t_{2g} manifold is derived primarily from transitions from O 1s core levels to O $2p_x/p_y$ states of the vanadyl oxygens that are hybridized with V $3d_{xz}$ and $3d_{yz}$ states; a lesser contribution to this resonance arises from transitions into O $2p_y$ states of bridging oxygen atoms hybridized with V $3d_{xy}$ states and O $2p_x$ states of chaining oxygen atoms hybridized with V $3d_{xy}$ states. The hybridization of the V=O oxygens with V $3d_{xz/yz}$ thus dominates the lineshape of the t_{2g} resonance in the XANES spectrum with the non-bonding V $3d_{xy}$ contributing much less, in stark contrast to the V L_{III}-edge spectrum, wherein the lowest lying "split-off" state is primarily V $3d_{xy}$ in origin.[30] These assignments thus allow for an orbital-specific description of changes in electronic structure as a function of the lithiation of V_2O_5 and provide unprecedented insight into charge localization phenomena.

Figure III.1e shows XANES spectra for a series of intercalated V_2O_5 samples with increasing values of x in $Li_xV_2O_5$. XANES resonances are collected at magic angle (54.7°) incidence to mitigate specific texturation effects.[35] Several trends are immediately discernible (since XANES probes empty orbitals, the diminution of a resonance, to first approximation, corresponds to occupation of states that give rise to the resonance): the first resonance in the V L_{III} spectrum corresponding to transitions to the split-off d_{xy} conduction band of V_2O_5 is strongly diminished with increasing lithiation consistent with the reduction of V_2O_5 upon lithiation (V^{5+} to V^{4+}) and indicating the occupation of the lowest lying conduction band states. Furthermore, at the O K-edge, the relative intensities of the transitions to the t_{2g} and e_g* (π* and σ*) states are greatly modified with the former resonances losing spectral weight. The origin of this

pronounced modification of spectral lineshapes is distinct from filling of the non-bonding V $3d_{xy}$ states and suggests a pronounced rehybridization of V—O bonding at the vanadyl oxygens (*vide infra*).

In contrast to ensemble spectra depicted in Figure III.1e, focusing the X-ray beam allows for acquisition of spatially resolved STXM data with *ca.* 25 nm spatial resolution, thereby allowing us to probe the lithiation of an individual nanowire immersed in a toluene solution of *n*-butyllithium for 1 min (Fig. III.2b) By finely raster scanning the sample, STXM provides a means to construct a spatially resolved map of the local perturbations to the electronic and geometric structure induced by ion intercalation. Indeed, X-ray imaging has contributed greatly to understanding of inhomogeneities in biomaterials and polymeric systems.[36,37] The absolute energy calibration, detector linearity (Fig. A.2), and beam point spread function are main sources of error for this technique and have been carefully addressed as described in the Methods section.[38]

Figure III.2a depicts the STXM image and integrated V L- and O K-edge spectra of an individual V_2O_5 nanowire with a diameter of ca. 200 nm. In contrast to the orientation-averaged ensemble XANES spectra presented in Figure 1e, well-resolved lineshapes are discernible for an individual single-crystalline V_2O_5 nanowire and the spectral transitions can be assigned as noted in supplementary Fig. III.1 and discussed above. Figure III.2b depicts the STXM image and corresponding integrated spectrum acquired for a V_2O_5 nanowire after chemical lithiation for 1 min. Pronounced differences are readily discernible in this spectrum; the transition attributed to a V $3d_{xy}$ final state at

515.6 eV is greatly diminished in intensity. Concomitantly, at the O K-edge, the t_{2g} peaks are broadened and diminished in relative intensity with respect to the e_g* peaks. In concordance with the ensemble XANES spectra (Fig. III.1e), the integrated element-specific spectrum in Figure III.2b suggests that the electrons donated by the inserted Li-ions have been transferred and reside on the V_2O_5 framework but are localized on the lowest-lying V=O $3d_{xz/yz}$—O 2p hybridized states of the conduction band, which have been substantially distorted as a result of lithiation.[17,39–41] Interestingly, upon delithiation by immersion in Br_2 solution the electronic structure for V_2O_5 is recovered in its entirety

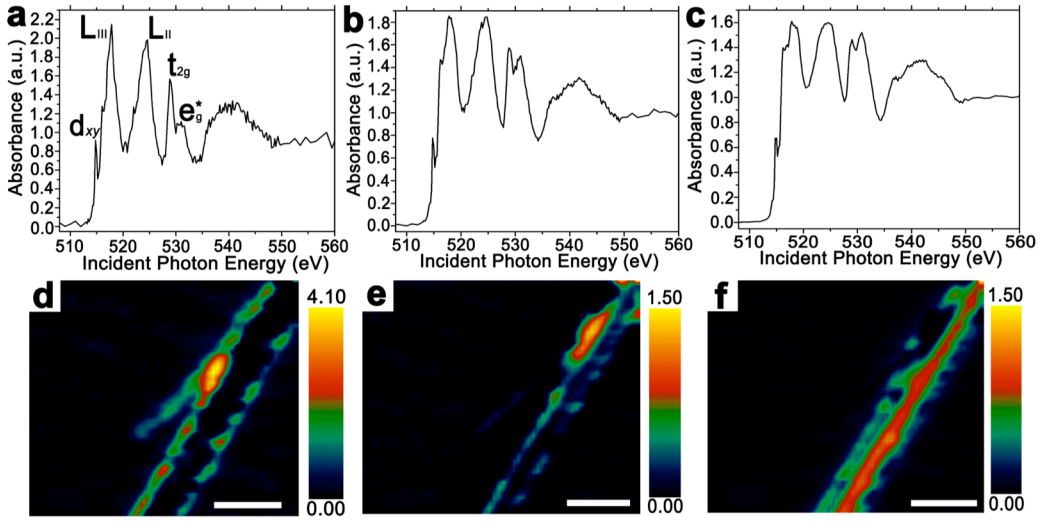

Figure III.3. Mapping Electron Density, Inhomogeneous Lithiation, and Local Structural Distortions Across a Single V_2O_5 Nanowire. Three distinct spectral contributions deconvoluted from region of interest analysis of Fig. 2b are plotted in panels (a)—(c) in order of increasing lithiation evidenced as a diminution of the V $3d_{xy}$ resonance at the V L_{III}-edge and the t_{2g}:e_g* ratio at the O K-edge. Intensity maps for each spectral contribution are plotted in (d)–(f) (scale bar, 200 nm), respectively, showing inhomogeneous regions of lithiation. A nonlinearity correction has been implemented as described by Collins and Ade and described in the Methods section.[38] All spectra have been pre- and post-edge normalized to a unitary absorption cross-section to depict the relative spectral intensities. The colour scale bars represent normalized optical density.

(Fig. III.2c) confirming that the electronic structure modulation observed in V_2O_5 derives directly from lithiation.

Unlike Figures III.2a and c wherein the spectra show little variation across the span of the nanowires, several distinct spectral contributions are discernible for the lithiated nanowire of Figure III.2b. A region of interest (ROI) analysis allows for identification of three distinct domains that are characterized by spectra individually plotted in Figures III.3a—c; these spectra correspond to different regions of the nanowire shown in Figure III.2b (the spectrum in Figure III.2b captures the integrated spectrum). In going from Figure III.3a to c, the intensity of the t_{2g} resonance is progressively diminished with respect to the e_g* resonance, indicating successively greater electronic reduction of the V_2O_5 framework; the accompanying maps in Figures III.3d—f indicate the spectral intensities of each of these components across the nanowire, suggesting the presence of distinct domains as a result of inhomogeneous lithiation. These maps are derived based on singular value decomposition of the image stack and by using as a reference the ROI spectra identified within different regions of the same image sequence. This operation produces a set of composition maps where intensities represent the signal strength of each of the spectral components (Figs. III.3a—c) in that highlighted area. Notably, Fig. A.3 shows a thickness map of the nanowire (determined after a nonlinearity correction) along with a cross-sectional SEM image of the surface of an individual nanowire that indicates that the domains visualized in Figure III.3a—c result from inhomogenous lithiation and do not reflect thickness variations. Figure III.3d represents the least lithiated domains within this sample and is

weighted most strongly at the periphery of the nanowire; based on the ensemble spectra depicted in Figure III.1e and previous angle-resolved spectra acquired for V_2O_5 nanowires[33], an extent of lithiation in the broad range $0.1 < x < 0.5$ can be surmised. Note that the intensities at the V L_{III} edge for the lithiated sample are substantially diminished as compared to unlithiated and delithiated V_2O_5 as a result of state blocking; occupation of conduction band states diminishes the intensity of the low-energy XANES

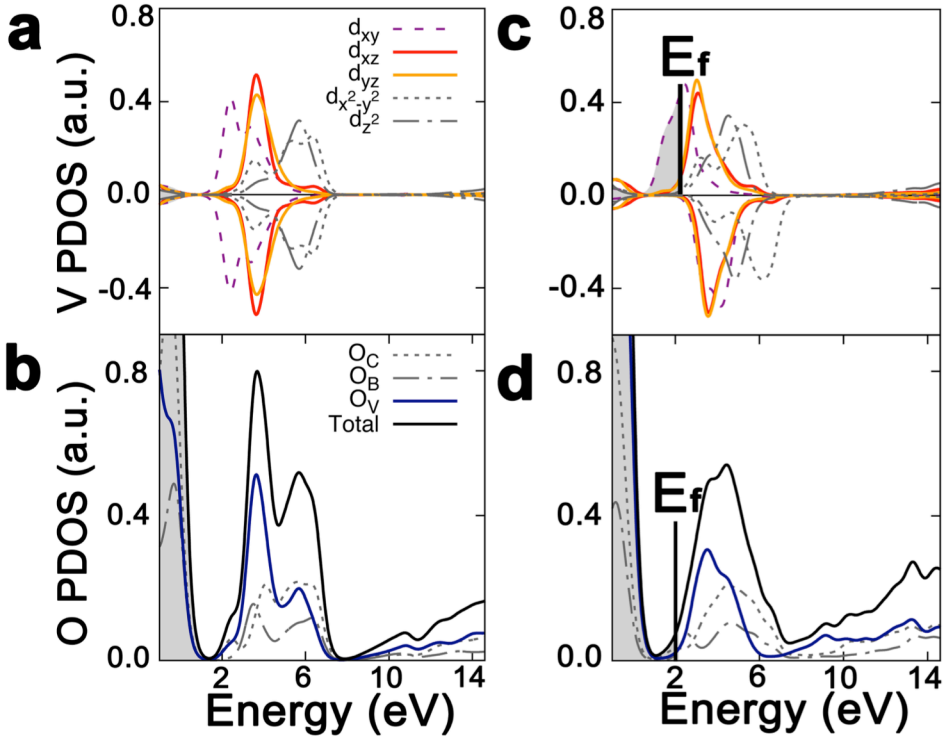

Figure III.4. Density of states calculation for V_2O_5 and LiV_2O_5. The GGA+*U* ground-state projected-DOS (pDOS) of pristine V_2O_5 (a–b) and the stoichiometric $Li_xV_2O_5$ (c–d) that adopts the pristine V_2O_5 vertical stacking order. The upper panels are the pDOS of vanadium in which the gray area indicates the occupied states. In the lower panels, the key components that are mainly responsible for the changes in the main peak intensity at the O K-edge are outlined by solid curves. The total pDOS (black curves) are the summation of p_x-, p_y-, and p_z-components from all three types of oxygen; chain (O_c), bridge (O_B) and vanadyl (O_V), with the corresponding stoichiometric ratio.

features. The interiors of the nanowires show two distinct spectral components depicted in Figures III.3e and III.3f with substantially greater extents of lithiation (estimated to be $0.5 < x < 0.9$ and $0.9 < x < 1.40$, respectively). In particular, Figure III.3f defines a highly reduced strip that runs across a large section of the nanowire. The reduction of the $3d_{xy}$ resonance at the V L_{III} edge correlates to the occupation of the lowest-lying levels in the conduction band of V_2O_5 by the electron ionized from the inserted Li atom. The resonance observed after lithiation arises from a superposition of remnant V^{5+} and reduced vanadium sites. In contrast, the diminished relative intensity of the low-energy t_{2g} peaks at the O K-edge is the result of an induced structural distortion and further polarization of the electron density on V_2O_5 caused by the heterogeneous insertion of Li-ions (*vide infra*). In other words, the V L_{III}-edge allows for direct evaluation of electron density on the vanadium sites, whereas the O K-edge unveils structural distortion of the vanadyl V=O bonds induced as a result of electron localization.

The increased lithiation at the core and the reduced lithiation of the surfaces is explicable based on the orientation of the nanowires (Fig. III.1d) and the preferred insertion of Li-ions between the layers. In essence, the nanowire is being viewed down the crystallographic *b*-axis and thus is enclosed at the top and bottom by *ab* planes that are impermeable to lithiation. The pronounced differences in lithiation likely further result from the stage ordering typical of layered materials[42,43]; the initial stochastic or defect-driven intercalation of Li-ions between two specific V_2O_5 layers results in a local expansion of the interlayer spacing and facilitates insertion of a second Li-ion within the same layer. Indeed, Fig. A.4 indicates a sequence of calculated V_2O_5 structures with

insertion of one Li-ion (Fig. A.4a) and then two possibilities for insertion of the second Li-ion: within the same layer (Fig. A.4b) and alternating layers (Fig. A.4c); insertion of Li-ions within the same layer is thermodynamically favored by -0.235 eV per formula unit.

To better understand the variations in the oxygen XANES spectra of the nanowires, GGA+*U* (*U* = 3.1 eV)[44] calculations were employed to examine the evolution of the electronic structure as a function of increasing insertion of Li ions.[44,45] The on-site Coulomb repulsive energy *U* is essential to capture the effects of strong electron correlation with vanadium 3d orbitals. Orthorhombic V_2O_5 (Fig. III.1a) is a dielectric material with a bandgap of *ca.* 2.3 eV;[16,46–48] the conduction band is primarily V 3d in character, whereas the valence band has an extensive O 2p contribution.[16,30] The projected density of states (pDOS) of pristine V_2O_5 is shown in Figures III.4a and b, with the valence band maximum (VBM) aligned at 0. The two spin channels are completely degenerate in this d^0 system with pure V^{5+}. In the crystal field of the slightly distorted [VO_5] square pyramid, the $3d_{xy}$ orbitals from the perfect octahedral t_{2g} group are further split into a high-energy component that overlaps with the degenerate $3d_{xz}$ and $3d_{yz}$ orbital and a lower-energy component that dominates the conduction band edge[49–51] (at *ca.* 2 eV above the VBM in Fig. III.4a). This lower energy $3d_{xy}$ orbital is approximately non-bonding and comprises two split-off bands. The prominent feature in the oxygen total pDOS results primarily from the strong hybridization of the V $3d_{xz}$ and $3d_{yz}$ orbitals with the vanadyl oxygen atom and indeed these features contribute to the sharp XANES resonance at 529 eV.[52] The secondary feature from the oxygen pDOS is

the typical e_g component and gives rise to the absorption peak at 531 eV. Even without core-hole effects, the ground-state pDOS can still reproduce these features in the V_2O_5 O K-edge spectrum (Fig. A.1b) and enables understanding of the trends observed upon lithiation.[53] With increasing, the donated electrons begin to occupy the non-bonding $3d_{xy}$ component at the band edge. We first consider a simple periodic system with pure $V^{4.5+}$ site, where the electron occupies only a quarter of all available $3d_{xy}$ orbitals (as in α-NaV_2O_5).[51,54] Even at this electron doping level, electron correlation effects are important. The two spin channels are significantly split as a result of the localization of spin states induced by local lattice distortions, which lifts the spin degeneracy as depicted by Figure III.4c. The donated electrons take on $3d_{xy}$ character and the localized spins[51,54,55] are arrayed along the orthorhombic *b*-axis of V_2O_5. Contrary to intuition, the observed diminution of t_{2g} intensity is not due to Pauli-blocking from electron occupation, since the Fermi level remains far below the main peak position in the quarter-filled case. Instead, the lifted spin degeneracy induced by the correlation effects and lattice distortion plays a much more important role in reducing the t_{2g} peak intensity. In short, the oxygen 2p components that strongly hybridize with the V 3d-orbitals are also split into two non-degenerate spin channels, leading to a severe drop in the main peak intensity (Fig. III.4d). Further details of the pDOS, illustrating this splitting, are depicted in Fig. A.5. Both the lifting of spin degeneracy and the lattice distortion caused by lithiation contribute to reduction of the intensity of the t_{2g} peak. The inserted Li-ions electrostatically attract the vanadyl oxygens towards them and create a pronounced distortion on the *a*-*c* plane (Fig. III.1b). Such a distortion further shifts the energetic

position of $3d_{xz}$-orbitals, resulting in a noticeable migration of t_{2g} intensity to higher spectral energies. Based on the abovementioned effects, the pDOS shown in Figure III.4d captures the specific origins of the evolution of the O K-edge spectra.

The Coulomb interaction between the spin-up and spin-down states, represented by the on-site Coulomb repulsion energy *U*, favors the removal of spin degeneracy along one spin polarization so as to lower the total energy of the system (Fig. A.6) and indeed this stabilization counteracts the elastic energy expended to bring about the distortion of the geometric structure depicted in Fig. A.7 (also see Movie A.1). In Figure A.6, we initiate a supercell with perfect V_2O_5 lattice symmetry and an added electron and relax the structure by enforcing spin degeneracy. The electron density also become delocalized in this case and this delocalized structure is ca. 0.22 eV higher in energy than the small polaron structure with a localized electron. These results further suggest that the stabilization of the small polaron in V_2O_5 is energetically favored both as a result of lattice distortion as well as the lifting of spin degeneracy.[56,57] The influence of the Li-ion on the small polaron is further discussed below.

In order to understand the localization of the electron density upon Li-ion intercalation, the electronic difference is calculated following equation III.2:

$$\Delta\rho(r) = \rho_{Li_xV_2O_5}(r) - \rho_{Li}(r) - \rho_{V_2O_5}(r) \quad \text{(EQUATION III. 2)}$$

where $\rho_{Li_xV_2O_5}(r)$ is the electron density of the Li-intercalated V_2O_5, $\rho_{Li}(r)$ of isolated Li atoms in the same position as in the total system and $\rho_{V_2O_5}(r)$ for V_2O_5. Fig. A.4 plots the increase and decrease in electron density of singly lithiated $Li_{0.125}V_2O_5$ and doubly lithiated $Li_{0.25}V_2O_5$ systems. The increase in electron density traces the contours of a V

$3d_{xy}$ orbital, indicating an electron localized in this lowest-lying state of the conduction band; in contrast, the electron density decrease is localized within bonds along the [VO_5] pyramid. To put it differently, the increased electron density localized on the V $3d_{xy}$ orbitals polarizes the V—O bonds and brings about a pronounced increase of the bond length. The coupled charge localization and distortion of the geometric structure further defines a small polaron as observed in the single-electron reduction case. Movie A.1 illustrates the localized distortion of the structure wherein the V atom shifts away from the intercalated Li-ion; the bridge and chain oxygen atoms distort away from the central vanadium atom reflecting increased bond lengths and the vanadyl oxygen atoms orient toward the intercalated Li-ions defining its cubooctahedral local coordination environment.

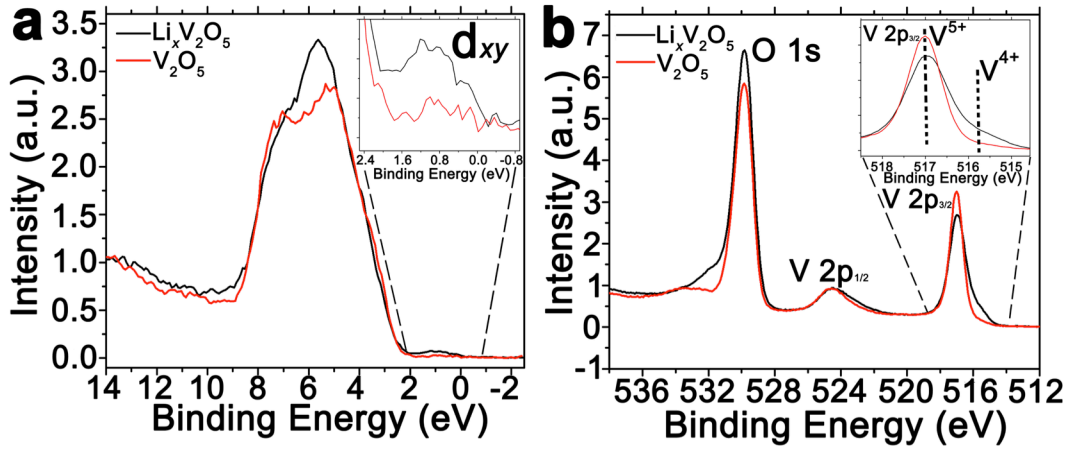

Figure III.5. Valence Band and Hard X-ray Photoemission Spectroscopy (HAXPES) Measurements of V_2O_5 and $Li_xV_2O_5$ (a) Valence Band spectra for pristine V_2O_5 (red) and $Li_xV_2O_5$ (black). The right inset depicts a magnification of the region showing the emergence of a feature below the Fermi level. As predicted by theory, HAXPES measurements clearly illustrate the appearance of a polaronic state below the Fermi level. (b) HAXPES performed on these samples demonstrates the existence of V^{4+} and V^{5+} sites at the V $2p_{3/2}$ peak.

Polaronic confinement in transition-metal oxides has been extensively examined using DFT calculations.[5,25,26] Ioffe and Patrina have previously attempted to correlate the conductivity of V_2O_5 to small polaron formation using electronic transport measurements.[27] However, direct atomic-scale evidence of polaron formation has thus far been elusive. The clear correlation of transitions related to final states involving the V $3d_{xy}$ level upon lithiation noted in Figure III.2 and the subsequent effect on the crystal structure of the material shown in the reduction of the t_{2g}/e_g* ratio clearly indicates that polaron formation plays a key role in limiting Li-diffusion within this material.

The energetic barrier to polaron diffusion within $Li_{0.125}V_2O_5$ was calculated. Previous studies have shown strongly disfavored Li migration along the *a*- and *c*-axes with migration barriers of 1.88 eV and 1.69 eV, respectively.[58] Fig. A.8a and A.8b show a schematic depiction of the path adopted by Li-ions between adjacent Li sites along the *b*-axis, with a calculated diffusion barrier of 0.22 eV.[19] The diffusion of Li-ions involves a change in the local coordination environment from 8→3→8 anions. Fig. A.8c illustrates the constrained trigonal planar transition state; the energetic barrier derives in large part from the substantial change of coordination number and the unfavorable coordination environment in the transition state. To further understand electron-polaron interactions with the intercalated Li-ion, the polaron formation energies are calculated for two separate pairs of vanadium positions (Fig. A.9). In the first case, the electron is localized on the V1—V2 pair (in proximity of the Li-ion), whereas in the second case the electron is localized on the V3-V4 pair (far from the Li-ion). The former configuration yields a formation energy of -0.41 eV/V_2O_5 unit suggesting that the

polaron is stabilized by an attractive interaction with the Li-ion. In contrast, the calculated formation energy for the latter configuration with the polaron situated at V3-V4 positions is 0.02 eV/V_2O_5, clearly a much less stable configuration for the polaron. Fig. A.19c indicates that the migration barrier for the V1-V2 polaron is 0.34 eV, whereas the comparable value for the V3—V4 pair is 0.03 eV. These calculations thus suggest that small polarons are preferentially stabilized adjacent to the intercalated Li-ions but this stabilization also entails a substantial barrier for migration of the polarons along the V_2O_5 framework.[56] In other words, the intercalated Li-ions play a critical role in stabilizing the polaron and determining its ease of migration.

Now turning our attention to the electronic consequences of Li-ion intercalation, the calculated orbital-projected density of states in Fig. A.10 suggest that lithiation should be accompanied by the appearance of a "mid-gap" state between the valence and conduction band. To examine the predictions of the appearance of a filled state derived from polaron formation in the upper valence band, hard X-ray photoemission spectroscopy (HAXPES) measurements have been performed for lithiated samples (Fig. III.5). The V $2p_{3/2}$ spectrum in Figure III.5b clearly indicates the presence of discrete V^{4+} and V^{5+} states. Most notably, the inset to Figure III.5a indicates the emergence of a feature not observed for orthorhombic V_2O_5 at ca. 1.0 eV below the Fermi level in the valence band spectrum that corroborates and serves as a distinctive signature of the mid-gap polaronic predicted by DFT. The appearance of this state provides definitive experimental evidence for localized electrons corresponding to stabilization of a small polaron.

The experimental results in concert with the calculations indicate that local structural distortions and the stabilization of small polarons impede electron diffusion within V_2O_5 and give rise to distinctive lithiation gradients.[42,59] The STXM images correspond to a map of electron density on the V_2O_5 framework, which further reflects the lithiation gradient as a result of the close association of localized electrons with Li-ions. As noted above, in $Li_xV_2O_5$, the Li-ion stoichiometry *x* determines the phase of the material and a series of phase transformations are evidenced with increasing lithiation. Barriers to diffusion of Li-ions thereby also influence the sequence of structural phase transformations. In other words, STXM provides a view of trapped electron density, which is correlated to lithiation gradients, further reflecting barriers to propagation of phase transformation within an individual $Li_xV_2O_5$ nanowire. The pronounced increase in high-rate performance as observed for nanostructures thus likely results much more facile phase nucleation enabled by easier electron and ion diffusion.

III.3 Conclusions

In summary, we have mapped the changes in electronic structure as well as local structural distortions induced by the lithiation of V_2O_5 using a combination of V L-edge and O K-edge XANES and STXM probes of the conduction band and HAXPES examination of the valence band; the spectra are interpreted with the assistance of DFT+U calculations. Specifically, we note the stabilization of distinctive domains within individual nanowires of lithiated V_2O_5 corresponding to the emergence of charge density gradients along the nanowires that can be correlated to inhomogeneous lithiation. These measurements provide the first view of highly anisotropic lithiation of layered materials

resulting from the peculiarities of their electronic and geometric structure. Spectral assignments verified by DFT modeling suggest that lithiation of V_2O_5 induces the localized reduction of specific vanadium sites with the electron derived from the ionized Li ion residing in neighboring V $3d_{xy}$ orbitals that are the lowest lying states in the conduction band. In a complementary fashion, O K-edge XANES spectra and STXM maps depict the local structural distortions induced by exchange interactions and small polaron formation as a result of strong modification of V—O hybridization along the vanadyl V=O bonds. DFT calculations confirm that electron density localization is sufficient to drive elastic distortion of the local atomic structure. The quasiparticle comprising the trapped electron and the local distortion constitutes a small polaron and polaronic signatures predicted by DFT have been verified by HAXPES studies. Delithiation of V_2O_5 brings about elimination of the polaron and complete recovery of the electronic structure. The small polaron formation directly evidenced in these studies is thought to be the origin of sluggish diffusion of Li-ions through the cathode, with a diffusion barrier of ca. 0.22 eV, limiting high rate performance. The strongly accelerated kinetics of lithiation observed upon scaling to nanometer-sized dimensions can also in large measure be attributed to the ability to circumvent the limitations of sluggish small polaron hopping at these sizes. The fundamental limitations to ion diffusion unveiled here suggest that V_2O_5 cathode materials will benefit from development of quasi-amorphous or highly porous materials where charge is not required to travel large distances or by devising novel lattice frameworks with lower extent of polaronic confinement. Quasi-amorphous or highly porous materials would have a greater contact

area with the electrolyte, thereby greatly limiting the range over which small polaron hopping needs to be sustained and mitigating the kinetic impediments imposed by stabilization of a polaron.

III.4 Methodology

III.4.1 Synthesis and Chemical Lithiation of V_2O_5 Nanowires

Synthesis and the subsequent lithiation of the V_2O_5 nanowires were carried out as previously reported.[15] Briefly, V_2O_5 nanowires were synthesized *via* hydrothermal reduction of bulk V_2O_5 (Sigma-Aldrich 99.5%) with oxalic acid (J.T. Baker) to prepare $V_3O_7{\cdot}H_2O$ nanowires followed by oxidation in air at 300˚C to obtain phase-pure V_2O_5 nanowires. Lithiation was carried out within a glove bag under Ar ambient *via* immersion of the powder in molar excess (4:1 Li:V_2O_5) of 2.5 M *n*-butyllithium solution in hexanes (Sigma-Aldrich) diluted to 0.025 M in toluene. Delithiation was accomplished by immersion of the lithiated samples in pure liquid Br_2 for 2 h, followed by washing with large amounts of hexanes. The samples are sealed within a glovebox for transport to synchrotrons for XANES and STXM measurements.

III.4.2 XANES Spectroscopy

XANES measurements were carried out at the National Synchrotron Light Source (NSLS) of Brookhaven National Laboratory at beamline U7A operated by the National Institute of Standards and Technology (NIST) with a toroidal mirror spherical grating monochromator using a 1200 lines mm^{-1} grating with a nominal energy resolution of 0.25 eV with a slit size of 30 x 30 μm. XANES spectra were collected in partial electron yield mode with a channeltron multiplier near the sample surface; the

detector was used with an entrance grid bias of -200 V bias to reject low-energy electrons; a charge compensation gun was used to avert the charging of the samples. The incident beam is linearly polarized 85% in the plane of the synchrotron ring. As XANES uses linearly polarized light and incorporates dipolar transitions, the absorption cross section transforms as follows:

$$\sigma(\hat{\varepsilon}) = \sigma_a sin^2\theta + \sigma_b cos^2\theta \quad \text{(EQUATION III. 3)}$$

where $\sigma(\hat{\varepsilon})$ is the Cartesian tensor for the absorption cross section derived from Fermi's Golden rule, σ_a and σ_b are distribution functions of crystallite orientation, and θ is the angle between the polarization vector and sample. If θ = 54.7˚, the isotropic average is:

$$\sigma(\theta) = 2\sigma_a + {}^{\sigma_b}/_{3} \quad \text{(EQUATION III. 4)}$$

and thus specific texturation effects are heavily mitigated at this angle. The partial electron yield (PEY) signals were normalized using the incident beam intensity to eliminate the effect of incident beam intensity fluctuations and monochromatic absorption features. The V L- and O K-edge spectra were acquired in a single scan. The data was collected along a metallic vanadium reference mesh for energy calibration. Pre-and-post edge normalization of the spectrum was performed using the Athena suite of programs.

III.4.3 Scanning Transmission X-ray Microscopy (STXM)

STXM measurements were performed at the SM (10-ID1) beamline of the Canadian Light Source (CLS), a 2.9 GeV third-generation synchrotron facility. A 25 nm outermost-zone zone plate was used to obtain a diffraction-limited spatial resolution better than 30 nm. A 500 line mm^{-1} plane grating monochromator (PGM) was used to

acquire the V L-edge and O K-edge spectral stacks. The incident photon flux (I_o) count rate was adjusted to be less than 20 MHz and optimized to ca. 17 MHz as read by the STXM detector within a hole located close to the sample of interest and measured at 560 eV by adjusting the exits slits to 17/16 μm (dispersive/non-dispersive). The V L- and the O K-edge stacks covered an energy range from 508—560 eV with energy steps of 0.2 eV in the region of interest and 1 eV in the continuum region beyond the specific elemental edges with dwell time of 1 ms for each section. Right circularly polarized light X-rays, generated by an elliptically polarized undulator (EPU) was used in the experiments. All STXM data were analyzed and processed using aXis2000 software (http://unicorn.mcmaster.ca/aXis2000.html). STXM maps are derived based on singular value decomposition of the image stack in aXis2000 and by using as a reference the ROI spectra identified within different regions of the same image sequence. This operation produces a set of composition maps where intensities represent the signal strength of each of the spectral components (Figs. III.3a—c) at each specific pixel of that highlighted area. To correct for the non-linearity of the detector, the flux was measured as a function of dispersive slit width for non-dispersive slit widths of 5 μm, 10 μm, 15 μm, 25 μm at 560 eV (Fig. A.2). The resultant curves were fit using the function as per the method described by Collins and Ade:[38]

$$I' = I_s(1 - e^{(-\kappa(x-x_0)})$$ (EQUATION III.5)

where I' is the measured flux, I_s is the detector saturation flux, κ is the rate at which measured flux approaches saturation, x is the dispersive slit width, and x_0 is a slit width

zero offset. The parameters extracted from the fit function allow for the measured flux to be corrected to the actual flux using the following relationship:

$$I = -I_s \, ln\left(1 - \frac{I'}{I_s}\right) \quad \text{(EQUATION III. 6)}$$

From this analysis, the quantum efficiency of the detector can be determined as a function of flux and is plotted in supplementary Figure III.2.[38] The experimental spectrum of the lithiated V_2O_5 nanowires was corrected by first extracting the average measured flux at each pixel from the image stack. The extracted flux was then corrected by calculating the actual flux, as in latter equation, yielding a spectrum representative of the actual flux values at each pixel. Due to the magnitude of correction being dependent upon the measured flux, a correction factor was then calculated for each pixel, which was then multiplied by the stack to yield a corrected image (Fig. III.3).

III.4.4 Hard X-ray Photoemission Spectroscopy (HAXPES)

HAXPES measurements were performed at the National Institute of Standards and Technology (NIST) bending magnetic beamline X24 of the National Synchrotron Light Source of Brookhaven National Laboratory. Measurements were performed at a ca. 4 keV photon energy with a pass energy of 500 eV and a Gaussian instrumental broadening of 0.45 eV. The higher excitation of HAXPES circumvents serious charging issues that are common to UV and soft X-ray photoelectron spectroscopy. No evidence of charging was observed during our measurements. The HAXPES spectra are energy aligned to the Fermi level of a gold foil reference in electrical contact with our samples, unless stated otherwise. To mitigate further energy alignment shifts from beam drift, the Au reference scans were measured before and after each spectrum.

III.4.5 Computational Details

The ground-state structural and electronic properties of V_2O_5 and the lithiated systems are obtained using density functional theory[60,61] with the Vienna *ab initio* simulation package (VASP)[62]. The exchange-correlation energies are calculated within the specific generalized-gradient approximation (GGA) of Perdew-Burke-Ernzerhof (PBE)[63]. The electron-ion interaction is treated with projector-augmented-wave (PAW) pseudopotentials[64,65], using a 400 eV plane-wave kinetic energy cut-off. A rotationally invariant DFT+U approach[45] is employed to describe the on-site Coulomb interaction of the spin-up and spin-down electrons, with U = 3.1 eV.[44] To converge the total energy, we sample the first Brillouin zone with a Monkhorst-Pack reciprocal-space grid of 6x6x6 k-points. All the atomic structures being considered have been relaxed until each Cartesian force component is no greater than 0.01 eV $Å^{-1}$. To guarantee highly resolved projected density of states (pDOS), we calculate Kohn-Sham eigen-energies based on the converged electron density on a grid of 24x24x24 k-points centered at the zone center (Γ-point). The pDOS is numerically broadened with a Fermi-Dirac smearing of 0.2 eV, approximately mimicking the intrinsic broadening due to the oxygen 1s core-hole lifetime. Higher resolution pDOS shown in the supplemental materials is obtained from the much smaller broadening of 0.03 eV. The Tkatchenko-Scheffler method was used to describe the van der Waals interaction between the layers of V_2O_5.[66] Lithium-ion diffusion barriers in α-$Li_{0.125}V_2O_5$ are calculated using the nudged-elastic band (NEB) method[67] as implemented in VASP. A total of seven images are calculated between the end-points to capture the energy landscape for lithium-ion diffusion. The end points are

optimized to a force tolerance of ±0.001 eV $Å^{-1}$, whereas the convergence criterion for the forces along the NEB path is 0.1 eV $Å^{-1}$.[68]

III.5 References

(1) Whittingham, M. S. Lithium batteries and cathode materials. *Chem. Rev.* **2004**, *104*, 4271–4301.

(2) Kang, B. and Ceder, G. Battery materials for ultrafast charging and discharging. *Nature* **2009**, *458*, 190–193.

(3) Kim, S. W.; Seo, D. H.; Ma, X.; Ceder, G.; and Kang, K. Electrode materials for rechargeable sodium-ion batteries: potential alternatives to current lithium-ion batteries. *Adv. Energy Mater.* **2012**, *2*, 710–721.

(4) Tarascon, J.-M. and Armand, M. Issues and challenges facing rechargeable lithium batteries. *Nature* **2001**, *414*, 359–367.

(5) Ping Ong, S.; Chevrier, V. L.; and Ceder, G. Comparison of small polaron migration and phase separation in olivine $LiMnPO_4$ and $LiFePO_4$ using hybrid density functional theory. *Phys. Rev. B* **2011**, *83*, 75112:1-7.

(6) Tarascon, J.-M. Key challenges in future Li-battery research. *Philos. Trans. A. Math. Phys. Eng. Sci.* **2010**, *368*, 3227–3241.

(7) Ghassemi, H.; Au, M.; Chen, N.; Heiden, P. A.; and Yassar, R. S. In situ electrochemical lithiation/delithiation observation of individual amorphous Si nanorods. *ACS Nano* **2011**, *5*, 7805–7811.

(8) Gu, M.; Parent, L. R.; Mehdi, B. L.; Unocic, R. R.; McDowell, M. T.; Sacci, R. L.; Xu, W.; Connell, J. G.; Xu, P.; Abellan, P.; et al. Demonstration of an

electrochemical liquid cell for operando transmission electron microscopy observation of the lithiation/delithiation behavior of Si nanowire battery anodes. *Nano Lett.* **2013**, *13*, 6106–6112.

(9) Kirshenbaum, K.; Bock, D. C.; Lee, C.-Y.; Zhong, Z.; Takeuchi, K. J.; Marschilok, A. C.; and Takeuchi, E. S. In situ visualization of $Li/Ag_2VP_2O_8$ batteries revealing rate-dependent discharge mechanism. *Science* **2015**, *347*, 149–154.

(10) Liu, H. *et al.* Capturing metastable structures during high-rate cycling of $LiFePO_4$ nanoparticle electrodes. *Science* **2014**, *344*, 12528171–12528177.

(11) Castro, L. *et al.* The spin-polarized electronic structure of $LiFePO_4$ and $FePO_4$ evidenced by in-lab XPS. *J. Phys. Chem. C* **2010**, *114*, 17995–18000.

(12) Chernova, N. A.; Roppolo, M.; Dillon, A. C.; and Whittingham, M. S. Layered vanadium and molybdenum oxides: batteries and electrochromics. *J. Mater. Chem.* **2009**, *19*, 2526–2552.

(13) Sides, C. R. and Martin, C. R. Nanostructured electrodes and the low-temperature performance of Li-ion batteries. *Adv. Mater.* **2005**, *17*, 125–128.

(14) Rui, X. *et al.* Ultrathin V_2O_5 nanosheet cathodes: realizing ultrafast reversible lithium storage. *Nanoscale* **2013**, *5*, 556–560.

(15) Horrocks, G. A.; Likely, M. F.; Velazquez, J. M.; and Banerjee, S. Finite size effects on the structural progression induced by lithiation of V_2O_5: a combined diffraction and Raman spectroscopy study. *J. Mater. Chem. A* **2013**, *1*, 15265-15277.

(16) Eyert, V. and Höck, K.-H. Electronic structure of V_2O_5: role of octahedral deformations. *Phys. Rev. B* **1998**, *57*, 12727–12737.

(17) Scanlon, D. O.; Walsh, A.; Morgan, B. J.; and Watson, G. W. An ab initio study of reduction of V_2O_5 through the formation of oxygen vacancies and Li intercalation. *J. Phys. Chem. C* **2008**, *112*, 9903–9911.

(18) Whittingham, M. S. The role of ternary phases in cathode reactions. *J. Electrochem. Soc.* **1976**, *123*, 315–320.

(19) Marley, P. M.; Horrocks, G. A.; Pelcher, K. E.; and Banerjee, S. Transformers: the changing phases of low-dimensional vanadium oxide bronzes. *Chem. Commun.* **2015**, *51*, 5181–5198.

(20) Yoo, H. D. *et al.* Mg rechargeable batteries: an on-going challenge. *Energy Environ. Sci.* **2013**, *6*, 2265–2279.

(21) Wang, Y. and Cao, G. Synthesis and enhanced intercalation properties of nanostructured vanadium oxides. *Chem. Mater.* **2006**, *18*, 2787–2804.

(22) Chan, C. K. *et al.* Fast, Completely reversible li insertion in vanadium pentoxide nanoribbons. *Nano Lett.* **2007**, *7*, 490–495.

(23) Galy, J. Vanadium pentoxide and vanadium oxide bronzes—structural chemistry of single (S) and double (D) layer $M_xV_2O_5$ phases. *J. Solid State Chem.* **1992**, *100*, 229–245.

(24) Baddour-Hadjean, R. and Pereira-Ramos, J.-P. Raman microspectrometry applied to the study of electrode materials for lithium batteries. *Chem. Rev.* **2010**, *110*, 1278–1319.

(25) Scanlon, D. O.; Morgan, B. J.; and Watson, G. W. Modeling the polaronic nature of p-type defects in Cu_2O: the failure of GGA and GGA + U. *J. Chem. Phys.* **2009**, *131*, 124703:1-8.

(26) Franchini, C.; Kresse, G.; and Podloucky, R. Polaronic hole trapping in doped $BaBiO_3$. *Phys. Rev. Lett.* **2009**, *102*, 6–9.

(27) Ioffe, V.A. and Patrina, I. B. Comparison of the small-polaron theory with the experimental data of current transport in V_2O_5. *Phys. Status Solidi* **1970**, *389*, 389–395.

(28) Reid, O. G. and Rumbles, G. Quantitative transient absorption measurements of polaron yield. *J. Phys. Chem. Lett.* **2013**, *4*, 2348–2355.

(29) Whittingham, M. S. and Dines, M. B. n-Butyllithium—an effective, general cathode screening agent. *J. Electrochem. Soc.* **1977**, *124*, 1387–1388.

(30) Maganas, D. *et al.* First principles calculations of the structure and V L-edge X-ray absorption spectra of V_2O_5 using local pair natural orbital coupled cluster theory and spin-orbit coupled configuration interaction approaches. *Phys. Chem. Chem. Phys.* **2013** *15*, 7260–7276.

(31) Stohr, J. *NEXAFS Spectroscopy*. **1992** (Springer).

(32) Schultz, B. J.; Dennis, R. V; Lee, V.; and Banerjee, S. An electronic structure perspective of graphene interfaces. *Nanoscale* **2014**, *6*, 3444–3466.

(33) Velazquez, J. M.; Jaye, C.; Fischer, D. A.l; and Banerjee, S. Near edge x-ray absorption fine structure spectroscopy studies of single-crystalline V_2O_5 nanowire arrays. *J. Phys. Chem. C* **2009**, *113*, 7639–7645.

(34) Goering, E.; Müller, O.; Klemm, M.; denBoer, M. L.; and Horn, S. Angle dependent soft-X-ray absorption spectroscopy of V_2O_5. *Philos. Mag. B* **1997**, *75*, 229–236.

(35) Pettifer, R. F. *et al.* Magic-angle theorem in powder x-ray-absorption spectroscopy. *Phys. Rev. B Condens. Matter Mater. Phys.* **1990**, *42*, 37–42.

(36) Ade, H., and Hitchcock, A. P. NEXAFS microscopy and resonant scattering: Composition and orientation probed in real and reciprocal space. *Polymer* **2008**, *49*, 643–675.

(37) Urquhart, S. G. *et al.* NEXAFS spectromicroscopy of polymers: overview and quantitative analysis of polyurethane polymers. *J. Electron Spectros. Relat. Phenomena* **1999**, *100*, 119–135.

(38) Collins, B. A., and Ade, H. Quantitative compositional analysis of organic thin films using transmission NEXAFS spectroscopy in an X-ray microscope. *J. Electron Spectros. Relat. Phenomena* **2012**, *185*, 119–128.

(39) Marley, P. M. *et al.* Charge Disproportionation and voltage-induced metal-insulator transitions evidenced in β-$Pb_xV_2O_5$ nanowires. *Adv. Funct. Mater.* **2013**, *23*, 153–160.

(40) Marley, P. M. *et al.* Electronic phase transitions of δ-$Ag_xV_2O_5$ nanowires: interplay between geometric and electronic structure. *J. Phys. Chem. C* **2014**, *36*, 21235-21243.

(41) Korotin, M. A.; Anisimov, V. I.; Saha-Dasgupta, T.; and Dasgupta, I. Electronic structure and exchange interactions of the ladder vanadates CaV_2O_5 and

MgV_2O_5. *J. Phys. Condens. Matter* **2000**, *12*, 113–124.

(42) Malik, R.; Zhou, F.; and Ceder, G. Kinetics of non-equilibrium lithium incorporation in $LiFePO_4$. *Nat. Mater.* **2011**, *10*, 587–590.

(43) Chueh, W. C. *et al.* Intercalation pathway in many-particle $LiFePO_4$ electrode revealed by nanoscale state-of-charge mapping. *Nano Lett.* **2013**, *13*, 866–872.

(44) Wang, L.; Maxisch, T.; and Ceder, G. Oxidation energies of transition metal oxides within the GGA+U framework. *Phys. Rev. B* **2006**, *73*, 195107:1-6.

(45) Dudarev, S. L.; Botton, G. A.; Savrasov, S. Y.; Humphreys, C. J.; and Sutton, A. P. Electron-energy-loss spectra and the structural stability of nickel oxide: an LSDA+U study. *Phys. Rev. B* **1998**, *57*, 1505–1509.

(46) Zhang, Y. *et al.* Novel V_2O_5/S composite cathode material for the advanced secondary lithium batteries. *Solid State Ionics* **2010**, *181*, 835–838.

(47) Suli, A.; Torok, M. I.; and Hevesi, I. On the capacitance of n-V_2O_5/p-Si heterojunctions. *Thin Solid Films* **1986**, *139*, 233–246.

(48) Wang, Y. *et al.* Synthesis of one-dimensional TiO_2/V_2O_5 branched heterostructures and their visible light photocatalytic activity towards rhodamine B. *Nanotechnology* **2011**, *22*, 225702:1-8.

(49) Chakrabarti, A. *et al.* Geometric and electronic structure of vanadium pentoxide: A density functional bulk and surface study. *Phys. Rev. B* **1999**, 59, 583–590.

(50) Bhandari, C.; Lambrecht, W. R. L.; and van Schilfgaarde, M. Quasiparticle self-consistent GW calculations of the electronic band structure of bulk and monolayer V_2O_5. *Phys. Rev. B* **2015**, *91*, 125116:1-12.

(51) Smolinski, H. *et al.* NaV_2O_5 as a quarter-filled ladder compound. *Phys. Rev. Lett.* **1998**, *80*, 5164–5167.

(52) Kolczewski, C. and Hermann, K. Ab initio DFT cluster studies of angle-resolved NEXAFS spectra for differently coordinated oxygen at the V_2O_5(010) surface. *Surf. Sci.* **2004**, *552*, 98–110.

(53) De Groot, F. High-resolution X-ray emission and X-ray absorption spectroscopy. *Chem. Rev.* **2001**, *101*, 1779–1808.

(54) Konstantinović, M. J. *et al.* Charge ordering and optical transitions of LiV_2O_5 and NaV_2O_5. *Phys. Rev. B* **2001**, *63*, 121102:1-4.

(55) Valentí, R.; Saha-Dasgupta, T.; Alvarez, J. V.; Požgajčić, K.; and Gros, C. Modeling the electronic behavior of γ-LiV_2O_5: a microscopic study. *Phys. Rev. Lett.* **2001**, *86*, 5381–5384.

(56) Ding, H. *et al.* Computational investigation of electron small polarons in α-MoO_3. *J. Phys. Chem. C* **2014**, *118*, 15565–15572.

(57) Maxisch, T.; Zhou, F.; and Ceder, G. Ab initio study of the migration of small polarons in olivine Li_xFePO_4 and their association with lithium ions and vacancies. *Phys. Rev. B* **2006**, *73*, 104301:1-6.

(58) Zhou, B.; Shi, H.; Cao, R.; Zhang, X.; and Jiang, Z. Theoretical study on the initial stage of magnesium battery based on V_2O_5 cathode. *Phys. Chem. Chem. Phys.* **2014**, *16*, 18578–18585.

(59) Zhou, F.; Marianetti, C. A.; Cococcioni, M.; Morgan, D.; and Ceder, G. Phase separation in Li_xFePO_4 induced by correlation effects. *Phys. Rev. B* **2004**, *69*,

201101:1-4.

(60) Kohn, W. and Sham, L. J. Self-consistent equations including exchange and correlation effects. *Phys. Rev.* **1965**, *140*, A1133–A1138.

(61) Hohenberg, P. and Kohn, W. Inhomogeneous electron gas. *Phys. Rev.* **1964**, *136*, B864–B871.

(62) Kresse, G. and Furthmüller, J. Efficiency of ab-initio total energy calculations for metals and semiconductors using a plane-wave basis set. *Comput. Mater. Sci.* **1996**, *6*, 15–50.

(63) Perdew, J. P.; Burke, K.; and Ernzerhof, M. Generalized gradient approximation made simple. *Phys. Rev. Lett.* **1996**, 77, 3865–3868. Errata: **1997**, *78*, 1396.

(64) Blöchl, P. E. Projector augmented-wave method. *Phys. Rev. B* **1994**, *50*, 17953–17979.

(65) Kresse, G. From ultrasoft pseudopotentials to the projector augmented-wave method. *Phys. Rev. B* **1999**, *59*, 1758–1775.

(66) Bučko, T.; Lebègue, S.; Hafner, J.; and Ángyán, J. G. Tkatchenko-Scheffler van der Waals correction method with and without self-consistent screening applied to solids. *Phys. Rev. B - Condens. Matter Mater. Phys.* **2013**, *87*, 1–15.

(67) Sheppard, D.; Terrell, R.; and Henkelman, G. Optimization methods for finding minimum energy paths. *J. Chem. Phys.* **2008**, *128*, 1–10.

(68) Liu, M. *et al.* Spinel compounds as multivalent battery cathodes : a systematic evaluation based on ab initio calculations. *Energy Environ. Sci.* **2015**, *8*, 964–974.

CHAPTER IV

STRIPING MODULATIONS AND STRAIN GRADIENTS WITHIN INDIVIDUAL PARTICLES OF A CATHODE MATERIAL UPON LITHIATION*

IV.1 Introduction

The fundamental mechanism of operation of a Li-ion battery involves the reversible migration of Li ions between an anode and a cathode, typically solid-state materials that provide a large difference in the chemical potential of inserted Li-ions.[1–3] Electrode materials are most often porous particulate networks bound together within a conductive matrix. Insertion of Li-ions within electrode materials can occur with continuous compositional modulation stabilizing a solid-solution across a broad range of stoichiometries,[4,5] or alternatively, involve one or more discontinuous phase transformations.[6–10] The insertion and extraction of Li-ions is inevitably accompanied by an alteration of lattice parameters and change of volume, which has substantial consequences for retention of the mechanical integrity of the electrodes.[11–14] The progressive deterioration of the accessible capacity of electrodes upon prolonged cycling is a major impediment to the broader utilization of intercalation batteries in large-area formats. Such deterioration appears to derive in some measure from inhomogeneous strain that causes mechanical pulverization of the electrode particles and results in loss of conduction pathways across the particulate network.[15,16] Delineating multiscale strain and compositional inhomogeneities in electrode materials has thus emerged as an urgent

---

*Reproduced with permission from De Jesus, L. R.; Stein, P.; Andrews, J. L.; Luo, Y.; Xu, B.-X.; Banerjee, S. Striping Modulations and Strain Gradients within Individual Particles of a Cathode Material upon Lithiation. *Mater. Horizons* **2018**, *5,* 486-498. Reproduced with permission from the Royal Society of Chemistry.

imperative but is not readily accessible given the intrinsic limitations of most local structure probes although coherent diffraction imaging, Raman microprobe analysis, neutron radiography, *in-situ* powder X-ray diffraction, and high-resolution electron microscopy methods have each provided insight into aspects of intercalation phenomena at specific length scales.[15,17–26] In this work, we demonstrate that principal component analysis of hyperspectral soft-X-ray scanning transmission X-ray microscopy (STXM) data allows for the "standard-free" delineation of local state of charge in individual V_2O_5 particles as well as ensembles of particles upon Li-ion intercalation. The compositional profiles are furthermore converted to strain maps, thereby providing a means of elucidating local inhomogeneities in stress and strain at phase boundaries.

It is increasingly apparent that the progression of intercalation-induced structural transformations within a matrix of particles is determined by highly localized intercalation phenomena rather than the global voltage profile.[27–31] The specific spatiodynamic propagation of phase transformations depends on the atomistic diffusion pathways defined by the crystal structure of the electrode material, variations in the surface state of the particle, the relative positioning of particles with respect to the current collector, desolvation reactions at the electrolyte interface, and the dynamics of lithiation of adjacent particles.[17,27–29,31–34] Such inhomogeneities have profound consequences for determining the proportion of actively intercalating electrode materials, define local "hot-spots" wherein the current is greatly amplified during charge/discharge processes, and consequently dictate localized energy dissipation profiles.[29,35,36] From the perspective of coupling of electrochemistry and mechanics,

phase inhomogeneities give rise to substantial stress at interfaces and such local stresses can indeed be large enough to induce fracture and electrode pulverization.[11,12,14,37–40] Several approaches have been developed as remedies to this problem ranging from the synthesis and development of smart template anode materials,[41–44] the synthesis of dichalcogenide/anode composites,[45] and the preparation of anode/carbonaceous-nanomaterial composites,[46–49] in order to mitigate of deterioration of the active anode material.

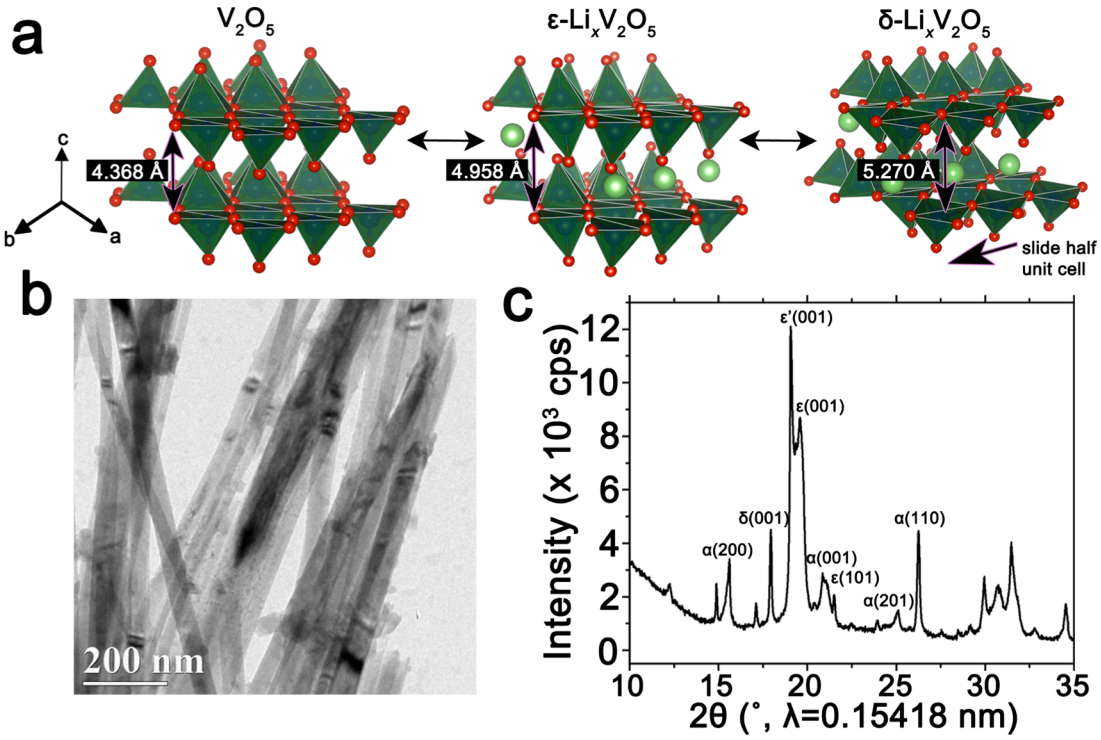

Figure IV.1. Intercalation-induced phase transformations in V_2O_5. (a) Atomic structure renditions of orthorhombic V_2O_5 and the ε- and δ-phases of $Li_xV_2O_5$. (b) Transmission electron microscopy (TEM) image of an ensemble of $Li_xV_2O_5$ nanowires after chemical lithiation. (c) Powder X-ray diffraction (XRD) pattern depicting the phase coexistence of several phases of $Li_xV_2O_5$ upon chemical lithiation of V_2O_5 nanowires by immersion in a 4:1 solution of *n*-butyllithium in hexanes for 15 min (an average composition of $Li_{0.30\pm0.08}V_2O_5$ is deduced based on ICP-MS analysis).

Elucidating compositional and phase inhomogeneities across electrodes is a considerable challenge since it requires examination not just of morphological variations but necessitates high-resolution mapping of chemical and structural speciation. Indeed, coherent diffraction imaging methods capture structural distortions but since they are limited to probing variations of the lattice constant do not directly map the state of charge or chemical composition. Hyperspectral X-ray imaging has emerged as a valuable tool for this purpose and allows for simultaneous examination of variances in atomistic and electronic structure.[29,30,32,50,51] In scanning transmission X-ray microscopy (STXM), raster scanned transmission images are acquired across a range of soft X-ray energies, allowing for evaluation of heterogeneities based on acquisition of an element-specific X-ray absorption near-edge structure spectrum at every pixel. X-ray microscopy has contributed to evaluation of intercalation mechanisms and hysteresis in $LiFePO_4$;[29,51–53] polaron formation and phase separation in $Li_xV_2O_5$ particles;[30,34,50,54] and spatial distribution of discharged products in Li-O batteries.[55] In recent work, Weker and collaborators have visualized the formation of cracks upon lithiation of Ge particles using *operando* transmission X-ray microscopy.[38] Statistical deconvolution of hyperspectral STXM data using methods such as principal component analysis (PCA)[56–58] can provide a powerful means to map chemical speciation with high spatial resolution but have not been hitherto used for mapping electronic-structure, compositional, or phase profiles of electrode materials. PCA provides a means to orthogonalize the hyperspectral dataset to eigenspectra and allows for mapping of discrete chemical components without requiring *a priori* knowledge of standard spectra, which oftentimes

are unavailable for intercalated phases. Herein, we demonstrate the use of PCA to evaluate electronic structure and phase inhomogeneities across nanowires of lithiated V_2O_5 based on STXM imaging at the V L- and O K-edges. We further demonstrate a method to develop compositional maps and to subsequently render such maps as stress and strain profiles across the nanowires. The methods demonstrated here provide a means to elucidate the spatial variances in chemical and phase speciation as well as strain generated as a result of intercalation-induced phase transformations. The multiscale evaluation of compositional and strain inhomogeneities provides mechanistic insight into the lithiation process and suggests the complex evolution of multiphasic domains within individual nanowires involving considerable differences between the core and the surface and compositional striping modulations along the surface contours of the nanowires.

IV.2 Results and Discussion

IV.2.1 Intercalation-Induced Structural Transformations upon Chemical Lithiation of a Cluster of V_2O_5 Wires

The orthorhombic phase of vanadium pentoxide (V_2O_5) depicted in Figure IV.1a is a canonical intercalation host with an abundance of interstitial sites and a readily accessible redox couple that allows for charged ionic species to be accommodated with accompanying reduction of vanadium sites.[59–61] Li-ion insertion within V_2O_5 initiates a series of phase transformations that bring about substantial structural distortions as depicted in Figure IV.1a.[60–63] Initial lithiation results in transformation to a slightly distorted α-$Li_xV_2O_5$ phase, which is stabilized within a concentration range of $x < 0.1$ in

$Li_xV_2O_5$. Upon increasing incorporation of Li-ions, ε-$Li_xV_2O_5$ is stabilized in the concentration range between $0.3 < x < 0.85$ (an incommensurate ε'-phase can be distinguished above $x > 0.53$); this structure is characterized by pronounced puckering of the apical oxygens as a result of electrostatic interactions with the inserted Li-ions as well as an expansion of the interlayer spacing in order to accommodate the increased concentrations of Li-ions. With further insertion of Li-ions, in the range $0.88 < x < 1.0$, δ-$Li_xV_2O_5$ is stabilized with a highly puckered structure characterized by the layers sliding by half a unit cell length along the *b* direction. Increasing the Li-ion concentration still further, beyond $x > 1$, brings about two irreversible phase transformations to highly distorted γ and ω phases. Herein, we focus on the reversible regime of Li-ion incorporation where structural modifications are anisotropic but less pronounced than upon stabilization of the γ- and ω-phases.[8] Previous STXM mapping results showed surprising phase segregation and intercalation gradients within individual nanowires of chemically lithiated V_2O_5.[50] Based on spectroscopic studies of electronic structure and density functional theory modeling, phase heterogeneities in this system have been attributed to two primary origins: (i) stage-ordering phenomena, *i.e.*, the preferential insertion of Li-ions into an already expanded layer;[10,64] and (ii) the formation of small polarons, which correspond to the coupling of an electron in the V_2O_5 framework with a local structural distortion.[50,54] Given the distinctive spectroscopic signatures of different $Li_xV_2O_5$ phases[50] at V L and O K-edges, arising from modifications to the electronic structure of V_2O_5 induced by lithiation, STXM is expected to be an effective probe not just of individual nanowires but ensembles of

particles where heterogeneities are a result of multiscale intercalation gradients.[34] Figure IV.1b depicts a transmission electron microscopy (TEM) image of a $Li_xV_2O_5$ nanowires prepared by chemical lithiation of hydrothermally grown V_2O_5 nanowires in *n*-butyllithium as per:[6,65]

$$V_2O_5 + xC_4H_9Li \rightarrow Li_xV_2O_5 + \tfrac{x}{2}C_8H_{18}(g) \quad \text{(EQUATION IV.1)}$$

Details of the synthesis and chemical lithiation of V_2O_5 nanowires are provided in the Methods section.[6,50] Chemical lithiation eliminates the directionality inherent in electrochemical lithiation experiments, allows for exposure to a globally invariant Li-ion flux, and furthermore can be performed without use of a binder. As such, it is a useful model for electrode processes and allows for examination of fundamental mechanisms underpinning intercalation phenomena. The powder X-ray diffraction (XRD) pattern in Figure IV.1c corresponds to V_2O_5 nanowires subject to chemical lithiation with a large molar excess of *n*-butyllithium for 15 min (an average composition of $Li_{0.30\pm0.08}V_2O_5$ is deduced based on ICP-MS analysis); considerable local phase-coexistence and heterogeneity is discernible with reflections from α-, ε-, ε'-, and δ-phases, as indexed in the pattern.[6,66–68] The performance of V_2O_5 as a cathode material is reflected in the first discharge cycle (Figure A.11) with a capacity of 355 $mAhg^{-1}$ at a constant 0.2 C rate. The transformation between the lithiated phases of V_2O_5 can be observed as plateaus at 3.4, 3.2, and 2.3 V for α–ε, ε–δ, and δ–γ phases, respectively, reflecting the sequence of transformations shown in Figure IV.1a. Transformation to the γ-phase is irreversible and further cycling retains the distorted γ' structure.

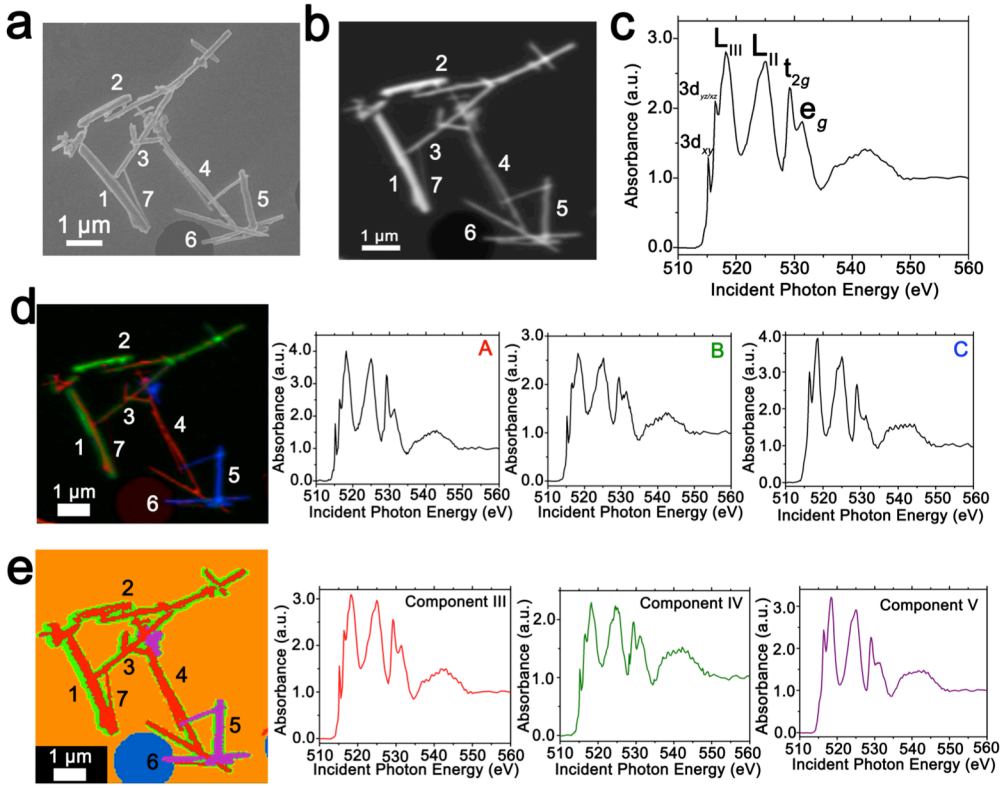

Figure IV.2. Mapping phase inhomogeneities using PCA and ROI deconvolution of hyperspectral STXM data. (a) Scanning electron microscopy image depicting the morphological features of a collection of V_2O_5 nanowires further examined by STXM. (b) Integrated STXM image acquired across the V L- and O K-edges (508 to 560 eV) for a cluster of V_2O_5 nanowires chemically lithiated for 15 min as described in the Methods section (resulting in an average composition of $Li_{0.30\pm0.08}V_2O_5$ based on ICP-MS analysis). (c) An integrated V L- and O K-edge X-ray absorption spectrum acquired for the entire region. Two distinct methods have been used to deconvolute the spectra into components that are mapped across the image. (d) Three spectral components denoted as **A—C** are identified in distinct regions and the spectral stacks are deconvoluted into graded combinations of the three components. The image depicts an intensity map of the three components with increasing extent of lithiation from **A—C**. (e) PCA is used to deconvolute the hyperspectral data into three discrete eigenspectra, denoted as components **III—V** (components **I** and **II** correspond to the background), and the intensities of the eigenspectra are plotted at each pixel. Several nanowires are delineated by numbers to facilitate discussion.

IV.2.2 Elucidation of Compositional Inhomogeneities in $Li_xV_2O_5$ by Singular Value Decomposition (SVD) and PCA Analysis of STXM Images

In order to spatially resolve phase inhomogeneities observed in ensemble XRD measurements, a cluster of interconnected chemically lithiated V_2O_5 nanowires has been examined using scanning electron and scanning transmission X-ray microscopy as shown in Figure IV.2. Figure IV.2a depicts a high-resolution scanning electron microscopy image, whereas Figure IV.2b shows the corresponding integrated STXM image constructed by scanning across the V L- and O K-edges from 508 to 560 eV. Figure IV.2c depicts the integrated X-ray absorption spectrum acquired for these nanowires. X-ray absorption spectroscopy involves the excitation of core electrons to unoccupied and partially occupied states, and thus principally maps the atom-projected unoccupied density of states of the excited solid.[30,69,70] Rigorous spectral assignments are now available for V L-edge and O K-edge absorption features of V_2O_5 based on first-principles simulations of excited state spectra and angle-resolved X-ray absorption spectroscopy measurements.[50,71–73] The V L-edge spectrum of V_2O_5 comprises V L_{III} and V L_{II} absorption features, corresponding to transitions from V $2p_{3/2} \rightarrow$ V $3d$ (*ca.* 518 eV) and V $2p_{1/2} \rightarrow$ V $3d$ (*ca.* 525 eV) states, respectively;[71,72] these features are separated by a spin-orbit splitting of *ca.* 7 eV. As a result of the operation of Coster—Kronig Auger decay processes, the V L_{II} absorption is subject to considerable spectral broadening and is consequently less informative as a probe of local electronic structure. In contrast, the V L_{III} absorption has well-resolved fine structure corresponding to transitions from singlet V $2p^6 3d^0$ to V $2p^5 3d^1$ states split by crystal field and multiplet effects.[50,72,74] The

first two sharp features correspond to distinct transitions from V 2p states to states of fairly "pure" V $3d_{xy}$ (*ca*. 515.6 eV) and V $3d_{xz/yz}$ (*ca*. 516.8 eV) character as labelled in Figure IV.2c. The O K-edge corresponds to transitions from O 1*s* states to states with O 2*p* character. As a result of the substantial hybridization between the O 2*p* and V 3*d* derived states, two distinct features can be resolved, reflecting the distorted octahedral crystal field splitting of the V 3*d*-derived states (denoted as t_{2g} and e_g in Fig. IV.2c). The features correspond to transitions of O 1*s* electrons to (i) O $2p_x$ and $2p_y$ states engaged in π interactions with the V 3d t_{2g} states (529.7 eV); and (ii) O $2p_x$ and $2p_y$ states engaged in direct σ interactions with V $3d_{x^2-y^2}$ (at *ca.* 531.6 eV), and $2p_z$ states engaged in σ-interactions with V $3d_{z^2}$ states (at *ca*. 533.1 eV).

The intercalation of Li-ions within V_2O_5 is coupled with redox chemistry at the vanadium sites, specifically the local reduction of V^{5+} sites to V^{4+} sites; the added electron occupies the lowest-lying states at the bottom of the conduction band, which in the case of V_2O_5 corresponds to a split-off conduction band that has primarily V $3d_{xy}$ character.[71–73,75] Li-ion insertion thus results in a significant diminution, or even disappearance, of the V L_{III} absorption feature at 515.6 eV as a result of Pauli blocking (owing to filling of the V $3d_{xy}$ state). Furthermore, the polarization, lattice distortion, and lifting of spin degeneracy in the V $3d^1$ system strongly modifies the ratio of the t_{2g} and e_g* features at the O K-edge; the intensity of the t_{2g} feature is gradually diminished as a function of increasing Li-ion concentration.[50] These two spectral modifications, which are directly correlated to Li-ion content, are of particular significance for statistical deconvolution of hyperspectral stacks.

Two distinct methods have been used to map spatial inhomogeneities. In the first case, based on examining integrated spectra across different regions of the image and given prior knowledge of evolution of V L_{III} and O K-edge X-ray absorption spectra with increasing Li-ion content,[30,34,50,54] three different components (A—C) are identified as plotted in Figure IV.2d. Notably, these components are spectra integrated within discrete regions of the image. Next, the spectral data at each pixel across the entire image is deconvoluted into a combination of the three component spectra using SVD. Spatial maps are then constructed reflecting the relative weights of each of the three components at each pixel as depicted in the left panel of Figure IV.2d. The components herein correspond to spectra characteristic of specific regions of the image. However, they do not represent "pure" spectra of individual phases and furthermore are based on approximations of spectral signatures of potential species used to facilitate selection.

Figure IV.3 maps the intensity of each of the three components individually across the region of interest. Components A—C depict stark differences with respect to the intensity of the transition to the V $3d_{xy}$ final state at the V L_{III} edge and the ratio between t_{2g} and e_g* components at the O K-edge, indicating a successive increase of lithiation from A—C (Fig. IV.2d). As a first finding, mapping of the spectral components clearly delineates that the ensemble XAS spectrum plotted in Figure IV.2c does not accurately remarkable spatial inhomogeneity of lithiation (state-of-charge) prevalent across this cluster of nanowires. Component A is assigned to a relatively low-Li-content α-phase, Component B represents the intermediate Li-content ε-phase, whereas Component C represents a substantially higher degree of lithiation. The almost

complete loss of the V $3d_{xy}$ absorption feature at 515.6 eV and the appearance of a strong $3d_{xz/yz}$ absorption feature at 516.8 eV are suggestive of a more substantial rearrangement of the crystal structure to accommodate a higher concentration of Li-ions; these spectral features are attributed to the substantially more distorted δ-$Li_xV_2O_5$ phase characterized by sliding of the layers along the *b* direction.

Seven individual nanowires have been labelled *1—7* as depicted in the images. Based on Figures IV.2 and IV.3, the nanowires on the top and left are relatively less lithiated, whereas the nanowires on the bottom right of the image are relatively more lithiated. No clear correlation is observed between the nanowire dimensions and the extent of lithiation. For instance, nanowire labelled *5* is much more extensively lithiated as compared to the nanowire labelled *7* even though Figure IV.2a shows that it is much thicker. Considering nanowires *1—3*, the SEM image suggests that these are individual faceted nanowires; Figures IV.2d and IV.3 suggest that these nanowires show considerable compositional variations, domain formation, and the coexistence of both Components A and B within each of the nanowires. Similarly, nanowire *6* shows the coexistence of Components A and C. While component B, which represents a relatively greater extent of lithiation is generally more predominant at the edges of the nanowires and along the nanowires at the apex of the region of interest, an alternating interleaved domain structure is observed suggestive of the stabilization of a complex domain structure upon cation insertion. Figure A.12 depicts high-resolution SEM images of various segments of the cluster of nanowires shown in Figure IV.2a. A consistent morphology is retained along the length of individual wires suggesting that the observed

modulations in the intensities of spectral components observed in Figures IV.2 and IV.3 result from compositional and not topographical variations. Figures IV.3d—f depicts an alternation of intensity along the length of select nanowires for each of the three components. Figure IV.3d indicates stripes of Li-poor Component A in nanowire *2*, whereas Figure IV.3f depicts stripes of the Li-rich Component C along nanowire *1*. Such stripe formation observed here is likely a result of the spinodal decomposition to Li-rich and Li-poor domains at the particle boundaries.[76,77] Intercalation of Li-ions within thin wires occurs faster laterally (along the edges) rather than transversally (through the nanowire) due to sluggish diffusion of ions; this results in pronounced compositional "stripes". Striping resulting from compositional heterogeneity has been indirectly evidenced in coherent diffraction imaging based on mapping of lattice constants and has been predicted by numerous phase field models.[15,31,65] However, to the best of our knowledge the images here represent the first direct evidence of compositional modulation along the length of Li-ion intercalated nanowires. Indeed, similar behaviour with compositional heterogeneities and modulations is observed in electrochemically lithiated samples extracted from samples discharged at 2.75 V in a coin cell configuration (Figure A.13). In the imaged ensemble of nanowires, core–shell behaviour and the formation of stripes is observed along the length of the nanowires.

Next, we examine an alternative "standard-free" treatment of the hyperspectral STXM data. PCA methods can be applied without *a priori* knowledge of spectral components and yield eigenspectra that maximize the variances within the spectral data integrated across the sample. Figure IV.2e depicts the three components, denoted as

III—V derived from such analysis. Components I and II correspond to the background. PCA analysis clearly distinguishes the background signal from a hole (depicted in blue in Fig. IV.2e) and the signal of the underlying silicon nitride grid (depicted in orange).

Utilizing an angle distance cutoff or normalized scalar to specify a radius below which pixels are not included mitigates differences arising primarily from thickness variations.[58] Figure A.14 depicts spatial maps of the principal components reflecting their weights at each pixel; Table A.1 summarizes the cluster weight percentage as evaluated in each of the dimensions. Figure A.15 depicts the separation of the pixels

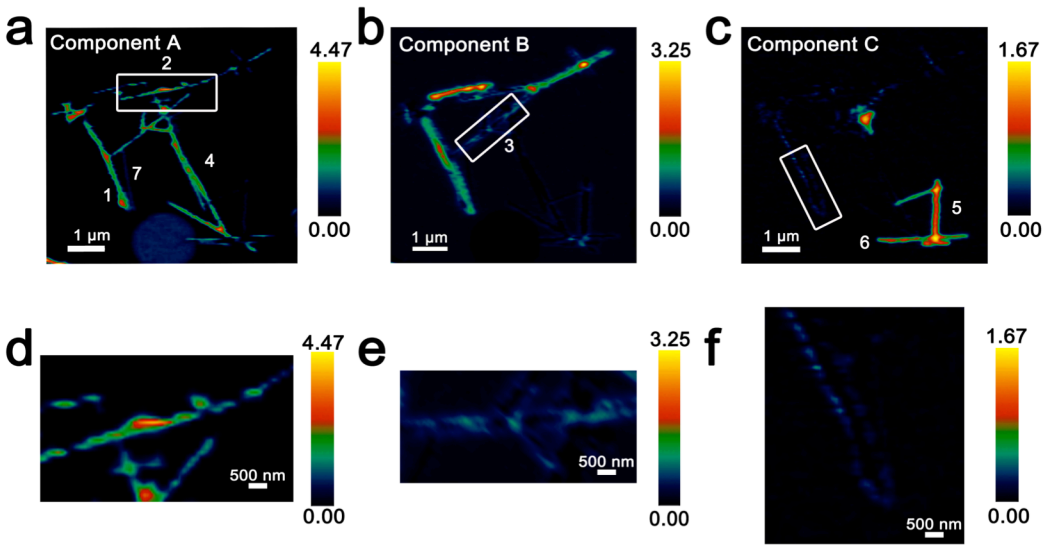

Figure IV.3. Intensity maps derived from region-of-interest singular value decomposition analysis of an ensemble of V_2O_5 nanowires lithiated for 15 min (resulting in an average composition of $Li_{0.30\pm0.08}V_2O_5$ based on ICP-MS analysis). a–c) Intensity maps depict the localization of the spectral signatures of components A—C in Figure IV.2d. Component A corresponds to the lowest extent of lithiation, whereas Component C corresponds to the highest lithaition, as determined by the relative intensity of the $3d_{xy}$ resonance and the t_{2g}:e_g* ratio. d–f) Modulations of spectral intensities within the boxed regions of the upper panels corresponding to the distribution of Li-rich and Li-poor domains within individual nanowires.

along three distinct pairs of component axes. Each pixel is classified (and thus colored) according to its position in the scatter plot, which shows effective separation along the component axes. In contrast to the overlapping coloration of different components in Figure IV.2d, in the PCA map of Figure IV.2e, each pixel is colored to reflect just the majority component. Even though eigenspectra are principally representative of the total spectral variances and do not directly correspond to experimental spectra, their lineshapes embed chemical information. While the single coloration at each pixel does not provide as granular of a compositional map as in Figure IV.2d (and thus modulations are not as clearly observed), they nevertheless delineate distinct compositional (and thus phase) gradients. Based on the intensity of the feature at 515.6 eV corresponding to the transition to the V $3d_{xy}$ state and the relative intensities of the t_{2g} and e_g absorptions at the O K-edge, Component III is a spectrum representative of V_2O_5 with a relatively low degree of lithiation; the higher weighting of this component at the nanowire cores is consistent with the slower lithiation of the core[6] albeit it is clear that as also observed in Figure IV.2d a clear core-shell structure is not established. Similarly, component IV reflects a higher degree of lithiation based on the relatively lower intensity of the V $3d_{xy}$ absorption at the V L-edge and the lower ratio of t_{2g}:e_g* intensities at the O K-edge; this component is weighted substantially at the edges of the nanowires. This component thus is analogous to component B in Figure IV.2d. The distribution of this component is discontinuous along the nanowire surfaces consistent with the compositional modulation noted in Figure IV.3. Remarkably, component V accurately captures the relatively highly lithiated δ-$Li_xV_2O_5$ spectral signature and such nanowires are clearly

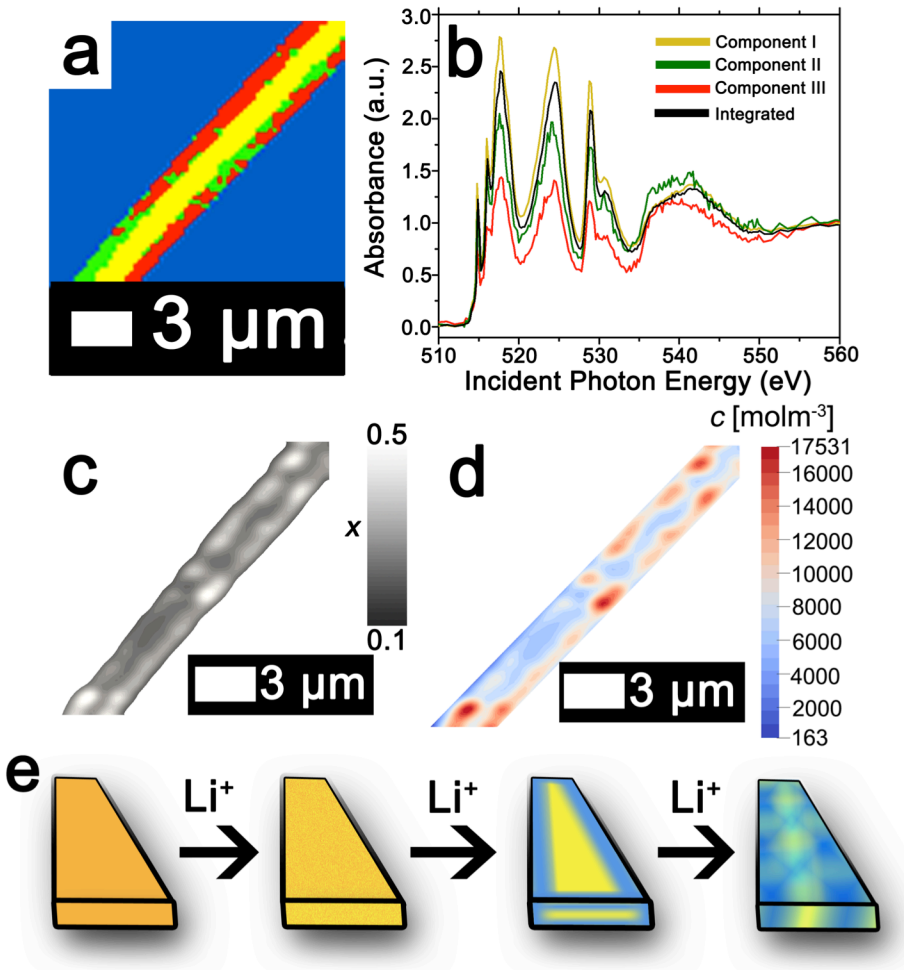

Figure IV.4. Mapping of the composition map onto a concentration distribution from PCA analysis of STXM data. (a) PCA map defining domains with varying extents of lithiation obtained from deconvolution of a STXM hyperspectral image acquired for an individual particle of V_2O_5 chemically lithiated for 1 min (an average composition of $Li_{0.28\pm0.07}V_2O_5$ is deduced based on ICP-MS analysis). (b) Integrated V L- and O K-edge spectrum and eigenspectra obtained from PCA analysis. Component I (yellow) is the least lithiated, followed by component II corresponding to an intermediate extent of lithiation (green), and finally component III, which corresponds to the highest extent of lithiation (the corresponding pixel-weighted scatterplots are plotted in Fig. A.13). (c) Using the nanowire contours, a finite element mesh has been created onto which the composition (x) data have been mapped. (d) Linear transformation of the composition by corresponding average phase concentrations then yields the concentration distribution over the nanowire. (e) Schematic depiction of the progression of Li-intercalation within V_2O_5 to the formation of stripes with Li-poor (yellow) and Li-rich (blue) domains.

distinguishable from the rest of the cluster in the PCA analysis. PCA analysis thus provides a standard-free means of orthogonalizing the STXM dataset and can delineate lithiation gradients and phase segregation in a chemically meaningful manner.

IV.2.3 Generation of Compositional, Stress, and Strain Maps from PCA Analysis of STXM Data

The ability to deconvolute hyperspectral X-ray microscopy data further facilitates the mapping of compositional, stress, and strain profiles across an individual particle. Figure IV.4a depicts the PCA map derived from STXM imaging of an individual particle with a diameter of *ca*. 3 μm upon chemical lithiation for 1 min (an average composition of $Li_{0.28\pm0.07}V_2O_5$ is deduced based on ICP-MS analysis). Figure IV.4b depicts the integrated V L- and O K-edge X-ray absorption spectrum and three eigenspectral components obtained from PCA analysis of the hyperspectral stack. Figure A.16a–c depict the scatter plots illustrating the scores of the spectrum at each pixel with respect to the three different components (the respective component weights are summarized in Table A.2); the selected principal components are seen to allow for effective classification of each of the pixels, which are mapped in Figure IV.4a. Components I—III correspond to increasing levels of lithiation based on the intensity of the V $3d_{xy}$ feature at the V L_{III} edge and the ratio of t_{2g}:e_g* intensities at the O K-edge. Notably, the extent of lithiation is lower as compared to Figure IV.2 given the reduced immersion time here. The components can be attributed to approximate values of Li-ion content based on the intensities of the V $3d_{xy}$ feature and the ratio of t_{2g}:e_g* intensities. The

yellow core is sparsely lithiated whereas the surface indicates modulation of Li-rich and Li-poor domains.

While STXM provides detailed compositional maps of electrode materials,[32,34,50,51] a major constraint is that it is a 2D imaging method whereas in order to obtain stress and strain maps, such as required to evaluate inhomogeneous coherent strain at phase boundaries, the thickness of the sample is required. Indeed, the thickness of the nanowire in Figure IV.4a can be estimated based on a quantitative measurement of the absorption cross-section; Figure A.17 (Supporting Information) indicates that the nanowire (*ca*. 245 nm in diameter) has a uniform thickness of *ca*. 79 nm along the diameter as delineated by the consistent height at two different regions spaced *ca*. 400 nm apart. The concentration of Li-ions (state of charge) in each cluster is furthermore required in order to precisely develop a compositional map; these values can be approximated based on the ratio between the t_{2g}:e_g* absorbances, which serve as a direct probe for the amount of Li intercalation in α-V_2O_5. The weights of the individual clusters (as delineated in Table A.2) provide a means to weight the contribution of the composition-specific components at each pixel, thereby enabling the development of a detailed composition map.

The composition map plotted in Figure IV.4c has been obtained from weighted superposition of the respective pixel-wise intensity data as described in the Methods section. Li-rich and Li-poor domains are clearly evidenced at the edges denoting clear segregation. The concentration map in Figure IV.4d maps the concentration of Li-ions across the particle. Domains demarcated in red denote regions of a locally enhanced ion

concentration reaching 1.75 x 10^4 mol·m^{-3} (x=0.41 in $Li_xV_2O_5$, corresponding to the ε-phase) at the edges of the nanowires, whereas the core is substantially less lithiated with a concentration of *ca.* 6.00 x 10^3 mol·m^{-3} (x=0.15 in $Li_xV_2O_5$, corresponding to the α-phase). Since the lattice parameters of $Li_xV_2O_5$ vary continuously as a function of Li-ion content (in ε-V_2O_5, a=11.420–11.377 Å; b=3.558 –3.570 Å),[78–80] the inhomogeneous compositional profile induces localized lattice mismatch and straining of the active material. Figure IV.4e depicts a schematic of the progression of Li-ion intercalation within V_2O_5 showing core—shell segregation followed by spinodal segregation of Li-poor and Li-rich domains as stripes as observed in Figure IV.4c.

In order to map stress and strain gradients resulting from compositional inhomogeneities, the nanowire geometry has been extracted from this map by the Marching Squares algorithm, yielding the outline curves of the nanowire. These data have been used to generate a planar finite element mesh. The corresponding spatial composition data have been mapped onto its nodes. A finite element simulation of the coupled chemo-mechanical behavior[81] yields stress and strain maps in the Cartesian reference frame. The stress and strain maps have been transformed onto the nanowire-aligned along the xi-eta coordinate system in order to facilitate interpretation. The incurred stress gradients have been mapped in a nanowire-aligned coordinate system, as depicted in Figures IV.5a and b. These maps depict the anisotropic deformation induced by the insertion of Li ions. The stress maps suggest that it is in particular the regions of high heterogeneity that exhibit high levels of stress. Clusters of high local ion concentrations tend to expand isotropically but are hindered by the surrounding material.

This can be observed in Figure IV.5a where the bands of high compressive longitudinal stress σ_ξ with magnitude of *ca*. 305 MPa are correspondent with bands of Li-rich domains (Fig. IV.4d). As illustrated in Figure IV.5c, the material in the outer layers of the nanowire is compressively strained along the longitudinal direction. In contrast, the core of the nanowire is subjected to tensile stresses of around 100 MPa, which is brought about by the expanding Li-rich edges "pulling" at the core of the nanowire. The lateral expansion of the nanowire is comparatively unconstrained, as is demonstrated by the low lateral stresses σ_η depicted in Figure IV.5b. The expansion of the V_2O_5 layers in order to accommodate Li-ions at the edges of the particles is expected to create tensile stresses that further induce significant compressive stress within the nanowire interiors as a result of the anisotropic distortion of the layered structure upon Li-ion intercalation (Fig. IV.1a). The inhomogeneity in direction and magnitude of stress establishes strain gradients across the particle as mapped in Figures IV.5c and d. Indeed, such strain gradients considerably alter intercalation and diffusion in active material,[81,82] and can underpin electromechanical degradation.[39,83] Such degradation can result in fracture of the particle and loss of capacity.[84,85] In contrast, recent studies suggest that tensile strain can induce modulation of electrochemical potentials by *ca*. 40 mV and bring about a doubling of Li-ion diffusion coefficients within V_2O_5.[83] The ability to extract concentration, stress, and strain profiles further renders STXM a valuable probe of intercalation phenomena. The pronounced strain gradients at phase boundaries provide a direct visualization of the implications of compositional inhomogeneities.

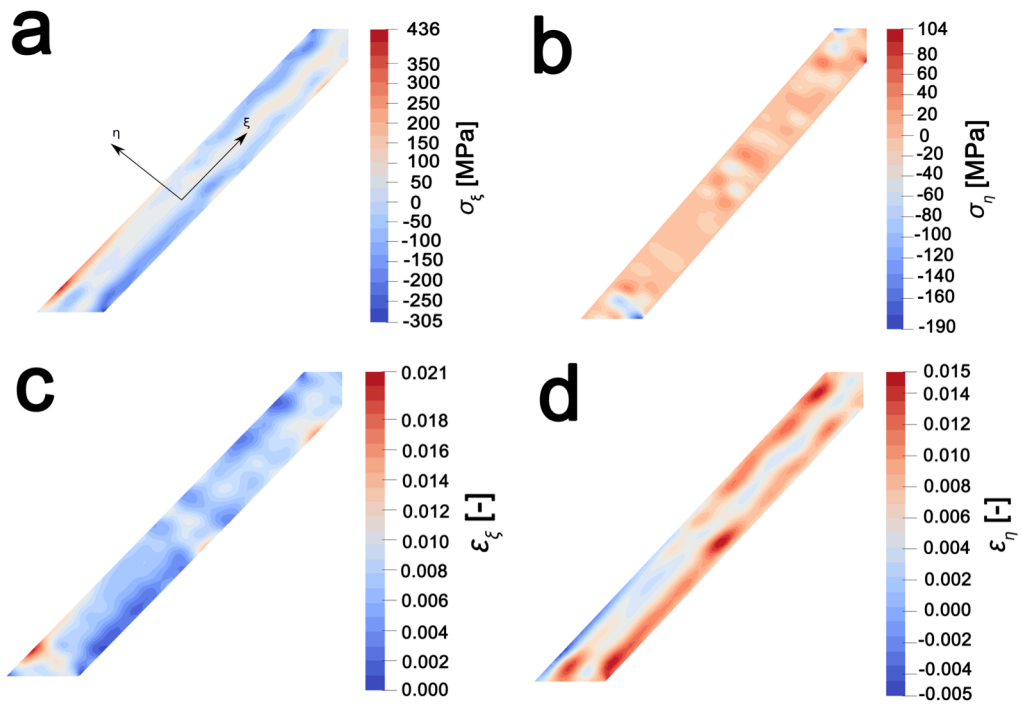

Figure IV.5. Stress and strain profiles derived from PCA maps. (a)–(b) Longitudinal and lateral stress maps, respectively; positive intensities reflect tensile stress, whereas, negative intensities reflect compressive stress. (c)–(d) Longitudinal and lateral strain maps, respectively, indicating inhomogeneous strain profiles resulting from intercalation of Li-ions.

IV.3 Conclusions

In conclusion, the initiation and progression of Li-ion intercalation within electrode materials is dominated by local phenomena and results in considerable inhomogeneity both within individual particles and across ensembles of adjacent particles. STXM serves as an effective element-specific probe of electronic structure, and since electronic structure is greatly modulated by cation intercalation, provides a spatially resolved view of distinct domains stabilized upon lithiation of transition metal oxides. Upon chemical lithiation of V_2O_5 nanowires, longitudinal and lateral domain

formation is evidenced within individual nanowires and is reflective of surface lithiation phenomena as well as compositional striping corresponding to separation of Li-rich and Li-poor domains at particle boundaries. Considerable compositional inhomogeneity is evidenced within an ensemble and appears to reflect selective deep lithiation of specific particles whereas adjacent particles are lithiated to a much lower extent. A principal component analysis treatment of STXM hyperspectral data allows for deconvolution of V L-edge and O K-edge spectra to principal components reflective of different lithiated phases and allows for reconstruction of domain maps without *a priori* knowledge of spectral profiles. Such an analysis allows for elucidation of intercalation gradients within individual nanowires. Mapping compositional and phase inhomogeneities is greatly consequential for determining the actively intercalating regions and localized current profiles. The compositional information gleaned from PCA analysis of STXM data in conjunction with determination of the nanowire thickness based on quantitative evaluation of the X-ray absorption cross-section as well as knowledge of lattice parameters of intercalated phases allows for mapping of stress gradients and strain across an individual particle. The significant disparity between domains subjected to compressive and tensile stress as a result of inhomogeneous lithiation is thought to underpin capacity loss. Mitigating such inhomogeneities requires the development of cathode materials that are able to accommodate Li-ions with less of a structural distortion and that can mitigate polaronic bottlenecks to Li-ion diffusion or structuring of electrodes to facilitate more homogeneous lithiation. Future work will focus on *in-situ* and *in-operando* STXM and ptychography studies of intercalation phenomena within

cathode and anode architectures in realistic device configurations in conjunction with electron microscopy such as to combine the excellent spatial resolution accessible from the latter methods with the energy resolution and high chemical sensitivity of synchrotron-based X-ray imaging.[24,25] Inhomogeneities will further be explored for "beyond Li" energy storage vectors such as multivalent cations.[86]

IV.4 Materials and Methods

IV.4.1 Chemical Lithiation of V_2O_5 Nanowires

Single-crystalline V_2O_5 nanowires were prepared by air oxidation of hydrothermally grown V_3O_7 nanowires as described in previous work.[6] Chemical lithiation of the nanowires was performed within a glove box filled with argon by immersion of powders in a solution of 2.5 M *n*-butyllithium (Sigma-Aldrich) in hexanes diluted to 0.025 M in heptane for a specific time interval (0.025 M of *n*-butyllithium to 0.55 mM of V_2O_5, corresponding to a *ca*. 4:1 molar excess of Li:V_2O_5). The samples were then washed within the glove box with copious amounts of hexanes to remove any unreacted lithium precursor. The recovered powder was allowed to dry under argon ambient.

IV.4.2 Inductively-Coupled Plasma Mass Spectrometry (ICP-MS)

The average Li-ion concentration of the solid lithiated V_2O_5 samples was determined by ICP-MS using a PerkinElmer NexION 300D instrument. Powder samples lithiated for a specific time were dissolved to achieve overall concentrations of 5–7 ppm in a 1 vol.% aqueous solution of HNO_3 solution (15 M).

IV.4.3 Powder X-ray Diffraction

Powder X-ray diffraction (XRD) measurements were performed using a Bruker D8-Focus Bragg−Brentano X-ray powder diffractometer with a Cu Kα radiation source (λ = 0.15418 nm).

IV.4.4 Microscopy Characterization

Transmission electron microscopy (TEM) images were obtained using a JEOL JEM-2010 instrument operated at an accelerating voltage of 200 kV. SEM images were acquired using a JEOL JSM-7500F FE-SEM operated at 2 kV.

STXM data were collected at the spectromicroscopy (SM) beamline 10ID-1 of the Canadian Light Source, Saskatoon, SK. The beamline is equipped with an elliptically polarized undulator source; incident soft X-rays were focused onto the sample of interest using a Fresnel zone-plate, which includes an order-sorting aperture to eliminate undesired diffraction orders. A plane grating monochromator with 500-line mm^{-1} was used for hyperspectral imaging at V L- and O K-edges. A dwell time of 1 ms was used for signal acquisition at each pixel. The image stacks were analyzed using the Principal Components Analysis (PCA) suite developed by Jacobsen and co-workers and aXis2000 (http://unicorn.mcmaster.ca/aXis2000.html).[87] Region of interest (ROI) maps were obtained by a SVD of the image stack and by using as a reference, spectral components identified within different regions of the stack. This procedure yields a set of composition maps where intensities represent the signal strength of each of the selected components. Thickness maps were developed by linearly scaling the V L- and O K-edge stack to a reference spectrum of $Li_xV_2O_5$ (spectrum scaled to a calculated elemental X-

ray absorption spectrum of a 1 nm thick material). Principal component analysis was performed to orthogonalize the data and reduce the noise of the spectral features. The hyperspectral stack was deconvoluted into components representing a linear combination of spectral signatures. The graded contributions of the orthogonalized spectral components at each pixel were subsequently determined, allowing for the construction of maps indicating the relative abundance of each of the orthogonalized components at each pixel within the area of interest.[57,58] Application of this analysis method allows for reconstruction of spatially resolved images from eigenspectra of complex samples without requiring *a priori* knowledge of reference spectra. The angle dependence cutoff was set to the point just before the highest pixel contribution; this substantially mitigates the effects of thickness variations and allows for mapping of variations in chemical signatures.

IV.4.5 Electrochemical Cycling

Galvanostatic cycling of V_2O_5 was carried out in a coin cell configuration against a Li metal anode using a Landt battery testing system (CT2001A) at a 0.2 C rate. The cathode is prepared by casting a mixture of active material (V_2O_5 nanowires), conductive carbon material (C45), and binder (polyvinylidene fluoride) in a 7:2:1 ratio, respectively, on the Al foil current collector. The electrolyte used was a 1.0 M solution of $LiPF_6$ in a (1:1 (*v*/*v*) mixture of diethyl carbonate and ethylene carbonate (Sigma Aldrich).

IV.4.6 Compositional & Strain Maps

Compositional and strain maps were generated by defining meshes using the PCA separated component maps. The starting points for the mesh generation procedure

are the maps shown in Figure A.18. These normalized intensities in images space represent intensities x_i; x=0.2 (a,d); x=0.4 (b,e); and x=0.5 (c,f) corresponding to various phases of $Li_xV_2O_5$. First, these images were subjected to a Gaussian filter to remove noise; subsequently, superposition of the pixel intensities, as weighted by the corresponding stoichiometric fraction x_i, yields a composition map in image space as shown in Figure A.19a. This image exhibits a relatively low resolution of 75 x 65 pixels. A continuous representation can be achieved by bilinear interpolation of the pixel data, resulting in the smooth composition map shown in Figure A.19b. In order to extract the nanowire geometry from image space, the Marching Square algorithm was applied with a user-defined threshold for the stoichiometric fraction x. The resulting nanowire outline curves, shown in Figure A.19b, were then used as input for the Finite Element mesh generator GMSH. The local stoichiometric fraction was mapped onto the nodes of the planar triangle mesh, was and scaled by the ion concentration (state-of-charge). The resulting finite element model was used to solve for the distribution of stresses and strains using the software package FEAP. To that end, linear isotropic material behavior was assumed together with a chemical eigenstrain model:

$$\sigma_{ij} = C_{ijkl}\varepsilon^{el}_{kl}, \varepsilon^{el}_{kl} = \varepsilon_{kl} - \frac{\Omega c}{3}\delta_{kl} \quad \text{(EQUATION IV.2)}$$

wherein σ_{ij} denotes the components of the symmetric second-order Cauchy stress tensor, C_{ijkl} are the components of the fourth-order elasticity tensor describing the elastic material properties, Ω is the partial molar volume of $Li_xV_2O_5$ under insertion of Li, and δ_{kl} are the components of the unit tensor. ε_{kl} are the strain components, more exactly, the components of the symmetric second-order infinitesimal strain tensor defined by

$$\varepsilon_{ij} = \frac{1}{2}(u_{i,j} + u_{j,i}) \quad \text{(EQUATION IV.3)}$$

where u_i denotes the components of the displacement vector and where $(\cdot)_{,i}$ denotes a partial derivative with respect to the i-th spatial coordinate. The ε_{kl}^{el} is the elastic strain, which is correlated directly to the stress. For the finite element simulations, the composition (state-of-charge) as determined by the image conversion process was used as a constant field causing eigenstrain according to Eq. IV.3. For simplicity, constant concentration-independent elastic parameters and a constant partial molar volume was approximated. In particular, a Young's modulus of E = 43 GPa, a Poisson's ration of v=0.3, and a partial molar volume of $\Omega = 2.415 \times 10^{-6}$ m^3mol^{-1} were used in the finite element simulations. Extension of the model to concentration-dependent parameters is, however, straightforward and will be implemented in future work when such constants become available for lithiated V_2O_5 phases. In order to exclude rigid-body displacements, the displacement components were constrained normal to the nanowire edges along the image borders. The resulting stresses and strains were finally transformed by standard techniques from the Cartesian coordinate frame to a nanowire-aligned planar coordinate system.

IV.5 References

(1) Etacheri, V.; Marom, R.; Elazari, R.; Salitra, G.; and Aurbach, D. Challenges in the development of advanced li-ion batteries: a review. *Energy Environ. Sci.* **2011**, *4*, 3243–3262.

(2) Goodenough, J. B. Rechargeable batteries: challenges old and new. *J. Solid State Electrochem.* **2012**, *16*, 2019–2029.

(3) Tarascon, J.-M.; Armand, M. Issues and challenges facing rechargeable lithium batteries. *Nature* **2001**, *414*, 359–367.

(4) Bai, P.; Cogswell, D. A.; and Bazant, M. Z. Suppression of phase separation in lifepo$_4$ nanoparticles during battery discharge. *Nano Lett.* **2011**, *11*, 4890–4896.

(5) Zeng, D.; Cabana, J.; Bréger, J.; Yoon, W.-S.; and Grey, C. P. Cation ordering in Li[$Ni_xMn_xCo_{(1-2x)}$]O_2-layered cathode materials: a nuclear magnetic resonance (NMR), pair distribution function, x-ray absorption spectroscopy, and electrochemical study. *Chem. Mater.* **2007**, *19*, 6277–6289.

(6) Horrocks, G. A.; Likely, M. F.; Velazquez, J. M.; and Banerjee, S. Finite size effects on the structural progression induced by lithiation of V_2O_5: a combined diffraction and raman spectroscopy study. *J. Mater. Chem. A* **2013**, *1*, 15265–15277.

(7) Laffont, L.; Delacourt, C.; Gibot, P.; Wu, M. Y.; Kooyman, P.; Masquelier, C.; and Tarascon, J. M. Study of the $LiFePO_4/FePO_4$ two-phase system by high-resolution electron energy loss spectroscopy. *Chem. Mater.* **2006**, *18*, 5520–5529.

(8) Delmas, C.; Maccario, M.; Croguennec, L.; Le Cras, F.; and Weill, F. Lithium deintercalation in lifepo$_4$ nanoparticles via a domino-cascade model. *Nat Mater* **2008**, *7*, 665–671.

(9) Brunetti, G.; Robert, D.; Bayle-Guillemaud, P.; Rouvière, J. L.; Rauch, E. F.; Martin, J. F.; Colin, J. F.; Bertin, F.; and Cayron, C. Confirmation of the domino-cascade model by $LiFePO_4/FePO_4$ precession electron diffraction. *Chem. Mater.*

2011, *23*, 4515–4524.

(10) Guo, Y.; Smith, R. B.; Yu, Z.; Efetov, D. K.; Wang, J.; Kim, P.; Bazant, M. Z.; and Brus, L. E. Li intercalation into graphite: direct optical imaging and cahn-hilliard reaction dynamics. *J. Phys. Chem. Lett.* **2016**, *7*, 2151–2156.

(11) Chen, C.-F.; Barai, P.; and Mukherjee, P. P. Diffusion induced damage and impedance response in lithium-ion battery electrodes. *J. Electrochem. Soc.* **2014**, *161*, A2138–A2152.

(12) Woodford, W. H.; Chiang, Y.-M.; and Carter, W. C. "Electrochemical Shock" of intercalation electrodes: a fracture mechanics analysis. *J. Electrochem. Soc.* **2010**, *157*, A1052–A1059.

(13) Cheng, Y.-T. and Verbrugge, M. W. Application of Hasselman's crack propagation model to insertion electrodes. *Electrochem. Solid-State Lett.* **2010**, *13*, A128–A131.

(14) Chen, C.-F. and Mukherjee, P. P. Probing the morphological influence on solid electrolyte interphase and impedance response in intercalation electrodes. *Phys. Chem. Chem. Phys.* **2015**, *17*, 9812–9827.

(15) Ulvestad, A.; Singer, A.; Cho, H. M.; Clark, J. N.; Harder, R.; Maser, J.; Meng, Y. S.; and Shpyrko, O. G. Single particle nanomechanics in operando batteries via lensless strain mapping. *Nano Lett.* **2014**, *14*, 5123–5127.

(16) Whittingham, M. S. Ultimate limits to intercalation reactions for lithium batteries. *Chem. Rev.* **2014**, *114*, 11414–11443.

(17) Nanda, J.; Remillard, J.; O'Neill, A.; Bernardi, D.; Ro, T.; Nietering, K. E.; Go,

J. Y.; and Miller, T. J. Local state-of-charge mapping of lithium-ion battery electrodes. *Adv. Funct. Mater.* **2011**, *21*, 3282–3290.

(18) Ulvestad, A.; Singer, A.; Clark, J. N.; Cho, H. M.; Kim, J. W.; Harder, R.; Maser, J.; Meng, Y. S.; and Shpyrko, O. G. Topological defect dynamics in operando battery nanoparticles. *Science.* **2015**, *348*, 1344–1347.

(19) Zhou, H.; An, K.; Allu, S.; Pannala, S.; Li, J.; Bilheux, H. Z.; Martha, S. K.; and Nanda, J. Probing multiscale transport and inhomogeneity in a lithium-ion pouch cell using in situ neutron methods. *ACS Energy Lett.* **2016**, *1*, 981–986.

(20) Yuan, Y.; Amine, K.; Lu, J.; and Shahbazian-Yassar, R. Understanding materials challenges for rechargeable ion batteries with in situ transmission electron microscopy. *Nat. Commun.* **2017**, *8*, 15806.

(21) Li, B.; Li, X.; Zai, J.; and Qian, X. Facile synthesis of porous Zn–Sn–O nanocubes and their electrochemical performances. *Nano-Micro Lett.* **2016**, *8*, 174–181.

(22) Li, B.; Qi, R.; Zai, J.; Du, F.; Xue, C.; Jin, Y.; Jin, C.; Ma, Z.; and Qian, X. Silica wastes to high-performance lithium storage materials: a rational designed Al_2O_3 coating assisted magnesiothermic process. *Small* **2016**, 5281–5287.

(23) Li, X.; Zai, J.; Xiang, S.; Liu, Y.; He, X.; Xu, Z.; Wang, K.; Ma, Z.; and Qian, X. Regeneration of metal sulfides in the delithiation process: the key to cyclic stability. *Adv. Energy Mater.* **2016**, *6*, 1601056:1-8.

(24) Song, J.; Xia, F.; Zhao, M.; Zhong, Y. L.; Li, W.; Loh, K. P.; Caruso, R. A.; and Bao, Q. Solvothermal growth of bismuth chalcogenide nanoplatelets by the

oriented attachment mechanism: an in situ PXRD study. *Chem. Mater.* **2015**, *27*, 3471–3482.

(25) Li, W.; Chen, D.; Xia, F.; Tan, J. Z. Y.; Song, J.; Song, W.-G.; and Caruso, R. A. Flowerlike WSe_2 and WS_2 microspheres: one-pot synthesis, formation mechanism and application in heavy metal ion sequestration. *Chem. Commun.* **2016**, *52*, 4481–4484.

(26) Li, W.; Xia, F.; Qu, J.; Li, P.; Chen, D.; Chen, Z.; Yu, Y.; Lu, Y.; Caruso, R. A.; and Song, W. Versatile inorganic-organic hybrid WO_x-ethylenediamine nanowires: synthesis, mechanism and application in heavy metal ion adsorption and catalysis. *Nano Res.* **2014**, *7*, 903–916.

(27) Orvananos, B.; Ferguson, T. R.; Yu, H.-C.; Bazant, M. Z.; and Thornton, K. Particle-level modeling of the charge-discharge behavior of nanoparticulate phase-separating li-ion battery electrodes. *J. Electrochem. Soc.* **2014**, *161*, A535–A546.

(28) Ferguson, T. R.; and Bazant, M. Z. Nonequilibrium thermodynamics of porous electrodes. *J. Electrochem. Soc.* **2012**, *159*, A1967–A1985.

(29) Lim, J.; Li, Y.; Alsem, D. H.; So, H.; Lee, S. C.; Bai, P.; Cogswell, D. A.; Liu, X.; Jin, N.; Yu, Y.; et al. Origin and hysteresis of lithium compositional spatiodynamics within battery primary particles. *Science.* **2016**, *353*, 566–571.

(30) Horrocks, G. A.; De Jesus, L. R.; Andrews, J. L.; and Banerjee, S. X-ray spectroscopy and imaging as multiscale probes of intercalation phenomena in cathode materials. *JOM* **2017**, *69*, 1469–1477.

(31) Yu, Y.; Farmand, M.; Kim, C.; Liu, Y.; Grey, C. P.; Strobridge, F. C.; Tyliszczak, T.; Celestre, R.; Denes, P.; Joseph, J.; et al. Three dimensional localization of nanoscale battery reactions using soft x-ray tomography. *arxiv.org/abs/1711.01525v1* **2017**, 1–36.

(32) Chueh, W. C.; El Gabaly, F.; Sugar, J. D.; Bartelt, N. C.; McDaniel, A. H.; Fenton, K. R.; Zavadil, K. R.; Tyliszczak, T.; Lai, W.; and McCarty, K. F. Intercalation pathway in many-particle $LiFePO_4$ electrode revealed by nanoscale state-of-charge mapping. *Nano Lett.* **2013**, *13*, 866–872.

(33) Yoo, H. D.; Liang, Y.; Dong, H.; Lin, J.; Wang, H.; Liu, Y.; Ma, L.; Wu, T.; Li, Y.; Ru, Q.; et al. Fast kinetics of magnesium monochloride cations in interlayer-expanded titanium disulfide for magnesium rechargeable batteries. *Nat. Commun.* **2017**, *8*, 1–10.

(34) De Jesus, L. R.; Zhao, Y.; Horrocks, G. A.; Andrews, J.; Stein, P.; Xu, B.-X.; and Banerjee, S. Lithiation across interconnected V_2O_5 nanoparticle networks. *J. Mater. Chem. A* **2017**, *5*, 20141–20152.

(35) Dreyer, W.; Guhlke, C.; and Huth, R. The behavior of a many-particle electrode in a lithium-ion battery. *Phys. D Nonlinear Phenom.* **2011**, *240*, 1008–1019.

(36) Li, Y.; El Gabaly, F.; Ferguson, T. R.; Smith, R. B.; Bartelt, N. C.; Sugar, J. D.; Fenton, K. R.; Cogswell, D. A.; Kilcoyne, A. L. D.; Tyliszczak, T.; et al. Current-induced transition from particle-by-particle to concurrent intercalation in phase-separating battery electrodes. *Nat. Mater.* **2014**, *13*, 1149–1156.

(37) Croy, J. R.; Kim, D.; Balasubramanian, M.; Gallagher, K.; Kang, S.-H.; and

Thackeray, M. M. Countering the voltage decay in high capacity $xLi_2MnO_3•(1–x)LiMO_2$ electrodes (M=Mn, Ni, Co) for Li-Ion batteries. *J. Electrochem. Soc.* **2012**, *159*, A781–A790.

(38) Weker, J. N.; Liu, N.; Misra, S.; Andrews, J. C.; Cui, Y.; and Toney, M. F. In situ nanotomography and operando transmission x-ray microscopy of micron-sized Ge particles. *Energy Environ. Sci.* **2014**, *7*, 2771.

(39) Barai, P. and Mukherjee, P. P. Stochastics of diffusion induced damage in intercalation materials. *Mater. Res. Express* **2016**, *3*, 104011:1-26.

(40) Hao, F. and Fang, D. Diffusion-induced stresses of spherical core-shell electrodes in lithium-ion batteries: the effects of the shell and surface/interface stress. *J. Electrochem. Soc.* **2013**, *160*, A595–A600.

(41) Li, X.; Wu, G.; Liu, X.; Li, W.; and Li, M. Orderly integration of porous TiO_2(B) nanosheets into bunchy hierarchical structure for high-rate and ultralong-lifespan lithium-ion batteries. *Nano Energy* **2017**, *31*, 1–8.

(42) Li, X.; Feng, Y.; Li, M.; Li, W.; Wei, H.; and Song, D. Smart hybrids of Zn_2GeO_4 nanoparticles and ultrathin G-C_3N_4 Layers: synergistic lithium storage and excellent electrochemical performance. *Adv. Funct. Mater.* **2015**, *25* , 6858–6866.

(43) Zhang, L. S.; Jiang, L. Y.; Chen, C. Q.; Li, W.; Song, W. G.; and Guo, Y. G. Programmed fabrication of metal oxides nanostructures using dual templates to spatially disperse metal oxide nanocrystals. *Chem. Mater.* **2010**, *22*, 414–419.

(44) Li, W.; Yin, Y.-X.; Xin, S.; Song, W.-G.; and Guo, Y.-G. Low-cost and large-

scale synthesis of alkaline earth metal germanate nanowires as a new class of lithium ion battery anode material. *Energy Environ. Sci.* **2012**, *5*, 8007.

(45) Li, X.; Li, W.; Li, M.; Cui, P.; Chen, D.; Gengenbach, T.; Chu, L.; Liu, H.; and Song, G. Glucose-assisted synthesis of the hierarchical TiO_2 nanowire@MoS_2 nanosheet nanocomposite and its synergistic lithium storage performance. *J. Mater. Chem. A* **2015**, *3*, 2762–2769.

(46) Liu, Y.; Si, L.; Du, Y.; Zhou, X.; Dai, Z.; and Bao, J. Strongly bonded selenium/microporous carbon nanofibers composite as a high-performance cathode for lithium-selenium batteries. *J. Phys. Chem. C* **2015**, *119*, 27316–27321.

(47) Zhou, X.; Yu, L.; and Lou, X. W. (David). Nanowire-templated formation of sno_2/carbon nanotubes with enhanced lithium storage properties. *Nanoscale* **2016**, *8*, 8384–8389.

(48) Zhou, X.; Yu, L.; and Lou, X. W. (David). Formation of uniform n-doped carbon-coated sno_2 submicroboxes with enhanced lithium storage properties. *Adv. Energy Mater.* **2016**, *6*, 1600451:1-6.

(49) Chen, Z.; Yan, Y.; Xin, S.; Li, W.; Qu, J.; Guo, Y. G.; and Song, W. G. Copper Germanate nanowire/reduced graphene oxide anode materials for high energy lithium-ion batteries. *J. Mater. Chem. A* **2013**, *1*, 11404–11409.

(50) De Jesus, L. R.; Horrocks, G. A.; Liang, Y.; Parija, A.; Jaye, C.; Wangoh, L.; Wang, J.; Fischer, D. A.; Piper, L. F. J.; Prendergast, D.; and Banerjee, S. Mapping polaronic states and lithiation gradients in individual V_2O_5 nanowires.

Nat. Commun. **2016**, *7*, 12022:1–9.

(51) Wolf, M.; May, B. M.; and Cabana, J. Visualization of electrochemical reactions in battery materials with x-ray microscopy and mapping. *Chem. Mater.* **2017**, *29*, 3347–3362.

(52) Yang, F.; Liu, Y.; Martha, S. K.; Wu, Z.; Andrews, J. C.; Ice, G. E.; Pianetta, P.; and Nanda, J. Nanoscale morphological and chemical changes of high voltage lithium-manganese rich nmc composite cathodes with cycling. *Nano Lett.* **2014**, *14*, 4334–4341.

(53) Boesenberg, U.; Meirer, F.; Liu, Y.; Shukla, A. K.; Dell'Anna, R.; Tyliszczak, T.; Chen, G.; Andrews, J. C.; Richardson, T. J.; Kostecki, R.; et al. Mesoscale phase distribution in single particles of $LiFePO_4$ following lithium deintercalation. *Chem. Mater.* **2013**, *25*, 1664–1672.

(54) Horrocks, G. A.; Braham, E. J.; Liang, Y.; De Jesus, L. R.; Jude, J.; Velázquez, J. M.; Prendergast, D.; and Banerjee, S. Vanadium K-edge X-ray absorption spectroscopy as a probe of the heterogeneous lithiation of V_2O_5: first-principles modeling and principal component analysis. *J. Phys. Chem. C* **2016**, *120*, 23922–23932.

(55) Olivares-Marín, M.; Sorrentino, A.; Lee, R. C.; Pereiro, E.; Wu, N. L.; and Tonti, D. Spatial distributions of discharged products of lithium-oxygen batteries revealed by synchrotron x-ray transmission microscopy. *Nano Lett.* **2015**, *15*, 6932–6938.

(56) De Jesus, L. R.; Dennis, R. V.; Depner, S. W.; Jaye, C.; Fischer, D. A.; and

Banerjee, S. Inside and outside: X-ray absorption spectroscopy mapping of chemical domains in graphene oxide. *J. Phys. Chem. Lett.* **2013**, *4*, 3144–3151.

(57) Lerotic, M.; Jacobsen, C.; Schäfer, T.; and Vogt, S. Cluster analysis of soft x-ray spectromicroscopy data. *Ultramicroscopy* **2004**, *100*, 35–57.

(58) Lerotic, M.; Jacobsen, C.; Gillow, J. B.; Francis, A. J.; Wirick, S.; Vogt, S.; and Maser, J. Cluster analysis in soft x-ray spectromicroscopy: finding the patterns in complex specimens. *J. Electron Spectros. Relat. Phenomena* **2005**, *144–147*, 1137–1143.

(59) Marley, P. M.; Abtew, T. A.; Farley, K. E.; Horrocks, G. A.; Dennis, R. V; Zhang, P.; and Banerjee, S. Emptying and filling a tunnel bronze. *Chem. Sci.* **2015**, *6*, 1712–1718.

(60) Chernova, N. A.; Roppolo, M.; Dillon, A. C.; and Whittingham, M. S. Layered vanadium and molybdenum oxides: batteries and electrochromics. *J. Mater. Chem.* **2009**, *19*, 2526–2552.

(61) Whittingham, M. S. Lithium batteries and cathode materials. *Chem. Rev.* **2004**, *104*, 4271–4301.

(62) Marley, P. M.; Horrocks, G. A.; Pelcher, K. E.; and Banerjee, S. Transformers: the changing phases of low-dimensional vanadium oxide bronzes. *Chem. Commun.* **2015**, *51*, 5181–5198.

(63) Murphy, D. W.; Christian, P. A.; DiSalvo, F. J.; and Waszczak, J. V. Lithium incorporation by vanadium pentoxide. *Inorg. Chem.* **1979**, *18*, 2800–2803.

(64) Persson, K.; Sethuraman, V. A.; Hardwick, L. J.; Hinuma, Y.; Meng, Y. S.; van

der Ven, A.; Srinivasan, V.; Kostecki, R.; and Ceder, G. Lithium diffusion in graphitic carbon. *J. Phys. Chem. Lett.* **2010**, *1*, 1176–1180.

(65) Whittingham, M. S.; Dines, M. B. n-Butyllithium—an effective, general cathode screening agent. *J. Electrochem. Soc.* **1977**, *124*, 1387–1388.

(66) Enjalbert, R. and Galy, J. A refinement of the structure of V_2O_5. *Acta Crystallogr.* **1986**, *C42*, 1467–1469.

(67) Satto, C.; Sciau, P.; Dooryhee, E.; Galy, J.; and Millet, P. The $\Delta \rightarrow \varepsilon \rightarrow \gamma$ LiV_2O_5 "high temperature" phase transitions evidenced by synchrotron x-ray powder diffraction analysis. *J. Solid State Chem.* **1999**, *109*, 103–109.

(68) Galy, J. Vanadium pentoxide and vanadium oxide bronzes—structural chemistry of single (S) and double (D) layer $M_xV_2O_5$ phases. *J. Solid State Chem.* **1992**, *100*, 229–245.

(69) Ade, H. and Hitchcock, A. P. NEXAFS microscopy and resonant scattering: composition and orientation probed in real and reciprocal space. *Polymer* **2008**, *49*, 643–675.

(70) Urquhart, S. G.; Hitchcock, A. P.; Smith, A. P.; Ade, H. W.; Lidy, W.; Rightor, E. G.; and Mitchell, G. E. NEXAFS spectromicroscopy of polymers: overview and quantitative analysis of polyurethane polymers. *J. Electron Spectros. Relat. Phenomena* **1999**, *100*, 119–135.

(71) Velazquez, J. M.; Jaye, C.; Fischer, D. A.; and Banerjee, S. Near edge x-ray absorption fine structure spectroscopy studies of single-crystalline V_2O_5 nanowire arrays. *J. Phys. Chem. C* **2009**, *113*, 7639–7645.

(72) Maganas, D.; Roemelt, M.; Hävecker, M.; Trunschke, A.; Knop-Gericke, A.; Schlögl, R.; and Neese, F. first principles calculations of the structure and V L-edge X-ray absorption spectra of V_2O_5 using local pair natural orbital coupled cluster theory and spin-orbit coupled configuration interaction approaches. *Phys. Chem. Chem. Phys.* **2013**, *15*, 7260–7276.

(73) Kolczewski, C. and Hermann, K. Ab initio dft cluster studies of angle-resolved NEXAFS spectra for differently coordinated oxygen at the V_2O_5(010) surface. *Surf. Sci.* **2004**, *552*, 98–110.

(74) Andrews, J. L.; De Jesus, L. R.; Tolhurst, T. M.; Marley, P. M.; Moewes, A.; and Banerjee, S. Intercalation-induced exfoliation and thickness-modulated electronic structure of a layered ternary vanadium oxide. *Chem. Mater.* **2017**, *29*, 3285–3294.

(75) Tolhurst, T. M.; Leedahl, B.; Andrews, J. L.; Marley, P. M.; Banerjee, S.; and Moewes, A. Contrasting 1D tunnel-structured and 2D layered polymorphs of V_2O_5: relating crystal structure and bonding to band gaps and electronic structure. *Phys. Chem. Chem. Phys.* **2016**, *18*, 15798–15806.

(76) Cogswell, D. A. and Bazant, M. Z. Coherency strain and the kinetics of phase separation in $LiFePO_4$ nanoparticles. *ACS Nano* **2012**, *6*, 2215–2225.

(77) Zhao, Y.; De Jesus, L. R.; Stein, P.; Horrocks, G. A.; Banerjee, S.; and Xu, B.-X. Modeling of phase separation across interconnected electrode particles in lithium-ion batteries. *RSC Adv.* **2017**, *7*, 41254–41264.

(78) Meulenkamp, E. A.; van Klinken, W.; and Schlatmann, A. R. In-situ X-ray

diffraction of Li intercalation in sol–gel V_2O_5 films. *Solid State Ionics* **1999**, *126*, 235–244.

(79) Baddour-Hadjean, R.; Raekelboom, E.; and Pereira-Ramos, J. P. New structural characterization of the $Li_xV_2O_5$ system provided by Raman spectroscopy. *Chem. Mater.* **2006**, *18*, 3548–3556.

(80) Dickens, P. G.; French, S. J.; Hight, A. T.; and Pye, M. F. Phase relationships in the ambient temperature $Li_xV_2O_5$ system ($0.1<x<1.0$). *Mater. Res. Bull.* **1979**, *14*, 1295–1299.

(81) Stein, P. and Xu, B. 3D isogeometric analysis of intercalation-induced stresses in Li-ion battery electrode particles. *Comput. Methods Appl. Mech. Eng.* **2014**, *268*, 225–244.

(82) Stein, P.; Zhao, Y.; and Xu, B.-X. Effects of surface tension and electrochemical reactions in li-ion battery electrode nanoparticles. *J. Power Sources* **2016**, *332*, 154–169.

(83) Muralidharan, N.; Brock, C. N.; Cohn, A. P.; Schauben, D.; Carter, R. E.; Oakes, L.; Walker, D. G.; and Pint, C. L. Tunable mechanochemistry of lithium battery electrodes. *ACS Nano* **2017**, *11*, 6243–6251.

(84) Xu, B.-X.; Zhao, Y.; and Stein, P. Phase field modeling of electrochemically induced fracture in Li-Ion battery with large deformation and phase segregation. *GAMM-Mitteilungen* **2016**, *39*, 92–109.

(85) Zhao, Y.; Xu, B.-X.; Stein, P.; and Gross, D. Phase-field study of electrochemical reactions at exterior and interior interfaces in Li-ion battery

electrode particles. *Comput. Methods Appl. Mech. Eng.* **2016**, *312*, 428–446.

(86) Andrews, J. L.; Mukherjee, A.; Yoo, H. D.; Parija, A.; Marley, P. M.; Prendergast, D.; Cabana, J.; Klie, R. F.; and Banerjee, S. Reversible Mg-ion insertion in a metastable one-dimensional polymorph of V_2O_5. *Chem* **2018**, *4*, 564–585.

(87) Jacobsen, C.; Wirick, S.; Flynn, G.; and Zimba, C. Soft X-ray spectroscopy from image sequences with sub-100 nm spatial resolution. *J. Microsc.* **2000**, *197*, 173–184.

CHAPTER V

LITHIATION ACROSS INTERCONNECTED V_2O_5 NANOPARTICLE NETWORKS*

V.1 Introduction

Lithium-ion batteries have in short order emerged as the dominant means of portable energy storage and have underpinned "off-the-grid" electrification of technologies spanning the range from consumer electronics to vehicular transportation.[1,2] The operating principle of this technology involves the closely coupled reversible transport of electrons and ions between a pair of host matrices that provide a large difference in the chemical potential of intercalated Li-ions.[3] The electrochemical insertion of Li-ions within several common host matrices, for instance, $FePO_4$,[4,5] lithium titanate, lithium nickel manganese oxides, or graphite, requires a structural phase transformation that inevitably necessitates energy dissipation, and as an activated first-order process is accompanied by a characteristic time scale and hysteresis.[3,6–9] Incomplete understanding of the dynamics and progression of cation insertion/extraction and concomitant phase transformation, particularly at the cathode,[6] represents a major impediment to the rational discovery of cathode materials and the predictive design of electrode architectures.

In the most commonly used configuration, the cathode of Li-ion batteries comprises porous composites of particles electrically interconnected to each other and the current collector with the help of conductive layers. It has become increasingly apparent that local differences such as particle size variations, distance from current collector, and surface states engender considerable heterogeneity in depth of discharge

*Reproduced with permission from De Jesus, L. R.; Zhao, Y.; Horrocks, G. A.; Andrews, J.; Stein, P.; Xu, B.-X.; Banerjee, S. Lithiation across Interconnected V_2O_5 Nanoparticle Networks. *J. Mater. Chem. A* **2017**, *5*, 20141–20152. Reproduced with permission from the Royal Society of Chemistry.

or extent of lithiation across cathode particles that are furthermore dependent on the charge/discharge rate and overpotential.[7,10–12] In other words, the sequence of transformation of particles within the electrodes is dominated by local phenomena and local Li-ion activities and not the global voltage profile. In the canonical cathode material, Li_xFePO_4, widely divergent phenomena spanning the range from particle-by-particle transformation ("mosaic instability") to concurrent intercalation have been observed, corresponding to a broad spread of heterogeneity, density of actively intercalating particles, and sequence of intercalation/deintercalation events.[12–17] For instance, Delmas *et. al.* have observed that Li_xFePO_4 particles are delithiated/lithiated sequentially.[13] Orvananos and co-workers have investigated the dynamics of interparticle phase separation[7] and developed a simplified two-particle model, wherein at a constant applied current, a particle that is closer to the separator undergoes rapid lithiation while simultaneously depleting a particle that is in closer proximity to the current collector (particle-by-particle).[9] The heterogeneity in lithiation of Li_xFePO_4 has beenattributed to the subtle balance between the local overpotential and the phase transformation barrier and is strongly dependent on the rate and particle size. In this material, stabilization of a metastable solid-solution phase furthermore provides an alternative lithiation route at fast rates for small particles.[18] From a practical perspective, such widespread inhomogeneities across the electrode and the resulting occurrence of hotspots as a result of high local current densities is thought to underpin electromechanical degradation and loss of cyclability, and as such needs to be mitigated to prolong operational lifetimes. Strategies to circumvent and mitigate these limitations

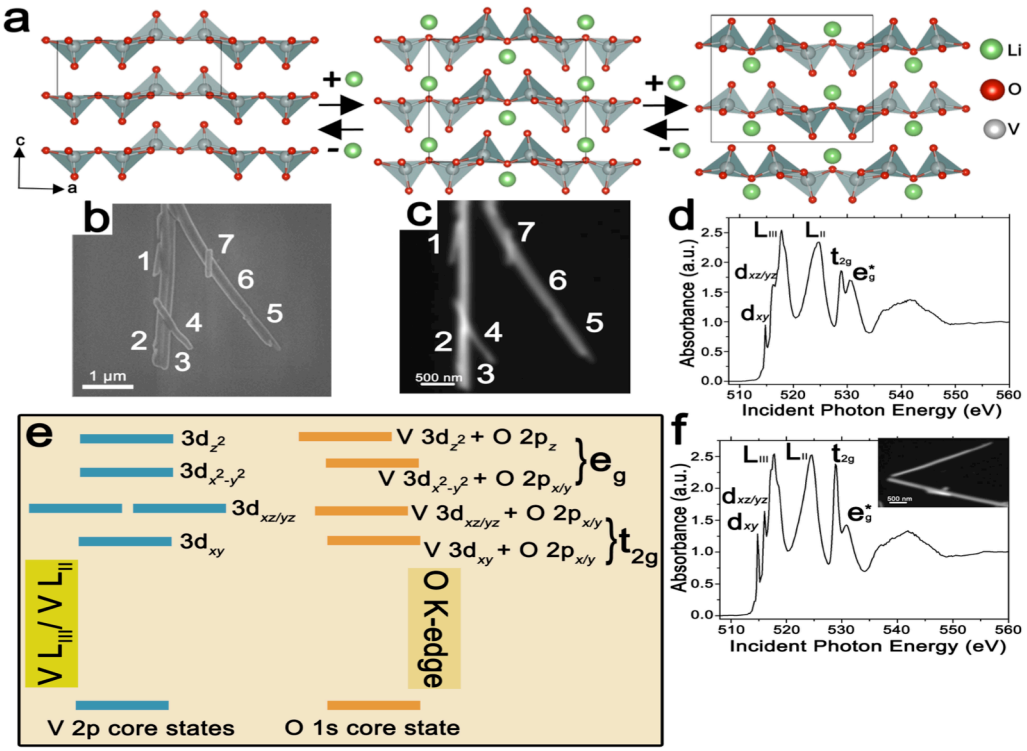

Figure V.1. Sequence of phase transformations induced by lithiation and the model system in aggregate. (a) The insertion of Li-ions within V_2O_5 (characterized by square pyramidal coordination of vanadium atoms) brings about a transformation to a mildly distorted α-phase ($x < 0.1$ in $Li_xV_2O_5$), followed by puckering and lattice expansion to accommodate an increased concentration of Li-ions ($0.3 < x < 0.8$) stabilizing the ε-phase, followed by displacement of layers with respect to each other to form a highly puckered δ-phase ($0.8 < x < 1$). (b) High-resolution scanning electron microscopy (HR-SEM) image of an interconnected network of V_2O_5 nanowires used as our model system (Fig. A.20). Lithiation gradients within the same cluster have been evaluated through scanning transmission X-ray microscopy at the V L and O K-edges; the integrated image is shown in (c) and the corresponding integrated spectrum of lithiated V_2O_5 is depicted in (d). The labels in (d) indicate the orbital symmetry of the final states as elucidated based on density functional theory calculations and angle-resolved X-ray absorption near-edge structure measurements[23,43,44]. Schematic depiction of crystal field splitting (corresponding to square pyramidal coordination of vanadium atoms by the oxide ligands) and electronic transitions observed in V L-edge and O K-edge X-ray absorption spectra for V_2O_5 derived from density functional theory calculations by Maganas *et. al* further verified by atom-projected density functional theory results discussed below.[43] The integrated spectrum (f) of a group of delithiated nanowires (inset) shows recovery of the electronic structure of V_2O_5.

have been developed for several Li-ion host materials. In the case of anode materials, increased rate capabilities and reduced degradation have been demonstrated upon coating the anode with a conductive carbonaceous matrix[19,20,21] and by increasing the porosity of the composite electrode.[22] These methods endow enhanced stability that alleviates the change in volume, which plagues many electrode materials allowing for improved diffusion of ions within the host.

Given the highly local nature of intercalation phenomena, recent attention has focused on mapping intercalation gradients across small ensembles of particles and individual particles using single-particle imaging methods.[10,12,23,24] Of particular interest, the stabilization of discrete domains with varying lithium content has been observed within Li_xFePO_4 platelets and has been attributed to surface-induced variations in extent of intercalation,[12] whereas in individual V_2O_5 nanowires such domains have been attributed to stage ordering phenomena and electron localization as a result of the stabilization of small polarons.[23,24] Such local measurements of intercalation profiles are imperative to elucidate phenomena not accessible from ensemble electrochemical measurements. As an example, micrometer-resolution Raman spectroscopy has been employed to locally map the state-of-charge of $Li_{1-x}(Ni_yCo_zAl_{1-y-z})O_2$. This provides an effective method to evaluate the inhomogeneous distribution of Li-ion content within an electrode under different aging protocols.[25] In this work, we use scanning transmission X-ray microscopy (STXM) to map lithiation gradients and ensuing phase transformation across an interconnected particle network, providing a direct measure of the competing

thermodynamics and kinetics of intercalation-induced phase transformations and resulting heterogeneities induced within a network of particles.

As our model system we select V_2O_5, which is a classical layered intercalation host for alkali ions, first proposed as such by Whittingham.[26] V_2O_5 crystallizes in an orthorhombic-layered structure and has several desirable characteristics as an intercalation host[27,28] including ample available interstitial sites, readily accessible V^{5+}/V^{4+} and V^{+4}/V^{3+} redox couples, a stable fully oxidized state, and a reasonable voltage difference with respect to commonly used anodes.[3,29,30] Unfortunately, V_2O_5 suffers from poor high-rate performance and complications with retention of capacity over extended cycling. The role of intercalation-induced phase transformations has been suggested with regards to the poor kinetics and loss of capacity but remains to be elucidated. Nevertheless, this material has attracted renewed interest as a potentially viable cathode material as a result of being one of a limited number of potential hosts for multivalent intercalation chemistries and the greatly modified phase diagram accessible by reducing the dimensions of the particle.[31,32] In addition, the electronic structure of the V_2O_5 system is sensitive to the intercalation of ions, allowing for a direct probe of the extent of lithiation.[23,24] Orthorhombic V_2O_5 is characterized by an *up-up-down-down* arrangement of [VO_5] square pyramids linked by corner- and edge-sharing oxygens to form 2D sheets; the infinite sheets thus formed are stacked along the crystallographic *c* axis as depicted in Figure 1a. The intercalation of Li-ions within this structure launches a series of structural phase transformations that are reversible up to a lithium-content of ca. one Li per V_2O_5.[33–35] At low concentrations of $x < 0.1$ in $Li_xV_2O_5$, an α-phase, only

slightly distorted from the orthorhombic structure is stabilized. With increasing lithiation, the ε-phase is stabilized (with a single-phase regime between $0.35 < x < 0.8$) and is characterized by expansion of the interlayer spacing along the *c* axis and in-plane puckering as the apical vanadyl oxygens are electrostatically drawn towards the intercalated Li-ions. Further lithiation above $x > 0.8$ induces more extensive puckering and sliding of the layers by half a unit cell length along the *b* direction, stabilizing the δ-phase of $Li_xV_2O_5$ in the range $0.88 < x < 1.0$[34] (Fig. 1a). Delithiation in this range of Li-ion concentrations is fully reversible back to orthorhombic V_2O_5. However, lithiation to $x > 1$ induces not just sliding of the layers but considerable distortion and inversion of the square pyramids as the layers adopt an *up-down-up-down* motif stabilizing a 3D γ-phase; delithiation hereinafter yields a metastable puckered γ'-phase and is not reversible back to the 2D layered geometry through the $\delta \rightarrow \varepsilon \rightarrow \alpha$ sequence.[3,28,36]

The sequence and reversibility of phase transformations in V_2O_5 is strongly dependent on particle size and rate.[31,37] For ultra-thin nanoplatelets with thicknesses on the order of 20—50 nm, our past work indicates that phase separation is strongly suppressed, whereas in nanowires that are 150—250 nm in diameter, phase heterogeneities are discernible from Raman and X-ray diffraction measurements. In recent work, STXM measurements indicate pronounced lithiation gradients and phase separation within individual V_2O_5 nanowires.[23] The inhomogenities are attributed to the following two origins: (i) electron localization within V $3d_{xy}$ orbitals couples to the structural distortion induced by Li-ion intercalation resulting in stabilization of small polarons that propagate anisotropically along the nanowires; (ii) stage ordering of Li-ion

intercalation in this layered material such that it is energetically preferable to lithiate the same layer after an initial lithiation event rather than initiating lithiation of a second layer.[23] Principal component analysis of ensemble V K-edge X-ray absorption near-edge structure (XANES) spectroscopy data suggests initial conversion to α-$Li_xV_2O_5$ followed by a two-phase regime wherein a highly lithiated phase grows at the expense of the low-lithiated phase.[24] However, the microscopic mechanisms of phase transformation and propagation are entirely unexplored, particularly with regards to multiple particles. In this work, we examine lithiation gradients and phase separation within a network of interconnected nanowires and observe considerable compositional and phase heterogeneity both within individual nanowires as well as across the different nanowires suggesting a pronounced role for interfaces in mediating Li-ion transport and thus phase propagation. Interfaces within the interconnected network clearly modify the local potentials and facilitate phase transformations in a manner very distinctive from individual nanowires. A phase-field diffusion-reaction model, which considers intraparticular diffusion, surface chemical reaction, and phase separation simultaneously, is developed to understand the observed intercalation gradients. Elucidating the phase separation profiles across interconnected networks suggests routes for designing mesoscale architectures with larger proportions of actively intercalating areas and with ordered cascades of lithiation/delithiation pathways.

V.2 Experimental

V.2.1 Chemical Lithiation of V_2O_5 Nanowires

Synthesis and the subsequent lithiation of the V_2O_5 nanowires were carried out as previously reported.[31] In summary, lithiation was carried out within a glove box filled with argon *via* immersion in a molar excess (4:1 Li:V_2O_5) of *n*-butyllithium solution (Sigma-Aldrich) in hexane for 1 h. Delithiation was accomplished by immersion of the lithiated samples in liquid Br_2 for 2 h, followed by washing with large amounts of hexanes. The samples were sealed within a glovebox for transport for synchrotron measurements. Contact angle measurements were acquired using an in-house goniometer setup wherein indium tin oxide-coated glass was coated with a layer of V_2O_5 nanowires and a 5μL droplet of hexanes was deposited on the sample.

V.2.2 Scanning Electron Microscopy (SEM) and Scanning Transmission X-ray Microscopy (STXM)

Wires were dispersed in isopropanol and drop-cast onto a 50nm thick Si_3N_4 window for characterization in SEM and subsequent STXM. SEM images were acquired by using a JEOL JSM-7500F FE-SEM at a working distance of 8.3 mm and operated at 2 kV. STXM measurements were performed at the SM (10-ID1) beamline of the Canadian Light Source (CLS), a 2.9 GeV third-generation synchrotron facility. A 25 nm outermost-zone zone plate and a 500 line mm^{-1} plane grating monochromator (PGM) was deployed to acquire the V L-edge and O K-edge spectral stacks. The incident photon flux (I_o) count rate was optimized to ca. 17 MHz as measured by the STXM detector within an empty hole and measured at 560 eV by adjusting the exits slits to 17/16 μm

(dispersive/non-dispersive). The V L- and the O K-edge stacks covered an energy range from 508—560 eV with energy steps of 0.2 eV in the region of interest and 1 eV in the continuum region beyond the specific elemental edges with dwell time of 1 ms for each section. Right circularly polarized light X-rays, generated by an elliptically polarized undulator (EPU) was used in the experiments in order to reduce polarization dependence of spectral intensities. All STXM data were analyzed and processed using aXis2000 software (http://unicorn.mcmaster.ca/aXis2000.html). STXM intensity maps were derived based on singular value decomposition (SVD) of the image stack in aXis2000 and by using as a reference the spectra identified within different regions of the same image sequence. Such an operation produces hyperspectral composition maps wherein intensities represent the location of the spectra signal strength (Figs. V.2a—c) at each specific pixel of that highlighted area.

Thickness maps were developed by fitting the V L- and O K-edge stack to a linearly scaled spectrum of $Li_xV_2O_5$ for an X-ray elemental profile of a 1 nm thick material, assuming the density to be 3.357 g cm^{-3}, as calculated by aXis2000. The elemental profile spectrum is in absorbance or optical density (OD), allowing the thickness of the sample to be evaluated quantitatively using a Beer law dependence of transmission with thickness.

V.2.3 Computational Details

The ground-state density of states (DOS) of V_2O_5 is obtained using density functional theory with the Vienna *ab-initio* simulation package (VASP). The exchange-correlation energies are determined within the specific generalized-gradient

approximation (GGA) of Perdew-Burke-Ernzerhof (PBE). The electron-ion interaction is treated with projector-augmented-wave (PAW) pseudopotentials by using a 400 eV plane-wave energy cut-off. A DFT+U approach is employed to describe the on-site Coulomb interaction with $U = 4.0$ eV. We sample the first Brillouin zone with a Monkhorst-Pack reciprocal-space grid of 6x6x6 k-points and the structure was relaxed until each force component is no greater than 0.01 eV $Å^{-1}$. To guarantee highly resolved projected density of states (pDOS), we calculate Kohn-Sham eigen-energies based on the converged electron density on a grid of 12x12x12 k-points. The pDOS is numerically broadened with a Fermi-Dirac smearing of 0.2 eV. The Tkatchenko-Scheffler method was used to describe the van der Waals interaction between the layers of V_2O_5. The phase field model for diffusion and reaction, Equation V.(2)-(4), are implemented in the open-source finite element program FEAP. For time integration, the backward Euler method is employed with adaptive time step control. Spatially higher order partial differential equations are solved using the B-spline based finite cell method.[38] The particles are immersed in a regular background Cartesian mesh and the geometries are represented by different sets of integration points, allowing for the representation of complex geometries. Surface quadrature points, which are located on particle-solution interface and on the particle-particle interfaces, are produced based on the surface mesh generated by NETGEN, where surface quadrature points are obtained from a standard six-point formula. The code has been parallelized at the assembly level by OpenMP. On these points, the corresponding modified Butler—Volmer models explained in the previous context are applied.

V.3 Results and Discussion

V.3.1 Spectral Assignments and Electronic Structure Signatures of Lithiated V_2O_5

Phase-pure single-crystalline V_2O_5 nanowires, prepared as described previously,[31] are chemically lithiated by reaction with *n*-butyllithium[36] for 1 h in hexanes as per:

$$V_2O_5 + x\ C_4H_9Li\ (\text{hexanes}) \rightarrow Li_xV_2O_5 + \frac{x}{2}\ C_8H_{18}(g) \qquad \text{(EQUATION V.1)}$$

Figure V.1b depicts a high-resolution scanning electron microscopy (HRSEM) image of a network of interconnected V_2O_5 nanowires lithiated for 1 h. These nanoparticles are interfaced but are not covalently bonded. Seven distinct regions can be distinguished as labeled in the Figure. Figure A.20 depicts a high-magnification view of the SEM image depicted in Figure V.1b, further allowing for visualization of the interconnected and demonstrating retention of nanowire integrity of the wire is not affected by the lithiation process. Chemical lithiation allows for elimination of a number of confounding parameters enabling examination of the role of interfaces across the interconnected network. Lithiation can occur at two-phase interfaces between the solution and the nanowire and does not require a three-phase contact between the electrolyte, conductor, and electrode such as required in an electrochemical reaction.[13] Furthermore, chemical lithiation in hexanes confines inter-particle charge and mass transport to interconnects. Notably, V_2O_5 is completely wet by hexanes (*n*-hexane has a low surface tension of 18.43 mN/m at 293K), as depicted by flash spreading and a contact angle measurement of 0˚ measured upon application of a liquid droplet to the prepared materials (Figure A.21). Finally, by performing this reaction within a large bath, the global Li-ion flux can

be assumed to be constant. Consequently, gradients in Li-ion concentrations and phases measured across this system can be directly attributed to specific particle morphologies and proximity to the other particles. Figure V.1c depicts the STXM image of this interconnected network and Figure V.1d shows the integrated V L- and O K-edge X-ray

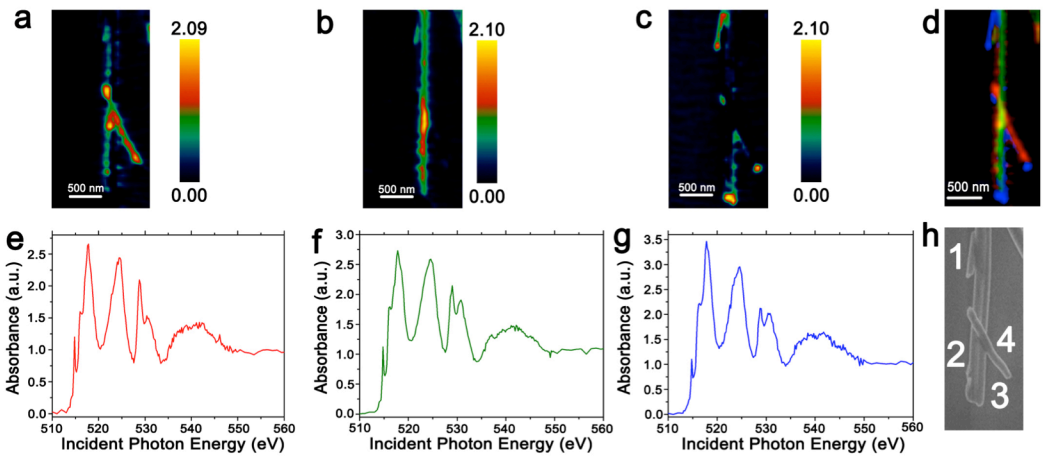

Figure V.2. Evaluating electronic structure inhomogeneities and phase separation in interconnected V_2O_5 wires. Region-of-interest analysis of the subgroup of particles in regions 1—4. (a)–(c) depict maps of three spectral components (colour-bars to the right depict the intensity of the spectrum at each pixel) identified by singular variable decomposition analysis that are plotted in (e)–(g). Based on the intensities of the V $3d_{xy}$ features at the V L_{III}-edge and the ratios of the t_{2g} to e_g intensities at the O K-edge, components e—g correspond to increasing lithiation (Table V.1). In each case, the yellow—red regions demarcate a greater contribution from the respective spectral component, whereas black—blue corresponds to relatively small spectral contributions within the specific regions. (d) An overlay of the three spectral components illustrating the compositional and phase heterogeneity across the interconnected network. Red, green, and blue regions demarcate majority contributions at the specific pixel from spectral components in (e), (f), and (g), respectively. The corresponding HRSEM image for this region is depicted in (h). The extent of global lithiation in V_2O_5 depends on the nature of the interconnects. The arrangement of particles in this Figure has been used to model the progression of lithiation by phase-field modelling, as depicted in Figure V.4 and in Movie A2.

absorption spectra acquired for these particles. The particle thicknesses can be directly evaluated from the transmission profiles as described in the Methods section. Region 1 is a small nanoparticle of *ca.* 50 nm in thickness and 1 μm in length (Fig. A.22) and is in direct contact with a longer nanowire denoted as region 2, which grows parallel to a second nanowire denoted as region 3; the latter two nanowires are each *ca.* 120 nm in thickness. Another nanowire denoted as region 4 has a thickness of *ca.* 55 nm and is interfaced directly with region 3 (Figure A.20b). Figure A.23 shows thickness profiles for regions 5—7. Region 6 is a long wire that is *ca.* 85 nm in thickness; region 5 is a domain within this nanowire that appears to be separated by a screw dislocation or surface step (Figure A.20c). Region 7 is a small particle *ca.* 20 nm in thickness and *ca.* 850 nm in length interfaced directly with region 6.

X-ray microscopy is a versatile and powerful probe of local electronic structure and has been used to elucidate chemical and structural inhomogeneities in various types of materials.[12,39–42] It is instructive to compare the integrated V L-edge and O K-edge spectrum acquired for the lithiated particle network plotted in Figure 1d with the stack acquired for delithiated V_2O_5 nanowires shown in Figure V.1f. Delithiation of the nanowires in liquid Br_2 induces full recovery of the electronic structure of orthorhombic V_2O_5 suggesting complete extraction of Li-ions[23,24,43,44] in Figure V.1f. The spectral changes in Figure V.1c thus directly stem from Li-ion intercalation within the nanowires. The integrated spectrum in Figure V.1d comprises a number of different spectroscopic signatures corresponding to varying extents of lithiation; the spatial

localization of these signals (inaccessible in an ensemble measurement) are plotted in Figures V.2 and V.3 and allow for mapping of lithiation gradients across the network.

The V L-edge features labelled as such in Figure 1f correspond to transitions from V $2p_{3/2} \rightarrow$ V 3d (centered at *ca*. 518 eV, labelled V L_{III}) and V $2p_{1/2} \rightarrow$ V 3d (centred at *ca*. 525 eV, labelled V L_{II}) states, respectively, consistent with dipole-selection rules for core-level electronic spectroscopy wherein transitions with a change of angular momentum quantum number $\Delta l = \pm 1$ are allowed with conservation of spin.[23,43,44] The separation of ca. 7 eV between these features corresponds to the spin-orbit coupling of V 2p states characteristic of pentavalent vanadium.[44,45] A Coster—Krönig Auger decay process renders the V L_{II} edge less descriptive, principally due to the broadening that accompanies this type of decay; nevertheless, the V L_{III} spectral features are characterized by fine-structure resonances and provide a sensitive view of the bottom of the conduction band in V_2O_5 (Figure A.24 shows the calculated orbital-projected density of states for V_2O_5). These absorption features correspond to transitions from a singlet V $2p^63d^0$ electronic configuration to V $2p^53d^1$ states that are rendered non-degenerate as a result of crystal field splitting (Fig. V.1e) and multiplet effects.[45] The first two sharp resonances that emerge at 515.6 eV and 516.8 eV, respectively, can be assigned to transitions to final states of $3d_{xy}$ and $3d_{xz/yz}$ character based on restricted open-shell configuration interaction with singles quantum chemistry calculations performed by Neese and co-workers.[43] The assignments are further borne out by angle-resolved XANES measurements that confirm the $3d_{xy}$ symmetry of the lowest-lying conduction band state of V_2O_5.[44] To a first approximation, Li-ion intercalation induces

reduction of vanadium atoms to tetravalent vanadium and as such the lowest lying V $3d_{xy}$ states are occupied creating a small polaron. Figure V.1d indicates that as a result of filling of the lowest-lying states in the unoccupied density of states (Fig. A.24), the V $3d_{xy}$ and V $3d_{xz/yz}$ features are strongly attenuated[23,24] (and are rendered "dark" in the integrated spectrum for the lithiated phase as a result of Pauli blocking). Indeed, the relative attenuation of these features serves as a signature of Li-ion insertion (and vanadium reduction).

The spectral features at the O K-edge correspond to transitions from O 1s to O 2p states; substantial hybridization between V 3d-O 2p orbitals results in two distinct sets of resonances (of t_{2g} and e_g character; Fig. V.1e) that are reflective of the crystal field splitting of the V 3d orbitals (Fig. A.24).[23,43,46] Based on eXcited-state Core-Hole (XCH) density functional theory calculations, the t_{2g} absorption feature (at *ca.* 529 eV) arises primarily from the hybridization of vanadyl oxygen $2p_{x/y}$ orbitals with the V $3d_{xz/yz}$ orbitals; this feature also has contributions from states derived from hybridization of $2p_y$ orbitals of bridging oxygen atoms and $2p_x$ orbitals of chaining oxygen atoms with V $3d_{xy}$ states (Fig. V.1e). In contrast, the e_g absorption (at *ca*. 531 eV) corresponds to transitions of O 1s core electrons to O 2p states hybridized with V $3d_z^2$ and V $3d_{x^2-y^2}$ states that are relatively raised in energy as a result of their end-on σ interactions. Figure 1d indicates that consistent with previous observations, Li-ion intercalation strongly modifies the O K-edge XANES spectrum.[23,24] In particular, the relative ratios of the t_{2g} and e_g intensities are greatly modified; the I_{t2g}/I_{eg} ratio is >>1 for the initial or delithiated V_2O_5 samples but is modified to ≤ 1 upon Li-ion intercalation. This change in t_{2g} intensity is principally

due to the influence of lithiation and electron localization on the electronic structure of V_2O_5. Specifically, lifting of the electron spin degeneracy is induced by the emergence of electron correlation (as the system goes from a V^{5+} $3d^0$ system to a mixed valence system with considerable V $3d^1$ sites) and the distortion of the structural lattice, which raises the energy of the π-bonded t_{2g} states.[23,24] The relative ratio of the t_{2g} and e_g absorption features (I_{t2g}/I_{eg}) serves as a second measure of the Li-ion concentration and thus the local level of lithiation a particle when evaluated by STXM.

V.3.2 STXM Mapping of Lithiation Across an Interconnected Particle Network

The interconnected network of particles shown in Figure V.1 has been divided into two subgroups; Figure V.2 shows STXM maps and spectral components identified across regions 1—4, whereas Figure V.3 depicts the corresponding data for regions 5—7 (Fig. A.20, depicts high-magnification SEM images). In Figure V.2, singular value decomposition (SVD) of the image stack yields three spectral components plotted as Figures V.2e—f. Based on the two measures noted above, the intensity of the V $3d_{xy}$ feature at the V L_{III}-edge and I_{t2g}/I_{eg} ratios, the three components depicted in Figures V.2e—g represent increasing extents of lithiation. Figure V.2e corresponds to a low degree of lithiation as is characteristic of α-$Li_xV_2O_5$. Indeed, the t_{2g} absorption feature is much higher in intensity as compared to the e_g feature (as also observed for unlithiated and delithiated V_2O_5 in Fig. V.1f).[23,24] In stark contrast, the t_{2g} and e_g absorption features are similar in intensity for the third spectral component plotted in Figure V.2g, which corresponds to a higher Li-content δ-$Li_xV_2O_5$ phase. The spatial localization of these components is mapped in Figures V.2a—c and allows for direct visualization of the

considerable compositional and thus phase heterogeneity across this region of interconnected particles. The thin nanowire denoted as region 1 as well as the tips of the other three nanowires are heavily lithiated and have been transformed to the δ-phase (Fig. V.2d). In contrast, nanowires 2 and 4 are sparsely lithiated and are in the α-phase. The nanowire denoted as region 3 shows an intermediate extent of lithiation corresponding to the ε-phase. The mapping of compositional heterogeneity using the

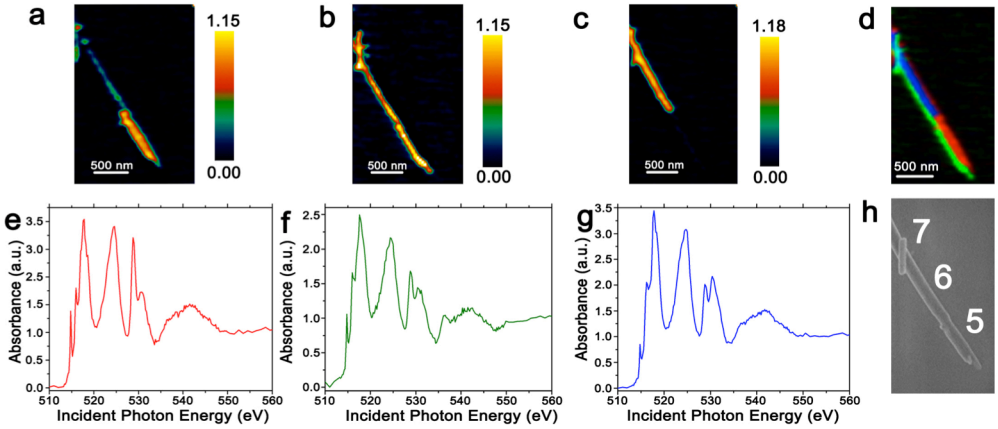

Figure V.3. Electronic structure inhomogeneities and phase separation within nanowires and across interfaces. Region-of-interest analysis of the subgroup of particles in regions 5-7. (a)–(c) depict maps of three spectral components (colour-bars to the right depict intensity of the spectrum at each pixel) identified by singular variable decomposition analysis that are plotted in (e)–(g). Based on the intensities of the V $3d_{xy}$ features at the V L_{III}-edge and the ratios of the t_{2g} to e_g intensities at the O K-edge, components e—g correspond to increasing lithiation (see Table V.1). In each case, the yellow—red regions demarcate a greater contribution from the respective spectral component, whereas black—blue corresponds to relatively small spectral contributions within the specific regions. (d) An overlay of the three spectral components illustrating the compositional and phase heterogeneity across the interconnected network. Red, green, and blue regions demarcate majority contributions at the specific pixel from spectral components in (e), (f), and (g), respectively. The corresponding HRSEM image for this region is depicted in (h).

electronic structure of V_2O_5 thus permits a detailed view of the influence of interconnects on the phase heterogeneity. It is apparent that in this system, Li-ion transport across the interconnected regions preferentially facilitates growth of the heavily lithiated phases within individual nanowires instead of nucleating heavily lithiated domains within every nanowire. Figures V.2a and d particularly depict the stark contrast in Li-ion content across the interfaces between (a) regions 1 and 2 and (b) regions 3 and 4. Regions 1 and 3 are strongly enriched in Li-ions and transformed to high-Li-content ε- and δ-phases, respectively, whereas the domains of nanowires 2 and 4 that are in direct contact are depleted of Li-ions. Notably, the tips of these two nanowires are heavily lithiated likely mediated by an entirely distinct mechanism involving insertion from the flux at narrower tips that are subjected to a high local potential gradient (marking a secondary nucleation event).[31,47–49] Li-ion transport across interfaces thus preferentially grows the highly lithiated domains in 1 and 3 without nucleating phase transformations within 2 and 4. Interestingly, nanowire 4 is less lithiated as compared to nanowire 3 despite being thinner suggesting that the specifics of interconnectivity rather than particle size determine the lithium content and thus spatial sequence of phase transformation. From a thermodynamic perspective, such a transport-driven segregation across the interfaces minimizes the creation of energetically expensive new interfaces, whereas from a kinetic perspective, diffusion across the interface and growth of the highly lithiated phases appears to require a lower activation energy as compared to phase nucleation. A phase-field model that reproduces this progression of phase transformations is further developed below. Interestingly, for a

bundle of nanowires that are closely interfaced across most of their length, discrete spectral components can be resolved (Fig. A.25), but are very similar suggesting that extended interfaces, unlike the interfaces in Figure V.1b, allow for equilibration and a relatively greater degree of phase homogeneity.

Figure V.3 indicates a similar mapping of lithiation and phase gradients across regions 5—7. Regions labeled 5 and 6 form part of the same nanowire but appear to be separated by a dislocation or surface step (Fig. A.20c) and show vastly different extents of lithiation. Figures V.3c and g indicate that region 6 is very heavily lithiated (δ-$Li_xV_2O_5$), whereas the bottom of region 5 has a very low Li-ion concentration (Fig. V.3a and e). The induction of a defect thus appears to serve as a barrier for Li-ion transport

Region	**I_{t2g}/I_{eg} (a.u.)**	**Estimated Li concentration *x* in $Li_xV_2O_5$**	**Phase**
1	1.185	1.1–1.3	δ
2-3	0.992	1.3–1.5	δ
4	1.694	0.0–0.31	α
5	2.132	0.0-0.1	α
6	0.829	1.4–1.5	δ
7	1.414	0.7–0.9	ε
V_2O_5	2.801	0	α
delithiated V_2O_5	2.763	0	α

Table V.1. Li-ion content across different regions of an interconnected particle network as deduced from I_{t2g}/I_{eg} ratios in O K-edge XANES spectra. The expected phases based on extent of lithiation are also listed as sketched in figure V.1a

and phase propagation. Transport limitations appear to limit growth of the lithiated phase across the defect. In addition, these defects appear to be affecting secondary lithiation at the tips that are apparent in Figure V.2c. It is noteworthy that while tips represent regions amenable to secondary nucleation as shown in Figure V.2c, their propensity to further insert Li-ions and nucleate higher lithiated phases will be modified by the specifics of the local geometry. Figure V.3d shows considerable heterogeneity across the same nanowire with three distinct striped domains along the nanowire length corresponding to low, intermediate and high lithiation. Region 7, the thin nanowire, is lithiated to the ε-phase with a Li-ion concentration of *ca*. 0.7-0.9. Region 7 appears to be equilibrated with one of the domains (lithiated to an intermediate extent) of the thicker nanowires but not with the heavily lithiated domain at the center of nanowire. The phase separation across regions 6 and 7 illustrate again that particle size is not the sole predictor of extent of lithiation.

A more quantitative perspective of the extent of lithiation across the interconnected network is provided by Figure A.26, which illustrates the $\Delta\mu(E)$ spectra[50] corresponding to the differential between each spectral component and the O K-edge spectrum of unlithiated V_2O_5. The spectra have been aligned to the e_g* peak, and thus the most negative change of t_{2g} intensity represents the highest degree of lithiation. Table V.1 depicts the I_{t2g}/I_{eg} ratio and the Li-ion concentration as well the phase deduced from this analysis. It is noteworthy that even domains 4 and 5 are lithiated to some extent consistent with our previous observations that stabilization of the low-Li-content α-phase proceeds homogeneously.[24] Combining high-resolution transmission electron

microscopy[21,22,51] with scanning transmission X-ray microscopy will allow for combining the spatial resolution of the former method with the electronic structure sensitivity of the latter method and will be the focus of future work.

V.3.3 Phase Field Modeling of Heterogeneity Across Interconnected Particle Networks

The initial insertion of Li-ions within layered structures is driven by locally high current densities and likely has some initial stochasticity.[23] Subsequent lithiation is driven by stage ordering phenomena wherein insertion of Li-ions within the same expanded layer is preferred over intercalation within a pristine layer as long as diffusion within the layer is not impeded by structural deformations (such as layer collapse) induced by a defect.[10] Indeed, the existence of dislocations has been related to capacity loss of the material as a result of induced strain and stress.[52,53] The observations of lithiation gradients and phase heterogeneities across the interconnected particle networks illustrated in Figures V.2 and V.3 suggest that increasing Li-ion content inserted from the external flux results in supersaturation of the low-Li-ion-concentration (α) phase and that nucleation of the higher concentration ε or δ phases is initiated at specific sites within the interconnected network. Subsequently, these phases grow along specific nanowires while depleting interconnected nanowires and establishing considerable phase heterogeneity across the network. A phase-field diffusion-reaction model incorporating phase separation across interconnected multiple particles has been developed to explore the dynamics of nucleation and growth as observed here. The lithium diffusion inside each particle is subject to the Cahn—Hilliard equation:

$$\frac{\partial c^{(p)}}{\partial t} = \nabla \bullet \left[M^{(p)} \nabla \left(\mu^{(p)} - k^{(p)} \nabla^2 c^{(p)} \right) \right] \qquad \text{(EQUATION V.2)}$$

where the superscript p ranges from 1 to the total number of the considered particles, c is the normalized lithium concentration with respect to the maximum concentration, t is the time and M is the mobility. The term $k^{(p)}\nabla^2 c^{(p)}$ represents the interfacial energetic penalty so that the growth of domain interfaces within a particle is not favored. The bulk chemical potential μ takes the regular solution expression as:

$$\mu^{(p)} = RT\left[\ln\left(\frac{c^{(p)}}{1-c^{(p)}}\right) + x\left(1-2c^{(p)}\right)\right] \qquad \text{(EQUATION V.3)}$$

where R is the gas constant, T is the absolute temperature, x is a phase parameter, which will allow for the co-existence of two phases when it has the value greater than 2. On the particle-electrolyte interface, the EQUATION V.1 is considered with the simplification that $x = 1$. The flux on the particle-electrolyte interface is modeled through the modified Butler—Volmer equation as:[54]

$$j_{ely\to(p)} = \frac{s^{(p)}a_{ely}^{\beta}a_{(p)}^{(1-\beta)}}{\tau\gamma}\left\{\exp\left(-\beta\frac{F\eta}{RT}\right) - \exp\left[(1-\beta)\frac{F\eta}{RT}\right]\right\} \qquad \text{(EQUATION V.4)}$$

where s is the molar concentration of the intercalation sites on the surface, a is the activity of lithium in different environments, β is the a symmetry factor for a forward and backward reaction, γ is the chemical activity coefficient of the transition state, and F is the Faraday constant. The overpotential η is defined as $\Delta\phi - V_{oc} + \eta^{(p)}/F$, where $\Delta\phi$ is the electro-static potential difference between the electrode and the electrolyte and V_{oc} is the open circuit voltage. The flux across the particle-particle interface is modelled in a similar fashion as EQUATION V.4, where the overpotential is defined as the chemical difference between the two particles.

Phase field modelling is ideal to evaluate this system since it allows for the determination of phase formation and diffusion without being computationally prohibitive.[55,56] In previous work, phase field modelling has helped elucidate mechanically coupled phase separation effects during Li-ion intercalation.[57,58]

The model assumes diffusion occurs from a constant potential external bath into the nanowires and across interconnects as constrained by conditions for chemical lithiation. Figure V.4 indicates a sequence of concentration profiles modelled using this approach for a network of particles approximating the geometry seen in Figure V.2. Movie A.2 depicts the evolution of lithiation within this group of particles. As a result of the increased surface area and local activities, lithiation is initiated at the tip and

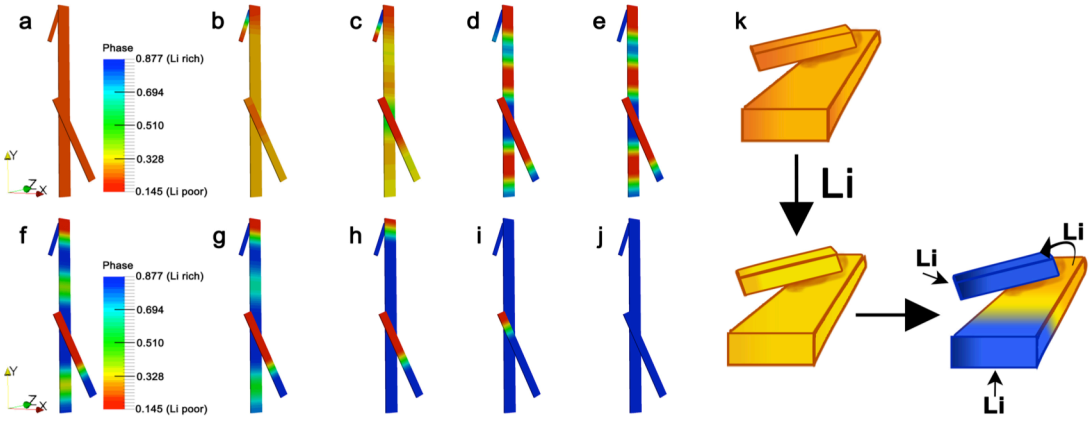

Figure V.4. Phase-field modeling of Li-ion insertion within an interconnected particle network. Li-ion diffusion within an interconnected particle network similar to Figure V.2 is simulated with a constant flux. (a)–(j) indicates snapshots from Movie A2. Lithiation starts with the smallest nanowire and indeed sections of other nanowires in contact with the actively lithiating domains are depleted. Once large domains adjacent to the interfaces have been homogenerously lithiated, secondary nucleation events are initiated are the tips as a result of high local potentials. Images (f) and (g) show concentration and phase profiles remarkably similar to Figure V.2. A schematic diagram of the proposed exchange evolution is shown in (k).

propagates across the nanowires. However, the contact area between the nanowires are important conduits for Li-ion transport and preferential lithiation of one nanowire occurs at the expense of an interfaced nanowire suggesting that the phase heterogeneity within the network is directly related to interparticle diffusion of Li-ions induced by the concentration-dependent phases. Movie A.3 and Figure A.27 compare the phase separation in the same two-particle configuration in two cases: in one case interparticle diffusion is allowed, whereas in the other case, the interface diffusion is prevented. Comparison of the results show clearly that when the particles are poorly connected, both particles get lithiated almost simultaneously, whereas a viable diffusion pathway between particles accelerates the lithiation of the smaller particle at the cost of the delayed lithiation of the bigger one.

Considering relevant numerical values, based on nudged elastic band density functional theory calculations, the diffusion coefficient for migration of Li-ions within α-V_2O_5 is 3.69×10^{-4} cm^2s^{-1}; this value reflects the migration barrier within the orthorhombic crystal structure assuming a perfect structure and is derived from the distortion of the structural framework upon Li-ion diffusion.[32] Experimental values measured for porous electrodes based on electrochemical analysis yields values of ca. 5.50×10^{-11} cm^2s^{-1}.[32,59,60] The differential arises in large measure from barriers to inter-particle transport and suggests that this parameter essentially entirely dominates diffusion within an electrode. Once a particle begins to lithiate, given a viable inter-particle diffusion pathway and the facile barrier to Li-ion diffusion within the single-crystalline domain, the lithiation front propagates across this particle before initiating

lithiation of an adjacent interconnected particle thereby resulting in phase separation across the network. Notably, this would not be true in the alternative extreme scenario where the diffusion of ions between particles is severely restricted; this would bring about the simultaneous lithiation of the interconnected particles without phase separation as observed in Figure A.27b. The experimentally observed distinct phase separation in the particles is thus attributed to the establishment of interfacial particle diffusion pathways. Furthermore, if lithiation were to proceed through stabilization of a continuous solid-solution (if nucleation and growth mechanisms were eliminated),[18,61] homogeneous nucleation would be expected across the network without manifestation of the phase heterogeneity observed here. This result suggests that the nature of interconnected networks assumes special significance for phase-transforming materials. As noted above, a change from phase-segregation to solid-solution process has been experimentally observed in $LiFePO_4$ at different rates of charging but has not been observed for V_2O_5 at the timescales examined thus far.[12,24] Figure V.4d suggests that after phase separation across interfaces, secondary nucleation events are preferentially initiated at the tips, mediated by the locally high potentials. Indeed, such events likely underpin the high Li-ion concentrations at the nanowire tips visible as hotspots in Figure V.2c. In particular, in Figure V.4f several aspects of phase heterogeneity observed in Figure V.2d are reproduced. For instance, the smallest particle (top left one) is first lithiated, and the interfaced part of the neighbouring particle (middle one) has a rather low extent of lithiation, which indicates a flux of lithation from the middle particle to the smaller particle. Next, the middle and the right particles start to be lithiated from their

particle tips. Finally, the middle particle appears to be drawing Li-ions from the right particle across the interface. Figure A.28 suggests that at low extents of lithiation, interconnected particles will relax to a homogeneous distribution, at intermediate lithiation, phase separation will occur predominantly across interfaces, and at high lithiation different domains will be stabilized within an individual nanowire.

In this model, the phase heterogeneity is considerably driven by kinetic barriers to phase nucleation. It is clear that the nature of interfaces strongly modify local activities and thus concentration profiles and the sequence of lithiation and ensuing phase transformation. In other words, the phase progression and dynamics of lithiation are greatly modified for a particle depending on its proximity and interface with adjacent particles in a network. The phase-field results are in concert with the acquired data through STXM for the subgroup of particles with the same arrangement (seen in Fig. V.2). The model reproduces the route taken by the Li-ions and the resulting spatial propagation of phase transformations across the interconnected particle network. Highly lithiated domains are stabilized preferentially at regions of high local current density such as tips and exchange occurs to the most thermodynamic favorable particle (most active material).

V.4 Conclusions

Mosaic instabilities and particle-by-particle intercalation have emerged as important constructs for understanding substantial heterogeneities in the concentration of actively intercalating particles and the sequence of phase transformations observed within cathode materials.[7,11,12,49,62,63,64] Using interconnected nanowires of V_2O_5, which

undergo a series of phase transformations with increasing lithiation, we demonstrate considerable heterogeneity of lithiation across domains of individual particles as well as across particles of an interconnected particle network. For the former, defects and structural distortions strongly influence Li-ion transport and thus phase nucleation and propagation. For the latter, we find that the nature of interconnects strongly modifies the phase heterogeneity and induces separation between Li-rich and Li-poor regions across interfaces. Once a system is supersaturated, nucleation of a high-Li-ion content occurs only on one side of the interface with concomitant depletion of the adjacent connected particle. The Li-rich phase subsequently propagates preferentially across a single nanowire instead of across the entire particulate network. Such a sequence is reproduced in phase-field simulations and suggests that phase separation across interfaces in interconnected networks stems in large measure from barriers to nucleating high Li-ion content phases. Secondary nucleation events are further facilitated at tips due to locally high activities. The propagation of Li-ions along "hot stripes" can be reconciled based on the stabilization of polarons and stage ordering within this system.[23,65,66] These findings suggest that mesoscale architectures can potentially be designed with interconnects to maximize the proportion of actively intercalating regions and to ensure better equilibration of local current densities.

V.5 References

(1) Goodenough, J. B. and Park, K.-S. The Li-ion rechargeable battery: a perspective. *J. Am. Chem. Soc.* **2013**, *135*, 1167–1176.

(2) Etacheri, V.; Marom, R.; Elazari, R.; Salitra, G.; and Aurbach, D. Challenges in

the development of advanced li-ion batteries: a review. *Energy Environ. Sci.* **2011**, *4*, 3243–3262.

(3) Whittingham, M. S. Lithium batteries and cathode materials. *Chem. Rev.* **2004**, *104*, 4271–4301.

(4) Ohzuku, T.; Ueda, A.; and Yamamoto, N. Zero-strain insertion material of $Li[Li_{1/3}Ti_{5/3}]O_4$ for rechargeable lithium cells. *J. Electrochem. Soc.* **1995**, *142*, 1431–1435.

(5) Ariyoshi, K.; Iwakoshi, Y.; Nakayama, N.; and Ohzuku, T. Topotactic two-phase reactions of $Li[Ni_{1/2}Mn_{3/2}]O_4(P4_332)$ in nonaqueous lithium cells. *J. Electrochem. Soc.* **2004**, *151*, A296–A303.

(6) Tarascon, J.-M. and Armand, M. Issues and challenges facing rechargeable lithium batteries. *Nature* **2001**, *414*, 359–367.

(7) Orvananos, B.; Ferguson, T. R.; Yu, H.-C.; Bazant, M. Z.; and Thornton, K. Particle-level modeling of the charge-discharge behavior of nanoparticulate phase-separating Li-ion battery electrodes. *J. Electrochem. Soc.* **2014**, *161*, A535–A546.

(8) Persson, K.; Sethuraman, V. A.; Hardwick, L. J.; Hinuma, Y.; Meng, Y. S.; van der Ven, A.; Srinivasan, V.; Kostecki, R.; and Ceder, G. Lithium diffusion in graphitic carbon. *J. Phys. Chem. Lett.* **2010**, *1*, 1176–1180.

(9) Dreyer, W.; Jamnik, J.; Guhlke, C.; Huth, R.; Moškon, J.; and Gaberšček, M. The thermodynamic origin of hysteresis in insertion batteries. *Nat. Mater.* **2010**, *9*, 448–453.

(10) Guo, Y.; Smith, R. B.; Yu, Z.; Efetov, D. K.; Wang, J.; Kim, P.; Bazant, M. Z.; and Brus, L. E. Li intercalation into graphite: direct optical imaging and Cahn-Hilliard reaction dynamics. *J. Phys. Chem. Lett.* **2016**, *7*, 2151–2156.

(11) Ferguson, T. R. and Bazant, M. Z. Nonequilibrium thermodynamics of porous electrodes. *J. Electrochem. Soc.* **2012**, *159*, A1967–A1985.

(12) Lim, J.; Li, Y.; Alsem, D. H.; So, H.; Lee, S. C.; Bai, P.; Cogswell, D. A.; Liu, X.; Jin, N.; Yu, Y.; et al. Origin and hysteresis of lithium compositional spatiodynamics within battery primary particles. *Science.* **2016**, *353*, 566 LP-571.

(13) Delmas, C.; Maccario, M.; Croguennec, L.; Le Cras, F.; and Weill, F. Lithium deintercalation in $LiFePO_4$ nanoparticles via a domino-cascade model. *Nat Mater* **2008**, *7*, 665–671.

(14) Brunetti, G.; Robert, D.; Bayle-Guillemaud, P.; Rouvière, J. L.; Rauch, E. F.; Martin, J. F.; Colin, J. F.; Bertin, F.; and Cayron, C. Confirmation of the domino-cascade model by $LiFePO_4/FePO_4$ precession electron diffraction. *Chem. Mater.* **2011**, *23*, 4515–4524.

(15) Chueh, W. C.; El Gabaly, F.; Sugar, J. D.; Bartelt, N. C.; McDaniel, A. H.; Fenton, K. R.; Zavadil, K. R.; Tyliszczak, T.; Lai, W.; and McCarty, K. F. Intercalation pathway in many-particle $LiFePO_4$ electrode revealed by nanoscale state-of-charge mapping. *Nano Lett.* **2013**, *13*, 866–872.

(16) Laffont, L.; Delacourt, C.; Gibot, P.; Wu, M. Y.; Kooyman, P.; Masquelier, C.; and Tarascon, J. M. Study of the $LiFePO_4/FePO_4$ two-phase system by high-resolution electron energy loss spectroscopy. *Chem. Mater.* **2006**, *18*, 5520–

5529.

(17) Badi, S.-P.; Wagemaker, M.; Ellis, B. L.; Singh, D. P.; Borghols, W. J. H.; Kan, W. H.; Ryan, D. H.; Mulder, F. M.; and Nazar, L. F. Direct synthesis of nanocrystalline $Li_{0.90}FePO_4$: observation of phase segregation of anti-site defects on delithiation. *J. Mater. Chem.* **2011**, *21*, 10085–10093.

(18) Liu, H.; Strobridge, F. C.; Borkiewicz, O. J.; Wiaderek, K. M.; Chapman, K. W.; Chupas, P. J.; and Grey, C. P. Capturing metastable structures during high-rate cycling of $LiFePO_4$ nanoparticle electrodes. *Science.* **2014**, *344*, 1–7.

(19) Luo, W.; Wang, Y.; Chou, S.; Xu, Y.; Li, W.; Kong, B.; Dou, S. X.; Liu, H. K.; and Yang, J. Critical thickness of phenolic resin-based carbon interfacial layer for improving long cycling stability of silicon nanoparticle anodes. *Nano Energy* **2016**, *27*, 255–264.

(20) Fang, Y.; Xiao, L.; Qian, J.; Cao, Y.; Ai, X.; Huang, Y.; and Yang, H. 3D graphene decorated $NaTi_2(PO_4)_3$ microspheres as a superior high-rate and ultracycle-stable anode material for sodium ion batteries. *Adv. Energy Mater.* **2016**, *6*, 2–9.

(21) Li, B.; Qi, R.; Zai, J.; Du, F.; Xue, C.; Jin, Y.; Jin, C.; Ma, Z.; and Qian, X. Silica wastes to high-performance lithium storage materials: a rational designed Al_2O_3 coating assisted magnesiothermic process. *Small* **2016**, *12*, 5281–5287.

(22) Li, B.; Li, X.; Zai, J.; and Qian, X. Facile synthesis of porous Zn–Sn–O nanocubes and their electrochemical performances. *Nano-Micro Lett.* **2016**, *8*, 174–181.

(23) De Jesus, L. R.; Horrocks, G. A.; Liang, Y.; Parija, A.; Jaye, C.; Wangoh, L.; Wang, J.; Fischer, D. A.; Piper, L. F. J.; Prendergast, D.; and Banerjee, S. Mapping polaronic states and lithiation gradients in individual V_2O_5 nanowires. *Nat. Commun.* **2016**, *7*, 12022:1–9.

(24) Horrocks, G. A.; Braham, E. J.; Liang, Y.; De Jesus, L. R.; Jude, J.; Velázquez, J. M.; Prendergast, D.; and Banerjee, S. Vanadium K-edge X-ray absorption spectroscopy as a probe of the heterogeneous lithiation of V_2O_5: first-principles modeling and principal component analysis. *J. Phys. Chem. C* **2016**, *120*, 23922–23932.

(25) Nanda, J.; Remillard, J.; O'Neill, A.; Bernardi, D.; Ro, T.; Nietering, K. E.; Go, J. Y.; and Miller, T. J. Local state-of-charge mapping of lithium-ion battery electrodes. *Adv. Funct. Mater.* **2011**, *21*, 3282–3290.

(26) Whittingham, M. S. Electrical energy storage and intercalation chemistry. *Science.* **1976**, *192*, 1126–1127.

(27) Marley, P. M.; Horrocks, G. A.; Pelcher, K. E.; and Banerjee, S. Transformers: the changing phases of low-dimensional vanadium oxide bronzes. *Chem. Commun.* **2015**, *51*, 5181–5198.

(28) Chernova, N. A.; Roppolo, M.; Dillon, A. C.; and Whittingham, M. S. Layered vanadium and molybdenum oxides: batteries and electrochromics. *J. Mater. Chem.* **2009**, *19*, 2526–2552.

(29) Wang, Z.; Su, Q.; and Deng, H. Single-layered V_2O_5 a promising cathode material for rechargeable Li and Mg ion batteries: an ab initio study. *Phys. Chem.*

Chem. Phys. **2013**, *15*, 8705–8709.

(30) Whittingham, M. S. The role of ternary phases in cathode reactions. *J. Electrochem. Soc.* **1976**, *123*, 315–320.

(31) Horrocks, G. A.; Likely, M. F.; Velazquez, J. M.; and Banerjee, S. Finite size effects on the structural progression induced by lithiation of V_2O_5: a combined diffraction and Raman spectroscopy study. *J. Mater. Chem. A* **2013**, *1*, 15265–15277.

(32) Parija, A.; Liang, Y.; Andrews, J.; De Jesus, L. R.; Prendergast, D.; and Banerjee, S. Topochemically de-intercalated phases of V_2O_5 as cathode materials for multivalent intercalation batteries: a first-principles evaluation. *Chem. Mater.* **2016**, *28*, 5611–5620.

(33) Satto, C.; Sciau, P.; Dooryhee, E.; Galy, J.; and Millet, P. The $\delta \rightarrow \varepsilon \rightarrow \gamma$ LiV_2O_5 "high temperature" phase transitions evidenced by synchrotron x-ray powder diffraction analysis. *J. Solid State Chem.* **1999**, *109*, 103–109.

(34) Galy, J.; Satto, C.; Sciau, P.; and Millet, P. Atomic modeling of the $\Delta \Leftrightarrow \varepsilon$ LiV_2O_5 phase transition and simulation of the XRD powder pattern evolution. *J. Solid State Chem.* **1999**, *146*, 129–136.

(35) Galy, J. Vanadium pentoxide and vanadium oxide bronzes—structural chemistry of single (S) and double (D) layer $M_xV_2O_5$ phases. *J. Solid State Chem.* **1992**, *100*, 229–245.

(36) Whittingham, M. S. and Dines, M. B., n-Butyllithium—an effective, general cathode screening agent. *J. Electrochem. Soc.* **1977**, *124*, 1387–1388.

(37) Chan, C. K.; Peng, H.; Twesten, R. D.; Jarausch, K.; Zhang, X. F.; and Cui, Y. Fast, completely reversible Li insertion in vanadium pentoxide nanoribbons. *Nano Lett.* **2007**, *7*, 490–495.

(38) Schillinger, D. and Ruess, M. The finite cell method: a review in the context of higher-order structural analysis of CAD and image-based geometric models. *Arch. Comput. Methods Eng.* **2015**, *22*, 391–455.

(39) Smith, A. P.; Ade, H. W.; Lidy, W.; Rightor, E. G.; and Mitchell, G. E. NEXAFS spectromicroscopy of polymers: overview and quantitative analysis of polyurethane polymers. *J. Electron Spectros. Relat. Phenomena* **1999**, *100*, 119–135.

(40) Ade, H. and Hitchcock, A. P. nexafs microscopy and resonant scattering: composition and orientation probed in real and reciprocal space. *Polymer* **2008,** *49*, 643–675.

(41) Yang, F.; Liu, Y.; Martha, S. K.; Wu, Z.; Andrews, J. C.; Ice, G. E.; Pianetta, P.; and Nanda, J. Nanoscale morphological and chemical changes of high voltage lithium-manganese rich NMC composite cathodes with cycling. *Nano Lett.* **2014**, *14*, 4334–4341.

(42) Boesenberg, U.; Meirer, F.; Liu, Y.; Shukla, A. K.; Dell'Anna, R.; Tyliszczak, T.; Chen, G.; Andrews, J. C.; Richardson, T. J.; Kostecki, R.; et al. mesoscale phase distribution in single particles of $LiFePO_4$ following lithium deintercalation. *Chem. Mater.* **2013**, *25*, 1664–1672.

(43) Maganas, D.; Roemelt, M.; Hävecker, M.; Trunschke, A.; Knop-Gericke, A.;

Schlögl, R.; and Neese, F. First principles calculations of the structure and V L-edge X-ray absorption spectra of V_2O_5 using local pair natural orbital coupled cluster theory and spin-orbit coupled configuration interaction approaches. *Phys. Chem. Chem. Phys.* **2013**, *15*, 7260–7276.

(44) Velazquez, J. M.; Jaye, C.; Fischer, D. A.; and Banerjee, S. Near edge X-ray absorption fine structure spectroscopy studies of single-crystalline V_2O_5 nanowire arrays. *J. Phys. Chem. C* **2009**, *113*, 7639–7645.

(45) Goering, E.; Müller, O.; Klemm, M.; denBoer, M. L.; and Horn, S. Angle dependent soft-x-ray absorption spectroscopy of V_2O_5. *Philos. Mag. B* **1997**, *75*, 229–236.

(46) Tolhurst, T. M.; Leedahl, B.; Andrews, J. L.; Marley, P. M.; Banerjee, S.; and Moewes, A. Contrasting 1D tunnel-structured and 2D layered polymorphs of V_2O_5: relating crystal structure and bonding to band gaps and electronic structure. *Phys. Chem. Chem. Phys.* **2016**, *18*, 15798–15806.

(47) Wang, J. J.; Yang, J.; Tang, Y.; Liu, J.; Zhang, Y.; Liang, G.; Gauthier, M.; Chen-Wiegart, Y. K.; Norouzi Banis, M.; Li, X.; et al. Size-dependent surface phase change of lithium iron phosphate during carbon coating. *Nat. Commun.* **2014**, *5*, 3415:1-8.

(48) Weker, J. N.; Liu, N.; Misra, S.; Andrews, J. C.; Cui, Y.; and Toney, M. F. In situ nanotomography and operando transmission x-ray microscopy of micron-sized Ge particles. *Energy Environ. Sci.* **2014**, *7*, 2771-2777.

(49) Abdellahi, A.; Akyildiz, O.; Malik, R.; Thornton, K.; and Ceder, G. Particle-size

and morphology dependence of the preferred interface orientation in $LiFePO_4$ nano-particles. *J. Mater. Chem. A* **2014**, *2*, 15437-15447.

(50) Love, C. T.; Korovina, A.; Patridge, C. J.; Swider-Lyons, K. E.; Twigg, M. E.; and Ramaker, D. E. Review of $LiFePO_4$ phase transition mechanisms and new observations from x-ray absorption spectroscopy. *J. Electrochem. Soc.* **2013**, *160*, A3153–A3161.

(51) Zai, J.; Liu, Y.; Li, X.; Ma, Z.; Qi, R.; and Qian, X. 3D Hierarchical Co–Al layered double hydroxides with long-term stabilities and high rate performances in supercapacitors. *Nano-Micro Lett.* **2017**, *9*, 1–9.

(52) Ulvestad, A.; Singer, A.; Clark, J. N.; Cho, H. M.; Kim, J. W.; Harder, R.; Maser, J.; Meng, Y. S.; and Shpyrko, O. G. Topological defect dynamics in operando battery nanoparticles. *Science.* **2015**, *348*, 1344–1347.

(53) Shadow Huang, H.-Y. and Wang, Y.-X. Dislocation based stress developments in lithium-ion batteries. *J. Electrochem. Soc.* **2012**, *159*, A815.

(54) Zhao, Y.; Xu, B.-X.; Stein, P.; and Gross, D. Phase-field study of electrochemical reactions at exterior and interior interfaces in Li-ion battery electrode particles. *Comput. Methods Appl. Mech. Eng*. **2016**, *312*, 428–446.

(55) Moelans, N.; Blanpain, B.; and Wollants, P. An introduction to phase-field modeling of microstructure evolution. *Calphad* **2008**, *32*, 268–294.

(56) Zhao, Y.; Stein, P.; and Xu, B.-X. Isogeometric analysis of mechanically coupled cahn-hilliard phase segregation in hyperelastic electrodes of Li-ion batteries. *Comput. Methods Appl. Mech. Eng.* **2015**, *297*, 325–347.

(57) Xu, B.-X.; Zhao, Y.; and Stein, P. Phase field modeling of electrochemically induced fracture in Li-ion battery with large deformation and phase segregation. *GAMM-Mitteilungen* **2016**, *39*, 92–109.

(58) Stein, P.; Zhao, Y.; and Xu, B.-X. Effects of surface tension and electrochemical reactions in Li-ion battery electrode nanoparticles. *J. Power Sources* **2016**, *332*, 154–169.

(59) Song, J.; Kim, J.; Kang, T.; and Kim, D. Design of a porous cathode for ultrahigh performance of a Li-ion battery: an overlooked pore distribution. *Sci. Rep.* **2017**, *7*, 42521-42528.

(60) Song, H. M.; Yoo, D. Y.; Hong, S. K.; Kim, J. S.; Cho, W. I.; and Mho, S. I. Electrochemical impedance analysis of V_2O_5 and pedot composite film cathodes. *Electroanalysis* **2011**, *23*, 2094–2102.

(61) Malik, R.; Zhou, F.; and Ceder, G. Kinetics of non-equilibrium lithium incorporation in $LiFePO_4$. *Nat. Mater.* **2011**, *10*, 587–590.

(62) Dreyer, W.; Guhlke, C.; and Huth, R. The Behavior of a many-particle electrode in a lithium-ion battery. *Phys. D Nonlinear Phenom.* **2011**, *240*, 1008–1019.

(63) Li, Y.; El Gabaly, F.; Ferguson, T. R.; Smith, R. B.; Bartelt, N. C.; Sugar, J. D.; Fenton, K. R.; Cogswell, D. A.; Kilcoyne, A. L. D.; Tyliszczak, T.; et al. Current-induced transition from particle-by-particle to concurrent intercalation in phase-separating battery electrodes. *Nat. Mater.* **2014**, *13*, 1149–1156.

(64) Zhou, H.; An, K.; Allu, S.; Pannala, S.; Li, J.; Bilheux, H. Z.; Martha, S. K.; and Nanda, J. Probing multiscale transport and inhomogeneity in a lithium-ion pouch cell using in situ neutron methods. *ACS Energy Lett.* **2016**, *1*, 981–986.

(65) Ioffe, V.A. and Patrina, I. B. Comparison of the small-polaron theory with the experimental data of current transport in V_2O_5. *Phys. Status Solidi* **1970,** *389*, 389–395.

(66) Franchini, C.; Kresse, G.; and Podloucky, R. Polaronic hole trapping in doped $BaBiO_3$. *Phys. Rev. Lett.* **2009**, *102*, 6–9.

CHAPTER VI

SUMMARY AND OUTLOOK

Electrodes of intercalation batteries are dynamically evolving entities that inevitably present time-dependent compositional heterogeneities. Diffusion limitations in cathode materials arise from ionic, electronic, and coupled ionic—electronic origins. Atomistic barriers such as constricted transition states and the stabilization of polarons influence the nucleation and propagation of intercalation-induced phase transformations and thereby lead to multiscale heterogeneities. In this dissertation, we have used α-V_2O_5 as a model system to develop mechanistic ideas of the origins of diffusion limitations making extensive reference to X-ray absorption/emission spectroscopy studies of local structure, STXM mapping of compositional domains, and first-principles DFT calculations. In addition, a limited study of graphene anode materials is also presented. The multiscale gridlock derived from ionic diffusion barriers, low electron mobilities, stabilization of polarons, and sequence of intercalation-induced transformations observed in V_2O_5 has many parallels in other transition metal oxide cathodes given commonalities in electron correlation and electronic conduction reliant on narrow 3d bands. Understanding the coupling of ionic, electronic, and thermal transport requires multiscale understanding spanning the range from atomistic phenomena to phase transitions within single particles and the sequential/parallel evolution of a network of interconnected particles. Achieving the facile diffusion of multivalent cations represents an especially formidable challenge given their higher ability to polarize the host lattices.

The rational design of electrode chemistries and architectures to mitigate diffusion limitations would benefit greatly from deeper mechanistic understanding. *Ex situ* measurements are frequently unable to capture the full complexity of phenomena manifested under operational conditions and oftentimes do not precisely describe metastable states, surface diffusion, and intermediate configurations mediating cation diffusion. *In situ* measurements that have started to become available are clearly imperative to bridge this critical gap in our understanding of these systems. Furthermore, redox processes at transition metal sites are distinctively sensitive to peculiarities of electronic structure and the stabilization and evolution of specific hybrid states at the conduction band edge. Understanding how electronic structure is correlated with atomistic structure and mapping its spatiotemporal evolution during charge/discharge processes is thus of fundamental importance to mechanistic understanding.

Several approaches to mitigate diffusion limitations are proposed based on current mechanistic understanding. First, nanostructuring and reduction of particle size can suppress phase boundaries and allow for single-phase lithiation (below a critical size for phase separation), curtail solid-state diffusion path lengths that have to be traversed by ions and polarons, and allow for better accommodation of strain induced by compositional gradients. Mesoscale inverse design approaches are necessary to define 3D architectures that can homogeneously intercalate Li- and multivalent cations. Alternatively, metastable phases of V_2O_5 provide access to a rich palette of structures with differently structured cation diffusion pathways and varying extents of covalency, thereby allowing for precise atomic-scale tunability of electron and ion diffusion. A vast

compositional space of metastable phases remains to be explored and makes available a considerable expanse of design space wherein design elements such as frustrated coordination and rigid sub-units can be sought. Combining the two approaches, through nanostructuring of metastable phases, also holds considerable promise as does surface exfoliation and the construction of atomically engineered 2D architectures. Multiscale design taking into consideration atomistic and electronic structure and spanning the range from single-particle phenomena to precise mesoscale structuring of networks is imperative to circumvent the many limitations of current energy storage constructs.

APPENDIX A

SUPPLEMENTARY FIGURES AND TABLES

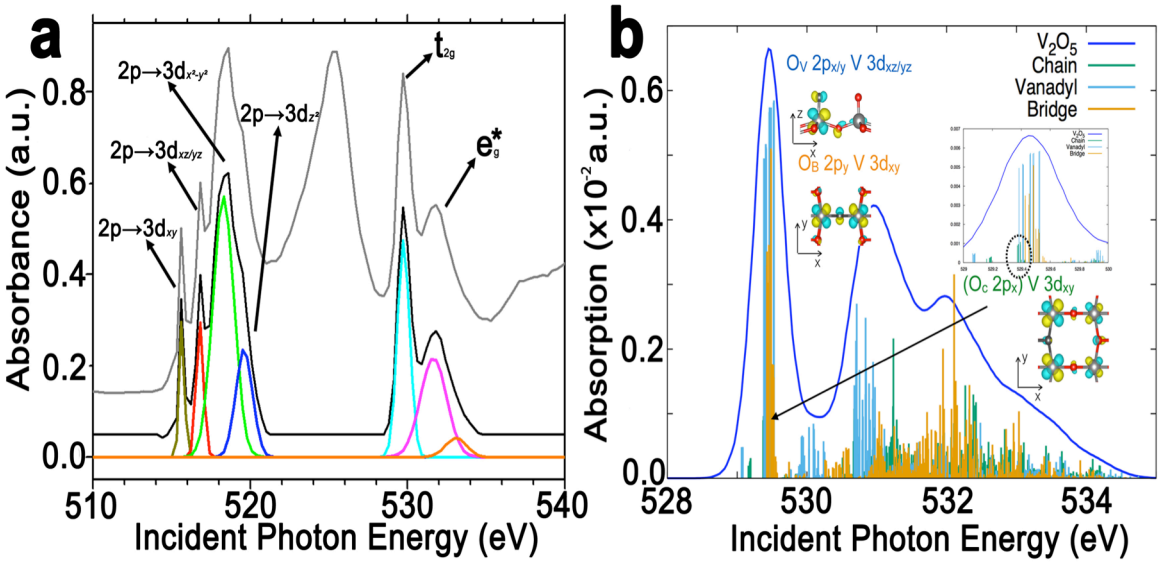

Figure A.1. Peak assignments for V L- and O K-edge X-ray absorption near edge structure (XANES) Spectra (a) Assignments of V L_{III}-edge spectral features to specific transitions measured for an individual V_2O_5 nanowire (b) *Ab-initio* calculated spectrum for V_2O_5 depicting major contributors for the t_{2g} and e_g* peaks at the O K-edge.

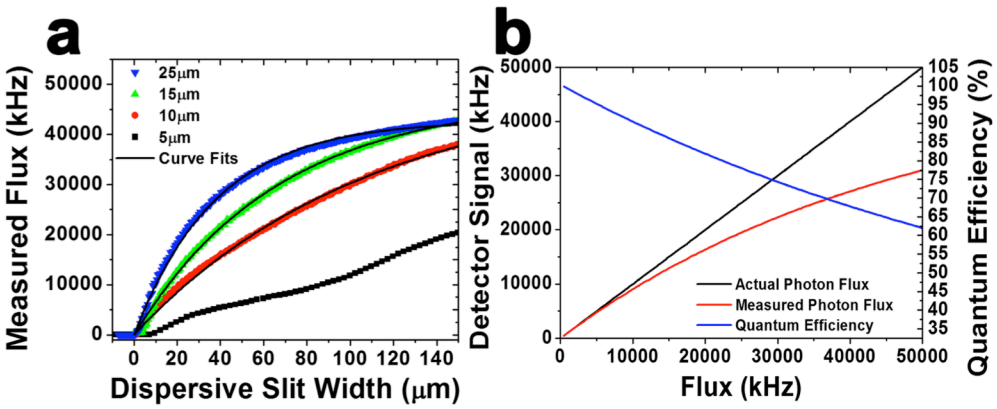

Figure A.2. Corrections for Detector Nonlinearity (a) Detector response as a function of dispersive slit widths for specified non-dispersive slit widths (5, 10, 15, and 25 μm). The latter three plots have been fitted by the function indicated as Equation III.5. The fits are indicated by solid lines. (b) Measured flux and quantum efficiency as a function of actual photon flux for a non-dispersive slit width of 25 μm.

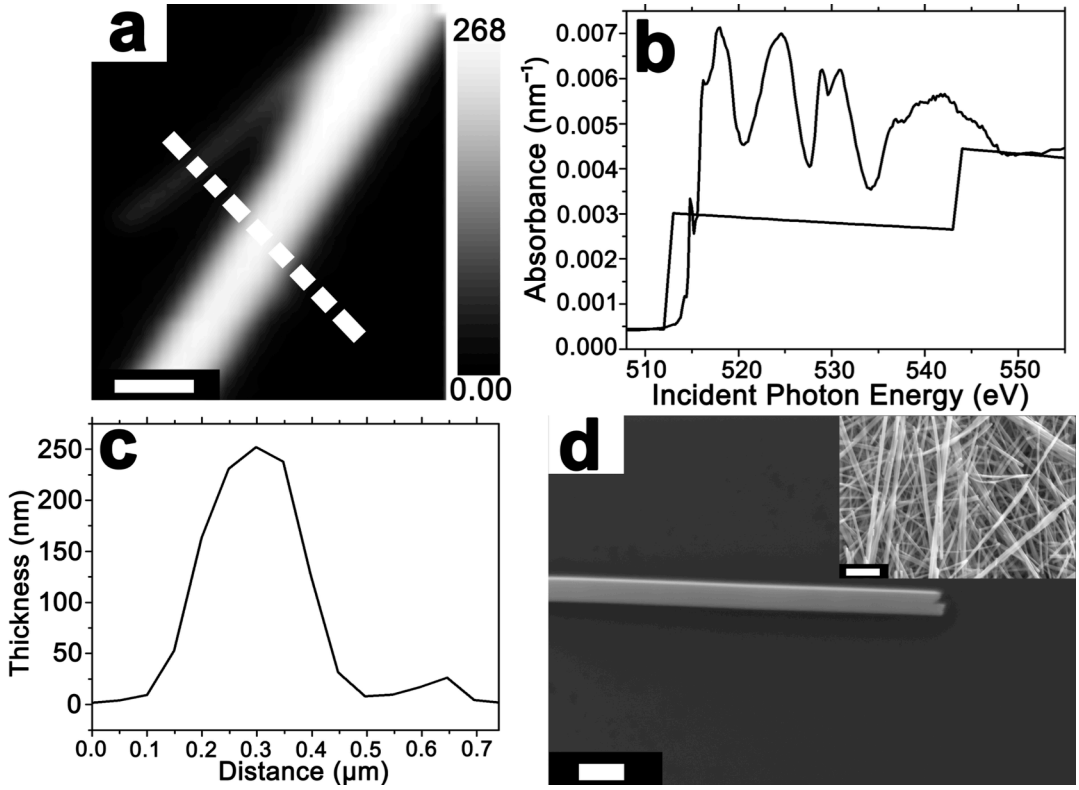

Figure A.3. V L- and O K-edge chemical imaging of a single lithiated V_2O_5 nanowire Thickness map (a) for a 1 min lithiated V_2O_5 nanowire where the gray scale represents the thickness in nm (scale bar, 200 nm), the dashed line represents the section surveyed in (c). Linearly scaled reference spectrum for $Li_xV_2O_5$ (b) used to construct the thickness map. High-resolution scanning electron microscopy images of a single V_2O_5 nanowire depicting a uniform rectangular cross-section (d) (scale bar, 200 nm).

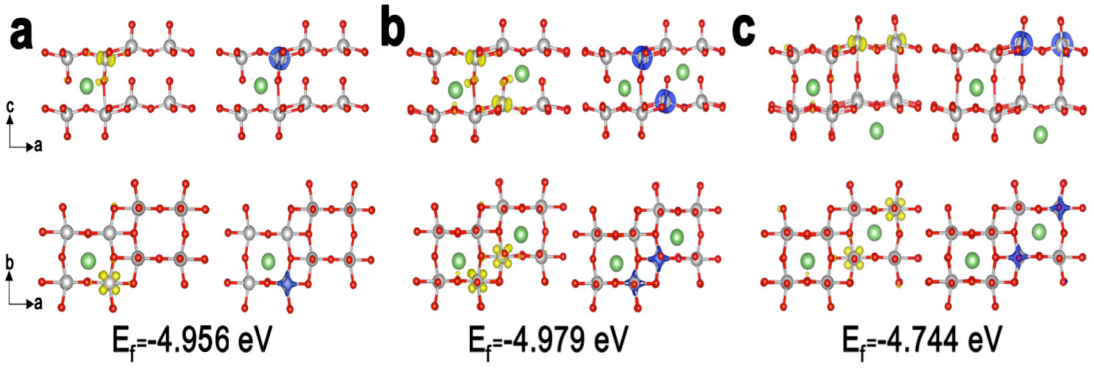

Figure A.4. Stage Ordering of Li-ion Insertion Charge density differences calculated for V_2O_5 with one intercalated Li-ion (a), two Li-ions incorporated within the same layer (b), and two Li-ions incorporated in alternate layers (c). The increase of charge density is depicted in yellow and decrease of charge density is depicted in blue. The increased charge density is observed to trace the contours of the V $3d_{xy}$ orbital. The decrease in charge density is localized between the bonds showing polarization of the bonds between V–O bonding. The calculated formation energies depict a preference for successive lithiation of the same layer, as compared to alternate layers.

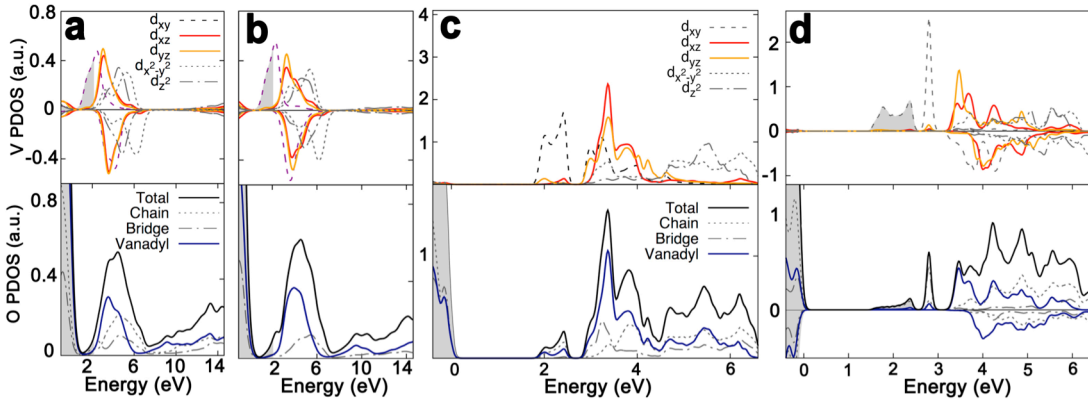

Figure A.5. Projected density of states (pDOS) (a) α-LiV_2O_5 and (b) δ-LiV_2O_5 Supplementary Figure III.4 demonstrates the impact of stacking order on the pDOS. It can be seen that in both cases the spin-up and –down channel are split much in the same manner, except that the d_{xz}-component blueshifts (red curves) to higher energies in δ-LiV_2O_5. This is because the relative gliding of the V_2O_5 layer in δ-LiV_2O_5 causes the inserted Li-ion to situate at the mid-point of two dangling vanadyl oxygens, which substantially magnifies the lattice distortion on the *ac* plane. pDOS broadened with 0.03 eV for (c) V_2O_5 and (d) α-LiV_2O_5. This directly corresponds to the calculated Fig. III.3. Two spin-components are shown for α-LiV_2O_5. The DFT+*U* calculation predicts that the lifting of spin degeneracy causes the spin-up and –down components of 3d states to be split by ca. 0.7 eV. The large spin-channel splitting is also evident in the oxygen 2p states, which is the primary cause for the diminution of the sharp t_{2g} resonance in the O K-edge absorption spectra.

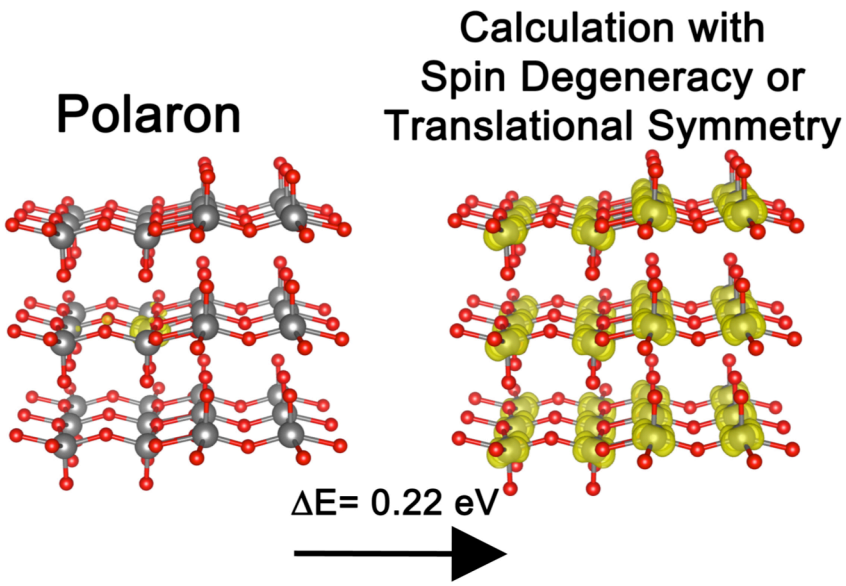

Figure A.6. Charge localization upon addition of a single electron in pristine V_2O_5 The polaron formation in the V_2O_5 structure is dependent of the electron spin. Enforcing spin-degeneracy on a supercell of V_2O_5 results in charge delocalization throughout V_2O_5 and a total energy increase of roughly 0.22 eV for the supercell with 24 V atoms. This suggests the polaron is energetically favorable due to correlation effects and is stabilized *via* symmetry breaking mechanisms.

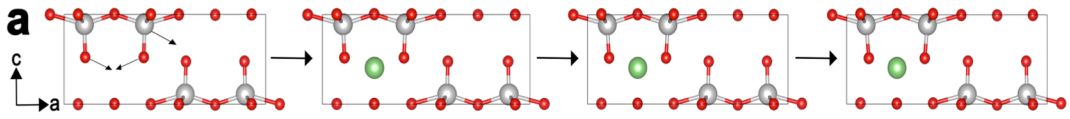

Figure A.7. Structural Distortion Induced by Polaronic Confinement A schematic depiction of the transformation of a single unit cell of V_2O_5 upon intercalation of a Li-ion. A sequence of structural changes is depicted with puckering of the apical oxygen towards the lithium ion and rearrangement of the vanadium ions away from the intercalated Li-ion. Movie A.1 illustrates the distortions induced in V_2O_5 upon lithiation.

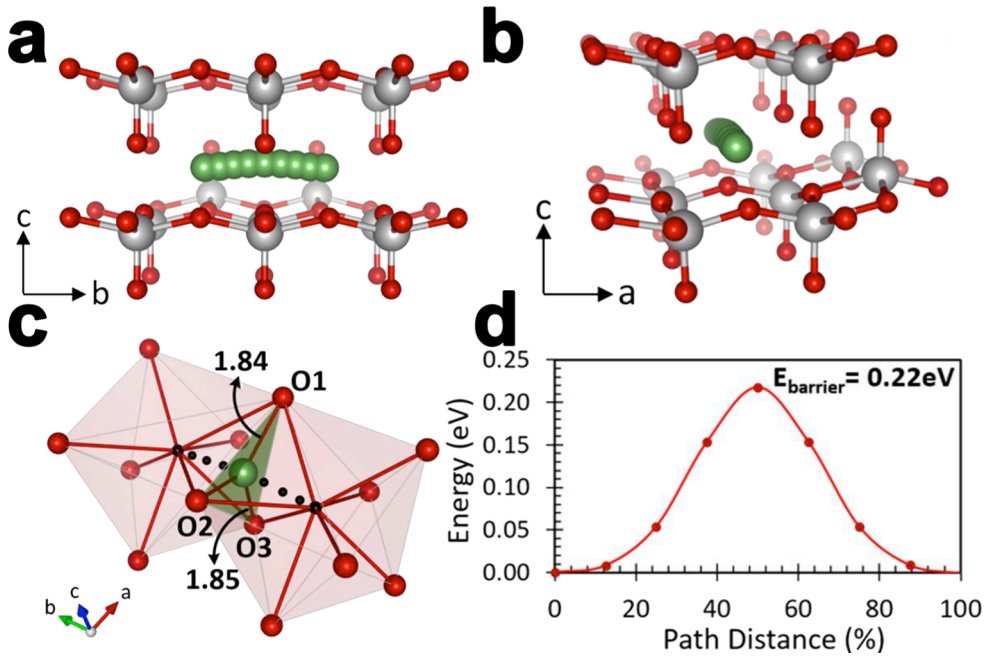

Figure A.8. Nudged elastic band studies of Li-ion Diffusion Pathways Schematic depicting the migration pathway adopted by a Li-ion along the *b*-axis; as observed along the *a*-axis (a) and the *b*-axis (b). A view of the oxygen coordination environment at the transition state in α-V_2O_5 (c). The minimum diffusion pathway energy is calculated to be 0.22 eV for a Li-ion moving along the *b*-axis of α-$Li_xV_2O_5$ (d).

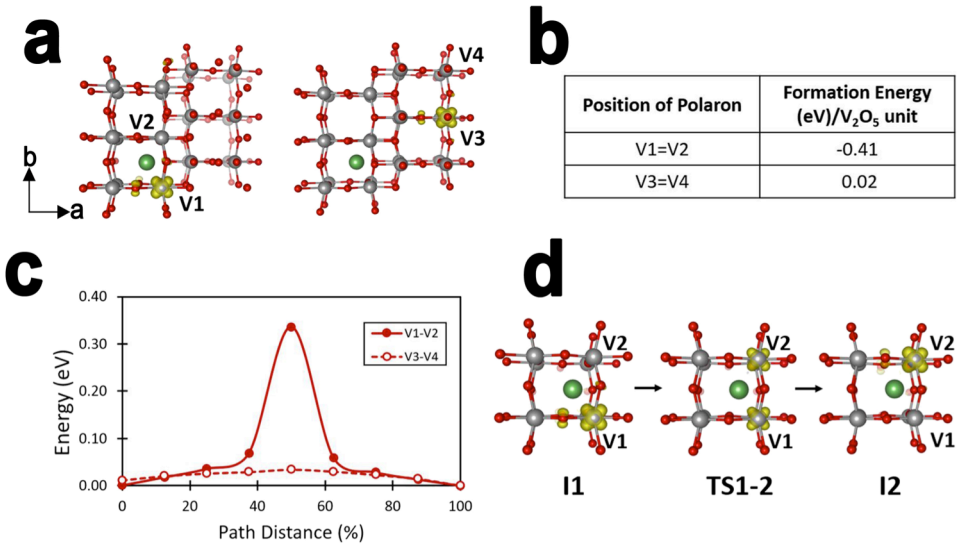

Figure A.9. Nudged elastic band studies of V^{4+} polaron diffusion pathways (a) The formation of a polaron at position V1 (or V2) close to the Li-ion or positions V3 and V4 relatively far from the Li-ion. (b) Tabulated values of formation energies for the two configurations depicted in (a). (c) Calculated migration barriers for hopping of polarons situated at (V1, V2) sites in proximity of the Li-ion (solid line) and relatively far away from the Li-ion (V3, V4) (dashed lines). The steps involved in polaron diffusion are depicted in (d) All the orbitals are plotted at a value of electron density equal to 0.015 $eÅ^{-3}$.

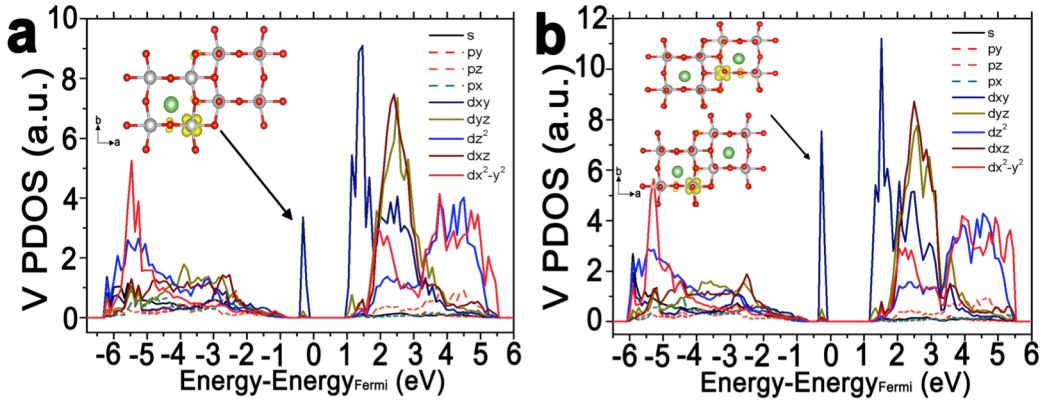

Figure A.10. Orbital-projected density of states for V_2O_5 with one- or two-inserted Li-ions A "mid-gap" state is observed to appear within the bandgap as a result of lithiation and is experimentally corroborated by the HAXPES results shown in Figure III.5.

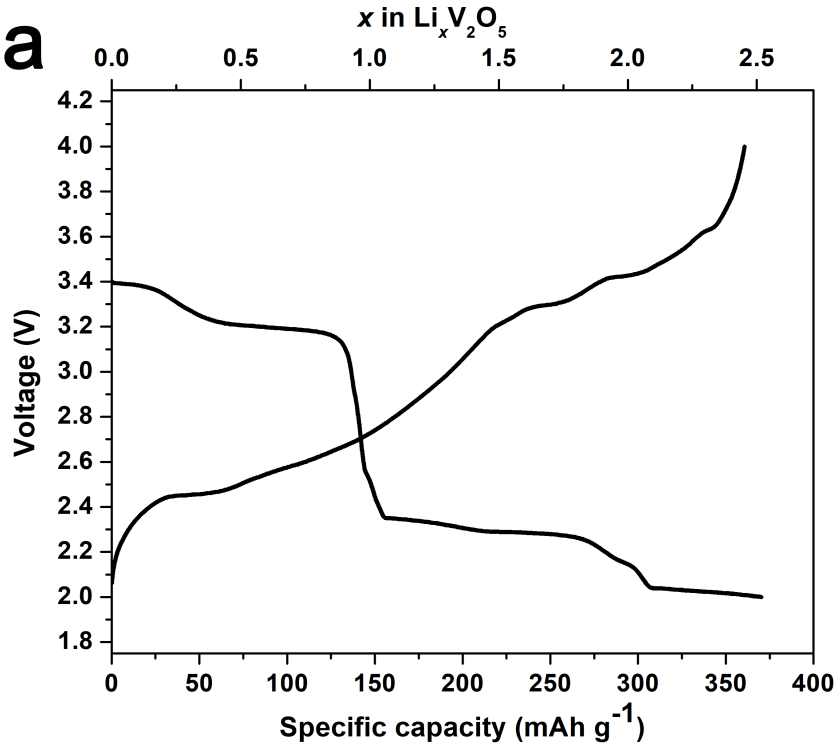

Figure A.11. Galvanostatic charge−discharge curves measured for V_2O_5 in a coin-cell configuration at a constant 0.2 C rate. The plateaus correspond to distinctive intercalation-induced phase transitions in V_2O_5: α→ε at 3.4 V, ε→δ at 3.2 V, and δ→γ at 2.3 V.

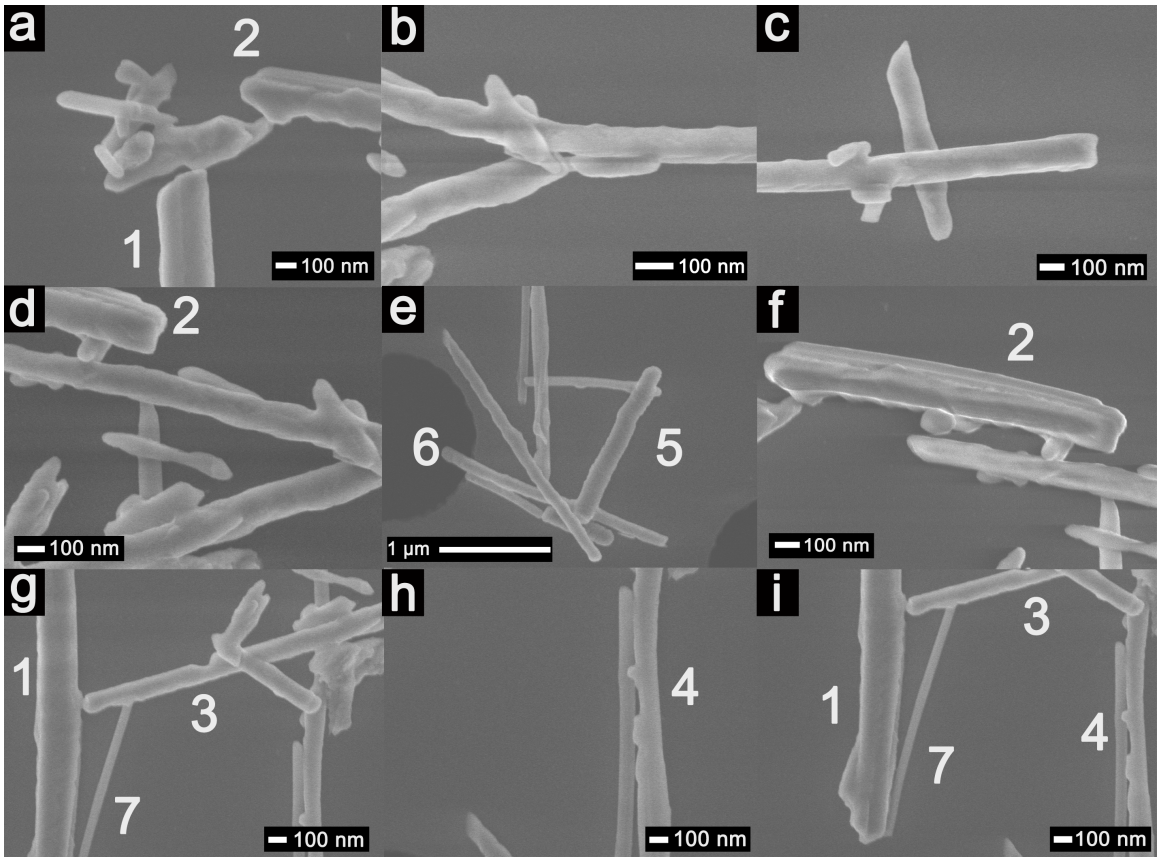

Figure A.12. High-resolution SEM images of the cluster of wires imaged by STXM . High-resolution images of segments of the interlaced wires depicted in Figure IV.2a. The segments are numbered as in Figures IV.2 and IV.3.

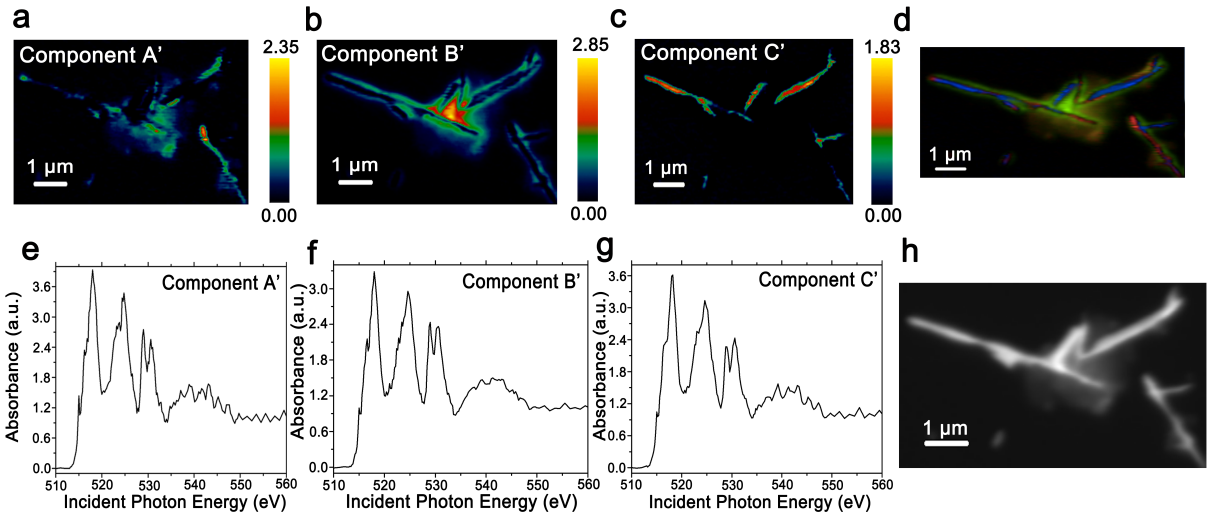

Figure A.13. Intensity maps derived from region-of-interest singular value decomposition of electrochemically lithiated samples at a discharge of 2.75 V. a–c) Intensity maps depict the location of the spectral signatures, Components A'—C' plotted in (e)-(g). (d) An overlay of the three spectral components illustrating the compositional and phase heterogeneity across the interconnected network. Red, green, and blue regions demarcate majority contributions at the specific pixel from spectral components in (e), (f), and (g), respectively. h) Integrated STXM image of the cluster of wires.

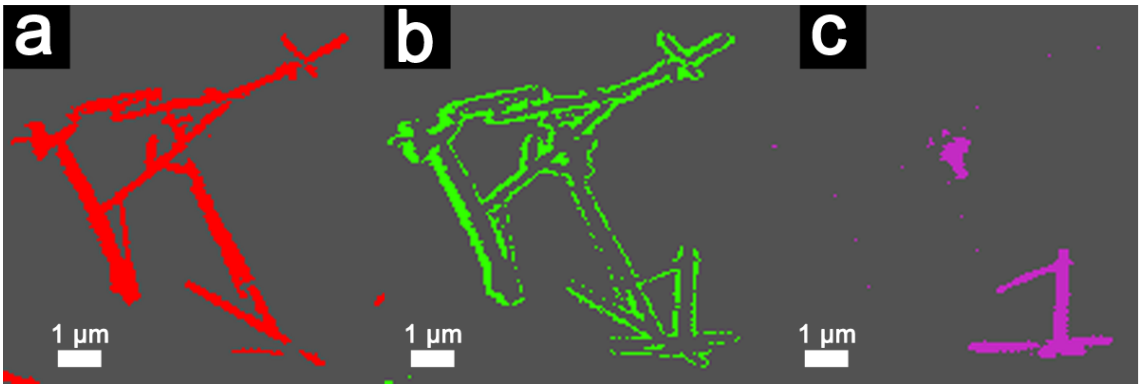

Figure A.14. Spatial Distribution of Components III—V as Deduced from PCA analysis of Hyperspectral STXM Data Acquired for an Ensemble of Lithiated V_2O_5 Nanowires. (a)–(c) show the spatial location of the separated components III—V generated by PCA of the hyperspectral stack. The corresponding eigenspectra are plotted in Fig. IV.2e.

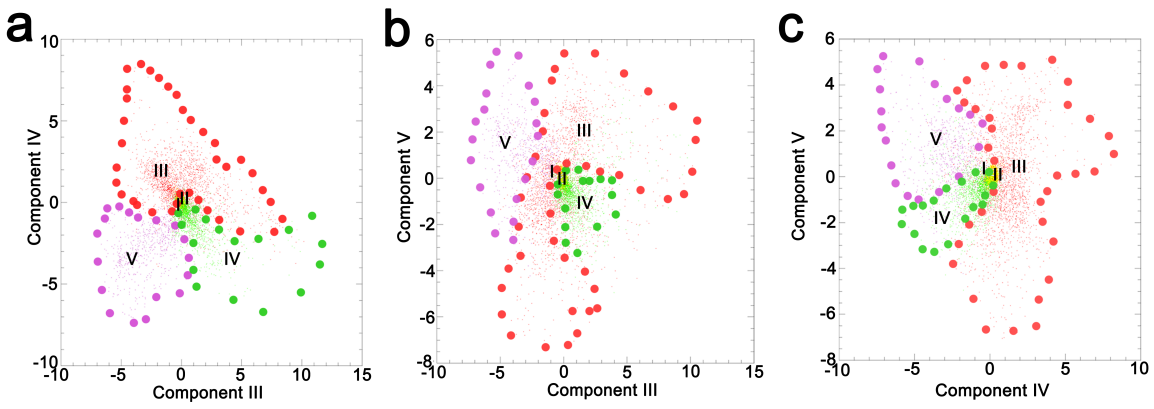

Figure A.15. Clustering of pixels in PCA analysis and spatial profiles of individual principal components. (a)–(c) show the comparison between components in terms of separation of generated pixels by PCA of the hyperspectral stack. Blue and yellow represent background components, whereas III, IV, and V correspond to the components with eigenspectra plotted in Figure IV.2e. Dotted lines establishing boundaries are guides to the eye.

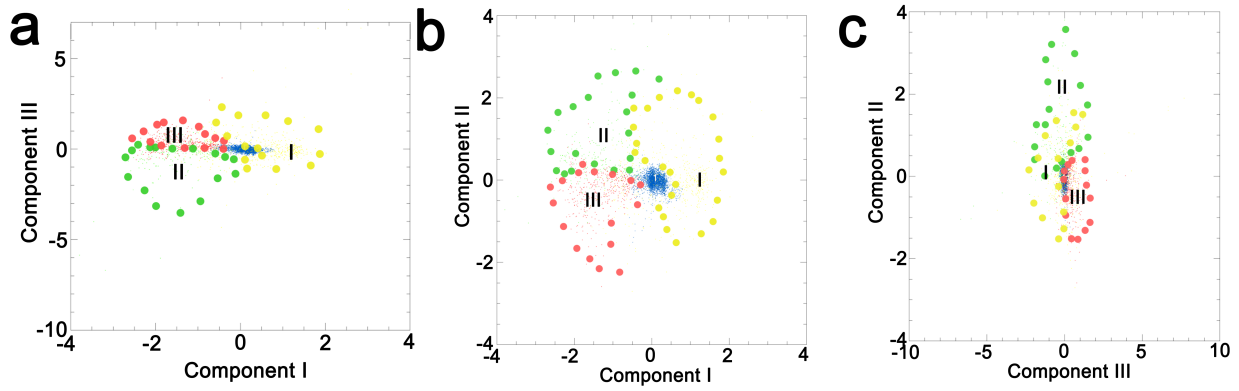

Figure A.16. PCA Analysis of STXM data acquired for an individual V_2O_5 nanowire after 1 min of chemical lithiation (an average composition of $Li_{0.28\pm0.07}V_2O_5$ is deduced based on ICP-MS analysis). (a–c) Scatter plots depicting the scores at each pixel for each of the three components. The analysis allows for effective classification of each of the pixel to three components. Dotted lines serve as a guide to the eyes.

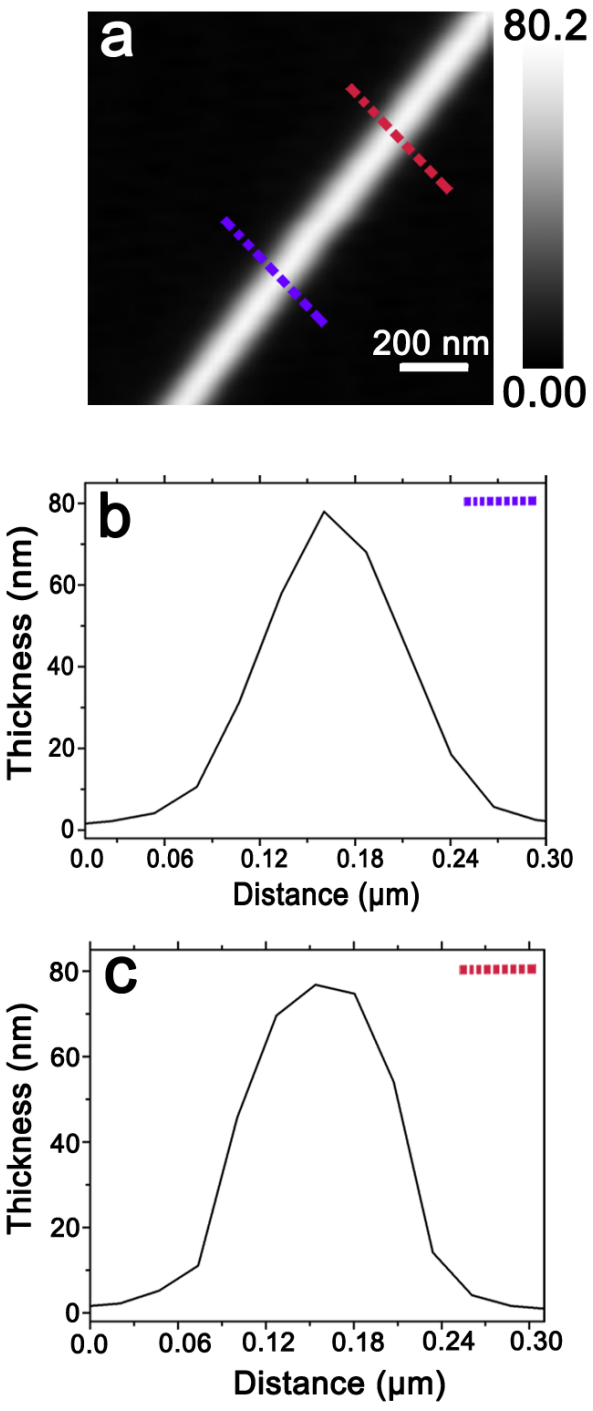

Figure A.17. Thickness map of an individual chemically lithiated V_2O_5 nanowire that is 245 nm in diameter. (a) Thickness map of the chemically lithiated V_2O_5 nanowire depicted in Figure IV.4., where the gray scale bar depicts the thickness in nm. The colored dashed lines represent the cross-sections measured in (b) and (c).

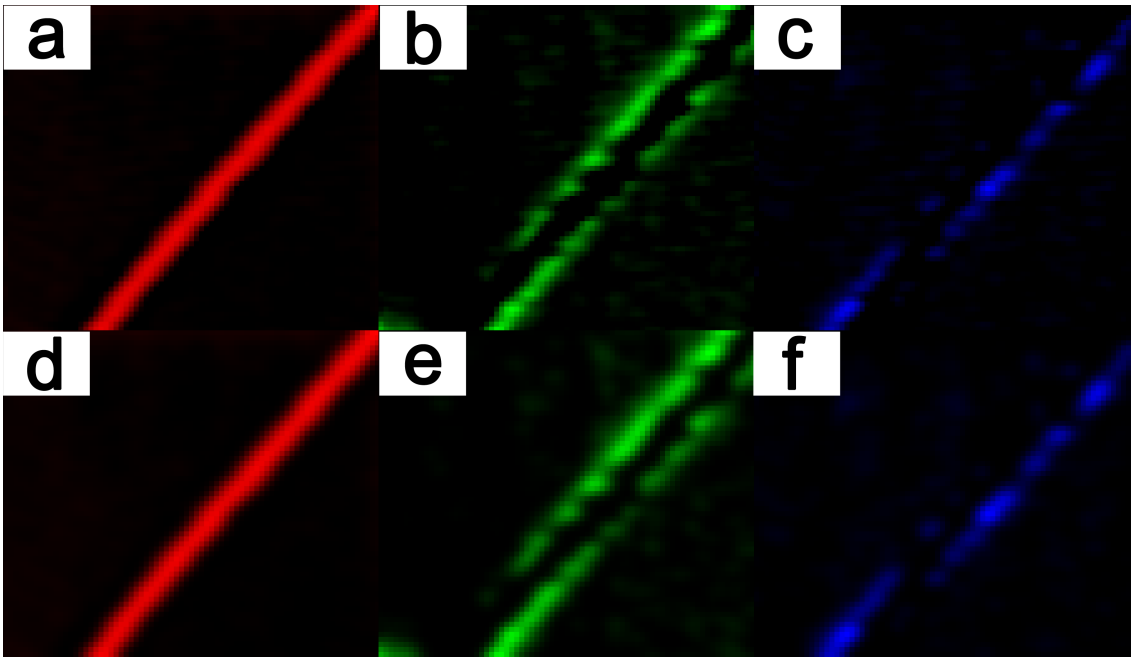

Figure A.18. Conversion of STXM scan data into a composition map. The normalized intensities in (a)–(c) were subjected to Gaussian filtering in order to remove noise (d)–(f).

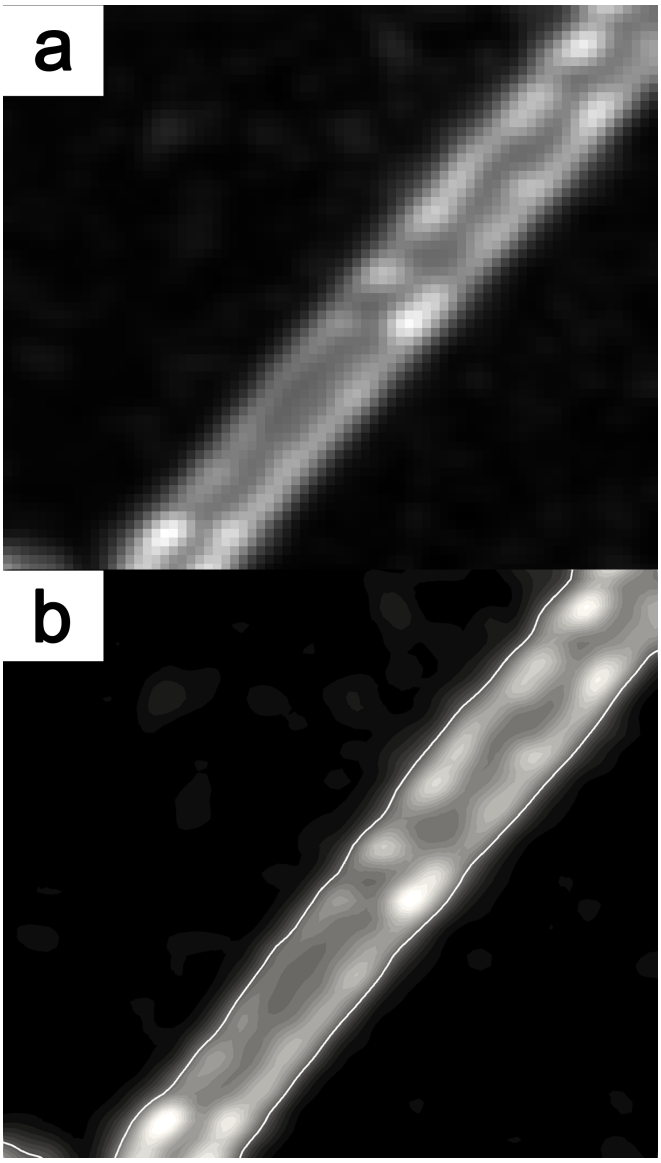

Figure A.19. Superposition of the filtered intensities. Using the stoichiometry fractions x_i as weighting factors, yields the distribution of x over the pixel space (a). Bilinear interpolation of the pixel data yields a smooth composition map in pixel space, from which the outlines of the nanowire geometry have been extracted using a Marching Cubes algorithm (b).

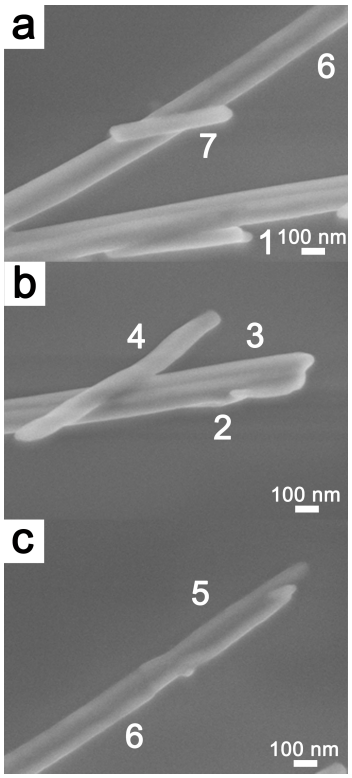

Figure A.20. Magified high-resolution SEM images of a cluster of lithiated particles. High-resolution SEM images providing a magnified view of the particle cluster shown in Figure V.1a. (a) Regions 1, 2, 3, 6, and 7; (b) region 4 sits atop regions 2 and 3 (intimate contact with 3); and (c) an imperfection (screw dislocation or surface step) separates one nanowire into regions 5 and 6.

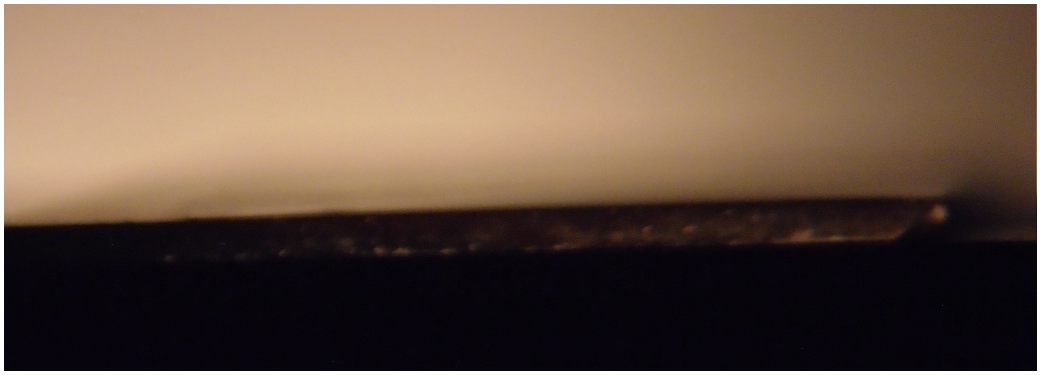

Figure A.21. Contact angle measurement of pristine V_2O_5 with a droplet of hexanes. Contact angle measurements for hexanes on a layer of V_2O_5 nanowires suggests immediate and complete spreading of the liquid droplet to a contact angle of 0°.

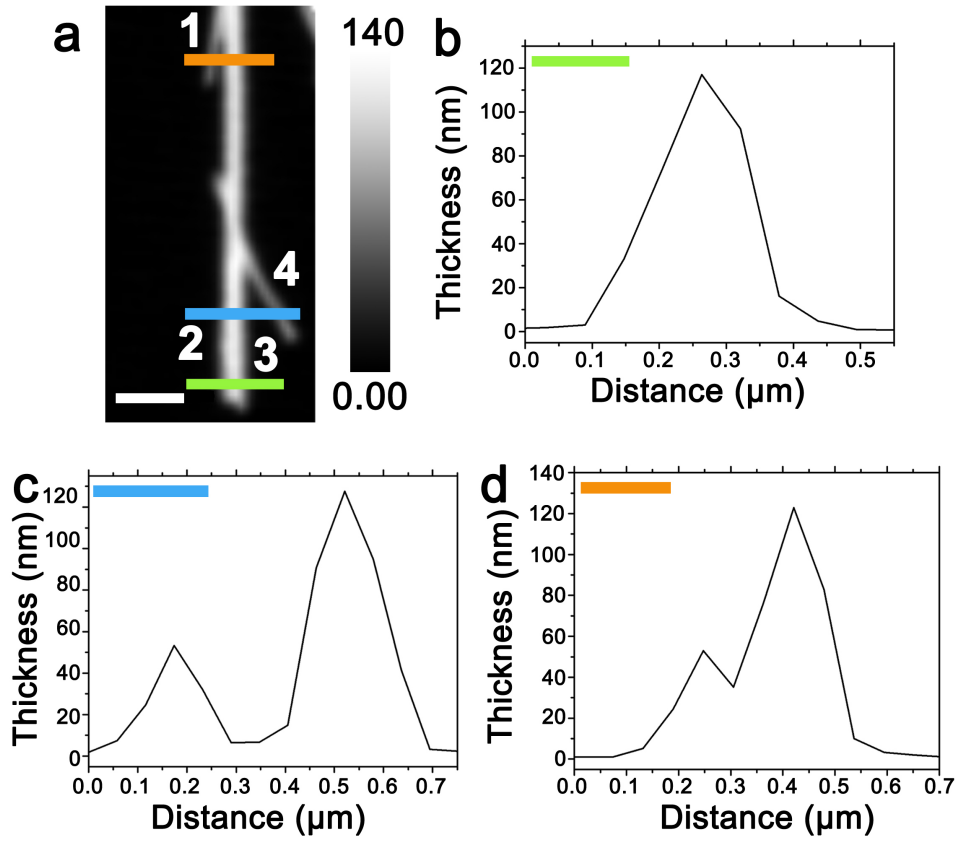

Figure A.22. Mapping of optical density in regions 1-4. Thickness map (a) for regions 1-4 correlated directly to Figure V.2.; the gray scale represents the thickness in nanometers. Several line profiles acquired across the optical density image are plotted and allow for elucidation of nanowire thicknesses of (b) regions 2-3; (c) regions 2-4, and (d) regions 1-3.

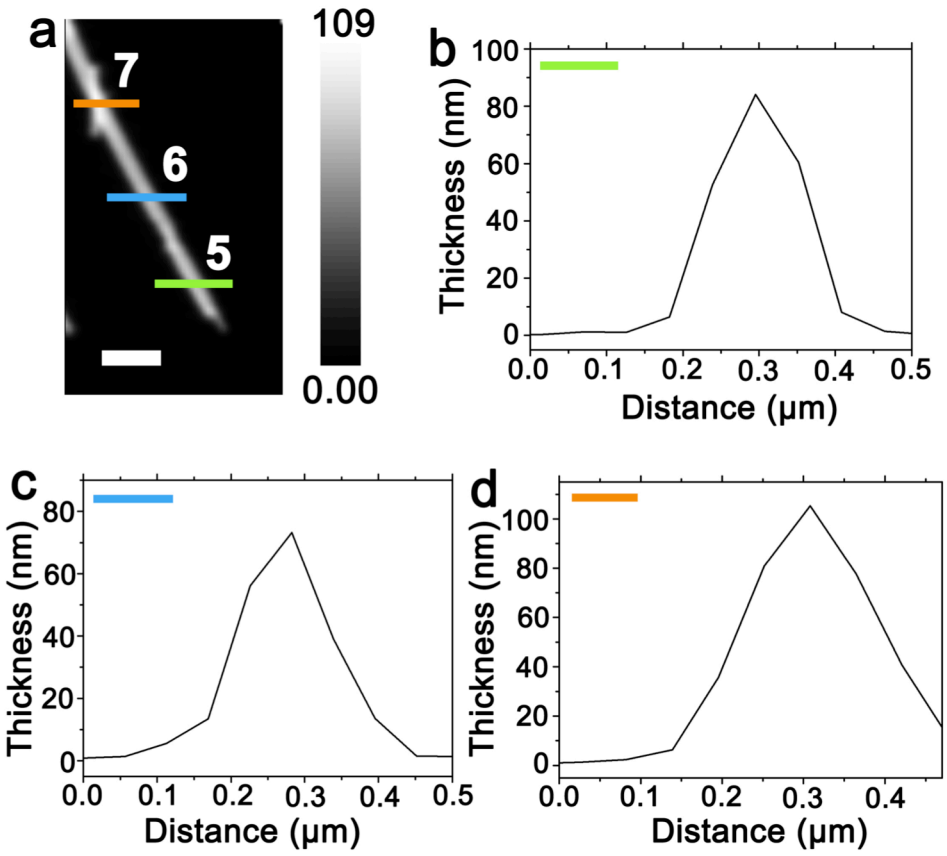

Figure A.23. Mapping of optical density in regions 5-7. Thickness map (a) for regions 5—7 correlated directly to figure 3; the gray scale represents the thickness in nm. Several line profiles acquired across the optical density image are plotted and allow for elucidation of nanowire thicknesses of (b) region 5; (c) region 6, and (d) region 7.

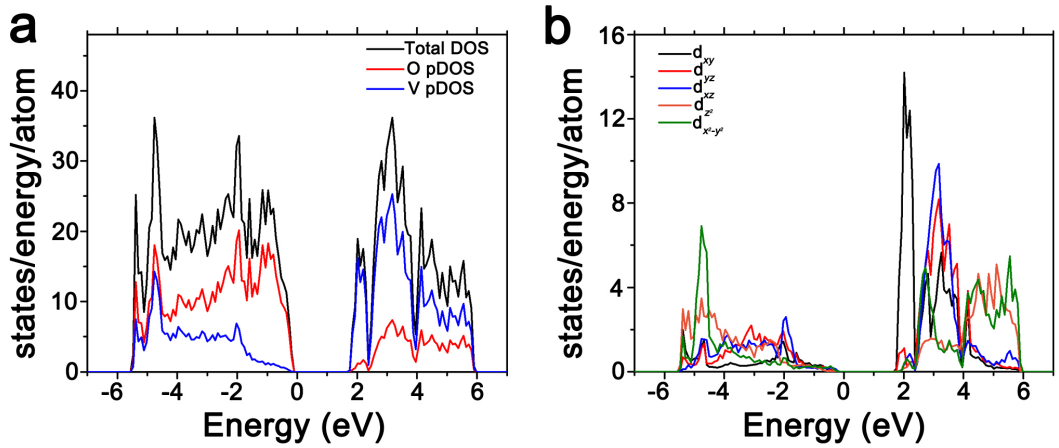

Figure A.24. Atom and orbital-projected density of states of V_2O_5. a) atom-projected density of states of V_2O_5 as calculated from density functional theory. The top of the valence band has predominantly O 2p character, whereas the bottom of the conduction band has predominantly V 3d character. b) Orbital-projected density of states indicating the splitting of the t_{2g} ($3d_{xy}$, $3d_{xz}$, and $3d_{yz}$) and e_g ($3d_{z2}$, $3d_{x2-y2}$) states as also indicated in Figure V.1e.

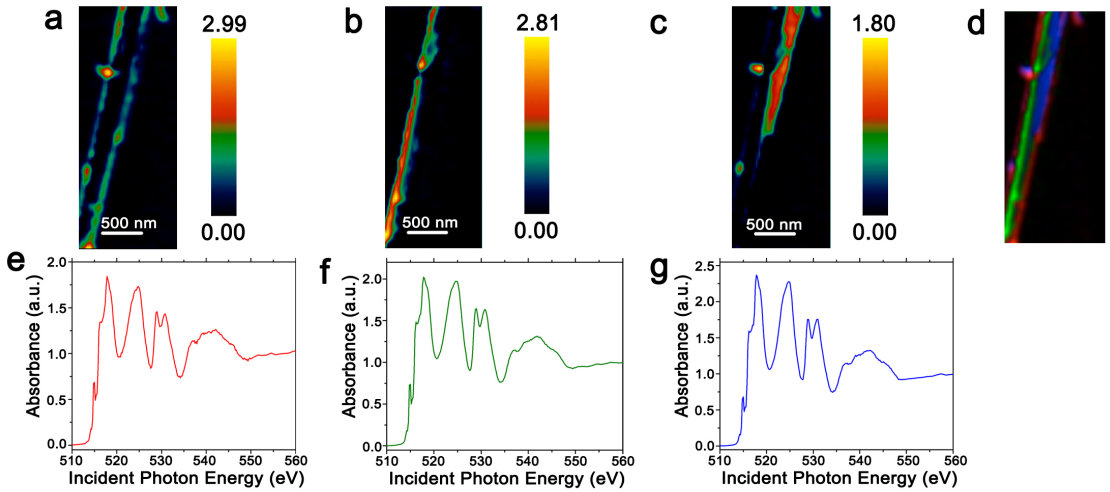

Figure A.25. Evaluating electronic structure inhomogeneities and phase separation in V_2O_5 nanowires with extended interfaces. STXM mapping of lithiation profiles across a bundle of closely interfaced nanowires. (a)–(c) depict maps of three spectral components identified by singular value decomposition analysis that are plotted in (e)–(g). While three spectral profiles can be resolved, they are closely related and correspond to the high Li-content δ-phase of $Li_xV_2O_5$. (d) An overlay of the three spectral components illustrating slight variations along the length of the nanowires.

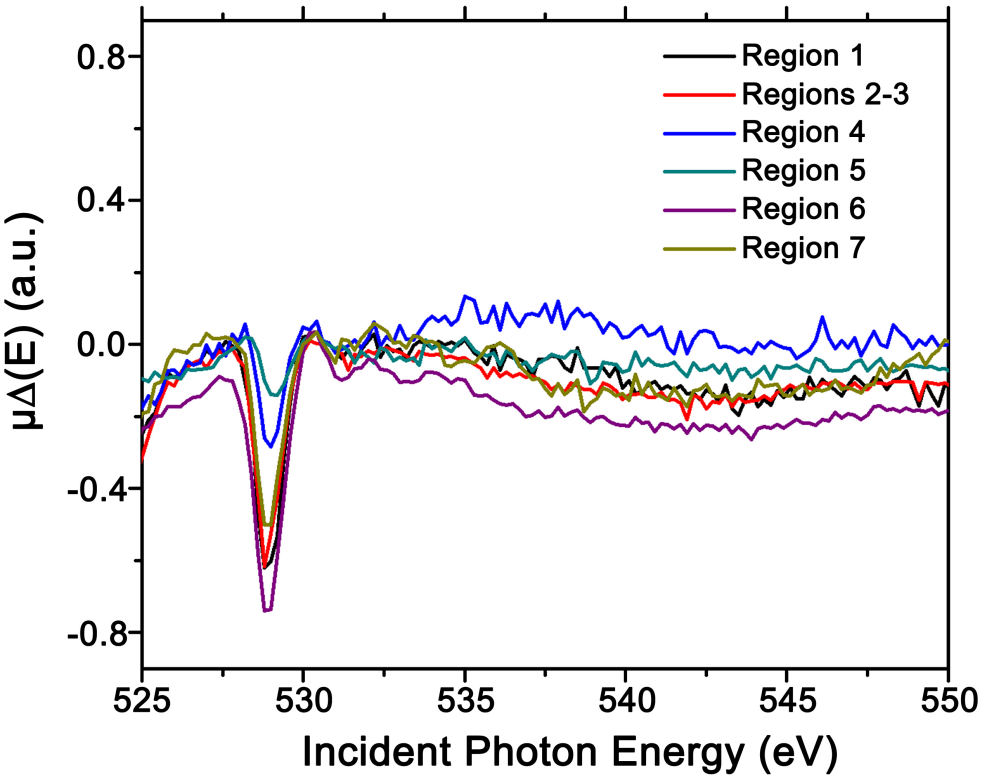

Figure A.26. Differential XANES Analysis of Spectral Data. The spectrum for an unlithiated sample was subtracted to the spectrum found for each region of the cluster of wires in Figure V.1. All the spectra have been normalized to the e_g absorption feature. The relative intensities allow for assignment of approximate Li-ion concentration.

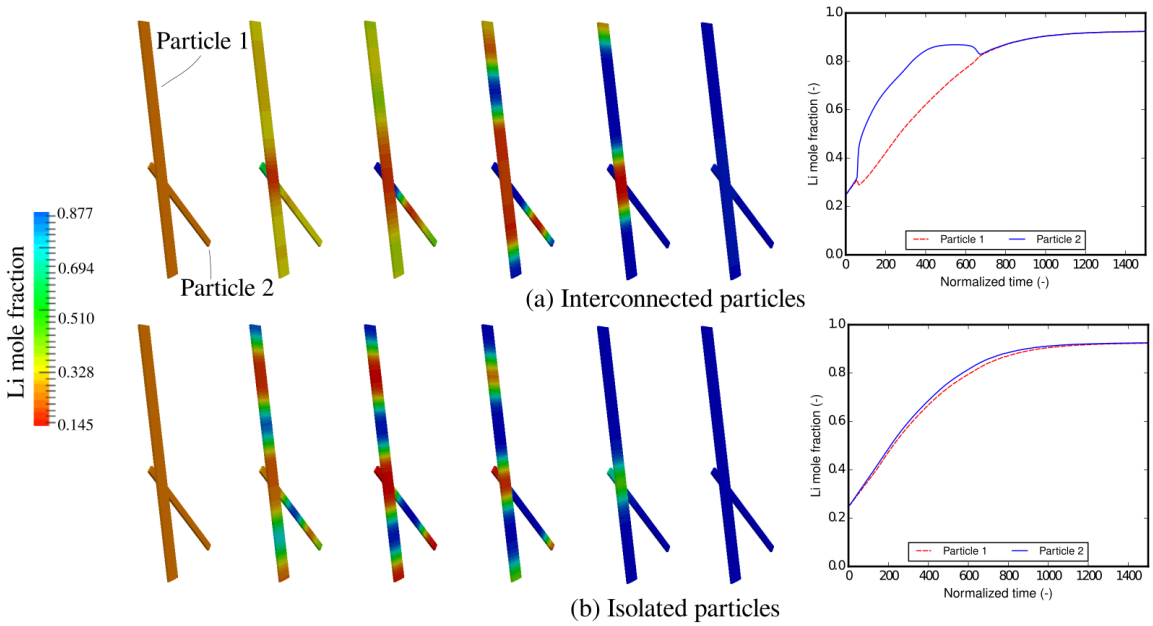

Figure A.27. Lithiation in the networks of two particles interconnected to each other (a) and isolated from one other (b). The particles are immersed in a lithium bath with constant potential and lithiated from a homogeneous lithium fraction of 0.25. The contour plots show the snapshots as a function of elapsed time. The curves show the evolution of lithium fraction in each particle: dashed line represents the larger particle, whereas the solid line represents the smaller particle. It is clear that during lithiation, isolated particles experience intraparticular phase separation and are fully lithiated almost at the same time, whereas in interconnected networks with interparticle diffusion allowed it is clear that the smaller particle gets lithiated faster than the connected particle.

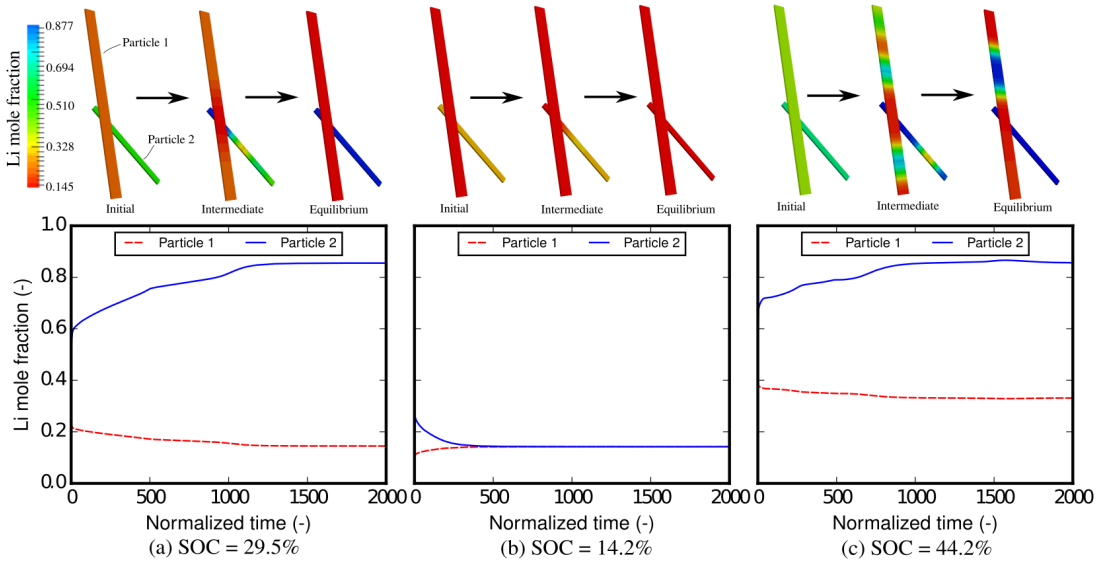

Figure A.28. Relaxation of interconnected two particles from non-equilibrium solid-solution with different overall State of Charge (SOC). Contour plots in the upper row show the sequence of relaxation with three different given initial SOC. Curves in the lower row show the respective lithium concentrations in each particle. The blue solid curve represents the smaller particle, whereas the dashed red curve represents the larger particle. The interparticular phase separation occurs when the overall lithium concentration stays in the spinodal region, as shown in (a). On the other hand, when the overall lithium concentration is too low, the complete network will merge into a homogeneous phase, as shown in (b). With increased overall concentration, as shown in (c), phase separation also appears inside a single particle at equilibrium.

Components	Cluster weights 1	Cluster weights 2	Cluster weights 3	Cluster weights 4	Cluster weights 5
I	0.104 (31.84%)	-0.0704 (21.62%)	0.0398 (12.21%)	-0.0858 (26.34%)	-0.0260 (7.99%)
II	1.75 (47.31%)	-1.62 (43.82)	-0.125 (3.38%)	0.166 (4.49%)	0.0372 (1.00%)
III	9.17 (75.36%)	1.74 (14.33%)	-0.0822 (0.68%)	0.948 (7.79%)	-0.225 (1.85%)
IV	4.19 (54.27%)	-1.10 (14.26%)	0.794 (10.28%)	-1.10 (13.09%)	-0.627 (8.11%)
V	7.51 (49.88%)	1.08 (7.20%)	-2.86 (18.99%)	-2.76 (18.31%)	0.846 (5.62%)

Table A.1. Summary of the cluster weights of each component deduced from the PCA analysis performed in Figure IV.2.

Components	Cluster weights 1	Cluster weights 2	Cluster weights 3	Cluster weights 4
1	0.00578 (2.92%)	0.121 (61.28%)	0.00463 (2.34%)	0.0661 (33.45%)
2	5.05 (91.89%)	0.421 (7.67%)	0.00355 (0.06%)	-0.0208 (0.38%)
3	1.18 (43.40%)	-1.14 (42.15%)	0.348 (12.86%)	0.0429 (1.58%)
4	1.33 (46.58%)	-1.14 (39.94%)	-0.377 (13.22%)	-0.00770 (0.27%)

Table A.2. Summary of the cluster weights of each component deduced from the PCA analysis performed in Figure IV.4.

Movie A.1 Structural distortion induced by lithium intercalation. Transformation of a single unit cell of V_2O_5 is characterized by the puckering of the apical oxygen towards the Li-ion, while the vanadium atoms rearrange by moving away. This distortion causes the localization of electron on the vanadium atom, creating a small polaron.

Movie A.2 Lithiation across two particles interconnected to each other

Movie A.3 Lithiation across two particles isolated to each other